



ScuDo
Scuola di Dottorato - Doctoral School
WHAT YOU ARE, TAKES YOU FAR



**UNIVERSITÀ
DEGLI STUDI
DI TORINO**

Doctoral Dissertation
Doctoral Program in Bioengineering and Medical-Surgical Sciences
(31th Cycle)

Ion-containing mesoporous bioactive glass particles for tissue applications

Alessandra Bari

Supervisors

Prof. Chiara Vitale Brovarone
Prof. Sonia Fiorilli, Co-Supervisor

Doctoral Examination Committee:

Prof. Isabel Izquierdo Barba, Referee, Universidad Complutense de Madrid
Prof. Giovanni Vozzi, Referee, Università Di Pisa-Centro Di Ricerca Piaggio

Politecnico di Torino
April 26, 2019

This thesis is licensed under a Creative Commons License, Attribution - Noncommercial - NoDerivative Works 4.0 International: see www.creativecommons.org. The text may be reproduced for non-commercial purposes, provided that credit is given to the original author.

I hereby declare that, the contents and organisation of this dissertation constitute my own original work and does not compromise in any way the rights of third parties, including those relating to the security of personal data.

.....

Alessandra Bari
Turin, April 26, 2019

Summary

The activities performed during the present PhD thesis were focused on the production, synthesis process optimisation and characterisation of calcium silicate mesoporous bioactive glasses (MBGs) that could be used for designing advanced biomedical devices to promote tissue regeneration when the normal healing process is hindered (*i.e.* in the case of a delayed bone healing and non-healing skin wounds).

In particular, the efforts were devoted to enrich the binary composition of these MBGs with different therapeutic ions in order to impart and enhance specific biological functions. The possibility to include these therapeutic species in the MBGs and to tailor their release allows to consider these materials as valid and potent alternatives to the traditional treatment in bone and wound healing applications.

In this context, a library of ion-containing nanomatrices was developed by substituting small amount (1%, 2% or 5% mol) of CaO with the specific ion precursor.

In detail, the following two types of nanomatrices were developed:

- Nano-sized particles (100-200 nm) with pore size of about 4 nm;
- Micro-sized particles (0.5-5 μm) with pore size of about 8 nm.

Both types of nanomatrices were characterized by ordered mesoporous structure with high specific surface area and pore volume, especially for the nano-sized particles, demonstrating that the successful ion incorporation occurred without hampering the formation of the mesostructure. Moreover, the bioactivity test performed on the nanomatrices demonstrated their good reactivity when soaked in Simulated Body Fluid (SBF), confirming that the incorporation of different metallic ions did not affect their ion exchange ability. The ion release test proved that all the nanomatrices were able to release the therapeutic ion with specific kinetics depending on the amount of the incorporated ion, the structural features of the nanomatrices and the release medium.

The second aim was to find the best synthesis procedures in terms of material properties, scalability, safety and cost-efficiency.

In order to achieve this goal, different synthesis procedures were tested. In particular, following the objective of avoiding the use of toxic solvents and enhancing the synthesis yield, a water-based sol-gel procedure using ammonia as

catalyst without sonication was selected as the best route to produce the nano-sized particles.

By following the same aim, the second type of nanomatrices (micro-sized particles) was produced by an aerosol-assisted spray-drying approach under mild acidic conditions due to its scalability and repeatability in an industrial environment.

To reach the final target of developing multifunctional platform able to promote tissue regeneration in the presence of bacterial infection, the MBGs in the SiO₂-CaO system were enriched by the following selected therapeutic ions:

- Copper for its antibacterial, pro-osteogenic and pro-angiogenic effect
- Cerium for the pro-osteogenic and antibacterial potential
- Silver for its well-known antibacterial effect

In this frame, the third aim was to investigate the therapeutic potential of these nanomatrices, in particular their antibacterial effect which was tested through the viable count test using both *Gram positive* (*S. Aureus*) and *Gram negative* (*P. aeruginosa*).

In details, the different sensitivity to Cu-containing samples shown by the bacteria strains was attributed to the differences in the bacteria structure and surfaces. For what concerns the Ce-containing nanomatrices, although the antibacterial test demonstrated a reduction of both *Gram positive* and *Gram negative* bacteria strains, it was not possible to find a clear correlation between the results, the experimental conditions and the bacteria structure. Finally, the antibacterial results of the Ag-containing particles were ascribed to the presence of accessible metal Ag compounds which, through the direct contact and the formation of interactions between silver and the sulfhydryl groups of the bacterial wall, led to the reduction of bacterial viable species by blocking their respiration.

The biological assessment performed on the optimized ion-containing nanomatrices leads to consider the Cu-containing MBGs as the most promising systems due to the possibility to find a proper therapeutic window within which they resulted both biocompatible and antibacterial. Among the Cu-containing MBGs, the MBG_SG_Cu0.5% and MBG_SD_Cu0.5%, providing the best results in terms of biocompatibility, deserve to be taken into account for further investigations, especially in terms of multifunctional systems able to release both therapeutic ion and specific drugs.

Acknowledgment

I would like to acknowledge the people who helped and supported this research work. In particular, I would like to thank the Profs. Chiara Vitale Brovarone and Sonia Fiorilli and all the IRIS group of the Department of Applied Science and Technology of Politecnico di Torino.

Furthermore, part of the experimental work was done in collaboration with other research groups, as reported in detail in the specific chapter, which I would like to thank:

- Department of Materials Science and Engineering, University of Sheffield, Sheffield, UK - Prof. Sheila MacNeil, Dr. Anthony J. Bullock and Dr. Joey Shepherd
- Nobil Bio Ricerche Srl, Portacomaro (AT), Italy - Dr. Marco Morra, Dr. Giorgio Iviglia and Dr. Elisa Torre

*A chi non teme il
cambiamento.*

Table of contents

.....	0
Summary	2
Acknowledgment	4
Table of contents	6
Thesis goals	16
CHAPTER 1	23
State of the Art	23
1.1 Introduction	23
1.2 Biomaterials	24
1.3 Bioactive glasses	24
1.3.1 Bone healing application	32
1.3.2 Wound healing application	33
1.4 Mesoporous bioactive glasses	35
1.4.1 MBG containing therapeutic elements and related biological response	38
CHAPTER 2	63
Materials and methods	63
2.1 Introduction	63
2.2 Synthesis of MBGs assisted by ultrasonication	64
2.2.1 Methanol-based sol-gel synthesis	64
2.2.2 Water-based sol-gel synthesis	65
2.2.2a Ammonium fluoride-catalysed water-based sol-gel synthesis	65
2.2.2b Ammonia-catalysed water-based sol-gel synthesis	66
2.3 Ammonia-catalysed water-based sol-gel synthesis (without sonication)	67
2.4 Synthesis of micro-sized MBG particles assisted by spray-dryer	67
2.5 Morphological, structural and compositional characterization	68
2.5.1 Morphological analysis: Field Emission Scanning Electron Microscopy (FE-SEM) and High-Resolution Transmission Electron Microscopy (HRTEM)	69
2.5.2 Compositional analysis: Energy Dispersive Spectroscopy (EDS), X-ray fluorescence spectroscopy (XRF), X-ray Photoelectron Spectroscopy (XPS) and Inductively Coupled Plasma Atomic Emission Spectrometry (ICP)	71
2.5.3 Textural properties: N ₂ adsorption-desorption measurements	73
2.5.4 Structural analyses: X-Ray Diffraction (XRD) and UV-visible Spectroscopy (UV-vis)	76
2.6 Ion release tests	78
2.6.1 Ion release test performed in SBF	78
2.6.2 Ion release test performed in DMEM	79

2.6.3 Ion release test performed in Tris HCl.....	79
2.7 Bioactivity test	80
2.8 Biological assessment	80
2.8.1 Biocompatibility test of ion-containing nanomatrices	80
2.8.2 Antibacterial tests.....	81
2.8.2.1 Investigation of antibacterial effect of ion-containing sample on <i>E. Coli</i> , <i>S. epidermidis</i> and <i>S. Aureus</i> bacterial planktonic growth using MTT assay	82
2.8.2.2 Investigation of antibacterial effect of ion-containing sample on <i>S. epidermidis</i> biofilm by metabolic activity evaluation	83
2.8.2.3 Investigation of antibacterial effect of ion-containing samples on <i>S. Aureus</i> and <i>P. Aeruginosa</i> by viable count method	85
2.8.2.4 Investigation of antibacterial effect of ion-containing samples on <i>S. aureus</i> and <i>P. aeruginosa</i> biofilm through metabolic activity and biofilm mass evaluation	86
2.8.3 Biological assessment on 3D tissue engineered skin model	87
2.8.3.1 Production of 3D tissue engineered skin model.....	88
2.8.3.2 Biocompatibility test on the 3D tissue engineered skin model.....	88
2.8.3.3 Investigation of antibacterial effect on <i>S. aureus</i> and <i>P. aeruginosa</i> biofilm on infected 3D tissue engineered skin model	89
CHAPTER 3	93
Results and discussion	93
3.1 Introduction.....	93
3.2 Characterization of mesoporous nano-sized matrices produced by ultrasonicator-assisted synthesis.....	94
3.2.1 Methanol-based synthesis results: MBG_US_m nanomatrices	94
3.2.1.1 MBG_US_m_SiO ₂ /CaO matrix.....	95
3.2.1.1a Morphological and structural characterization of MBG_US_m_SiO ₂ /CaO	95
3.2.1.1b Bioactive behaviour of MBG_US_m_SiO ₂ /CaO in SBF	97
3.2.1.2 Copper-containing MBG_US_m: MBG_US_m_Cu2%, MBG_US_m_Cu5%	98
3.2.1.2a Morphological and structural characterization of copper-containing MBG_US_m samples	98
3.2.1.2b Copper ion release from copper-containing MBG_US_m in SBF	103
3.2.1.2c Bioactive behaviour of MBG_US_m_Cu2% in SBF.....	103
3.2.1.2d Antibacterial potential evaluation of MBG_US_m_Cu2%	105
3.2.1.3 Strontium-containing MBG_US_m: MBG_US_m_Sr1%.....	110
3.2.1.3a Morphological and structural characterization of MBG_US_m_Sr1%	111
3.2.1.3b Strontium ion release from MBG_US_m_Sr1% in SBF	113
3.2.1.3c Bioactive behaviour of MBG_US_m_Sr1% in SBF.....	113
3.2.1.4 Strontium-copper co-containing MBG_US_m: MBG_US_m_CuSr2%	114
3.2.1.4a Morphological and structural characterization of MBG_US_m_CuSr2%	115
3.2.1.4b Strontium and copper ion release from MBG_US_m_CuSr2% in SBF	116
3.2.1.4c Bioactive behaviour of MBG_US_m_CuSr2% in SBF	117
3.2.2 Water-based synthesis results: MBG_US_w nanomatrices	119
3.2.2.1 Copper-containing MBG_US_w_I: MBG_US_w_I_Cu2%.....	119
3.2.2.1a Morphological and structural characterization of MBG_US_w_I_Cu2%	120

3.2.2.1b	Copper ion release from MBG_US_w_I_Cu2% in DMEM.....	122
3.2.2.2	Silver-containing MSn: MSn_US_w_I_Ag2%*.....	123
3.2.2.2a	Morphological and structural characterization of MSn_US_w_I_Ag2%*	123
3.2.2.2b	Silver ion release from MSn_US_w_I_Ag2%* in DMEM	126
3.2.2.3	Cerium-containing MSn_US_w_I: MSn_US_w_I_Ce2%*	126
3.2.2.3a	Morphological and structural characterization of MSn_US_w_I_Ce2%*	126
3.2.2.2b	Cerium ion release from MSn_US_w_I_Ce2%* in DMEM	129
3.2.2.4	Un-doped MBG_US_w_II: MBG_US_w_II_SiO ₂ /CaO.....	129
3.2.2.4a	Morphological and structural characterization of MBG_US_w_II_ SiO ₂ /CaO	130
3.3	Morphological and structural characterization of optimized sol-gel nanomaterials ..	132
3.3.1	Morphological and structural characterization of base-catalysed sol-gel nanomaterials	132
3.3.1.1	Copper-containing MBG_SG: MBG_SG_Cu2%	132
3.3.1.1a	Morphological and structural characterization of MBG_SG_Cu2%	133
3.3.1.1b	Copper ion release from MBG_SG_Cu2% in Tris HCl	135
3.3.1.1c	Bioactive behaviour of MBG_SG_Cu2% in SBF.....	135
3.3.1.2	Cerium-containing MBG_SG: MBG_SG_Ce1% and MBG_SG_Ce2% ..	136
3.3.1.2a	Morphological and structural characterization of cerium-containing MBG_SG samples	137
3.3.1.2b	Cerium ion release from cerium-containing MBG_SG samples in Tris HCl	138
3.3.1.2c	Bioactive behaviour of cerium-containing MBG_SG samples in SBF..	139
3.3.1.3	Silver-containing MBG_SG: MBG_SG_Ag0.1% and MBG_SG_Ag2% ..	139
3.3.1.3a	Morphological and structural characterization of silver-containing MBG_SG samples	140
3.3.1.3b	Silver ion release from silver-containing MBG_SG samples in Tris HCl	142
3.3.2	Morphological and structural characterization of aerosol-assisted spray-drying nanomaterials	143
3.3.2.1	Un-doped MBG_SD: MBG_SD_SiO ₂ /CaO	143
3.3.2.1a	Morphological and structural characterization of MBG_SD_SiO ₂ /CaO	144
3.3.2.1b	Bioactive behaviour of MBG_SD_SiO ₂ /CaO in SBF.....	146
3.3.2.2	Copper-containing MBG_SD: MBG_SD_Cu2%	146
3.3.2.2a	Morphological and structural characterization of MBG_SD_Cu2%	147
3.3.2.2b	Copper ion release from MBG_SD_Cu2% in Tris HCl	149
3.3.2.2c	Bioactive behaviour of MBG_SD_Cu2% in SBF.....	150
3.3.2.3	Strontium-containing MBG_SD: MBG_SD_Sr1%	151
3.3.2.3a	Morphological and structural characterization of MBG_SD_Sr1%	151
3.3.2.3b	Strontium ion release from MBG_SD_Sr1% in SBF	153
3.3.2.3c	Bioactive behaviour of MBG_SD_Sr1% in SBF.....	153
3.3.2.4	Strontium-copper co-containing MBG_SD: MBG_SD_CuSr2%	155
3.3.2.4a	Morphological and structural characterization of MBG_SD_CuSr2%..	155
3.3.2.4b	Strontium and copper ion release from MBG_SD_CuSr2% in SBF	156
3.3.2.4c	Bioactive behaviour of MBG_SD_CuSr2% in SBF	157
3.3.2.5	Cerium-containing MBG_SD: MBG_SD_Ce1% and MBG_SD_Ce2% ..	158

3.3.2.5a Morphological and structural characterization of cerium-containing MBG_SD.....	158
3.3.2.5b Cerium ion release from MBG_SD_Ce1% and from MBG_SD_Ce2% in Tris HCl.....	160
3.3.2.5c Bioactive behaviour of cerium-containing MBG_SD samples in SBF..	161
3.3.2.6 Silver-containing MBG_SD: MBG_SD_Ag0.1% and MBG_SD_Ag2%.	161
3.3.2.6a Morphological and structural characterization of silver-containing MBG_SD samples.....	162
3.3.2.6b Silver ion release from MBG_SD_Ag0.1% and MBG_SD_Ag2% in Tris HCl.....	164
3.3.2.7 Cerium-containing silica SD: MSm_SD_Ce2%*.....	164
3.3.2.7a Morphological and structural characterization of MSm_SD_Ce2%*....	165
3.3.2.7b Cerium ion release from MSm_SD_Ce2%* in DMEM.....	167
3.3.2.8 Silver-containing silica SD: MSm_SD_Ag2%*.....	168
3.3.2.8a Morphological and structural characterization of MSm_SD_Ag2%* ...	168
3.3.2.8b Silver ion release from MSm_SD_Ag2%* in DMEM.....	171
3.4 Final considerations.....	171
CHAPTER 4.....	179
Antibacterial tests of ion-substituted nano- and micro-sized MBGs.....	179
4.1 Introduction.....	179
4.2 Antibacterial property of MBG_SD_Cu2% and MBG_SG_Cu2% against planktonic bacteria.....	181
4.3 Antibacterial property of MBG_SD_Ce2% and MBG_SG_Ce2% against planktonic bacteria.....	182
4.4 Antibacterial property of MBG_SD_Ag2% and MBG_SG_Ag2% against planktonic bacteria.....	184
CHAPTER 5.....	188
Biological assessment of optimized ion-containing nanomatrices.....	188
5.1 Introduction.....	188
5.1.1 Biological assessment of Cu-containing nano- and micro-sized MBGs.....	189
5.1.1.1a Biocompatibility of MBG_SG_Cu2% and MBG_SD_Cu2%.....	189
5.1.1.1b Antibacterial activity of MBG_SG_Cu2% against bacterial biofilms...	190
5.1.1.1c Biological assessment of MBG_SG_Cu2% on 3D skin models.....	192
5.1.1.2 Biocompatibility test results of MBG_SG_Cu0.5% and MBG_SD_Cu0.5%.....	193
5.1.2 Biocompatibility test results of Ce-containing nanomatrices.....	194
5.1.3 Biocompatibility test results of Ag-containing nanomatrices.....	195
5.2 Final considerations.....	196
CHAPTER 6.....	198
Conclusions and perspectives.....	198
Ringraziamenti.....	202

List of Tables

Table 1.1: Some of material characteristics which may influence the host response.....	26
Table 1.2: Some of the main host response phenomena to biomaterials.....	27
Table 2.1: Sample composition and reagent amount used in the methanol-based ultrasonicator-assisted sol-gel synthesis.....	65
Table 2.2: Sample composition and reagent amount used in the water-based ultrasonicator-assisted sol-gel procedure, using NH ₄ F as catalyst.....	66
Table 2.3: Sample composition and reagent amount used in the water-based ultrasonicator-assisted sol-gel procedure, using NH ₄ OH as catalyst.....	66
Table 2.4: Sample composition and reagent amount used in the water-based sol-gel procedure, using NH ₄ OH as catalyst.....	67
Table 2.5: Sample composition and reagent amount used in the spray-drying synthesis....	68
Table 2.6: Experimental setup of ion release test in SBF.....	79
Table 2.7: Experimental setup of ion release test in DMEM.....	79
Table 2.8: Experimental setup of ion release test in Tris HCl.....	80
Table 3.1: List of MBG_US_m compositions.....	95
Table 3.2: Structural features of MBG_US_m_SiO ₂ /CaO.....	96
Table 3.3: Structural features of copper-containing samples.....	101
Table 3.4: Deconvoluted contributions of Cu2p core level and relative percentages.....	102
Table 3.5: Structural features of MBG_US_m_Sr1%.....	112
Table 3.6: Structural features of MBG_US_m_CuSr2%.....	116
Table 3.7: Composition of samples produced by water-based ultrasonicator-assisted sol-gel routes.....	119
Table 3.8: Structural features of MBG_US_w_I_Cu2%.....	122
Table 3.9: Structural features of MSn_US_w_I_Ag2%*.....	124
Table 3.10: Structural features of MSn_US_w_I_Ce2%*.....	128
Table 3.11: Structural features of MBG_US_w_II_SiO ₂ /CaO.....	131
Table 3.12: List of MBG_SG compositions.....	132
Table 3.13: Structural features of MBG_SG_Cu2%.....	134
Table 3.14: Structural features of cerium-containing of MBG_SG.....	138
Table 3.15: Silver-containing MBG_SG nanoparticles.....	140
Table 3.16: Structural features of silver-containing MBG_SG.....	141
Table 3.17: List of MBG_SD compositions.....	143
Table 3.18: Structural features of MBG_SD_SiO ₂ /CaO.....	145
Table 3.19: Structural features of MBG_SD_Cu2%.....	149
Table 3.20: Structural features of MBG_SD_Sr1%.....	153
Table 3.21: Structural features of MBG_SD_CuSr2%.....	156
Table 3.22: Structural features of cerium-containing of MBG_SD.....	160
Table 3.23: Structural features of silver-containing MBG_SD.....	163
Table 3.24: Structural features of MSm_SD_Ce2%*.....	166
Table 3.25: Structural features of MSm_SD_Ag2%*.....	170
Table 4.1: Summary of Cu ²⁺ released in Tris HCl.....	181
Table 4.2: Summary of Ag ⁺ release in Tris HCl.....	184

List of Figures

Figure: Thesis goals.....	18
Figure 1.1: Sequence of events which occurred during the inflammation and wound healing processes.....	28
Figure 1.2: Sequence of reactions at the interface of a bioactive material and body fluid.....	30
Figure 1.3: Physiological bone healing process.....	32
Figure 1.4: Physiological wound healing process.....	34
Figure 1.5: Mesoporous structure formation using CTAB (hexadecyltrimethylammonium bromide) as surfactant.....	36
Figure 1.6: Schematic phase diagram of CTAB.....	37
Figure 1.7: MBG synthesis through EISA process.....	37
Figure 1.8: Therapeutic effects of the most used metallic ions.....	39
Figure 1.9: Mechanism of action of copper ion released.....	41
Figure 1.10: Role of the calcium sensing receptor.....	44
Figure 1.11: Actions of strontium on osteoblast differentiation (A) and on osteoclast differentiation (B).....	45
Figure 1.12: Schematic representation of the molecular mechanism of migration and differentiation of BMSCs induced by cerium.....	48
Figure 1.13: Link between osteoporosis and magnesium deficiency.....	49
Figure 1.14: Antibacterial mode of action of silver particles.....	50
Figure 1.15: Osteoblastic bone formation mechanism influenced by zinc.....	51
Figure 1.16: Osteoclastic bone resorption mechanism influenced by zinc.....	52
Figure 1.17: Summary of relevant biological effects of therapeutic ions.....	53
Figure 2.1: Flow chart of the synthesis procedure selection process.....	64
Figure 2.2: FE-SEM functioning (A) and interaction between the electron beam and the sample (B).....	69
Figure 2.3: Physisorption isotherm classification.....	74
Figure 2.4: Hysteresis loop classification.....	75
Figure 2.5: Diffraction phenomenon.....	76
Figure 2.6: Viable count method experimental conditions.....	86
Figure 2.7: Experimental setup of antibacterial test against <i>S. aureus</i> and <i>P. aeruginosa</i> biofilm.....	87
Figure 3.1: FE-SEM image, EDS spectrum and atomic % (inset) of MBG_US_m_SiO ₂ /CaO.....	95
Figure 3.2: N ₂ adsorption-desorption isotherm of MBG_US_m_SiO ₂ /CaO and related DFT pore size distribution (inset).....	96
Figure 3.3: Wide-angle XRD spectrum of MBG_US_m_SiO ₂ /CaO.....	97
Figure 3.4: FE-SEM images of MBG_US_m_SiO ₂ /CaO after 1 day (A) and 7 days of soaking in SBF (B) and related EDS spectra (C, D).....	98
Figure 3.5: FE-SEM image of MBG_US_m_Cu2% (A), EDS spectrum (B), TEM image (C) and EDS mapping analysis of MBG_US_m_Cu2% (D); FE-SEM image of MBG_US_m_Cu5% (E), related EDS spectrum (inset), TEM image of MBG_US_m_Cu5% (F).....	100
Figure 3.6: N ₂ adsorption-desorption isotherms of MBG_US_m_Cu2% (red) and MBG_US_m_Cu5% (green).....	101

Figure 3.7: Wide-angle XRD spectrum of MBG_US_m_Cu2% (red) and MBG_US_m_Cu5% (green).....	101
Figure 3.8: XPS deconvoluted spectra in the Cu2p3/2 region for MBG_US_m_Cu2% (A) and MBG_US_m_Cu5% (B).....	102
Figure 3.9: Cu ²⁺ release profiles of MBG_US_m_Cu2% (black) and MBG_US_m_Cu5% (red) in SBF.....	103
Figure 3.10: FE-SEM images of MBG_US_m_Cu2% after 3 days (A) and 7 days (B) of soaking in SBF and XRD pattern of MBG_US_m_Cu2% after soaking in SBF for 7 days (C); EDS spectra of MBG_US_m_Cu2% after 3 days (D') and 7 days (D'') of soaking in SBF.....	105
Figure 3.11: Dose-dependence viability of E. coli RB, S. aureus 8325-4 and S. epidermidis RP62A bacterial strains cultured with MBG_US_m_SiO ₂ /CaO and MBG_US_m_Cu2% suspensions.....	107
Figure 3.12: Dose-dependence viability of E. coli RB, S. aureus 8325-4 and S. epidermidis RP62A bacterial strains cultured with MBG_US_m_SiO ₂ /CaO and MBG_US_m_Cu2% extracts collected after 3h (A) and after 24h (B).....	108
Figure 3.13: Bacterial viability and morphology of biofilms treated with MBG_US_m_SiO ₂ /CaO and MBG_US_m_Cu2% suspensions (2 mg/mL): effect on S. epidermidis RP62A biofilm formation cultures (A, B) and effect on the formation of a stable staphylococcal biofilm (C, D).....	109
Figure 3.14: Bacterial viability and morphology of biofilms treated with extracts of MBG_US_m_SiO ₂ /CaO and MBG_US_m_Cu2%: effect of undiluted supernatants collected at 24 h on S. epidermidis RP62A biofilm growing cultures (A, B) and on the formation of a stable staphylococcal biofilm (C, D).....	110
Figure 3.15: FE-SEM image of MBG_US_m_Sr1%.....	111
Figure 3.16: EDS spectrum of MBG_US_m_Sr1%.....	111
Figure 3.17: N ₂ adsorption-desorption isotherm of MBG_US_m_Sr1% and related DFT pore size distribution (inset).....	112
Figure 3.18: Sr ²⁺ release profile of MBG_US_m_Sr1% in SBF.....	113
Figure 3.19: FE-SEM image of MBG_US_m_Sr1% after 7 days of soaking in SBF and its magnification.....	114
Figure 3.20: FE-SEM image of MBG_US_m_CuSr2% and related EDS spectrum (inset).....	115
Figure 3.21: N ₂ adsorption-desorption isotherm of MBG_US_m_CuSr2% and related DFT pore size distribution of (inset).....	116
Figure 3.22: Ion release curve of MBG_US_m_CuSr2%.....	117
Figure 3.23: MBG_US_m_CuSr2% after 7 days of soaking in SBF with EDS spectrum (inset).....	118
Figure 3.24: Wide-angle XRD spectra of MBG_US_m_CuSr2% before soaking in SBF(A) and MBG_US_m_CuSr2% after 7 days of soaking in SBF (B).....	118
Figure 3.25: FE-SEM image of MBG_US_w_I_Cu2%.....	120
Figure 3.26: EDS spectrum of MBG_US_w_I_Cu2%.....	120
Figure 3.27: EDS mapping of MBG_US_w_I_Cu2%.....	121
Figure 3.28: N ₂ adsorption-desorption isotherm of MBG_US_w_I_Cu2% and DFT pore size distribution of MBG_US_w_I_Cu2% (inset).....	122
Figure 3.29: Cu ²⁺ release profile of MBG_US_w_I_Cu2% in DMEM.....	123
Figure 3.30: FE-SEM image of MSn_US_w_I_Ag2%* and related EDS spectrum.....	124

Figure 3.31: N ₂ adsorption-desorption isotherm of MSn_US_w_I_Ag2%* and related DFT pore size distribution (inset).....	124
Figure 3.32: Diffuse reflectance UV–vis spectrum of MSn_US_w_I_Ag2%*.....	125
Figure 3.33: Wide-angle XRD spectrum of MSn_US_w_I_Ag2%*.....	125
Figure 3.34: Ag ⁺ release profile of MSn_US_w_I_Ag2%* in DMEM.....	126
Figure 3.35 FE-SEM image of MSn_US_w_I_Ce2%*.....	127
Figure 3.36: N ₂ adsorption-desorption isotherm of MSn_US_w_I_Ce2%* and related DFT pore size distribution (inset).....	127
Figure 3.37: Diffuse reflectance UV–vis spectrum of MSn_US_w_I_Ce2%*.....	128
Figure 3.38: Wide-angle XRD spectrum of MSn_US_w_I_Ce2%*.....	129
Figure 3.39: Ce ³⁺ release profile of MSn_US_w_I_Ce2%* in DMEM.....	129
Figure 3.40: FE-SEM image of MBG_US_w_II_SiO ₂ /CaO and related EDS spectrum.....	130
Figure 3.41: N ₂ adsorption-desorption isotherm of MBG_US_w_II_SiO ₂ /CaO and DFT pore size distribution of MBG_US_w_II_SiO ₂ /CaO (inset).....	131
Figure 3.42: FE-SEM image of MBG_SG_Cu2% (A), EDS mapping analysis of MBG_SG_Cu2% single particle (B), EDS spectrum of MBG_SG_Cu2% (C).....	133
Figure 3.43: Wide-angle XRD spectrum of MBG_SG_Cu2%.....	134
Figure 3.44: N ₂ adsorption-desorption isotherm of MBG_SG_Cu2% and related DFT pore size distribution (inset).....	134
Figure 3.45: Cu ²⁺ release curve of MBG_SG_Cu2% in Tris HCl.....	135
Figure 3.46: FE-SEM image of MBG_SG_Cu2% after 7 days of soaking in SBF.....	136
Figure 3.47: Wide-angle XRD of MBG_SG_Cu2% after 7 days of soaking in SBF.....	136
Figure 3.48: FE-SEM images of MBG_SG_Ce1% (A) and MBG_SG_Ce2% (B).....	137
Figure 3.49: N ₂ adsorption-desorption isotherm of MBG_SG_Ce1% (A) and MBG_SG_Ce2% (B); DFT pore size distribution of MBG_SG_Ce1% (C) and MBG_SG_Ce2% (D).....	138
Figure 3.50: Ce ³⁺ release profiles of MBG_SG_Ce1% (A) and MBG_SG_Ce2% (B)....	139
Figure 3.51: FE-SEM images of MBG_SG_Ag0.1% (A) and MBG_SG_Ag2%.....	140
Figure 3.52: N ₂ adsorption-desorption isotherm of MBG_SG_Ag0.1% (A) and MBG_SG_Ag2% (B); DFT pore size distribution of MBG_SG_Ag0.1% (C) and MBG_SG_Ag2% (D).....	141
Figure 3.53: Wide-angle XRD spectrum of MBG_SG_Ag0.1% (A) and MBG_SG_Ag2% (B).....	142
Figure 3.54: Silver ion release from MBG_SG_Ag0.1% (A) and from MBG_SG_Ag2% (B).....	142
Figure 3.55: FE-SEM image of MBG_SD_SiO ₂ /CaO.....	144
Figure 3.56: N ₂ adsorption-desorption isotherm of MBG_SG_SiO ₂ /CaO and related DFT pore size distribution.....	145
Figure 3.57: Wide-angle XRD analysis of MBG_SD_SiO ₂ /CaO.....	145
Figure 3.58: FE-SEM (A) and EDS spectrum (B) of MBG_SD_SiO ₂ /CaO after 7 days of soaking in SBF.....	146
Figure 3.59: FE-SEM image of MBG_SD_Cu2% (A), EDS mapping analysis of MBG_SD_Cu2% single particle (B), EDS spectrum of MBG_SD_Cu2% (C).....	147
Figure 3.60: Wide-angle XRD analysis of MBG_SD_Cu2%.....	148
Figure 3.61: N ₂ adsorption-desorption isotherm of MBG_SD_Cu2% and related DFT pore size distribution (inset).....	148
Figure 3.62: Cu ²⁺ release curve of MBG_SD_Cu2% in Tris HCl.....	149
Figure 3.63: FE-SEM of MBG_SD_Cu 2% after 14 day of soaking in SBF (A) and high magnification of A image (B).....	150

Figure 3.64: Wide-angle XRD analysis of MBG_SD_Cu2%.....	150
Figure 3.65 FE-SEM image of MBG_SD_Sr1% and related EDS spectrum.....	151
Figure 3.66: Elemental mapping of MBG_SD_Sr1% particle: SEM image of the analysis area (A), and distribution of silicon (B), calcium (C) and strontium (D).....	152
Figure 3.67: N ₂ adsorption-desorption isotherm of MBG_SD_Sr1% and related DFT pore size distribution (inset).....	152
Figure 3.68: Sr ²⁺ release curve of MBG_SD_Sr1% in SBF.....	153
Figure 3.69: FE-SEM images of MBG_SD_Sr1% after 1 day (A) and 7 days (B) of soaking in SBF.....	154
Figure 3.70: Wide-angle XRD analysis of MBG_SD_Sr1% after 7 days of soaking in SBF.....	154
Figure 3.71: FE-SEM image of MBG_SD_CuSr2% with related EDS spectrum (inset)..	155
Figure 3.72: N ₂ adsorption-desorption isotherm of MBG_SD_CuSr2% and related DFT pore size distribution (inset).....	156
Figure 3.73: Ion release curve of MBG_SD_CuSr2%.....	157
Figure 3.74: MBG_SD_CuSr2% after 7 days of soaking in SBF with EDS spectrum (inset).....	157
Figure 3.75: MBG_SD_CuSr2% before soaking in SBF (A) and MBG_SD_CuSr2% after 7 days of soaking in SBF (B).....	158
Figure 3.76: FE-SEM image of MBG_SD_Ce1% (A) and MBG_SD_Ce2% (B).....	159
Figure 3.77: N ₂ adsorption-desorption isotherm of MBG_SD_Ce1% (A) and MBG_SD_Ce2% (B); DFT pore size distribution of MBG_SD_Ce1% (C) and MBG_SD_Ce2% (D).....	159
Figure 3.78: Ce ³⁺ release profiles of MBG_SD_Ce1% (A) and MBG_SD_Ce2% (B)....	160
Figure 3.79: Wide-angle XRD analysis of MBG_SD_Ce2% after 14 days of soaking in SBF.....	161
Figure 3.80: FE-SEM images of MBG_SD_Ag0.1% (A) and MBG_SD_Ag2% (B).....	162
Figure 3.81: N ₂ adsorption-desorption isotherm of MBG_SD_Ag0.1% (A) and MBG_SD_Ag2% (B); DFT pore size distribution of MBG_SD_Ag0.1% (C) and MBG_SD_Ag2% (D).....	163
Figure 3.82: Wide-angle XRD spectra of MBG_SD_Ag0.1% (A) and MBG_SD_Ag2% (B).....	164
Figure 3.83: Ag ⁺ release profiles of MBG_SD_Ag0.1% (A) and MBG_SD_Ag2% (B)..	164
Figure 3.84: FE-SEM image of MSm_SD_Ce2%*.....	165
Figure 3.85: EDS spectrum of MSm_SD_Ce2%*.....	165
Figure 3.86: N ₂ adsorption-desorption isotherm of MSm_SD_Ce2%* and related DFT pore size distribution (inset).....	166
Figure 3.87: Diffuse reflectance UV-vis spectrum of MSm_SD_Ce2%*.....	166
Figure 3.88: Wide-angle XRD spectrum of MSm_SD_Ce2%*.....	167
Figure 3.89: Ce ³⁺ release profile of MSm_SD_Ce2%* in DMEM.....	168
Figure 3.90: FE-SEM image of MSm_SD_Ag2%*.....	168
Figure 3.91: EDS spectrum of MSm_SD_Ag2%* and related element atomic %	169
Figure 3.92: N ₂ adsorption-desorption isotherm of MSm_SD_Ag2%* and related DFT pore size distribution (inset).....	169
Figure 3.93: Diffuse reflectance UV-vis spectrum of MSm_SD_Ag2%*.....	170
Figure 3.94: Wide-angle XRD spectrum of MSm_SD_Ag2%*.....	171
Figure 3.95: Ag ⁺ release profile of MSm_SD_Ag2%* in DMEM.....	171

Figure 4.1: Survival rate of S235 after exposure to MBG_SD_Cu2%, MBG_SG_Cu2% and related extracts after 1 day, 3 days and the 8 days of soaking.....	181
Figure 4.2: Survival rate of SOM1 after exposure to MBG_SD_Cu2%, MBG_SG_Cu2% and related extracts after 1 day, 3 days and 8 days of soaking.....	182
Figure 4.3: Survival rate of S235 after exposure to MBG_SD_Ce2%, MBG_SG_Ce2% and related extracts after 1 day, 3 days and the 8 days of soaking.....	183
Figure 4.4: Survival rate of SOM1 after exposure to MBG_SD_Ce2%, MBG_SG_Ce2% and related extracts after 1 day, 3 days and the 8 days of soaking.....	184
Figure 4.5: Survival rate of S235 after exposure to MBG_SD_Ag2%, MBG_SG_Ag2% and related extracts after 1 day, 3 days and the 8 days of soaking.....	185
Figure 4.6: Survival rate of SOM1 after exposure to MBG_SD_Ag2%, MBG_SG_Ag2% and related extracts after 1 day, 3 days and the 8 days of soaking.....	185
Figure 5.1: Quantification of cell viability through MTT assay for MBG_SG_Cu2% and MBG_SD_Cu2% compared with polystyrene (negative control) (A); optical images of cells after 72 h of incubation with MBG_SG_Cu2% and MBG_SD_Cu2% at concentration of 100 µg/mL, compared to cells seeded on polystyrene plate (B).....	190
Figure 5.2: MBG_SG_Cu2% preventive action on the formation of biofilms using the measure of bacterial metabolic activity (A) MBG_SG_Cu2% ability to disrupt pre-existing biofilms using the measure of bacterial metabolic activity (B) MBG_SG_Cu2% preventive action on the formation of biofilms using the measure of optical density of the biofilm with higher values indicating greater biofilm formation (C) MBG_SG_Cu2% ability to disrupt pre-existing biofilms using the measure of optical density of the biofilm with higher values indicating biofilm formation to larger extent (D). n=3, error bars = SEM, ANOVA statistics.....	191
Figure 5.3: Cytotoxicity of MBG_SG_Cu2% sample and industrial standard Acticoat Flex 3 [®] after 24 h of incubation with the tissue engineered skin models.....	192
Figure 5.4: MBG_SG_Cu2% preventive action on the formation of biofilms on the infected 3D skin model (A) and MBG_SG_Cu2% ability to disrupt pre-existing biofilms on the infected 3D skin model (B). n = 3, plotting mean ± standard deviation, ANOVA statistics used.....	193
Figure 5.5: Quantification of cell viability through MTT assay for MBG_SG_Ce1%, MBG_SD_Ce1%, MBG_SG_Ce2% and MBG_SD_Ce2% compared with polystyrene (negative control) (A); optical images of cells after 72 h of incubation with MBG_SG_Ce1%, MBG_SD_Ce1%, MBG_SG_Ce2% and MBG_SD_Ce2% at concentration of 1 mg/mL, compared to cells seeded on polystyrene plates (B).....	194
Figure 5.6: Optical images of cells after 72 h of incubation with MBG_SG_Ag_2%, at concentration of 1 mg/mL, compared to cells seeded on polystyrene plates.....	195
Figure 5.7: Quantification of cell viability through MTT assay for MBG_SG_Ag2% compared with polystyrene (negative control).....	195

Thesis goals

Natural and synthetic materials have been used in the biomedical field in the last decades in order to replace or repair damaged tissues [1]. Different studies have been conducted in this field and, based on the obtained results and the specific needs that have changed over the time, the definition and the type of developed biomaterials have adapted to the requirements. The combination of materials science and biological science knowledge led to the final concept of biomaterial that is now defined as an engineered substance which has to direct a specific positive interaction when in contact with the human body. Within the field of biomaterials, bioactive bioceramics show the higher biocompatibility and the ability to induce the formation of a hydroxyapatite layer, similar to the natural component of bone [2]. Inside this major class, bioactive glasses have gathered an even higher interest. First invented in 1967 by Larry Hench, bioactive glasses have been used in commercial formulations for different applications, such as tooth root repair and ear prostheses. Over the years, the morphological and textural features of bioactive glasses have been modified in order to improve their biological performances.

In particular, a promising class of bioactive glasses is represented by Mesoporous Bioactive Glasses (MBGs) which paved the way for multifunctional bioactive materials, since their first appearance in 2004 [3]. These biomaterials, prepared for the first time by Prof. Dr Zhao's research group, were produced by combining the sol-gel method with supramolecular chemistry of surfactants and presented a highly ordered structure with uniform pore size leading to excellent bone-forming bioactivity. Thanks to the very high surface area and pore volume, which are typical properties of these materials, MBGs are gaining increasing interest in the field of tissue regeneration, as in addition to the bioactive properties, they can host drug molecules of different size, due to the tailorable pore size, and can release them with controlled kinetics [4,5].

A big step forward in this context is represented by the incorporation of therapeutic ions in the glass network of the MBGs in order to impart and enhance specific functions. Since the biological effect of some therapeutic ions (*i.e.* pro-osteogenic, pro-angiogenic and antibacterial effects) is well-known [6], the possibility to include these species in MBG composition and to release them in a

tailorable way make these materials interesting candidates for biomedical applications. By comparing them with drugs and growth factors, the therapeutic ions have the following advantages:

- 1) They are less prone to the alteration during the manufacturing;
- 2) They could modify cellular functions by interacting with other ions through the activation of ion channels or by binding with macromolecules;
- 3) They are cheaper than the growth factors and recombinant proteins.

These characteristics make these species valid and potent alternatives to the traditional treatments in bone and wound healing applications. In fact, the traditional treatments, which consist in bone grafting procedures and wound dressings, are not always suitable/sufficient to allow the full recovery, as extensively described in chapter 1. To deal with these types of disease, pro-osteogenic and/or pro-angiogenic effects are only two of the requested properties. In addition, to treat these pathologies and avoid the non-healing and inflammation problems, it is important to guarantee an antibacterial effect [7].

In this scenario, the MOZART project (Mesoporous matrices for localized pH-triggered release of therapeutic ions and drugs) was defined and planned. The final objective of this project, funded by the European Community (programme Horizon 2020) and coordinated by Politecnico di Torino (Prof. C. Vitale-Brovarone), is to develop a library of mesoporous inorganic nanomatrices (MBGs and ordered mesoporous carbons, OMCs) containing therapeutic ions and loaded with specific drugs to be used as multifunctional platform in the treatment of delayed bone healing and non-healing skin wounds. In MOZART, the release of ions and drugs is triggered by a self-immolative polymer and the incorporation in a thermosensitive gel allows to introduce and maintain the particles in the site of interest.

In this context, the present PhD thesis was focused on the study of the influence of different synthesis routes and the incorporation of ion on the morphology and structure of the developed MBGs. Moreover, the *in vitro* biological assessment allowed the evaluation of the full potential of these MBGs as biomaterials.

In particular, the first aim of this PhD thesis was to produce calcium silicate mesoporous bioactive glass (MBG) particles containing different amount of therapeutic ions that could be used for designing advanced biomedical devices in tissue regeneration (*i.e.* the delayed bone healing and non-healing skin wounds). The developed MBG particles will be referred to nanomatrices within the whole thesis due to the presence of nanopores of regular size and shape.

The second aim was to find the best synthesis procedures in terms of material properties, scalability, safety and cost-efficient synthesis routes.

The third aim was to investigate the therapeutic potential of these nano- and micro-sized matrices, in particular their antibacterial effect.

In the following figure, the thesis goals are displayed.

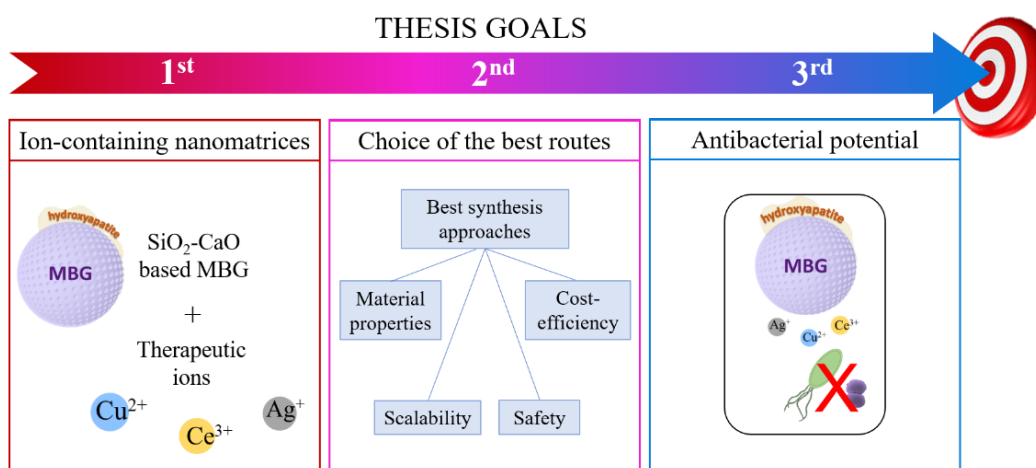


Figure: Thesis goals

In order to achieve these goals, the activities performed during my PhD were devoted to the optimisation of the synthesis procedures, as well as on the study regarding the most suitable amount of the ions needed for each targeted application and, finally, on the preliminary studies of the antibacterial properties of the ion-containing MBGs.

MBGs in the binary system ($\text{SiO}_2\text{-CaO}$) were produced by using different synthesis routes, in order to obtain a library of materials with high specific surface area (in the range of hundreds m^2/g) and accessible pore volume, characterised by different pore size and morphology.

In details, the synthesis procedures were improved based on the results of the morphological and compositional characterisation and the release properties. Furthermore, with the aim to obtain scalable nanomaterials, the final selection of the synthesis routes was completed, by discarding those involving the use of toxic chemical reagents and several synthesis steps. During this selection process, the recommendations provided by Nanolith, an industrial partner of the MOZART consortium, were followed, in view of the effective scaling-up of the procedures in an industrial relevant environment (TRL 5). Among the explored routes, a procedure based on the aerosol assisted spray-drying approach was adopted with the final aim to obtain a water-based process under mild acidic conditions [8]. Furthermore, this approach is particularly attractive due to its scalability and repeatability in an industrial environment. The particles obtained through this procedure have micrometric dimension ($0.5\text{-}5\ \mu\text{m}$) and pores ranging between $7\text{-}8\ \text{nm}$.

In order to obtain smaller particles, in the range of $100\text{-}200\ \text{nm}$ with pores ranging between $2\ \text{and}\ 4\ \text{nm}$, a second synthesis approach was developed by testing different procedures, as reported in chapter 2. In details, aiming to achieve both the reduction of the toxic solvents and an enhanced synthesis yield, the initial ultrasound-assisted method using methanol as solvent [9] was replaced by water-based ultrasound-assisted methods. Subsequently, based on the cost-analysis conducted by Nanolith, the ultra-sonication step was also removed. Based on the

characterisation results, the water-based sol-gel procedure using ammonia as catalyst was chosen to produce the second type of MBGs [10].

To reach the target of developing a multifunctional platform able to promote tissue regeneration in the presence of bacterial infection, the selected therapeutic ions were:

- Copper for its antibacterial, pro-osteogenic and pro-angiogenic effect [11]
- Cerium for the pro-osteogenic and antibacterial potential [12]
- Silver for its well-known antibacterial effect [13]

In this study, the antibacterial effect of these ions has been considered crucial to face the complications induced by the presence of bacteria in an open fracture or in a chronic wound and the current limitations and problems regarding the administration of antibiotics (resistant bacteria, cost) [14].

Focusing on chronic wounds, when the skin is not intact, bacteria could exceed the limits considered normal and the commensal microfloras of the human body could colonise in a pathogenic way. Although this still represents an open issue, it seems that a level of bacteria growth $> 10^5$ organisms per gram of human tissue (also called colony forming unit, CFU) leads to wound infection [15,16]. When the equilibrium between internal bacteria and host response is unbalanced, the normal healing process of open fracture and wound could proceed in a compromised way, leading to a delay in the recovery, morbidity, mortality and overall to an increase in the treatment cost [16,17]. Biomedical materials with antibacterial properties should be able to reduce/prevent the bacteria colonisation. For this reason, usually antibacterial tests are performed on materials to understand their antibacterial potential.

In this context, during my research activity, several antibacterial tests were conducted aiming to understand the potential of the MBG nanomatrices. Among them, some antibacterial tests were carried out in a more physiologically relevant environment (3D skin model) to obtain a more detailed overview of both antibacterial potential and toxic effect of the developed nanomatrices. A preliminary antibacterial evaluation was carried out in collaboration with the *Department of Materials Science and Engineering of University of Sheffield*, during my six months period in Sheffield in the group of Prof. Sheila MacNeil (consortium partner in the MOZART project). Different types of antibacterial tests and experimental setups were explored in order to evaluate and optimize the proper conditions for testing the nanomatrices, as described in chapter 2. The antimicrobial potentials of the MBG particles and of the released ions were studied by viable count method using strains of *S. aureus* and *P. aeruginosa* (that are considered the most common bacteria strains in open wound [18]).

To study the biological response of the developed MBGs, *in vitro* biological tests were carried out in collaboration with *Nobil Bio Ricerche Srl* and the *Department of Materials Science and Engineering of the University of Sheffield*, both consortium partners in the MOZART project. The test procedures are reported in chapter 2; whereas, the results are reported and discussed in the chapter 5.

Nobil Bio Ricerche Srl assessed the cytocompatibility of the ion-containing nano- and micro-sized MBG particles through qualitatively and quantitatively evaluation. The effect exerted by the nanomatrices on fibroblast cells were explored by direct observation under the inverted microscope and MTT measurements.

In addition to the antibacterial test, Prof. Sheila MacNeil's research group at the *Department of Materials Science and Engineering* of the *University of Sheffield* dealt with the manufacturing of 3D skin models, prepared according to MacNeil et al. [19], which were then exploited in order to assess the biocompatibility of the nanomatrices and, after causing an infection, their antibacterial potential. The related results are presented in chapter 5.

References

- [1] D.F. Williams, On the nature of biomaterials, *Biomaterials*. 30 (2009) 5897–5909. doi:10.1016/j.biomaterials.2009.07.027.
- [2] S.M. Best, A.E. Porter, E.S. Thian, J. Huang, Bioceramics: Past, present and for the future, *J. Eur. Ceram. Soc.* 28 (2008) 1319–1327. doi:10.1016/j.jeurceramsoc.2007.12.001.
- [3] X. Yan, C. Yu, X. Zhou, J. Tang, D. Zhao, Highly ordered mesoporous bioactive glasses with superior in vitro bone-forming bioactivities, *Angew. Chemie - Int. Ed.* 43 (2004) 5980–5984. doi:10.1002/anie.200460598.
- [4] I. Izquierdo-Barba, M. Vallet-Regí, Mesoporous bioactive glasses: Relevance of their porous structure compared to that of classical bioglasses, *Biomed. Glas.* 1 (2015) 140–150. doi:10.1515/bglass-2015-0014.
- [5] M. Vallet-Regí, Nanostructured mesoporous silica matrices in nanomedicine, *J. Intern. Med.* 267 (2010) 22–43. doi:10.1111/j.1365-2796.2009.02190.x.
- [6] V. Mouriño, J.P. Cattalini, A.R. Boccaccini, Metallic ions as therapeutic agents in tissue engineering scaffolds: an overview of their biological applications and strategies for new developments, *J. R. Soc. Interface.* 9 (2012) 401–419. doi:10.1098/rsif.2011.0611.
- [7] C. Wu, J. Chang, Multifunctional mesoporous bioactive glasses for effective delivery of therapeutic ions and drug/growth factors, *J. Control. Release.* 193 (2014) 282–295. doi:10.1016/j.jconrel.2014.04.026.
- [8] G. Molino, A. Bari, F. Baino, S. Fiorilli, C. Vitale-Brovarone, Electrophoretic deposition of spray-dried Sr-containing mesoporous bioactive glass spheres on glass–ceramic scaffolds for bone tissue regeneration, *J. Mater. Sci.* 52 (2017) 9103–9114. doi:10.1007/s10853-017-1026-5.
- [9] A. Bari, N. Bloise, S. Fiorilli, G. Novajra, M. Vallet-Regí, G. Bruni, A. Torres-Pardo, J.M. González-Calbet, L. Visai, C. Vitale-Brovarone, Copper-containing mesoporous bioactive glass nanoparticles as multifunctional agent for bone regeneration, *Acta Biomater.* 55 (2017) 493–504. doi:10.1016/j.actbio.2017.04.012.
- [10] C. Pontremoli, M. Boffito, S. Fiorilli, R. Laurano, A. Torchio, A. Bari, C. Tonda-Turo, G. Ciardelli, C. Vitale-Brovarone, Hybrid injectable platforms for the in situ delivery of therapeutic ions from mesoporous glasses, *Chem. Eng. J.* 340 (2018) 103–113. doi:10.1016/j.cej.2018.01.073.
- [11] C. Wu, Y. Zhou, M. Xu, P. Han, L. Chen, J. Chang, Y. Xiao, Copper-containing mesoporous bioactive glass scaffolds with multifunctional properties of angiogenesis capacity, osteostimulation and antibacterial activity, *Biomaterials*. 34 (2013) 422–433. doi:10.1016/j.biomaterials.2012.09.066.
- [12] D.S. Morais, S. Fernandes, P.S. Gomes, M.H. Fernandes, P. Sampaio, M.P. Ferraz, J.D. Santos, M.A. Lopes, N. Sooraj Hussain, Novel cerium doped glass-reinforced hydroxyapatite with antibacterial and osteoconductive properties for bone tissue regeneration, *Biomed. Mater.* 10 (2015) 55008. doi:10.1088/1748-6041/10/5/055008.
- [13] M. Kawashita, S. Tsuneyama, F. Miyaji, T. Kokubo, H. Kozuka, K.

- Yamamoto, Antibacterial silver-containing silica glass prepared by sol-gel method, *Biomaterials*. 21 (2000) 393–398. doi:10.1016/S0142-9612(99)00201-X.
- [14] S. Kaya, M. Cresswell, A.R. Boccaccini, Mesoporous silica-based bioactive glasses for antibiotic-free antibacterial applications, *Mater. Sci. Eng. C*. 83 (2018) 99–107. doi:10.1016/j.msec.2017.11.003.
- [15] M. Clinmicrorevs, P. Bowler, D.G. Armstrong, 2001 . Bowler et al . *Wound Microbiology and Associated Approaches to Wound*, 14 (2016) 244–269. doi:10.1128/CMR.14.2.244.
- [16] M.C. Robson, Wound infection: A failure of wound healing caused by an imbalance of bacteria, *Surg. Clin. North Am.* 77 (1997) 637–650. doi:10.1016/S0039-6109(05)70572-7.
- [17] T.P. Schaer, S. Stewart, B.B. Hsu, A.M. Klibanov, Hydrophobic polycationic coatings that inhibit biofilms and support bone healing during infection, *Biomaterials*. 33 (2012) 1245–1254. doi:10.1016/j.biomaterials.2011.10.038.
- [18] K. Kirketerp-Møller, P. Jensen, M. Fazli, K.G. Madsen, J. Pedersen, C. Moser, T. Tolker-Nielsen, N. Høiby, M. Givskov, T. Bjarnsholt, Distribution, organization, and ecology of bacteria in chronic wounds, *J. Clin. Microbiol.* 46 (2008) 2717–2722. doi:10.1128/JCM.00501-08.
- [19] S. MacNeil, J. Shepherd, L. Smith, Production of Tissue-Engineered Skin and Oral Mucosa for Clinical and Experimental Use, in: *3D Cell Cult.*, 2011: pp. 129–153. doi:10.1007/978-1-60761-984-0.

CHAPTER 1

State of the Art

1.1 Introduction

In this research work, a library of mesoporous bioactive glasses has been produced with different techniques in order to obtain scalable materials for biomedical applications. Some therapeutic ions were selected with the aim to produce multifunctional nanomatrices to be used in advanced devices for promoting bone healing and wound healing applications in compromised clinical situations.

In this chapter, a literature review on bioactive glasses is given. After a brief and general description of the concept of biomaterials, a focus on the specific class of bioactive glasses is presented in section 1.3. The discovery of the bioactive glasses, the requirements which they have to meet, the common production techniques and their applications are described. In particular, in sub-sections 1.3.1 and 1.3.2, bone healing and wound healing applications and the current approaches to face these clinical problems are discussed.

In paragraph 1.4.1, the description of the sub-category related to mesoporous bioactive glasses containing therapeutic elements is presented. These materials are gaining increasing interest within the scientific community thanks to the wide range of possible application and the potential use as alternative treatments in place of conventional ones.

Their versatility is due to the different therapeutic ions which could be used and to explain this concept, an exhaustive overview of the biological effect of the most common therapeutic ions is given. In particular, the mechanism of action is discussed, and an overview of the most representative results obtained for ion-containing biomaterials is reported.

1.2 Biomaterials

The first official definition of “biomaterial”, introduced by the European Society of Biomaterials in 1987, stated that a biomaterial is “*a non-viable material used in a medical device, intended to interact with biological systems*”[1]. In 2009, Williams, as conclusion of a dissertation on the new types of substance engineered to perform functions within health care, provided the new following definition:

“A biomaterial is a substance that has been engineered to take a form which, alone or as part of a complex system, is used to direct, by control of interactions with components of living systems, the course of any therapeutic or diagnostic procedure, in human or veterinary medicine.”

Williams, therefore, classified as biomaterials all the substances which can direct the course of a treatment through the monitoring of the interactions with the living systems, so, all the materials which are involved either in promotion of events, as in regeneration of tissue, or in prevention of event, as in antibacterial activity, or a combination of both.

Within the field of biomaterials science, bioceramics represent a category in large expansion with several applications in restoration and replace of damaged tissues. The reason of this increasing interest is linked to the capability of these materials to solve some of the issues of an ageing population [2].

Bioceramics are divided into two categories based on the properties and the timeline. The first generation was formed by inert ceramics whose aim was to induce a minimal biological response when introduced in the human body. This first attempt of implanted ceramics experimented some problems as the creation of a fibrous capsule which led to the develop of the second generation of ceramics. These bioactive materials may be resorbable or non-resorbable ceramics which could interact with the body and create a controlled bond with bone or soft tissue in the physiological environment [2]. The main advantage of bioactive ceramics is their high reactivity resulting in the formation of an apatite-like phase, similar to the one present in bones. Some representatives of this category of biomaterials are calcium phosphates and glasses.

1.3 Bioactive glasses

Inventions come from a specific need, in every fields. Therefore, also the bioactive glasses have been invented to overcome the problem of the formation of a fibrous tissue which occurred when materials, supposed to be inert, were implanted in the body. Larry Hench in 1967 started to face the problem and discovered that specific compositions of glass, in the $\text{Na}_2\text{O}-\text{CaO}-\text{P}_2\text{O}_5-\text{SiO}_2$ system, were able to repair tissue by forming a bond with them [3]. Small rectangular implants of this type of bioactive glass, called 45S5 (commercial name Bioglass[®]), were produced by melting technique, cast and tested in a rat femoral implant model. The hydroxyapatite layer developed on 45S5 surface after soaking

in solution which did not contain phosphate or calcium was compared to the interfacial hydroxyapatite crystals observed *in vivo* in the rat model [4]. Since this discovery, several experiments were carried out in order to understand the nature, the formation kinetics and strength of the formed surface bonds. Subsequently, Bioglass[®] has been used in different commercial formulations [4]. In 1984, the first Bioglass[®] device, commercialized in the United States, was used to replace the bone and to restore hearing through transmission of sounds from tympanic membrane to the cochlea. Compared to other prostheses of that time, this device, which was tradenamed as MEP[®], was able to create a bond with both soft and hard tissue [5]. The second commercial product of Bioglass[®] was known as ERMI[®] in 1988 and it was used to repair tooth roots in fresh tooth extraction site. This conical-shaped device proved to be more stable and long-lasting than the materials available for the same purpose at that time.

The non-widespread clinical use of these types of medical devices finds a reason on the surgeon needs: their monolithic shapes made them less suitable in the cases where the device had to fit a specific defect site or had to be pressed into it. Hence, in 1993 a new product was produced and sold with the name “PerioGlas[®]”. This product, in the form of particles with size ranging from 90 to 710 μm , is still used for the regeneration of bone around the root to preserve the tooth [5]. Building on the success of PerioGlas[®], a particulate-shaped device was considered also in orthopaedic disease treatment. The so-called NovaBone[®] has been introduced in 2000 into the European market and it is still sold for general orthopaedic bone grafting in non-load bearing body parts.

These are only some examples of commercial devices based on Bioglass[®] but they well represent the progress in research with its ever-changing requirements: the initial effort made on the studies of material for the repair of a damaged tissue left the scene to the research of an active material able to interact with cells and help the regeneration of tissue [4].

Apart from silica-based glasses, borate and phosphate glasses received increasing interest due to their positive aspects.

Borate bioactive glasses, for example, are able to convert more rapidly and completely to hydroxyapatite than the silica counterpart, due to their reactivity and lower chemical durability [6]. *In vitro* studies showed that borate glasses support cell proliferation and differentiation [7]. The main concern associated with borate glasses in biomedical application is related to the toxicity of boron released in static condition [6].

Phosphate-based glasses were introduced in 1980 in medical field and then they gained an increasing interest in both hard and soft tissue regeneration due to their solubility and tailored dissolution rate [8]. The peculiarity of this type of glass to be spun makes them suitable as guide for muscle or nerve repair [9].

In general, all the bioactive glass types have to meet the following requirements to be considered suitable biomaterial:

1. Biocompatibility: the non-toxicity of the glasses is the main point as the material has to be cytocompatible and promote the cell proliferation and cell adhesion;
2. No inflammatory response;
3. Bioactivity.

Many scientists tried to give a uniform description of the concept of biocompatibility but there still exists a deal of uncertainty to explain the manner in which a foreign material and the tissue could mutually co-exist. William in 2008 [10] started his Leading Opinion with the consideration that biocompatibility is the most important factor which distinguishes a biomaterial from any other material. In Table 1.1, the major features of the materials which may affect the host response are listed.

It is worth noting that the host response is influenced by surface and bulk characteristics which interact with the materials in a different way and extent.

Table 1.1: Some of material characteristics which may influence the host response [10]

Bulk material composition, micro- (or nano)-structure, morphology Crystallinity and crystallography Elastic constants Water content, hydrophobic–hydrophilic balance Macro-, micro-, nano-porosity Surface chemical composition, chemical gradients, surface molecular mobility Surface topography Surface energy Surface electrical/electronic properties Corrosion parameters, ion release profile, metal ion toxicity (for metallic materials) Degradation profile, degradation product form and toxicity (for polymeric materials) Leachables, additives, catalysts, contaminants and their toxicity (for polymeric materials) Dissolution/degradation profile, degradation product toxicity (for ceramic materials) Wear debris release profile

Other than the material variables, the reactions that may occur have to be taken into account to understand if the implant is successful or not. Some of the main phenomena are summarised in Table 1.2.

Table 1.2: Some of the main host response phenomena to biomaterials [10]

Protein adsorption and desorption characteristics
Generalised cytotoxic effects
Neutrophil activation
Macrophage activation, foreign body giant cell production, granulation tissue formation
Fibroblast behaviour and fibrosis
Microvascular changes
Tissue/organ specific cell responses (e.g. osteoclasts and osteoblasts for bone, endothelial proliferation)
Activation of clotting cascade
Platelet adhesion, activation, aggregation
Complement activation
Antibody production, immune cell responses
Acute hypersensitivity/anaphylaxis
Delayed hypersensitivity
Mutagenic responses, genotoxicity
Reproductive toxicity
Tumour formation

The interaction between proteins and other macromolecules with the biomaterials is a key mediator for the cell behaviour: the protein could stimulate the cell in a way which will favour tissue repair or regeneration. Osteoblastic cells, for example, showed a dependence on two adsorbed glycoproteins, vitronectin and fibronectin, for the initial cell adhesion and spreading [11].

The final definition of biocompatibility given by Williams is the following:

“Biocompatibility refers to the ability of a biomaterial to perform its desired function with respect to a medical therapy, without eliciting any undesirable local or systemic effects in the recipient or beneficiary of that therapy, but generating the most appropriate beneficial cellular or tissue response in that specific situation, and optimising the clinically relevant performance of that therapy”.

Closely related to biocompatibility is the concept of inflammatory response: the biomaterials cause a sequence of events when introduced in the body, which may provoke adverse reactions such as fibrosis, coagulation, infection and device-mediated inflammation [12]. First of all, the concept that a biomaterial has not to induce an inflammatory response is incorrect.

Anderson in 2008 [13] explained in his review that the host reactions to biomaterials are the following: injury, blood–material interactions, provisional matrix formation, acute inflammation, chronic inflammation, granulation tissue development, foreign body reaction, and fibrosis/fibrous capsule development (Figure 1.1).

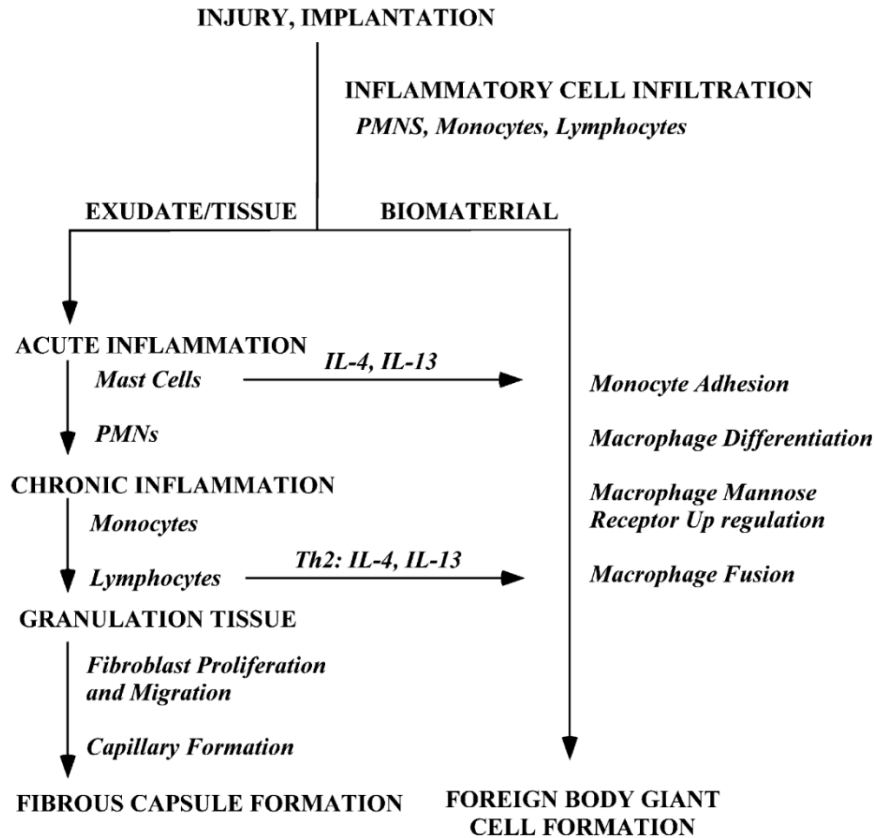


Figure 1.1: Sequence of events which occurred during the inflammation and wound healing processes [13]

As mentioned before, the first stage after implantation is represented by the interaction between blood and material through the host proteins adsorbed to the biomaterial interface. The types, levels and conformation of these proteins determine the success or the failure of such implant, and, vice versa, the types, concentrations and conformations of the new layer (surface-adsorbed proteins) are related to the biomaterial properties. The formed provisional matrix, which is the initial thrombus/blood clot at the interface, represents a supply of structural, chemical and cellular components for the following processes: the type of bioactive agents (cells, cytokines, growth factors..), the amount and their release kinetics from the provisional matrix influence the process of wound healing and inflammatory response.

Then acute and chronic inflammations occur: the acute inflammation usually lasts less than one week, and it is governed by neutrophil and mast cells; the chronic inflammation, instead, is less uniform histologically and is characterised by the presence of mononuclear cells (lymphocytes and plasma cells). The persistence of the inflammatory response beyond three weeks indicates the presence of an infection.

If the inflammatory responses are controlled, the granulation tissues and the formation of a fibrous capsule are identified by the presence of macrophages, fibroblasts and formation of capillaries which lead the formation of the new healing

tissue. Between the granulation tissue (and the following fibrous capsule) and the biomaterial, a one to two cell-layer of monocytes, macrophages and foreign body giant cells (derived by the foreign body reaction) is formed [13]. The domination of the body giant cell response, without control, could diminish the positive effect on the target cells and could lead to the degradation of the implant [13,14].

Hence, it is clear that the events and the agents involved in the failure of an implant are almost the same of the healing process and the difference lies in the controllability and the duration of such events [14].

As discussed previously, the capability of the biomaterial to interact with the bone through the formation of a carbonate substituted hydroxyapatite-like layer represented a big discovery and a step forward in the medical application. The mechanism of bioactivity has been largely described and studied by several authors and it is composed by a sequence of reactions which take place on the surface in contact with body fluids [6,15]. As shown in Figure 1.2, the first 5 reactions, which occur at the interface with the fluid containing H^+ and H_3O^+ ions, are followed by 7 cellular-dependent reactions responsible to the proliferation and differentiation of osteoblast and the generation of new bone.

The rapid exchange of Na^+ from the glass surface ($Si-O-Na^+$) with H^+ and H_3O^+ ions in solution is followed by the breaking of Si-O-Si bonds of the glass which causes a release of $Si(OH)_4$ in solution and the formation of silanols (Si-OH) at the interface.

During the third step, the polycondensation of an amorphous SiO_2 -rich layer depleted in Na^+ and Ca^{2+} occurs on the surface. Then, Ca^{2+} and PO_4^{3-} groups migrate from the glass and from the solution through the SiO_2 -rich layer, leading to the deposition of an amorphous calcium phosphate layer on the top of the SiO_2 -rich layer.

The calcium-phosphate layer continues to grow through the incorporation of calcium and phosphate groups from the solution and starts to crystallize, forming a hydroxyl carbonate apatite (HCA).

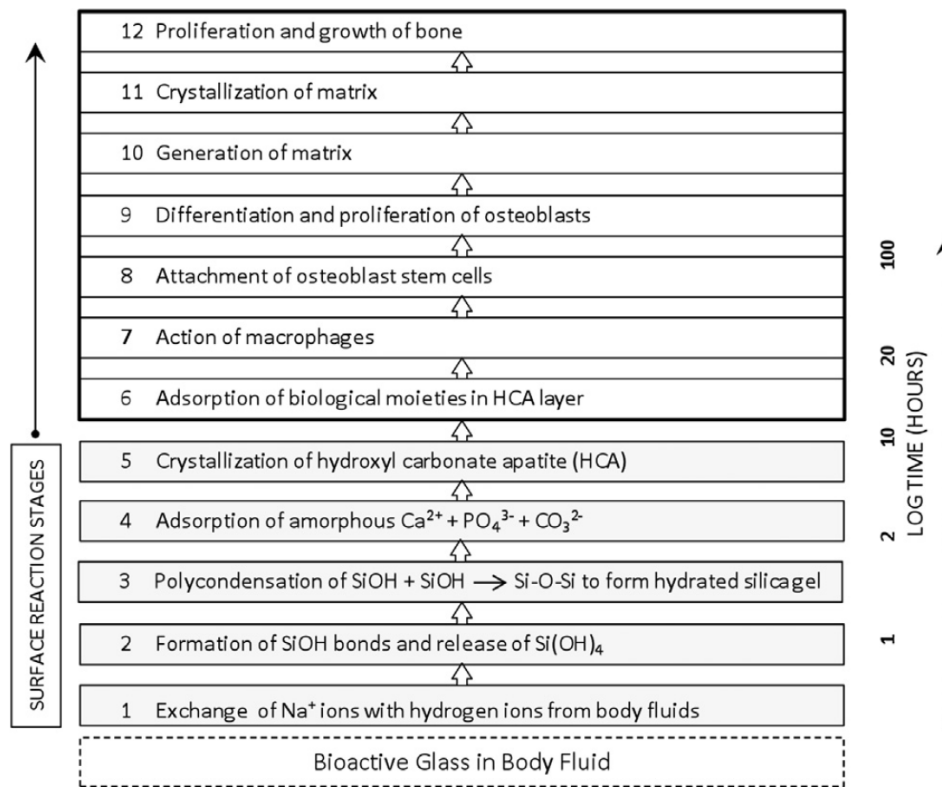


Figure 1.2: Sequence of reactions at the interface of a bioactive material and body fluid [15]

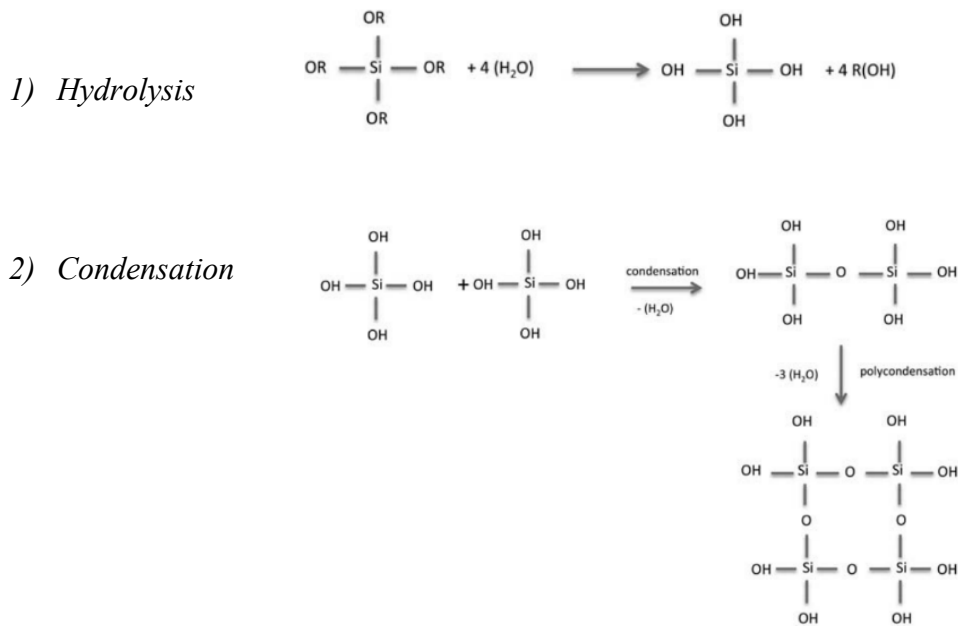
The following steps involve the biological components, such as growth factors, followed by the proliferation and differentiation of osteoprogenitor cells. The bone-forming cells create extracellular matrix which, through the mineralization, provokes the formation of nanocrystals and collagen on the glass surface [6,15].

The most common techniques to obtain bioactive glass are: the melt-quenching route and the sol-gel route.

Considering that the first bioactive glass (45S5) was produced by melt-quenching technique, this is considered the traditional route. In order to obtain a glass by this route it is necessary a fusion of stoichiometric amounts of the different precursors (e.g. SiO_2 , P_2O_5 , Na_2CO_3 , CaCO_3) and their following quenching. In brief, the different precursors are mixed together, and the as-obtained powders are transferred in a platinum or alumina crucible and melted in a high resistance furnace at high temperature (between 1100 and 1650°C, up to 3 hours, depending on the composition of the glass). The molten glass is then poured into moulds to obtain a specific shape or it can be quenched in cold water, obtaining the so-called “frits” which is easily powdered through ball milling. Finally, the glass is annealed using a temperature below the glass transition temperature in order to remove the internal stresses. The main limitation of this technique is linked to the composition suitable to be melted: a content of less than 10% of alkali oxide makes the glass viscosity too high to be melted [8,16].

The sol-gel approach, an alternative to the traditional melt-quenching route, involves hydrolysis and polycondensation reactions which lead the formation of a

gel (a network composed by interconnected pores and polymeric chains), from a sol (dispersion of colloidal particles with a diameter ranging between 1 and 100 nm in a liquid), which is later aged, dried and dehydrated. The sol-gel route starts with the preparation of the sol which is composed by a mixture of all the alkoxides or organometallic precursors. During the second step, the hydrolysis of the liquid alkoxide precursors occurs in a solvent. The hydrolysis of the silicon alkoxide (*i.e.* tetraethyl orthosilicate (TEOS)) usually by water elicits the formation of silanol groups (Si(OH)₄) which interact and form Si-O-Si bonds. Finally, the polycondensation process leads to the formation of a silica network (SiO₂). Reactions 1 and 2 illustrate the hydrolysis and condensation processes, respectively (R=CH₃, C₂H₅, C₃H₇) [16].



The two reactions occur simultaneously, and their kinetics depend on the pH, composition, concentration of the species, temperature, precursor, pressure and R, where R represents the moles of water on moles of TEOS.

Therefore, the formation of the sol is followed by the gelation process in which the condensation and cross-linking of silica particles elicit the creation of a three-dimensional network characterised by a sharp increase of viscosity.

During the gel aging step, the polycondensation and reprecipitation of the gel provoke a decrease in porosity, an increase in the strength and the phase transformation which causes a marked change of the physical properties. The next step is represented by the drying process necessary to remove the liquid from the pores of the formed 3D network. The drying is a critical step due to the possible formation of cracks caused by capillary stresses within the gel network. Finally, the resulting gel is heat-treated to ensure the complete sintering and the pore removal [16,17].

Compared to the conventional glass production route, the sol-gel technique allows to synthesize material with reduced amount of contaminants, resulting from the several process steps (grinding, fritting, etc.) typical of melt-quenching route.

Furthermore, as mentioned before, there is a compositional limitation dictated by the impossibility to produce a glass with high SiO₂ content by melting. The low content of silica and the big amount of alkali species of the traditional bioactive glass produced by melting makes it difficult to maintain high level of purity due to its high reactivity and its tendency to incorporate impurities [18].

In addition, the sol-gel approach offers the possibility to obtain product in several forms and shapes, such as fibers, foams and nano/micro sized particles [18,19]. In particular, the capability to produce nanoparticles is very appealing in the medical field. Considering that cells and biomaterials interact firstly at the nanoscale and that the biological components are in the same dimension range, the nanoscience is particularly interesting in the tissue engineering approaches [20].

The nanosize of a biomaterial affects its bioactive behaviour, cellular response and surface reaction kinetics (*i.e.* ion release, dissolution). For what concerns the bioactivity, the nanometric dimensions are strictly connected to high specific surface area and, consequently, to very fast ion exchange reactions and high protein adsorption ability. As far as cellular responses are concerned, the nanoscale properties of materials influence the surface chemistry and the interactions with proteins, thus the subsequent cell adhesion [20].

1.3.1 Bone healing application

Bone tissue is the most transplanted tissue, second only to blood [21]. The annual fracture rate exceeds 12 million in the United States alone and non-union fractures represent up to 10% [22].

The bone repair is a biologically process which results in the restoration of skeletal tissue to normal functionality. The fracture healing could be divided into four stages which occur simultaneously and involved the presence of numerous growth factors and cytokines: hematoma formation, soft callus and hard callus formation, bone remodelling (Figure 1.3) [22,23]. In details, after the injury, the disruption of blood vessels causes the formation of the hematoma; during the second stage the angiogenesis process, the intramembranous ossification and the cartilage formation occur; then the callus starts to mineralize and, finally, the remodelling occurs by replacement of large fracture callus with secondary lamellar bone.

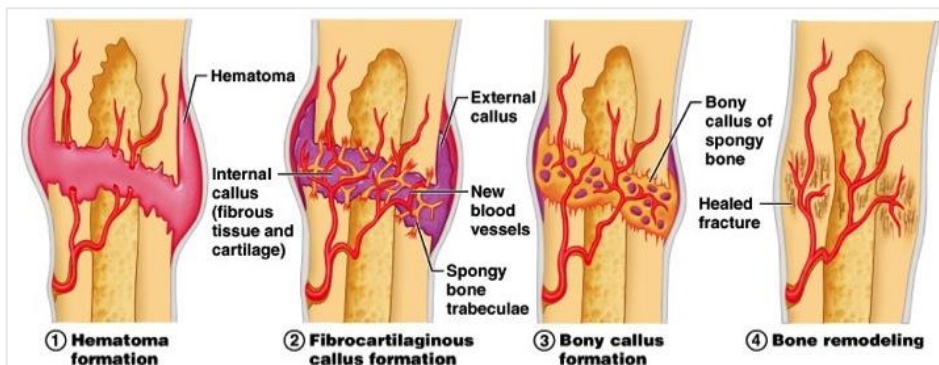


Figure 1.3: Physiological bone healing process

The bone grafting procedures represent the gold standard for the treatment of several bone defects, such as gaps at fracture sites, delayed unions and non-unions, spinal fusion [24].

The bone grafting procedure consists on transplanting bone from one site to the site of defect and the implants are classified as autograft and allograft. These types of graft are distinguished by the provenience site of the materials, but they have to meet the same requirements [21,25]:

- 1) Osteointegration: the ability to create a bond with the bone, avoiding the formation of a fibrous tissue
- 2) Osteoconduction: the potential to support the growth of new bone through blood supply
- 3) Osteoinduction: the property to induce the differentiation of stem cells towards osteogenic phenotypes
- 4) Osteogenesis: the capability to induce bone formation by cells present within the graft material (if present)

The most common and effective bone graft material is the autologous one (autograft) and includes cancellous and cortical bone graft. It is usually harvested from iliac crest and it respects all the requirements, thanks to the cells which survive from the transplantation.

Nevertheless, the autograft procedure has some downsides: extensive operation time, donor site morbidity, limited supply and it is not suitable for all the patients (*e.g.* elderly, infant or patient with a malignant disease) [21,25].

An alternative to autograft is represented by allograft, a bone graft from a different individual of the same species. Regional tissue bank distributed the allograft in different forms (fresh, frozen or freeze-dried) and as cortical or cancellous implant. The allografts undergo tissue processing and sterilisation in order to avoid any viral transmission and therefore no viable cells are present in allograft (this type of graft does not meet the forth requirement). The processing involves a change in the mechanical properties of the original bone which becomes weaker and prone to fracture [21,25].

Considering the limitations of the current strategies and the increasing demand due to the gradual aging of the population, the development of bone-graft alternatives is highly necessary. Among bone-graft substitutes, bioactive glasses possess both osteointegrative and osteoconductive properties [21,26].

1.3.2 Wound healing application

Since their discovery, bioactive glasses have been extensively studied for their application in bone healing. Only recently, their use in the treatment of wound has gained recognition [6,27].

The wound healing is a complex process composed by a cascade of events which can be affected resulting in chronic, non-healing wounds which represent a great burden to both the patient and the health care system [28]. The physiological

wound healing process involves 4 steps (Figure 1.4): haemostasis, inflammation, proliferation and remodelling. During the inflammatory phase it is important to keep the damaged wound clean from pathogens and foreign material. The vasodilation permits to localize in the wound site monocytes and neutrophils which differentiate into macrophages. The role of macrophages is to phagocytose the tissue debris, secrete growth factors and cytokines, small proteins which promote tissue proliferation. The proliferative phase is characterised by the production of collagen and ground substance which lay the basis for the production of the new tissue. The supply of this area is guaranteed by the new blood vessels created by the growth of endothelial cells. Finally, after 2-3 weeks, the physiologic wound healing process ends with the restoration of the collagen type to the usual one and when the wound tissue undergoes to a full cross-linking [28].

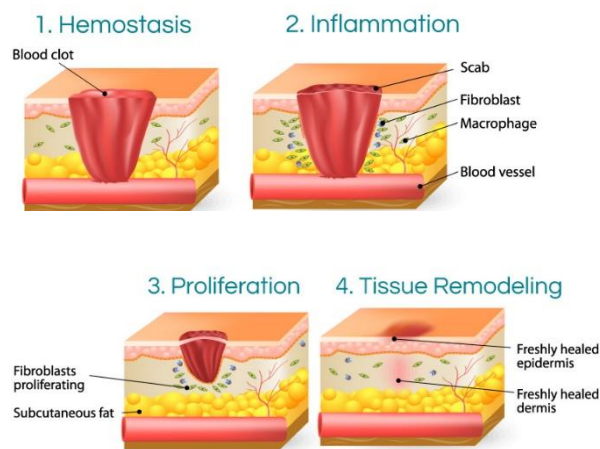


Figure 1.4: Physiological wound healing process

Considering the complexity of this process and the multitude of factors involved in it, chronic (non-healing) wounds may occur. Among critical factors in managing chronic wound, the low oxygen tension (*e.g.* 5 mmHg) is a limit for the cell proliferation and an enhancer of microbial growth, which is related to a longer inflammation phase and a delay in the repair [28,29]. Angiogenesis, which is a critical step in the wound healing process, is the physiological process of new blood vessel formation from pre-existing vasculature; it is involved in all the tissue regeneration phenomena due to the need to transport nutrients for the growing cells and to remove waste products [30]. The failure of this aspect ultimately results in chronic wounds [29].

There are extreme situations (such as in the presence of haemorrhages) in which the use of traditional treatments (*e.g.* palliative wound dressings) are not sufficient and useful to decrease the mortality risk and the potential use of biomaterial represents an established challenge by now [30,31]. Several investigations on the administration or topical application of growth factors, including the vascular endothelial growth factor (VEGF) and fibroblast growth factor (FGF) types, gave promising results. Both VEGF and FGF are mitogens which play an important role in angiogenesis. Nevertheless, their high tendency to diffuse, their short half-life

and the difficulty to control the release kinetics caused a limited success [32,33]. To solve the problems related to the administration of growth factor, the use of gene therapy or the incorporation of such growth factor in a structure (*e.g.* scaffold) have been proposed. But also in this case, there are some difficulties due to the high cost and the conditions necessary to produce these constructs, such as the high temperatures and the solvents which could alter/damage the growth factor [34].

A robust and appealing alternative is represented by the use of materials which could enhance the expression and secretion of the growth factors by the organism, instead of administering or delivering them. To this purpose, different studies demonstrated that the direct/indirect contact and the dissolution products of bioactive glasses can stimulate the secretion of VEGF from fibroblast [5,35]. *In vivo* evidences confirmed the ability of bioactive glasses to stimulate new vessel networks [33]. Furthermore, the promotion of the proliferation and the activity of fibroblast and the release of Ca^{2+} from bioactive glass are key factors in the promotion of the wound healing process [32,36].

1.4 Mesoporous bioactive glasses

According to IUPAC definition, solids can be divided into 3 categories based on their pore size, with 100 nm as upper limit. In particular, the so-called mesoporous materials are characterised by pore diameters ranging between 2 and 50 nm [37].

The possibility to create an ordered mesoporous structure was firstly experimented in silica-based materials, in the early 90s, by two research groups (Kuroda's group at Waseda University and Kresge's group at Mobil Oil Company). The mechanism which leads to the formation of the mesoporous structure is the combination of the use of a surfactant and the subsequent condensation of inorganic silica precursors (Figure 1.5) [38]. The surfactants are amphiphilic molecules, composed by a lyophilic head group and a lyophobic tail which, in water, form micelles with the head groups forming the outer surface and the tails pointing toward the center [39]. Thanks to the removal of the surfactant, which acts as template for the pores, through calcination or solvent extraction, a mesoporous structured material with high surface area, large pore volume and abundance of silanol groups on the surface is obtained. The first application of this material was for catalytic purposes and, only, in 2001 Maria Vallet-Regí proposed the use of mesoporous silica for biomedical application, as drug delivery systems due to the excellent ability to load and release biological active molecules in a controllable way [38].

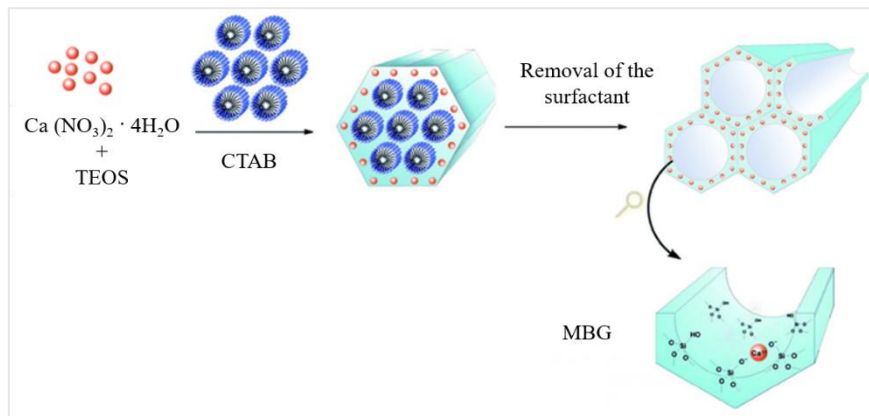


Figure 1.5: Mesoporous structure formation using CTAB (hexadecyltrimethylammonium bromide) as surfactant

Furthermore, after some years, in the 2006, the same researchers demonstrated the bioactive behaviour of mesoporous silicas which were able to induce the precipitation of hydroxyapatite when soaked in simulated body fluid (SBF). However the kinetics of the hydroxyapatite layer formation, too slow when compared to the conventional sol-gel glasses, did not allow to consider the mesoporous silica as a real innovation in tissue regeneration field, *e.g.* bone application [38,40]. The real advance was represented by the possibility to produce a material combining the compositions of conventional sol-gel glasses and the structural features of mesoporous silicas.

The mesoporous bioactive glasses (MBGs) were firstly synthesized by an evaporation-induced self-assembly (EISA) process, using a non-ionic block polymer (Pluronic P123 [(ethylene oxide, EO)₂₀(propylene oxide, PO)₇₀(EO)₂₀]) as structure-directing agent. The EISA process, described for the first time by Brinker et al. [41] in 1999, allowed to overcome the following two obstacles: (i) difficulty to obtain an ordered micellar phase using the typical temperature (100°C) requested by the aging and drying stages and (ii) the presence of CaO, acting as network modifier, which could hamper the interactions between silica and surfactant [38].

Self-assembly is a spontaneous organisation through non-covalent bonds (Van der Waals forces, hydrogen bonds, electrostatic interactions, etc.). This process begins with a homogeneous solution of soluble silica species and surfactant prepared in ethanol/water with a $c_0 \ll cmc$, as starting concentration, where cmc is the critical micellar concentration (Figure 1.6). The progressive evaporation of ethanol leads to a system which becomes more concentrated and drives the self-assembly of inorganic-surfactant micelles and their organisation into liquid crystalline mesophase [38,39,41].

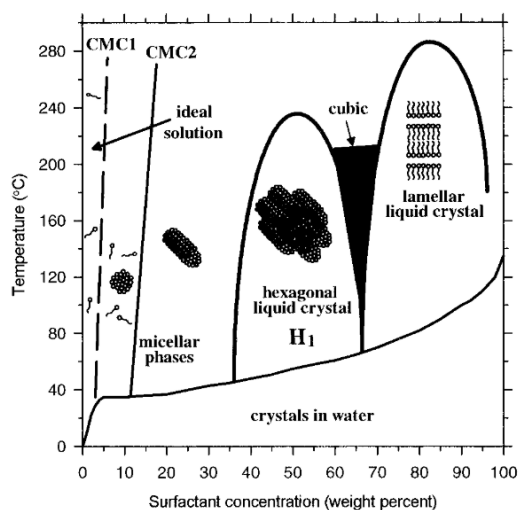


Figure 1.6: Schematic phase diagram of CTAB [39]

In a typical MBG synthesis (Figure 1.7), the starting solution is composed by inorganic specie precursors (*e.g.* TEOS, $\text{Ca}(\text{NO}_3)_2$, TEP), surfactant (cationic or non-ionic), the volatile solvent (usually ethanol) and a catalyst (usually HCl). The sol resulting from the mixing of the starting solution is then transferred in a Petri dish and undergoes an EISA process. The following calcination of the dried gel allows to remove the surfactant [42].

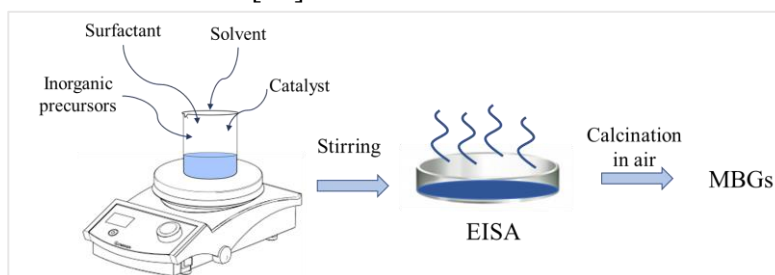


Figure 1.7: MBG synthesis through EISA process

The synthesis procedure allows to tailor the structural features and textural characteristics by modulating some parameters, such as surfactant nature and concentration, solvent, pH, temperatures (as in the case of mesoporous silica) and the presence of network modifiers (only in the case of MBGs).

For what concerns the nature of surfactant, it can be possible to distinguish three types of surfactant, depending on their head group chemistry and charge: (i) cationic, the hydrophilic group carries a positive charge; (ii) anionic if the head group carries a negative charge, (iii) nonionic if the hydrophilic group is not charged [39].

The influence of the nature of the surfactant in MBG structure was investigated by Arcos et al. [43], who produced by EISA method three different bioactive mesoporous microspheres, using one cationic (CTAB) and two nonionic amphiphilic triblock copolymers (Pluronic P123 $[(\text{EO})_{20}(\text{PO})_{70}(\text{EO})_{20}]$ and Pluronic F127 $[(\text{EO})_{106}(\text{PO})_{70}(\text{EO})_{106}]$). This study confirmed that the textural parameters depended on the surfactant chain length. The use of a cationic surfactant

led to a more ordered structure characterised by smaller pore size and higher surface area values, compared to nonionic surfactant-based materials [43,44].

In the case of mesoporous bioactive glasses, textural and structural properties can be tailored by the addition of CaO and P₂O₅ in the silica network. In particular, CaO acts as network modifier leading to a decrease of the silica network connectivity [38,40].

Although the composition of MBGs exerts an essential influence on bioactive behaviour, the textural parameters of these materials are also crucial in this regard. The highly uniform and accessible pore-size arrangement allows to obtain higher surface area and pore volume values, compared to traditional sol-gel and melt bioactive glasses with the same composition. These characteristics have been considered to be the main factors for the superior *in vitro* bioactivity. The combination of calcium and high surface area values provokes a faster and larger ion leaching, both calcium and silicon ions, when in contact with SBF. The release of Ca²⁺ determines a drop in pH which allows a formation of octacalcium phosphate, a precursor of hydroxyapatite [45,46].

The *in vitro* bioactive response is influenced also by the pore structure: the three-dimensional pore system provides an easier ion exchange with the surrounding medium [47].

As stated before, the silica-based mesoporous materials can be used as drug-delivery system thanks to the high pore volume which permits to host drug molecules in the nanometric scale. The huge amount of silanol groups (Figure 1.5) present in the silica surface allows the functionalisation with different organic groups (*i.e.* alkoxyhanes) potentially leading to a tailorable drug loading and release [40].

1.4.1 MBG containing therapeutic elements and related biological response

Several authors focused their attention to the possibility to enhance the positive effects of bioactive glasses and to impart specific biological functions. The most common way to move this step forward is represented by the incorporation, into the silica framework, of metallic ions which were proved to exert specific functions (*e.g.* antibacterial effect, pro-angiogenic potential, pro-osteogenic potential).

As shown in the following schematic illustration (Figure 1.8), some ions could exert more than one therapeutic effect leading to the production of multifunctional platform to be used in several applications.

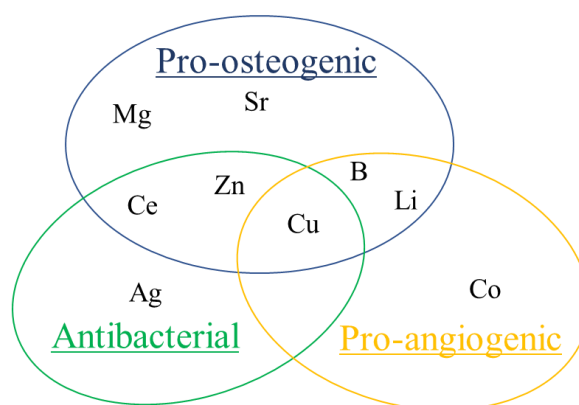


Figure 1.8: Therapeutic effects of the most used metallic ions

Although the same positive effects could be obtained by incorporating growth factor, recombinant protein or by using other genetic engineering approaches, there are several advantages in using therapeutic ions [48]:

- 4) The fabrication methods of biomaterials are not always compatible with growth factors, drugs and recombinant protein due to the high temperatures, solvent involved and pressure which can provoke the degradation of pharmacological molecules; these parameters do not affect, instead, the therapeutic ions, which are more stable;
- 5) The metallic ions could modify cellular functions by interacting with other ions through the activation of ion channels or by binding with macromolecules;
- 6) The metallic therapeutic ions are cheaper than the growth factors and recombinant proteins.

Inorganic ions present in the healthy human body and involved in bone metabolism and in angiogenesis process are maintained at a physiological level and follow a specific pathway. Nevertheless, anomalous inorganic ion metabolism causes pathology, such as the Wilson's disease in which copper reaches toxic concentration levels in all body tissues [48–50].

Therefore, the potential cytotoxicity of the ions released by modified MBGs must be carefully investigated. The uncontrolled release, in terms of concentration and release kinetics, may lead to adverse reactions such as inflammation or immune reactions. Furthermore, some metal ions can change their ionic state and become highly toxic, as, for example, Cr (VI), at variance of Cr(III), which acts as calcium supplement and promotes insulin sensitivity [49].

Biological response to copper

Copper is a metal ion present in trace amount in adult male (~100 mg) which can exist in biological systems in two oxidation states (Cu^+ and Cu^{2+} , reduced and oxidized forms, respectively), which allows copper to coordinate different ligands (Cu^+ prefers sulfur donar ligands, while Cu^{2+} nitrogen ones). Cu is an essential

element as catalyst and cofactor for enzymes which plays a role in blood clotting, energy supply, oxygen transport and cellular metabolism [51,52].

It has been extensively reported that copper is a hypoxia mimicking element. The hypoxia is a condition of low oxygen pressure which plays a pivotal role in the blood vessel formation. The hypoxia inducible factor-1 (HIF-1) is composed by HIF-1 α and HIF-1 β . While the second is usually expressed by the cells, the expression of HIF-1 α depends on the oxygen concentration. In fact, under hypoxic condition, HIF-1 α accumulates and goes into the nucleus where dimerizes with the other subunit (HIF-1 β) to form the HIF-1. HIF-1 binds to the hypoxia-responsive element (HRE) and leads to the overexpression of VEGF, which is a fundamental regulator of blood vessel growth, which stimulates endothelial cell proliferation, migration and the creation of tubular structures [53–55].

The pro-angiogenic effect was demonstrated in several studies on copper-containing bioactive glasses. Lin and co-workers [56] carried out a study on silicate 13-93 scaffold containing different amount of copper (from 0 to 2 wt.%). They showed that Cu ions released from the scaffold containing 2 wt.% of copper were able to promote the growth of new vessels in the fibrous tissue of rat calvarial defects and that the number of new capillaries increased with the increasing of copper concentration. More recently, the effect of copper-containing MBGs on zebrafish model was investigated [57]. MBG particles based on SiO₂-CaO-P₂O₅ composition and modified with 5%mol of copper were soaked in DMEM in different concentration up to 3000 mg L⁻¹. The extracts after up to 5 days of incubation and the suspension prior to start the experiment were tested on bovine aortic endothelial cells (BAEC) and in zebrafish embryo *in vivo* assay, respectively. The experiments proved a potential cytotoxicity of both copper-containing and copper-free MBGs at high concentration. Nevertheless, the ionic products of 5% Cu-containing sample using a concentration of 300 mg L⁻¹ caused a vasodilation and an increase in the thickness of sub-intestinal vessel from 6.03 to 7.58 μ m, using the zebrafish embryo assay.

The enhanced secretion of VEGF from fibroblast was analysed by Dziadek et al. [58], which reported that bioactive glasses containing 1% mol of copper were associated to an increase in VEGF secretion compared to sample without copper, confirming its essential role in the VEGF expression.

Concerning the negative effect of copper-containing material, although the toxic ion threshold depends on the cell type involved in the experiments and on the specific conditions, it seems that a potential cytotoxic effect of copper ion may exist due to the formation of an excess of hydroxyl radicals, produced by the copper-catalysed reaction between superoxide and hydrogen peroxide [56,59–61].

In vivo experiment in a goat model after anterior cruciate ligament (ACL) reconstruction confirmed the close connection between osteogenesis and angiogenesis effect of copper [55]. Polyethylene terephthalate (PET) artificial ligament graft coated by copper-containing bioactive glass was pulled into the bone tunnel after native ACL removal. After 12 weeks, tibial-graft complexes were harvested and analysed through histological and immunohistochemical

examinations. As far as Cu-containing BG/PET graft is concerned, histological results demonstrated more new bone tissue at the interface and into the graft, confirming the osteointegration, compared to BG/PET graft. Furthermore, the CD31 (a transmembrane protein involved in the early vascular growth) expression was significantly higher in Cu-containing graft. The same authors showed that copper-containing coating was effective in promoting HIF-1 α , BMP2 and S100A10 (which are osteogenesis-related genes) and the Ca²⁺ concentrations in cells.

The pro-osteogenic potential of Cu²⁺ ions found further evidence in several works on different cell lines. Burghardt et al. [62] proved that Cu²⁺ ions released from a titanium implant were able to stimulate a complete differentiation of human bone marrow derived mesenchymal stem cells to osteoblasts which led to the expression of collagen type I and the complete mineralization. Alkaline phosphatase (ALP), osteocalcin (OCN) and osteopontin (OPN) activity were investigated in several studies [56,62–64] which confirmed that copper could stimulate the cells to perform osteogenic function.

The antibacterial effect of copper has been known since ancient Egyptian, between 2600 and 2200 B.C. and, from this moment, numerous studies were conducted in order to exploit this beneficial effect [65].

Although the mechanism is not fully elucidated yet, a suggestion on the action of copper ions was described by Grass et al. [65]. As shown in Figure 1.9, the rupture of the membrane due to the copper ions dissolved in the medium causes the loss of cytoplasmic content (Figure 1.9A and B); moreover, the generation of reactive oxygen species (ROS) causes stress and a further cell damage (Figure 1.9C). As last step, genomic and DNA starts to degrade (Figure 1.8D).

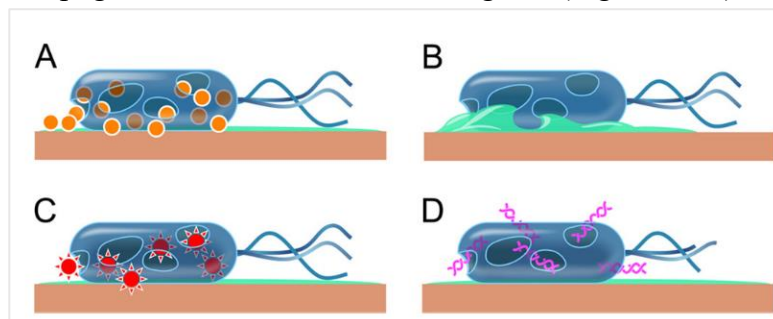


Figure 1.9: Mechanism of action of copper ion released [65]

The antibacterial property of copper-containing MBG scaffold was tested by Wu et al. [64] against *Escherichia Coli* (*E. Coli*). After 7 days of incubation, the number of survived bacteria was highly reduced, and the antibacterial mechanism was ascribed to the redox potential of copper causing damage to bacteria and producing hydroxyl radicals which can participate in some reactions detrimental to molecules. In another work [62], Cu²⁺ ions released in a final concentration of 1.75 mM from a titanium implant were sufficient to kill adherent *Staphylococcus aureus* (*S. aureus*) biofilm within 24h. Bacteria within biofilms are more resistant than planktonic bacteria and represent the main cause of infection associated to implants: bacteria adhere and form the biofilm, which becomes thicker and hinder the

penetration of the antibacterial agent [62,66]. Furthermore, some bacteria may differentiate into a biofilm specific phenotype and become more resistant. The viable count method was used by Mulligan et al. [66] to analyse the antibacterial effect of increasing Cu content in phosphate-based glasses on *Staphylococcus Sanguis* (*S. Sanguis*). By 24h, a 2.6 log reduction of viable bacteria colonies was encountered and was ascribable to the presence of copper.

An in-depth study on copper-containing MBGs was conducted by our group [67] in order to analyse the bacterial viability of two gram-positive bacteria (*S. aureus* and *S. epidermidis*) and one gram-negative (*E. coli*) using two different experimental conditions to evaluate the antibacterial effect of the synthesized nanoparticles and their extracts. Moreover, the effect of both nanoparticles and their extract was investigated against on *S. epidermidis* biofilm. The authors showed that with longer incubation time and higher suspension of nanoparticles (2 mg mL^{-1}) the bacterial viability for both *E. coli* and *S. aureus* has been reduced by 70-75% and by 50% for *S. epidermidis*. For what concerns the extract action, after 24 h a cell viability reduction was observed but it was less marked compared to the use of the particles. The same evidence was encountered also in the case of biofilm. For detailed description of these results see section 3.2.1.2 of the “Results and discussion” chapter.

Biological response to boron

Boron is one of the trace elements present in human body. It has been reported that boron intakes equal to 1-3 mg/day have positive effects on bone and brain health. Furthermore, it has a key role in several processes including embryo genesis, inflammatory and immune response [68,69].

Boron-containing MBG scaffold was developed using two different concentrations of boron (5 and 10 %mol) by Wu and co-workers [70]. In order to understand the effect on osteoblast response, cells were cultured on the surface of the scaffolds which were analysed after 1 and 7 days. The number and the spreading of the osteoblast increased with time and numerous filopodia ensured the close contact between the material and the osteoblast. An *in vivo* evaluation of B-modified bioactive glass particles was carried out by Gorustovich et al. [71] by implanting them in rat tibia bone marrow. After 15 days of implantation, the histomorphometric analysis demonstrated that the partial substitution of silicon by boron enhances the bone formation in the early stage and leads to a thicker bone tissue, characterised by Ca/P ratio similar to the hydroxyapatite one [72].

The pro-angiogenic potential of the ionic dissolution products from different boron-containing bioactive glass compositions has been investigated [73]. The cell viability, cell morphology and VEGF secretion from bone marrow stromal cell were evaluated. The authors speculated that both the cytocompatibility and the VEGF secretion depended on the release of Si and B ions and the composition 5.5%Na₂O 11.1%K₂O 4.6%MgO 18.5% CaO 56.6%B₂O₃ 3.7%P₂O₅ 0%SiO₂ (in wt.) was found to be toxic for the cells. On the other hand, the boron released (between 0-10 ppm) from other compositions (5.9%Na₂O 12.0K₂O 5.5%MgO 22.6%CaO

12.5%B₂O₃ 4.0%P₂O₅ 37.5%SiO₂ and 5.9%Na₂O 12.0K₂O 5.5%MgO 22.6%CaO 25%B₂O₃ 4.0%P₂O₅ 25%Si in wt.) promoted the cell mitochondrial activity and improved the release of VEGF.

A 45S5 bioglass containing 2% of boron (in wt.) was produced and its ionic dissolution products were used to test the pro-angiogenic capacity by evaluating the vasculature of the embryonic quail chorioallantoic membrane (CAM assay) [74]. The test with 45S5 undoped showed no pro-angiogenic effect but did not affect the normal vessel development in the CAM assay. The B-containing glasses, instead, allow the release of a sufficient amount of ion able to promote the angiogenesis, evidenced by the higher expression of the $\alpha v\beta 3$ which is an integrin significantly up-regulated during angiogenesis and vascular remodelling. It has been speculated by the authors that the effects observed could be explained by the fact that borate causes the stimulation of the secretion of cytokines and/or growth factors with pro-angiogenic potential and the proliferation of endothelial cells of the vessel.

Biological response to cobalt

Cobalt is another trace element present in human body and represents the metal constituent of vitamin B₁₂.

One of the most studied property of cobalt is its ability to enhance the angiogenesis process by miming the hypoxia through the stabilization of HIF-1 α [75,76].

The biological response of cobalt-containing bioactive glass/collagen composite scaffolds was studied by Quinlan et al. [77] through tests on cytocompatibility and pro-angiogenic effect. In this work, two sizes of bioactive glass were produced for the composite: (i) cobalt-containing bioactive glass particles with an average size of 38 μm and (ii) cobalt-containing bioactive glass particles with an average size of 100 μm . They proved that the particle size had an effect on the biological response of the composite and, in particular, the larger particles gave better results in terms of VEGF gene expression by HUVECs, VEGF protein production and vascular tubule formation. These results have been associated to the different release kinetics of the samples: the bigger particles at later timepoints released a lower concentration compared to the smaller ones. In fact, although the released concentration was below the toxic level (3-12 ppm) [78], the faster rate influence in a negative way the biological response.

Wu and co-workers investigated the relation between the Co²⁺ released from MBG scaffold and the hypoxia [78]. They found that both amounts of cobalt (2 and 5% mol) induced a significant hypoxic cascade with an increase of VEGF protein secretion, HIF-1 α and VEGF expression in BMSCs. But, the 5%mol Co-containing MBG scaffold showed a slightly less cell proliferation compared to 2%mol Co-containing scaffold.

What is clear is that cobalt, more than the other ions, could have a beneficial effect but, in large dose or with an uncontrolled release kinetics, could produce detrimental effect and induce cell apoptosis, inflammatory response and genotoxic effect [79].

Biological response to strontium

Strontium is a divalent cation which plays a pivotal physiological role in bone metabolism. Considering its effect on osteoclastogenesis, osteoblastogenesis and adipogenesis, strontium ranelate, a compound containing two atoms of Sr, is considered an alternative strategy to treat osteoporosis disease. Osteoporosis is a very common disease which affects predominantly postmenopausal women. The bone embrittlement lined to this pathology is caused by an imbalance between osteoblast action (bone deposition) and osteoclast action (bone resorption). Strontium ranelate was shown in osteopenic models and osteoporotic patients to increase the bone quality due to its property to activate osteoblast pathways and hinder osteoclast ones [80].

The calcium-sensing receptor (CaSR) is capable to sense divalent cations, such as Ca^{2+} which has similar charge, charge to size ratio and electronic configuration to Sr^{2+} and was proposed as a hypothetic mediator of the effect of strontium in the bone metabolism (Figure 1.10).

The activation of CaSR by strontium could have a double effect: promotion of osteoblast activity and inhibition of osteoclast activity, as evidenced in Figure 1.10. The increase in osteoblastogenesis is due to the activation of different signaling pathways (Wnt/ERK1/2-MAPK) which induces to osteoblast differentiation. On the other hand, strontium could inhibit the differentiation and resorbing activity of osteoclast by activation of CaSR. Furthermore, it could induce osteoclast apoptosis.

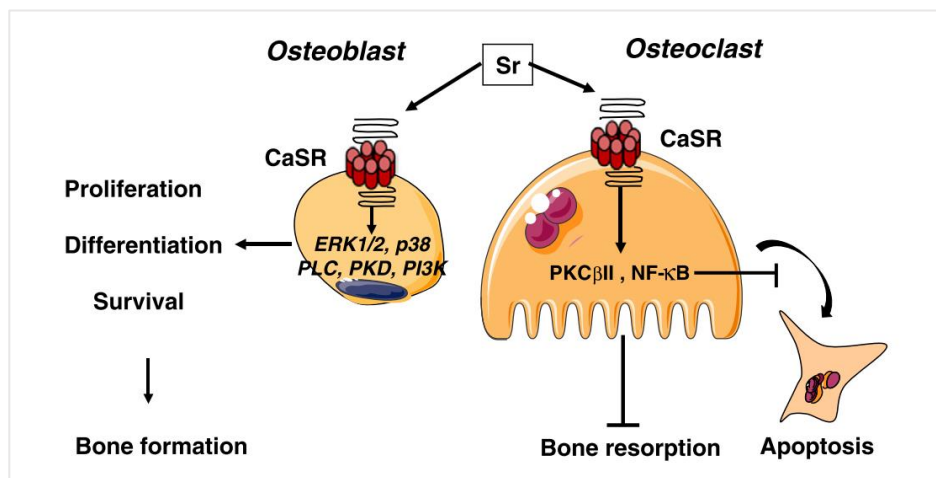


Figure 1.10: Role of the calcium sensing receptor [80]

Other important pathways in bone cells, such as nuclear factor of activated Tc (NFATc), Wingless/Integrated (Wnt) and RANK/RANKL/OPG, seem to be involved in Sr²⁺-induced effects (Figure 1.11).

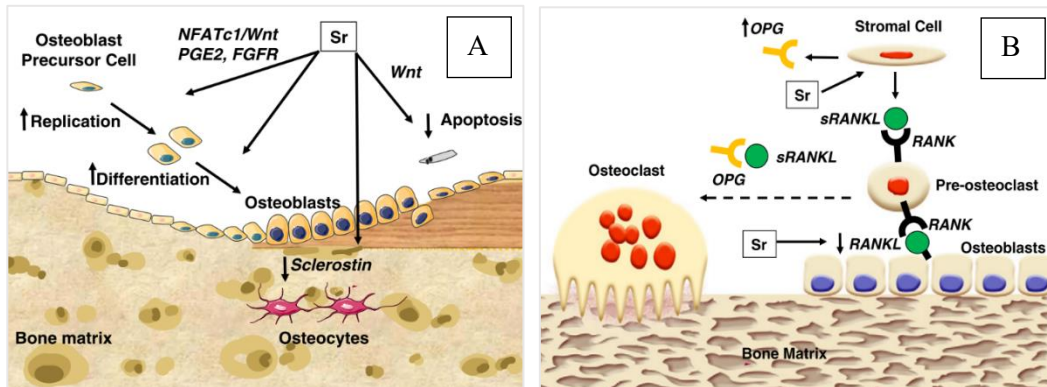


Figure 1.11: Actions of strontium on osteoblast differentiation (A) and on osteoclast differentiation (B) [80]

NFAT (NFATc1 to NFATc5) are five transcription factors involved in the differentiation of several cells. The activation of NFATc through Sr²⁺ provokes the upregulation of gene expression involved in osteoblastic differentiation. Also the Wnt signaling pathway, which is an important mechanism controlling the bone metabolism, is influenced by Sr²⁺ [80].

The involvement of Sr²⁺ in osteoclast differentiation could be explained considering RANK/RANKL/osteoprotegerin (OPG), where RANKL is the acronym of receptor activator of nuclear factor-kappaB ligand. OPG is important in bone density and mass regulation, while RANKL plays a role in osteoclastogenesis and bone resorption. As shown in Figure 1.11B, OPG associates with RANKL thus preventing its binding with RANK which is an important factor for osteoclast differentiation. Sr²⁺ promote the overexpression of OPG and reduce the expression of RANKL, reducing pre-osteoclast differentiation [80].

The effect of strontium on osteoclast and osteoblast activities has been studied by Gentleman et al. [81] by substituting calcium with strontium in bioactive glasses. They showed that the ions released were non-cytotoxic to Saos-2 cells. Moreover, the osteoclast differentiation was assessed by measuring the erosion pit area formed on calcium phosphate-coated chamber well slides, treated with the dissolution ions from strontium-substituted BG. Considering that the erosion pit area is an indicator of osteoclast activity, its reduction, as assessed by the authors, confirmed the potential of strontium to inhibit the osteoclast differentiation. The proliferation of osteoblast and the ALP activity evidenced the ability of the BG to stimulate the osteoblastogenesis when directly in contact with cells.

Fiorilli and co-workers [82] evaluated the biological response of two types of Sr-containing mesoporous bioactive glasses characterised by different particle size, structure features and ion release kinetics. The fibroblast morphology and the cell viability confirmed the non-toxicity of the matrices. Concerning the inflammatory response, both materials did not increase the IL6 and of IL1 β expression, which are

two mediators of the inflammatory response. By evaluating of RANKL and OPG genes, the authors found that both mesoporous bioactive glasses reduced osteoclast activity with a RANKL/OPG ratio in favour of OPG.

Biological response to lithium

Lithium is another metal element present in trace quantity in the human body which has been widely used in the treatment of bipolar disease. It has also been proved that lithium ions can be used in bone tissue engineering application because they are capable to activate the Wnt signalling pathway by inhibiting glycogen synthase kinase 3 β (GSK-3 β) which is an enzyme that phosphorylates β -catenin in the cytoplasm [83,84].

It has been proved that the activation of Wnt/ β -catenin signalling by LiCl induced the proliferation, migration and survival of microvascular endothelial cells *in vitro*, which are typical effects of VEGF. Nevertheless, the *in vivo* experiments on mice with oxygen induced retinopathy did not confirm the *in vitro* results suggesting that the β -catenin and Wnt/ β -catenin signalling increase is not sufficient to induce retinal capillary repair *in vivo* [85]. The use of lithium as vasculogenesis factor needs further studies.

The cementogenic differentiation ability, which leads to the formation of cementum (the substance which covers the tooth root), of Li⁺ free and incorporated into mesoporous bioactive glass scaffold was investigated by Han et al. [86]. They found that both free lithium and lithium incorporated induced a positive effect on culture of human periodontal ligament-derived cells (hPDLCs). In particular, the incorporation of 5% mol Li⁺ ion-containing MBG scaffold showed an enhanced cell proliferation and differentiation. Furthermore, an increase in ALP, OPN and OCN expression was noticed.

Biological response to cerium

Cerium is the first of lanthanide series, also known as rare-earths elements, and is characterised by an ionic radius similar to calcium although with a higher charge. Thanks to this feature, Ce³⁺ can act as Ca²⁺ ions, hence they can have high affinity to Ca²⁺ sites on biological species [87–89].

Differently from the most of lanthanides, cerium is stable in physiological solution in both oxidized (Ce⁴⁺) and reduced (Ce³⁺) forms and the successful shift between these two states of cerium oxide nanoparticles has been used in some studies [90,91]. Cerium oxide nanoparticles (CeONP) adopt a cubic crystalline structure in which eight oxygen anions surround a cerium atom and every oxygen atom occupies a tetrahedral position. The ability to mutate between Ce⁴⁺ and Ce³⁺ and the presence of vacancies, or defects, explain the use of CeONP as catalyst, antioxidant-enzyme-like agent (superoxide dismutase mimic, catalase mimic peroxidase-like mimic) and as hydroxyl and nitric oxide radical scavenging agent [91]. In particular, this last peculiarity has been exploited to target oxidative stress-related diseases and chronic inflammations. In biological systems, the oxidative stress is the result of an imbalance between ROS and nitrogen species production,

which can cause (i) toxicity or (ii) act as signalling molecules based on their concentration, position and intracellular conditions. In normal situations, an excessive production of ROS can be counteracted by cells, through mechanism such as enzyme antioxidants. However, beyond a certain limit or in presence of disease, these active species can provoke damage or oxidative stress which plays a role in aging and in several human diseases, such as chronic inflammation, diabetes, cardiovascular diseases. The capability of CeONP to scavenge almost all kinds of these active species was tested and makes this nanoparticles potential antioxidant agent [88,91–93].

Apart from the CeONP, the use of cerium compounds in biomedicine has been investigated in different applications, such as vomiting-related disease, burn wounds characterised by the presence of bacteria. In this last application, the combination of $\text{Ce}(\text{NO}_3)_3$ and silver sulfadiazine has been exploited in a commercial cream (distributed in Europe with the name of Flammacerium®) due to its ability to reduce bacterial colonisation, suppress the immune response and allow a more rapid re-epithelialization [89].

The antibacterial effect of cerium has been explained through different mechanisms and almost associated to the presence of Ce^{3+} [94–96]. It has been reported that Ce^{3+} ions rapidly bind to *E. Coli*, inhibit its respiration and enter cytoplasm through the penetration of outer and inner membrane. As stated before, the antibacterial mechanism of ceria, instead, was attributed to the oxidative stress following the reduction from Ce(IV) and Ce(III).

The osteoconductive and antibacterial properties of cerium-containing glass-reinforced hydroxyapatite have been elucidated in the work of Morais et al. [97]. The addition of cerium did not influence the general features of the composite, enhancing the biological effects of the material. In details, the antibacterial properties of the material have been tested against *S. aureus*, *S. epidermidis* and *P. aeruginosa* by evaluating the bacterial adhesion on the surfaces. The study revealed a different action against the Staphylococci strains and Pseudomonas: the presence of Ce decreases the bacterial adhesion of the gram-positive strains, compared to the composite without cerium, but it has no effect against the gram-negative. The authors speculated that this different action could be related to the bacterial morphology: the bacillus shape of the Staphylococci strains has more contact point with material with an increase of adhesion; in addition, the gram-negative bacteria present a complex wall composed by peptidoglycan layer and lipidic membrane being less permeable to cerium ions.

In the same work, human osteoblastic-like cell was used to test the effect of this material on cell attachment, adhesion and spreading. The cerium-substituted composite allowed the adhesion with the production of filopodia and a well-organised F-actin cell cytoskeleton. In addition, they proved that the presence of cerium had an inductive effect on cell proliferation and an up-regulation on ALP and BMP-2 expression.

The partial substitution of calcium with cerium in hydroxyapatite nanoparticles was examined by Lin and co-workers [98]. The antibacterial test confirmed that the

inhibition zone became bigger with the increase of cerium amount, also due to an increase of solubility of cerium-substituted hydroxyapatite particles.

In vivo study [99] on mouse demonstrated that Ce^{3+} ions were able to promote the proliferation of primary mouse osteoblasts (OBs) in all the tested concentrations, ranging between 10^{-9} and 10^{-4} mol L⁻¹. Differently from the proliferation, the effect of Ce^{3+} ions on differentiation is dose dependent with an inhibition of osteoblast differentiation at higher concentration.

A plausible molecular mechanism of the promotion of bone marrow stromal cells (BMSCs) migration and differentiation by cerium ions was explained by Hu and co-workers [100]. As shown in the schematic representation in Figure 1.12, it seems that cerium promotes the osteogenic differentiation of BMSCs through the Smad-dependent BMP signaling pathway.

In details, BMP, responsible for promoting osteogenic differentiation, binds BMPR2, which recruits and phosphorylates BMPR1, leading to the regulation of cell differentiation and growth through phosphorylation and translocation in the nucleus of the protein Smad1/5/8. This protein leads to an up-regulation of the genes related to osteogenic differentiation (Runx2 and SDF-1) [100].

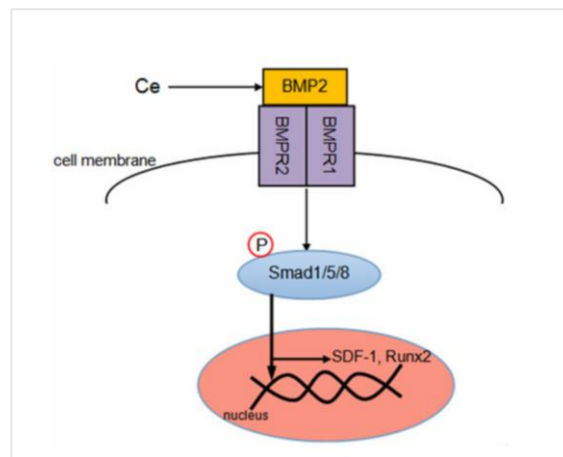


Figure 1.12: Schematic representation of the molecular mechanism of migration and differentiation of BMSCs induced by cerium [100]

Biological response to magnesium

Magnesium is the fourth most numerous cations in human body, present in bone tissue and, for only 1.0%, in extracellular matrix. Several cellular functions, such as potassium and calcium ion transport, signal transduction, cell proliferation and energy source are influenced by Mg [101].

The role of magnesium on proliferation and differentiation of human bone-derived cells (HBDCs) has been investigated by Zreiqat [102] in order to obtain surface modification of prosthetic implants. They demonstrated that the presence of Mg^{2+} led to an increase of osteoblast adhesion and a higher expression of the integrin receptors $\beta 1-$, $\alpha 5-$, $\alpha 3\beta 1-$, $\alpha 5\alpha 1-$. These integrin receptors are the mediator between the biomaterial and the cells. The integrins, in fact, regulate the gene

expression by transducing the signal from the extracellular to the intracellular environment, influencing the cell migration, proliferation and apoptosis.

The magnesium deficiency is linked with osteoporosis [103]. Several studies related to the deficiency of magnesium in humans gave an explanation about the relation between bone weakness and lack of magnesium (Figure 1.13). First of all, the magnesium deficiency has been linked to several causes such as diet, mutations on hereditary single-gene, alcohol, drugs.

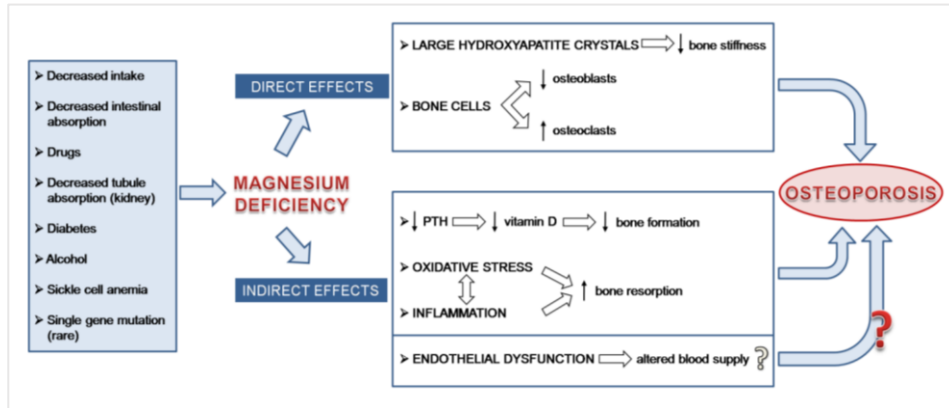


Figure 1.13: Link between osteoporosis and magnesium deficiency [103]

This lack of magnesium influences in a direct and indirect way the bone density:

- **Direct effects:** the hypomagnesemia influences the dimension of the new formed crystals of apatite which are larger than no-deficient Mg individuals and, thus, are not able to bear normal load. Furthermore, it leads to a decrease of markers related to osteoblastic activity and an increase in osteoclast number
- **Indirect effects:** the magnesium deficiency affects the parathyroid hormone (PTH) and the vitamin D which play a key role in the calcium homeostasis; it promotes also inflammation with the promotion of an oxidative stress as consequence. It is also speculated by the authors that the hypomagnesemia causes endothelial dysfunction followed by a decrease in blood vessel, and, as said before, there is a straight connection between blood supply and bone formation.

Biological response to silver

The antibacterial property of silver is well-known and exploited since ancient time due to the broad spectrum of action, which is very important when a polymicrobial colonisation occurs [104].

The antibacterial mechanism of silver is not fully elucidated yet, but three different modes of action have been proposed (Figure 1.14):

- 1- Uptake of free silver ions as such or as dissolution product of silver nanoparticles followed by disruption of ATP production, DNA mutation and cytoplasm shrinkage
- 2- Silver nanoparticles and silver ions can catalyse reactions with an excessive production of ROS
- 3- Silver nanoparticles interact directly with bacteria membrane and penetrate inside the cell, increase permeability and disturb the respiration [105]

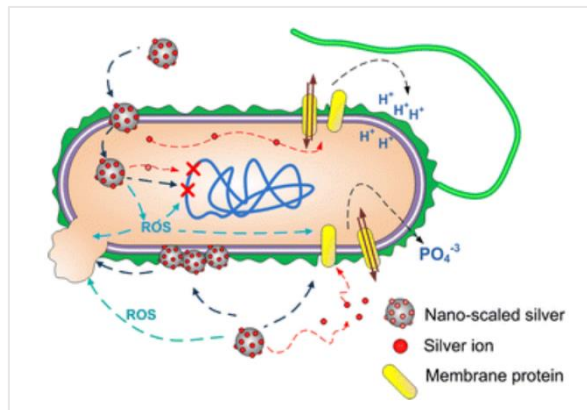


Figure 1.14: Antibacterial mode of action of silver particles [105]

In the frame of dental pulp tissue infection, the antibacterial action of silver ions was exploited by Lee et al. [106] by doping with silver ions bioactive glass nanoparticles (BGn) and testing them against *E. coli*, *S. oralis*, *E. faecalis*, and *S. mutans* bacteria strains, which are recognised as the most common species in dental pulp infection. The antibacterial functions were assessed through *in vitro* assay by counting the colonies forming unit (CFU) and *in vivo* by using an infected dental pulp tissue defect model generated in rat. The *in vitro* test confirmed that a concentration of $40 \mu\text{g mL}^{-1}$ was sufficient to reduce the bacterial viability to less than 10% for *E. coli* and *S. oralis*, a higher amount ($160 \mu\text{g mL}^{-1}$) was necessary to reduce to 20% the bacterial viability of *E. faecalis*. The Ag-containing BGn was not effective against *S. mutans*. The *in vivo* test conducted against *E. faecalis*, demonstrated that the BGn containing silver was more effective than free tetracycline, an antibiotic drug.

Silver-containing MBGs were produced by EISA process and investigated for their antibacterial potential against *S. aureus* by Gargiulo and co-workers [107]. In this work, the Ag-MBGs, incubated for 20 h in nutrient broth medium killed about 99% of bacteria colonies. The authors speculated that this effect could be associated to the Ag^+ ions dissolved from the crystalline AgCl developed after incubation in the growth medium, rich of Cl^- .

With the same antibacterial purpose, Dai and co-workers [108] conducted an in-depth study in order to obtain mesoporous silica spheres containing calcium and silver to control rapid haemorrhage. They demonstrated that only the exchange of

silver ions allowed a reduction of $> 4\log_{10}$ of *E. coli* and *S. aureus* bacteria strains and that the compounds without silver did not show any antibacterial activity. The authors proposed another explanation of silver's antibacterial mechanism in which silver ions induce the inactivation of proteins in bacteria by interaction with thiol groups. The obtained results on coagulation cascade, platelet adhesion, blood clotting, antibacterial activity suggested the potential use of this compound for wound dressing.

Biological response to zinc

More than 1000 human proteins contain zinc, as essential element. Furthermore, several key physiological processes are regulated by Zn, such as cellular response, oxidative stress, DNA repair and cell apoptosis. While few studies are focused on the damages related to Zn excess, various studies confirmed that the Zn deficiency may lead to chromosomal mutations, lined to the individual cancer risk [109].

In addition, zinc plays a pivotal role in the growing and maintenance of bone. It has been demonstrated that zinc has a stimulatory effect on osteoblastic bone formation and mineralization and on inhibition of osteoclastic bone resorption, resulting an important factor in osteoporosis [23].

The role of zinc in the cell differentiation, cell proliferation and mineralization are schematically shown in Figure 1.15. It seems that zinc can stimulate the gene expression of different proteins such as Runx2/Cbfa1 (the transcription factor for differentiation into osteoclastic cell), collagen I, ALP and OCN. In addition, zinc leads to an increase in the production of growth factors involved in human osteoblast proliferation (IGF-I and TGF- β 1) [23].

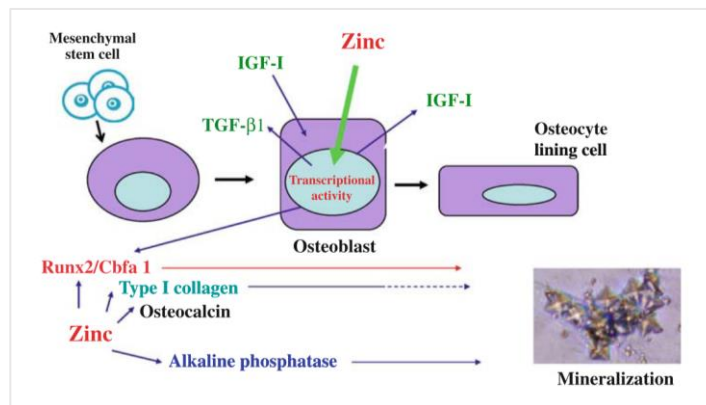


Figure 1.15: Osteoblastic bone formation mechanism influenced by zinc [23]

In the case of bone resorption, zinc is able to suppress the activity of osteoclast by inhibiting the action of RANKL in pre-osteoclasts, which is a receptor involved in osteoclast differentiation (Figure 1.16). Moreover, zinc stimulates the gene expression of OPG in osteoblastic cell and induces a factor which influences the osteoclastic lineage [23].

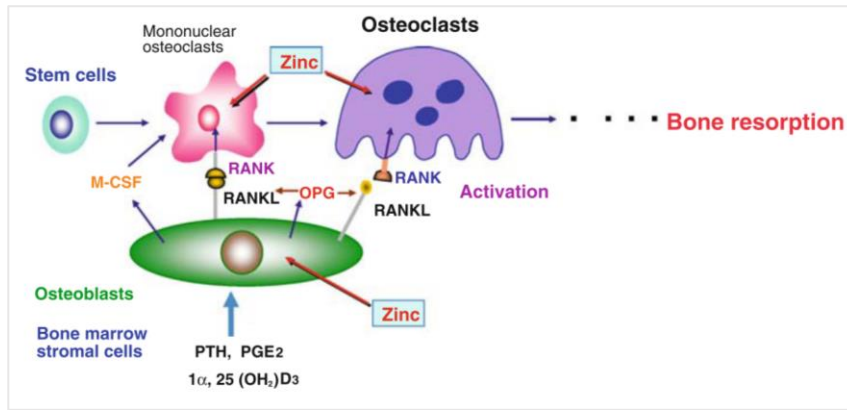


Figure 1.16: Osteoclastic bone resorption mechanism influenced by zinc [23]

The incorporation of Zn in bioactive glass has been investigated by different authors [110,111]. The studies confirmed the stimulation of osteoblast differentiation, proved by an increase of ALP activity with the increase of culture time. Furthermore Balamurugan and co-workers [110] investigated the osteoblastic cell morphology by scanning electronic microscopy (SEM) and evidenced the formation of filopodia and the increase in cell number, confirming the cytocompatibility of the zinc-substituted bioactive glass.

Varmette et al. [112] conducted a study on Zn-containing bioactive glasses to investigate the reduction of inflammation on murine macrophage cells after induction of inflammation by lipopolysaccharide (LPS) which is a large molecule composed by lipid and polysaccharide, found in the outer membrane of gram-negative bacteria. They discovered that bioactive glass in the ternary system containing 5 and 11% mol of zinc induced a reduction of tumor necrosis factor alpha (TNF α), which represents the “first in line” cytokine promoting the cascade of pro-inflammatory cytokine production.

The antibacterial potential of both zinc oxide nanoparticles and Zn²⁺ were analysed in different works [113,114]. The antibacterial activities of zinc ions were tested against five microorganisms and proved that the contribution of the overall antimicrobial activity was the complexation of Zn²⁺ by molecules present in the broth which caused a higher and faster dissolution of ions from ZnO. Apart from zinc ions dissolved from ZnO, also the same ZnO was found to have antibacterial properties against a broad spectrum of bacteria strains. The SEM investigation showed a dramatic change in bacteria cell morphology due to the increased levels of oxidative stress after administration of ZnO.

In Figure 1.17, the most relevant biological effects of the therapeutic ions are summarized.

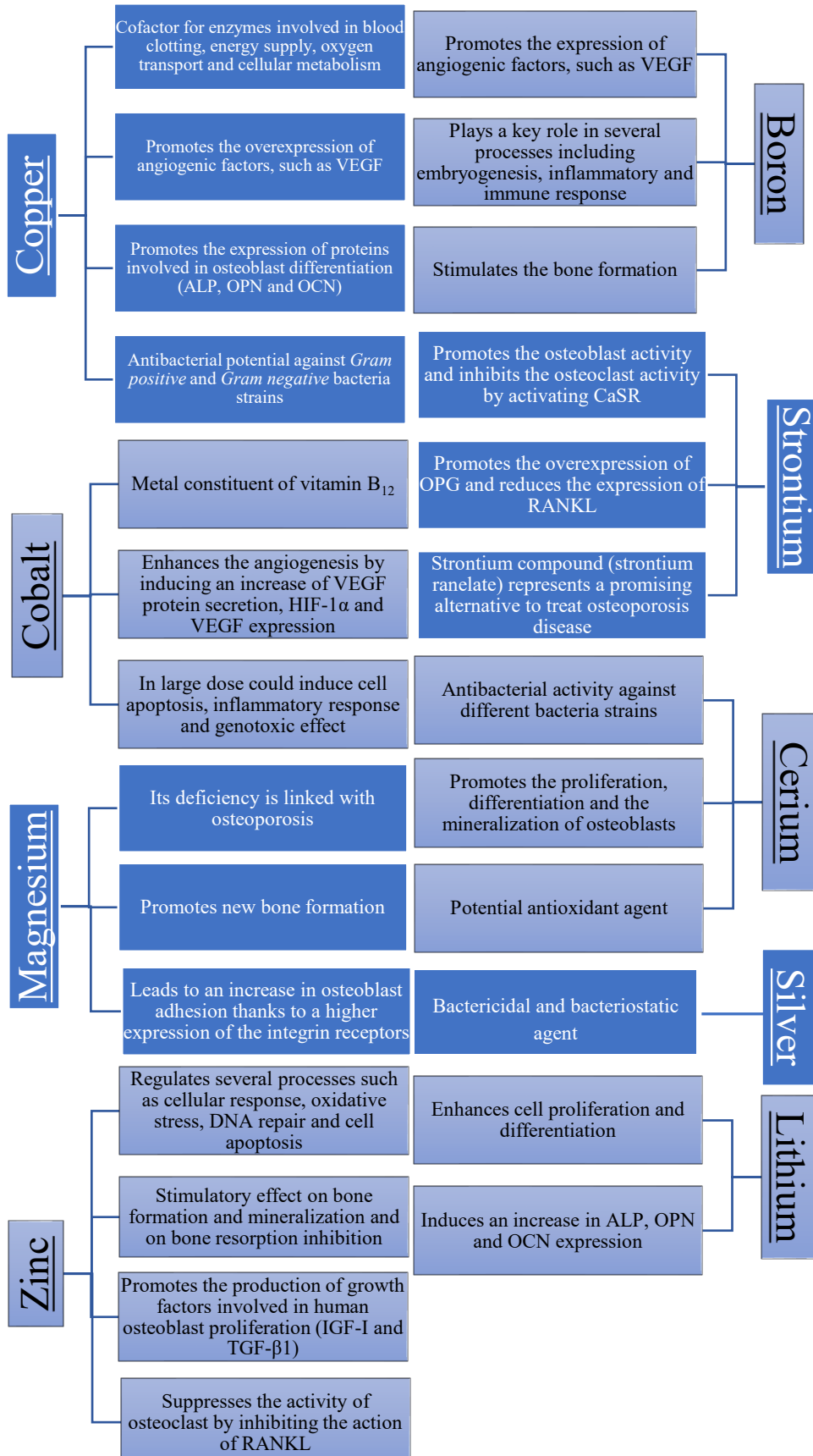


Figure 1.17: Summary of relevant biological effects of therapeutic ions

References

- [1] D.F. Williams, On the nature of biomaterials, *Biomaterials*. 30 (2009) 5897–5909. doi:10.1016/j.biomaterials.2009.07.027.
- [2] M. Vallet-Regí, Evolution of bioceramics within the field of biomaterials, *Comptes Rendus Chim*. 13 (2010) 174–185. doi:10.1016/j.crci.2009.03.004.
- [3] S.M. Best, A.E. Porter, E.S. Thian, J. Huang, Bioceramics: Past, present and for the future, *J. Eur. Ceram. Soc.* 28 (2008) 1319–1327. doi:10.1016/j.jeurceramsoc.2007.12.001.
- [4] L.L. Hench, The story of Bioglass®, *J. Mater. Sci. Mater. Med.* 17 (2006) 967–978. doi:10.1007/s10856-006-0432-z.
- [5] J.R. Jones, Review of bioactive glass: From Hench to hybrids, *Acta Biomater.* 9 (2012) 4457–4486. doi:10.1016/j.actbio.2012.08.023.
- [6] M.N. Rahaman, D.E. Day, B. Sonny Bal, Q. Fu, S.B. Jung, L.F. Bonewald, A.P. Tomsia, Bioactive glass in tissue engineering, *Acta Biomater.* 7 (2011) 2355–2373. doi:10.1016/j.actbio.2011.03.016.
- [7] N.W. Marion, W. Liang, G.C. Reilly, D.E. Day, M.N. Rahaman, J.J. Mao, Borate glass supports the in vitro osteogenic differentiation of human mesenchymal stem cells, *Mech. Adv. Mater. Struct.* 12 (2005) 239–246. doi:10.1080/15376490590928615.
- [8] G. Kaur, O.P. Pandey, K. Singh, D. Homa, B. Scott, G. Pickrell, A review of bioactive glasses: Their structure, properties, fabrication and apatite formation, *J. Biomed. Mater. Res. - Part A*. 102 (2014) 254–274. doi:10.1002/jbm.a.34690.
- [9] C. Vitale-Brovarone, G. Novajra, J. Lousteau, D. Milanese, S. Raimondo, M. Fornaro, Phosphate glass fibres and their role in neuronal polarization and axonal growth direction, *Acta Biomater.* 8 (2012) 1125–1136. doi:10.1016/j.actbio.2011.11.018.
- [10] D.F. Williams, On the mechanisms of biocompatibility, *Biomaterials*. 29 (2008) 2941–2953. doi:10.1016/j.biomaterials.2008.04.023.
- [11] C.J. Wilson, R.E. Clegg, D.I. Leavesley, M.J. Percy, Mediation of biomaterial–cell interactions by adsorbed proteins: a review, *Tissue Eng.* 11 (2005) 1–18. doi:10.1089/ten.2005.11.1.
- [12] L. Tang, J.W. Eaton, Inflammatory responses to biomaterials, *Am. J. Clin. Pathol.* 103 (1995) 466–471. doi:10.1093/ajcp/103.4.466.
- [13] J.M. Anderson, A. Rodriguez, D.T. Chang, Foreign body reaction to biomaterials, *Semin. Immunol.* 20 (2008) 86–100. doi:10.1016/j.smim.2007.11.004.
- [14] D.F. Williams, There is no such thing as a biocompatible material, *Biomaterials*. 35 (2014) 10009–10014. doi:10.1016/j.biomaterials.2014.08.035.

- [15] L.L. Hench, N. Roki, M.B. Fenn, Bioactive glasses: Importance of structure and properties in bone regeneration, *J. Mol. Struct.* 1073 (2014) 24–30. doi:10.1016/j.molstruc.2014.03.066.
- [16] G. Kaur, G. Pickrell, N. Sriranganathan, V. Kumar, D. Homa, Review and the state of the art: Sol–gel and melt quenched bioactive glasses for tissue engineering, *J. Biomed. Mater. Res. - Part B Appl. Biomater.* 104 (2016) 1248–1275. doi:10.1002/jbm.b.33443.
- [17] J. Zarzycki, Past and present of sol-gel science and technology, *J. Sol-Gel Sci. Technol.* 8 (1997) 17–22. doi:10.1007/BF02436811.
- [18] R. Li, A.E. Clark, L.L. Hench, An investigation of bioactive glass powders by sol-gel processing., *J. Appl. Biomater.* 2 (1991) 231–239. doi:10.1002/jab.770020403.
- [19] I. Izquierdo-Barba, A.J. Salinas, M. Vallet-Regí, Bioactive glasses: from macro to nano, *Int. J. Appl. Glas. Sci.* 4 (2013) 149–161. doi:10.1111/ijag.12028.
- [20] M. Erol-Taygun, K. Zheng, A.R. Boccaccini, Nanoscale bioactive glasses in medical applications, *Int. J. Appl. Glas. Sci.* 4 (2013) 136–148. doi:10.1111/ijag.12029.
- [21] P. V. Giannoudis, H. Dinopoulos, E. Tsiridis, Bone substitutes: An update, *Injury.* 36 (2005) S20–S27. doi:10.1016/j.injury.2005.07.029.
- [22] B.S. Klosterhoff, S. Nagaraja, J.J. Dedania, R.E. Guldberg, N.J. Willett, Material and mechanobiological considerations for bone regeneration, Elsevier Inc., 2016. doi:10.1016/B978-0-12-802792-9.00005-7.
- [23] M. Yamaguchi, Role of nutritional zinc in the prevention of osteoporosis, *Mol. Cell. Biochem.* 338 (2010) 241–254. doi:10.1007/s11010-009-0358-0.
- [24] K. Kaveh, R. Ibrahim, M.Z.A. Bakar, T.A. Ibrahim, Bone grafting and bone graft substitutes, *J. Anim. Vet. Adv.* 9 (2010) 1055–1067. doi:10.3923/javaa.2010.1055.1067.
- [25] W.R. Moore, S.E. Graves, G.I. Bain, Synthetic bone graft substitutes, *ANZ J. Surg.* 71 (2001) 354–361. doi:10.1046/j.1440-1622.2001.02128.x.
- [26] E. Gentleman, J.M. Polak, Historic and current strategies in bone tissue engineering: Do we have a hope in Hench?, *J. Mater. Sci. Mater. Med.* 17 (2006) 1029–1035. doi:10.1007/s10856-006-0440-z.
- [27] G. Jell, M.M. Stevens, Gene activation by bioactive glasses, *J. Mater. Sci. Mater. Med.* 17 (2006) 997–1002. doi:10.1007/s10856-006-0435-9.
- [28] G. Han, R. Ceilley, Chronic wound healing: A review of current management and treatments, *Adv. Ther.* 34 (2017) 599–610. doi:10.1007/s12325-017-0478-y.
- [29] X. Wang, F. Cheng, J. Liu, J.H. Smatt, D. Gepperth, M. Lastusaari, C. Xu, L. Hupa, Biocomposites of copper-containing mesoporous bioactive glass and nanofibrillated cellulose: Biocompatibility and angiogenic promotion in chronic wound healing application, *Acta Biomater.* 46 (2016) 286–298. doi:10.1016/j.actbio.2016.09.021.
- [30] V. Miguez-Pacheco, L.L. Hench, A.R. Boccaccini, Bioactive glasses beyond bone and teeth: Emerging applications in contact with soft tissues, *Acta*

- Biomater. 13 (2015) 1–15. doi:10.1016/j.actbio.2014.11.004.
- [31] P. Rhee, C. Brown, M. Martin, A. Salim, D. Plurad, D. Green, L. Chambers, D. Demetriades, G. Velmahos, H. Alam, Quikclot use in trauma for hemorrhage control: Case series of 103 documented uses, *J. Trauma - Inj. Infect. Crit. Care.* 64 (2008) 1093–1099. doi:10.1097/TA.0b013e31812f6dbc.
- [32] C. Lin, C. Mao, J. Zhang, Y. Li, X. Chen, Healing effect of bioactive glass ointment on full-thickness skin wounds, *Biomed. Mater.* 7 (2012) 045017. doi:10.1088/1748-6041/7/4/045017.
- [33] A.A. Gorustovich, J.A. Roether, A.R. Boccaccini, Effect of bioactive glasses on angiogenesis: A review of in vitro and in vivo evidences, *Tissue Eng. Part B Rev.* 16 (2010) 199–207. doi:10.1089/ten.teb.2009.0416.
- [34] S. Kargozar, F. Baino, S. Hamzehlou, R.G. Hill, M. Mozafari, Bioactive glasses: sprouting angiogenesis in tissue engineering, *Trends Biotechnol.* 36 (2018) 430–444. doi:10.1016/j.tibtech.2017.12.003.
- [35] R.M. Day, Bioactive glass stimulates the secretion of angiogenic growth factors and angiogenesis in vitro, *Tissue Eng.* 11 (2005) 768–777. doi:10.1089/ten.2005.11.768.
- [36] F. Baino, S. Hamzehlou, S. Kargozar, Bioactive glasses: Where are we and where are we going?, *J. Funct. Biomater.* 9 (2018) 25. doi:10.3390/jfb9010025.
- [37] K.S.W. Sing, Reporting physisorption data for gas/solid systems with special reference to the determination of surface area and porosity (Recommendations 1984), *Pure Appl. Chem.* 57 (1985) 603–619. doi:10.1351/pac198557040603.
- [38] I. Izquierdo-Barba, M. Vallet-Regí, Mesoporous bioactive glasses: Relevance of their porous structure compared to that of classical bioglasses, *Biomed. Glas.* 1 (2015) 140–150. doi:10.1515/bglass-2015-0014.
- [39] N.K. Raman, M.T. Anderson, C.J. Brinker, Template-based approaches to the preparation of amorphous, nanoporous silicas, *Chem. Mater.* 8 (1996) 1682–1701. doi:10.1021/cm960138+.
- [40] M. Vallet-Regí, I. Izquierdo-Barba, M. Colilla, Structure and functionalization of mesoporous bioceramics for bone tissue regeneration and local drug delivery, *Philos. Trans. R. Soc. A Math. Phys. Eng. Sci.* 370 (2012) 1400–1421. doi:10.1098/rsta.2011.0258.
- [41] C.J. Brinker, Y.F. Lu, A. Sellinger, H.Y. Fan, Evaporation induced self-assembly: Nanostructures made easy, *Adv. Mater.* 11 (1999) 579–585.
- [42] X.X. Yan, H.X. Deng, X.H. Huang, G.Q. Lu, S.Z. Qiao, D.Y. Zhao, C.Z. Yu, Mesoporous bioactive glasses. I. Synthesis and structural characterization, *J. Non. Cryst. Solids.* 351 (2005) 3209–3217. doi:10.1016/j.jnoncrysol.2005.08.024.
- [43] D. Arcos, A. López-Noriega, E. Ruiz-Hernández, O. Terasaki, M. Vallet-Regí, Ordered mesoporous microspheres for bone grafting and drug delivery, *Chem. Mater.* 21 (2009) 1000–1009. doi:10.1021/cm801649z.

- [44] F. Hoffmann, M. Cornelius, J. Morell, M. Fröba, Silica-based mesoporous organic-inorganic hybrid materials, *Angew. Chemie - Int. Ed.* 45 (2006) 3216–3251. doi:10.1002/anie.200503075.
- [45] I. Izquierdo-Barba, D. Arcos, Y. Sakamoto, O. Terasaki, A. López-Noriega, M. Vallet-Regí, High-performance mesoporous bioceramics mimicking bone mineralization, *Chem. Mater.* 20 (2008) 3191–3198. doi:10.1021/cm800172x.
- [46] M. Vallet-Regí, A.J. Salinas, D. Arcos, Tailoring the structure of bioactive glasses: From the nanoscale to macroporous scaffolds, *Int. J. Appl. Glas. Sci.* 7 (2016) 195–205. doi:10.1111/ijag.12205.
- [47] X. Yan, C. Yu, X. Zhou, J. Tang, D. Zhao, Highly ordered mesoporous bioactive glasses with superior in vitro bone-forming bioactivities, *Angew. Chemie - Int. Ed.* 43 (2004) 5980–5984. doi:10.1002/anie.200460598.
- [48] V. Mouriño, J.P. Cattalini, A.R. Boccaccini, Metallic ions as therapeutic agents in tissue engineering scaffolds: an overview of their biological applications and strategies for new developments, *J. R. Soc. Interface.* 9 (2012) 401–419. doi:10.1098/rsif.2011.0611.
- [49] K.H. Thompson, C. Orvig, Boon and bane of metal ions in medicine, 300 (2003) 936–939. doi:10.1126/science.1083004.
- [50] A. Hoppe, N.S. Güldal, A.R. Boccaccini, A review of the biological response to ionic dissolution products from bioactive glasses and glass-ceramics, *Biomaterials.* 32 (2011) 2757–2774. doi:10.1016/j.biomaterials.2011.01.004.
- [51] B.E. Kim, T. Nevitt, D.J. Thiele, Mechanisms for copper acquisition, distribution and regulation, *Nat. Chem. Biol.* 4 (2008) 176–185. doi:10.1038/nchembio.72.
- [52] M.L. Turski, D.J. Thiele, New roles for copper metabolism in cell proliferation, signaling, and disease, *J. Biol. Chem.* 284 (2009) 717–721. doi:10.1074/jbc.R800055200.
- [53] W. Feng, F. Ye, W. Xue, Z. Zhou, Y.J. Kang, Copper regulation of hypoxia-inducible factor-1 activity, *Mol. Pharmacol.* 75 (2009) 174–182. doi:10.1124/mol.108.051516.
- [54] A. Ahluwalia, A. S. Tarnawski, Critical role of hypoxia sensor - HIF-1 α in VEGF gene activation. Implications for angiogenesis and tissue injury healing, *Curr. Med. Chem.* 19 (2012) 90–97. doi:10.2174/092986712803413944.
- [55] H. Li, J. Li, J. Jiang, F. Lv, J. Chang, S. Chen, C. Wu, An osteogenesis/angiogenesis-stimulation artificial ligament for anterior cruciate ligament reconstruction, *Acta Biomater.* 54 (2017) 399–410. doi:10.1016/j.actbio.2017.03.014.
- [56] Y. Lin, W. Xiao, B.S. Bal, M.N. Rahaman, Effect of copper-doped silicate 13-93 bioactive glass scaffolds on the response of MC3T3-E1 cells in vitro and on bone regeneration and angiogenesis in rat calvarial defects in vivo, *Mater. Sci. Eng. C.* 67 (2016) 440–452. doi:10.1016/j.msec.2016.05.073.
- [57] L.B. Romero-Sánchez, M. Mari-Beffa, P. Carrillo, M.Á. Medina, A. Díaz-

- Cuenca, Copper-containing mesoporous bioactive glass promotes angiogenesis in an in vivo zebrafish model, *Acta Biomater.* 68 (2018) 272–285. doi:10.1016/j.actbio.2017.12.032.
- [58] M. Dziadek, B. Zagrajczuk, E. Menaszek, K. Dziadek, K. Cholewa-Kowalska, A simple way of modulating in vitro angiogenic response using Cu and Co-doped bioactive glasses, *Mater. Lett.* 215 (2018) 87–90. doi:10.1016/j.matlet.2017.12.075.
- [59] J.C. Wataha, C.T. Hanks, Z. Sun, Effect of cell line on in vitro metal ion cytotoxicity, *Dent. Mater.* 10 (1994) 156–161. doi:0109-5641(94)90025-6 [pii].
- [60] J.I. Ueda, M. Takai, Y. Shimazu, T. Ozawa, Reactive oxygen species generated from the reaction of copper(II) complexes with biological reductants cause DNA strand scission, *Arch. Biochem. Biophys.* 357 (1998) 231–239. doi:10.1006/abbi.1998.0811.
- [61] M.J. Burkitt, A critical overview of the chemistry of copper-dependent low density lipoprotein oxidation: Roles of lipid hydroperoxides, α -tocopherol, thiols, and ceruloplasmin, *Arch. Biochem. Biophys.* 394 (2001) 117–135. doi:10.1006/abbi.2001.2509.
- [62] I. Burghardt, F. Lüthen, C. Prinz, B. Kreikemeyer, C. Zietz, H.G. Neumann, J. Rychly, A dual function of copper in designing regenerative implants, *Biomaterials.* 44 (2015) 36–44. doi:10.1016/j.biomaterials.2014.12.022.
- [63] M. Shi, Z. Chen, S. Farnaghi, T. Friis, X. Mao, Y. Xiao, C. Wu, Copper-doped mesoporous silica nanospheres, a promising immunomodulatory agent for inducing osteogenesis, *Acta Biomater.* 30 (2016) 334–344. doi:10.1016/j.actbio.2015.11.033.
- [64] C. Wu, Y. Zhou, M. Xu, P. Han, L. Chen, J. Chang, Y. Xiao, Copper-containing mesoporous bioactive glass scaffolds with multifunctional properties of angiogenesis capacity, osteostimulation and antibacterial activity, *Biomaterials.* 34 (2013) 422–433. doi:10.1016/j.biomaterials.2012.09.066.
- [65] G. Grass, C. Rensing, M. Solioz, Metallic copper as an antimicrobial surface, *Appl. Environ. Microbiol.* 77 (2011) 1541–1547. doi:10.1128/AEM.02766-10.
- [66] A.M. Mulligan, M. Wilson, J.C. Knowles, The effect of increasing copper content in phosphate-based glasses on biofilms of *Streptococcus sanguis*, *Biomaterials.* 24 (2003) 1797–1807. doi:10.1016/S0142-9612(02)00577-X.
- [67] A. Bari, N. Bloise, S. Fiorilli, G. Novajra, M. Vallet-Regí, G. Bruni, A. Torres-Pardo, J.M. González-Calbet, L. Visai, C. Vitale-Brovarone, Copper-containing mesoporous bioactive glass nanoparticles as multifunctional agent for bone regeneration, *Acta Biomater.* 55 (2017) 493–504. doi:10.1016/j.actbio.2017.04.012.
- [68] F.H. Nielsen, Is boron nutritionally relevant?, *Nutr. Rev.* 66 (2008) 183–191. doi:10.1111/j.1753-4887.2008.00023.x.
- [69] F.H. Nielsen, The emergence of boron as nutritionally important throughout

- the life cycle, *Nutrition*. 16 (2000) 512–514.
- [70] C. Wu, R. Miron, A. Sculean, S. Kaskel, T. Doert, R. Schulze, Y. Zhang, Proliferation, differentiation and gene expression of osteoblasts in boron-containing associated with dexamethasone deliver from mesoporous bioactive glass scaffolds, *Biomaterials*. 32 (2011) 7068–7078. doi:10.1016/j.biomaterials.2011.06.009.
- [71] A.A. Gorustovich, J.M.P. López, M.B. Guglielmotti, R.L. Cabrini, Biological performance of boron-modified bioactive glass particles implanted in rat tibia bone marrow, *Biomed. Mater.* 1 (2006) 100–105. doi:10.1088/1748-6041/1/3/002.
- [72] V. Uskoković, D.P. Uskoković, Nanosized hydroxyapatite and other calcium phosphates: Chemistry of formation and application as drug and gene delivery agents, *J. Biomed. Mater. Res. - Part B Appl. Biomater.* 96 B (2011) 152–191. doi:10.1002/jbm.b.31746.
- [73] P. Balasubramanian, L. Hupa, B. Jokic, R. Detsch, A. Grünwald, A.R. Boccaccini, Angiogenic potential of boron-containing bioactive glasses: in vitro study, *J. Mater. Sci.* 52 (2017) 8785–8792. doi:10.1007/s10853-016-0563-7.
- [74] L.A. Haro Durand, G.E. Vargas, N.M. Romero, R. Vera-Mesones, J.M. Porto-López, A.R. Boccaccini, M.P. Zago, A. Baldi, A. Gorustovich, Angiogenic effects of ionic dissolution products released from a boron-doped 45S5 bioactive glass, *J. Mater. Chem. B*. 3 (2015) 1142–1148. doi:10.1039/c4tb01840k.
- [75] W. Fan, R. Crawford, Y. Xiao, Enhancing in vivo vascularized bone formation by cobalt chloride-treated bone marrow stromal cells in a tissue engineered periosteum model, *Biomaterials*. 31 (2010) 3580–3589. doi:10.1016/j.biomaterials.2010.01.083.
- [76] T. Tanaka, I. Kojima, T. Ohse, J.R. Ingelfinger, S. Adler, T. Fujita, M. Nangaku, Cobalt promotes angiogenesis via hypoxia-inducible factor and protects tubulointerstitium in the remnant kidney model, *Lab. Investig.* 85 (2005) 1292–1307. doi:10.1038/labinvest.3700328.
- [77] E. Quinlan, S. Partap, M.M. Azevedo, G. Jell, M.M. Stevens, F.J. O'Brien, Hypoxia-mimicking bioactive glass/collagen glycosaminoglycan composite scaffolds to enhance angiogenesis and bone repair, *Biomaterials*. 52 (2015) 358–366. doi:10.1016/j.biomaterials.2015.02.006.
- [78] C. Wu, Y. Zhou, W. Fan, P. Han, J. Chang, J. Yuen, M. Zhang, Y. Xiao, Hypoxia-mimicking mesoporous bioactive glass scaffolds with controllable cobalt ion release for bone tissue engineering, *Biomaterials*. 33 (2012) 2076–2085. doi:10.1016/j.biomaterials.2011.11.042.
- [79] L.O. Simonsen, H. Harbak, P. Bennekou, Cobalt metabolism and toxicology—A brief update, *Sci. Total Environ.* 432 (2012) 210–215. doi:10.1016/j.scitotenv.2012.06.009.
- [80] Z. Saidak, P.J. Marie, Strontium signaling: Molecular mechanisms and therapeutic implications in osteoporosis, *Pharmacol. Ther.* 136 (2012) 216–226. doi:10.1016/j.pharmthera.2012.07.009.

- [81] E. Gentleman, Y.C. Fredholm, G. Jell, N. Lotfibakhshaiesh, M.D. O'Donnell, R.G. Hill, M.M. Stevens, The effects of strontium-substituted bioactive glasses on osteoblasts and osteoclasts in vitro, *Biomaterials*. 31 (2010) 3949–3956. doi:10.1016/j.biomaterials.2010.01.121.
- [82] S. Fiorilli, G. Molino, C. Pontremoli, G. Iviglia, E. Torre, C. Cassinelli, M. Morra, C. Vitale-Brovarone, The incorporation of strontium to improve bone-regeneration ability of mesoporous bioactive glasses, *Materials (Basel)*. 11 (2018). doi:10.3390/ma11050678.
- [83] M. Arioka, F. Takahashi-Yanaga, M. Sasaki, T. Yoshihara, S. Morimoto, M. Hirata, Y. Mori, T. Sasaguri, Acceleration of bone regeneration by local application of lithium: Wnt signal-mediated osteoblastogenesis and Wnt signal-independent suppression of osteoclastogenesis, *Biochem. Pharmacol.* 90 (2014) 397–405. doi:10.1016/j.bcp.2014.06.011.
- [84] C.M. Hedgepeth, L.J. Conrad, J. Zhang, H.C. Huang, V.M.Y. Lee, P.S. Klein, Activation of the Wnt signaling pathway: A molecular mechanism for lithium action, *Dev. Biol.* 185 (1997) 82–91. doi:10.1006/dbio.1997.8552.
- [85] L.F. Zeilbeck, B. Müller, V. Knobloch, E.R. Tamm, A. Ohlmann, Differential angiogenic properties of lithium chloride in vitro and in vivo, *PLoS One*. 9 (2014). doi:10.1371/journal.pone.0095546.
- [86] P. Han, C. Wu, J. Chang, Y. Xiao, The cementogenic differentiation of periodontal ligament cells via the activation of Wnt/ β -catenin signalling pathway by Li⁺ ions released from bioactive scaffolds, *Biomaterials*. 33 (2012) 6370–6379. doi:10.1016/j.biomaterials.2012.05.061.
- [87] C.A. Barta, K. Sachs-Barrable, J. Jia, K.H. Thompson, K.M. Wasan, C. Orvig, Lanthanide containing compounds for therapeutic care in bone resorption disorders, *Dalt. Trans.* (2007) 5019–5030. doi:10.1039/b705123a.
- [88] K. Wang, R. Li, Y. Cheng, B. Zhu, Lanthanides - The future drugs?, *Coord. Chem. Rev.* 190–192 (1999) 297–308. doi:10.1016/S0010-8545(99)00072-7.
- [89] S.P. Fricker, The therapeutic application of lanthanides, *Chem. Soc. Rev.* 35 (2006) 524–533. doi:10.1039/b509608c.
- [90] T. Naganuma, E. Traversa, The effect of cerium valence states at cerium oxide nanoparticle surfaces on cell proliferation, *Biomaterials*. 35 (2014) 4441–4453. doi:10.1016/j.biomaterials.2014.01.074.
- [91] C. Xu, X. Qu, Cerium oxide nanoparticle: A remarkably versatile rare earth nanomaterial for biological applications, *NPG Asia Mater.* 6 (2014) e90. doi:10.1038/am.2013.88.
- [92] P. Eriksson, A.A. Tal, A. Skallberg, C. Brommesson, Z. Hu, R.D. Boyd, W. Olovsson, N. Fairley, I.A. Abrikosov, X. Zhang, K. Uvdal, Cerium oxide nanoparticles with antioxidant capabilities and gadolinium integration for MRI contrast enhancement, *Sci. Rep.* 8 (2018) 1–12. doi:10.1038/s41598-018-25390-z.
- [93] S.M. Hirst, A.S. Karakoti, R.D. Tyler, N. Sriranganathan, S. Seal, C.M. Reilly, Anti-inflammatory properties of cerium oxide nanoparticles, *Small*.

- 5 (2009) 2848–2856. doi:10.1002/sml.200901048.
- [94] J.M. Sobek, D.E. Talburt, Effects of the rare earth cerium on *Escherichia coli*, *J. Bacteriol.* 95 (1968) 47–51.
- [95] Y.F. Goh, A.Z. Alshemary, M. Akram, M.R. Abdul Kadir, R. Hussain, In-vitro characterization of antibacterial bioactive glass containing ceria, *Ceram. Int.* 40 (2014) 729–737. doi:10.1016/j.ceramint.2013.06.062.
- [96] A. Chen, Q. Shi, Y. Ouyang, Y. Chen, Effect of Ce³⁺ on membrane permeability of *Escherichia coli* cell, *J. Rare Earths.* 30 (2012) 947–951. doi:10.1016/S1002-0721(12)60159-8.
- [97] D.S. Morais, S. Fernandes, P.S. Gomes, M.H. Fernandes, P. Sampaio, M.P. Ferraz, J.D. Santos, M.A. Lopes, N. Sooraj Hussain, Novel cerium doped glass-reinforced hydroxyapatite with antibacterial and osteoconductive properties for bone tissue regeneration, *Biomed. Mater.* 10 (2015) 55008. doi:10.1088/1748-6041/10/5/055008.
- [98] Y. Lin, Z. Yang, J. Cheng, Preparation, characterization and antibacterial property of cerium substituted hydroxyapatite nanoparticles, *J. Rare Earths.* 25 (2007) 452–456. doi:10.1016/S1002-0721(07)60455-4.
- [99] J. Zhang, C. Liu, Y. Li, J. Sun, P. Wang, K. Di, Y. Zhao, Effect of cerium ion on the proliferation, differentiation and mineralization function of primary mouse osteoblasts in vitro, *J. Rare Earths.* 28 (2010) 138. doi:10.1007/s12011-013-9655-2.
- [100] Y. Hu, Y. Du, H. Jiang, G. Jiang, Cerium promotes bone marrow stromal cells migration and osteogenic differentiation via Smad1 / 5 / 8 signaling pathway, *Int J Clin Exp Pathol.* 7 (2014) 5369–5378.
- [101] T. Okuma, Magnesium and bone strength, *Nutrition.* 17 (2001) 679–680. doi:10.1016/S0899-9007(01)00551-2.
- [102] H. Zreiqat, C.R. Howlett, A. Zannettino, P. Evans, G. Schulze-Tanzil, C. Knabe, M. Shakibaei, Mechanisms of magnesium-stimulated adhesion of osteoblastic cells to commonly used orthopaedic implants, *J. Biomed. Mater. Res.* 62 (2002) 175–184. doi:10.1002/jbm.10270.
- [103] S. Castiglioni, A. Cazzaniga, W. Albisetti, J. Maier, Magnesium and osteoporosis: Current state of knowledge and future research directions, *Nutrients.* 5 (2013) 3022–3033. doi:10.3390/nu5083022.
- [104] A. Balamurugan, G. Balossier, D. Laurent-Maquin, S. Pina, A.H.S. Rebelo, J. Faure, J.M.F. Ferreira, An in vitro biological and anti-bacterial study on a sol-gel derived silver-incorporated bioglass system, *Dent. Mater.* 24 (2008) 1343–1351. doi:10.1016/j.dental.2008.02.015.
- [105] C. Marambio-Jones, E.M.V. Hoek, A review of the antibacterial effects of silver nanomaterials and potential implications for human health and the environment, *J. Nanoparticle Res.* 12 (2010) 1531–1551. doi:10.1007/s11051-010-9900-y.
- [106] J.H. Lee, A. El-Fiqi, N. Mandakhbayar, H.H. Lee, H.W. Kim, Drug/ion co-delivery multi-functional nanocarrier to regenerate infected tissue defect, *Biomaterials.* 142 (2017) 62–76. doi:10.1016/j.biomaterials.2017.07.014.
- [107] N. Gargiulo, A.M. Cusano, F. Causa, D. Caputo, P.A. Netti, Silver-

- containing mesoporous bioactive glass with improved antibacterial properties, *J. Mater. Sci. Mater. Med.* 24 (2013) 2129–2135. doi:10.1007/s10856-013-4968-4.
- [108] C. Dai, Y. Yuan, C. Liu, J. Wei, H. Hong, X. Li, X. Pan, Degradable, antibacterial silver exchanged mesoporous silica spheres for hemorrhage control, *Biomaterials*. 30 (2009) 5364–5375. doi:10.1016/j.biomaterials.2009.06.052.
- [109] R. Sharif, P. Thomas, P. Zalewski, M. Fenech, The role of zinc in genomic stability, *Mutat. Res. - Fundam. Mol. Mech. Mutagen.* 733 (2012) 111–121. doi:10.1016/j.mrfmmm.2011.08.009.
- [110] A. Balamurugan, G. Balossier, S. Kannan, J. Michel, A.H.S. Rebelo, J.M.F. Ferreira, Development and in vitro characterization of sol-gel derived CaO-P2O5-SiO2-ZnO bioglass, *Acta Biomater.* 3 (2007) 255–262. doi:10.1016/j.actbio.2006.09.005.
- [111] A. Oki, B. Parveen, S. Hossain, S. Adeniji, H. Donahue, Preparation and in vitro bioactivity of zinc containing sol-gel-derived bioglass materials, *J. Biomed. Mater. Res. - Part A.* 69 (2004) 216–221. doi:10.1002/jbm.a.20070.
- [112] E.A. Varmette, J.R. Nowalk, L.M. Flick, M.M. Hall, Abrogation of the inflammatory response in LPS-stimulated RAW 264.7 murine macrophages by Zn- and Cu-doped bioactive sol-gel glasses, *J. Biomed. Mater. Res. - Part A.* 90 (2009) 317–325. doi:10.1002/jbm.a.32098.
- [113] J. Pasquet, Y. Chevalier, J. Pelletier, E. Couval, D. Bouvier, M.A. Bolzinger, The contribution of zinc ions to the antimicrobial activity of zinc oxide, *Colloids Surfaces A Physicochem. Eng. Asp.* 457 (2014) 263–274. doi:10.1016/j.colsurfa.2014.05.057.
- [114] Y. Xie, Y. He, P.L. Irwin, T. Jin, X. Shi, Antibacterial activity and mechanism of action of zinc oxide nanoparticles against *Campylobacter jejuni*, *Appl. Environ. Microbiol.* 77 (2011) 2325–2331. doi:10.1128/AEM.02149-10.

CHAPTER 2

Materials and methods

2.1 Introduction

The aim of this PhD research was to develop a library of ion-containing mesoporous nanomatrices which can exert different therapeutic effects to meet the needs of tissue regeneration applications and overcome the limitations of the traditional treatments, as widely described in the previous chapter. The amount and the type of therapeutic ions added during the synthesis were selected to create agents with peculiar features, such as antibacterial, pro-osteogenic and pro-angiogenic properties. To this purpose, different synthesis routes were tested and optimized in order to produce two main different categories of nanomatrices: nano-sized particles with diameter ranging between 100 and 200 nm and pores in the range of 2-4 nm, and micro-sized particles with size in the range of 500 and 5 μm and bigger pores of about 7-8 nm.

In this chapter, the synthesis procedures adopted to obtain the mesoporous nanomatrices are described.

In particular, a selection process (Figure 2.1) was carried out following the general aim to reduce/avoid inflammable organic solvents, strongly acidic solutions and energy-consuming steps in view of an easier scaling-up of the manufacturing process.

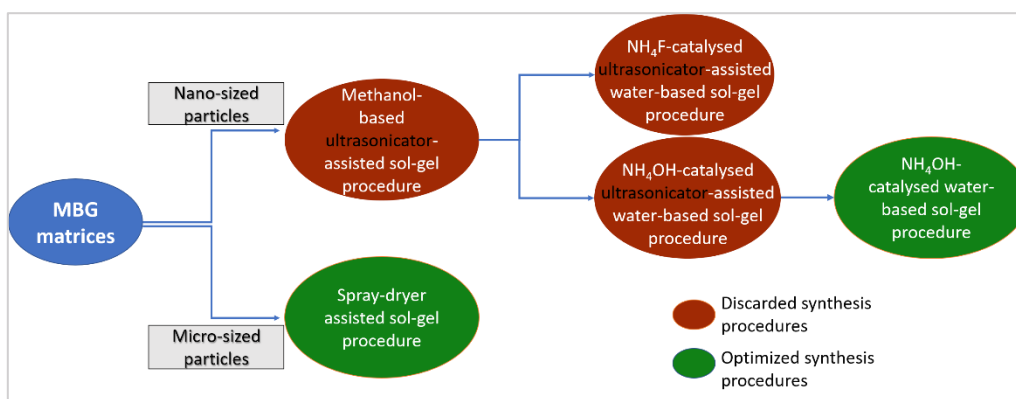


Figure 2.1: Flow chart of the synthesis procedure selection process

In this regard, in paragraphs 2.2, 2.3 and 2.4 the different synthesis procedures and the sample compositions are presented, followed by the description concerning the morphological, structural and compositional characterization techniques, the different ion release procedures and the method followed to assess the bioactive behaviour. Subsequently, a large part of this chapter is dedicated to the biological assays carried out through the collaboration with different research groups, as highlighted in the specific sub-paragraphs. In details, the biocompatibility and the antibacterial tests using selected nanomatrices are described.

Finally, an advanced biological assessment by using 3D skin models is reported in section 2.8.3.

2.2 Synthesis of MBGs assisted by ultrasonication

In order to produce nano-sized particles with pores around 3 nm, different procedures were tested. Among them, the first route investigated was a methanol-based ultrasonicator-assisted sol-gel procedure obtained by modifying a procedure reported by El-Fiqi et al. [1]. The ultrasound waves allow a better disintegration of the particles and the production of fine dispersions thanks to the cavitation phenomenon. The results were promising (described in section 3.2.1 of “Results and discussion” chapter) but the involvement of toxic inflammable solvent and the use of an energy-consuming step (ultra-sonication) did not meet the sought safety and scalability requirements.

2.2.1 Methanol-based sol-gel synthesis

In details, the as-synthesized nanomatrices, the molar composition and the amount of the ion precursors used during the synthesis are listed in Table 2.1. The therapeutic ion-containing nanomatrices were obtained by substituting part of calcium with the chosen amount of therapeutic ion.

For this synthesis, the reagents were all purchased from Sigma-Aldrich.

Part of the work described in this chapter has been published during the PhD period [2].

Briefly, 5 g of cetyltrimethylammonium bromide (CTAB, $\geq 98\%$) was completely dissolved by stirring in 120 mL of absolute methanol, whose pH was adjusted to 12.5 by adding about 30 mL of NH_4OH . Into this solution, proper amounts of calcium nitrate tetrahydrate ($\text{Ca}(\text{NO}_3)_2 \cdot 4\text{H}_2\text{O}$, 99%) and therapeutic ion precursor (see Table 2.1) were dissolved. In a separate batch, 0.895 g of tetraethyl orthosilicate (TEOS, 99%) were dissolved in 30 mL of absolute methanol and was then added to the first solution with the simultaneous application of ultrasounds using a SONOPULS Ultrasonic Homogenizers HD 3200. The output power was 150W in a 10 s on/10 s off cycle for 20 min. This solution was stirred at room temperature for 24 h. Then the precipitate was separated by centrifugation (Hermle Labortechnik Z326) at 5000 rpm for 5 min, washed one time with distilled water and two times with absolute ethanol. The final precipitate was dried at 70 °C for 12 h and calcined at 600 °C in air for 5 h at a heating rate of 1 °C/min using a Carbolite 1300 CWF 15/5.

Table 2.1: Sample composition and reagent amount used in the methanol-based ultrasonicator-assisted sol-gel synthesis

Name	Composition (%mol)	Reagents (g)		
		TEOS	$\text{Ca}(\text{NO}_3)_2 \cdot 4\text{H}_2\text{O}$	Therapeutic ion precursor
MBG_US_m_SiO ₂ /CaO	85 SiO ₂ /15 CaO	0.895	0.179	/
MBG_US_m_Cu2%	85 SiO ₂ /13 CaO/2 CuO	0.895	0.156	<u>CuCl₂</u> : 0.014
MBG_US_m_Cu5%	85 SiO ₂ /10 CaO/5 CuO	0.895	0.119	<u>CuCl₂</u> : 0.034
MBG_US_m_Sr1%	85 SiO ₂ /14 CaO/1 SrO	0.895	0.168	<u>SrCl₂ · 6H₂O</u> : 0.014
MBG_US_m_CuSr2%	85 SiO ₂ /13 CaO/1 CuO/1 SrO	0.895	0.156	<u>CuCl₂</u> : 0.007 <u>SrCl₂ · 6H₂O</u> : 0.016

2.2.2 Water-based sol-gel synthesis

With the aim of avoiding the use of toxic solvent and improving the synthesis yield, two different water-based procedures assisted by the ultrasonicator were adopted and the related description are reported in sections 2.2.2.a and 2.2.2.b.

2.2.2a Ammonium fluoride-catalysed water-based sol-gel synthesis

A water-based ultrasonicator-assisted approach, using NH_4F as catalyst, was adopted with the aim to produce mesoporous silicate-based systems by carrying out changes to a procedure previously reported in literature [3]. Table 2.2 reports the samples, the molar composition and the reagent amounts used during this synthesis. As can be noticed, the same route was followed to produce both ion-containing mesoporous bioactive glass (MBG) and mesoporous silica (MSn) systems.

As previously, the reagents were all purchased from Sigma-Aldrich.

In details, 1.8 g of CTAB, 3 g of NH_4F (Sigma-Aldrich) and a specific amount of $\text{Ca}(\text{NO}_3)_2 \cdot 4\text{H}_2\text{O}$ (only for MBG systems) were dissolved in 500 mL of distilled water and left under stirring for 1 h at 80 °C. Subsequently, a proper amount of therapeutic ion precursors, previously dissolved in 1 mL of ethanol, was mixed with 9 mL of TEOS. The latter solution was added drop wise to the first one, with the simultaneous application of high-power ultra-sounds (150 W in a 10 s on/10 s off cycle for 20 min) using a SONOPULS Ultrasonic Homogenizers HD 3200. After 4 h of stirring, the supernatant was separated by centrifugation (Hermle Labortechnik Z326) at 5000 rpm for 5 min and washed, and redispersed one time with distilled water and one time with ethanol. The final precipitate was dried at 70 °C for 12 h. Finally, the surfactant was removed by calcination at 600 °C in air for 5 h at a heating rate of 1 °C/min using a FALC FM 8,2.

Table 2.2: Sample composition and reagent amount used in the water-based ultrasonicator-assisted sol-gel procedure, using NH_4F as catalyst

Name	Composition (%mol)	Reagents (g)		
		TEOS	$\text{Ca}(\text{NO}_3)_2 \cdot 4\text{H}_2\text{O}$	Therapeutic ion precursor
MBG_US_w_I_Cu2%	85 SiO_2 /13 CaO /2 CuO	8.460	1.470	CuCl_2 : 0.128
Msn_US_w_I_Ag2%*	98 SiO_2 /2 AgO	8.460	/	AgNO_3 : 0.141
Msn_US_w_I_Ce2%*	98 SiO_2 /2 CeO	8.460	/	$\text{CeCl}_3 \cdot 7\text{H}_2\text{O}$: 0.308

2.2.2b Ammonia-catalysed water-based sol-gel synthesis

A base-catalysed water-based route, involving the use of ammonia as catalyst, was used to produce the calcium-silicate nano-sized sample MBG_US_w_II_ SiO_2 /CaO (Table 2.3). By adding the ultrasonication step, a procedure developed by Wu et al. [4] was modified. In particular, 6.6 g of CTAB and 12 mL of NH_4OH were dissolved in 600 mL of double distilled water. After 30 min of stirring, 28.2 g of TEOS and 5.64 g of $\text{Ca}(\text{NO}_3)_2 \cdot 4\text{H}_2\text{O}$ were added with the simultaneous application of high-power ultra-sounds (150 W in a 10 s on/10 s off cycle for 20 min) using a SONOPULS Ultrasonic Homogenizers HD 3200 and left under stirring for 3 h. The as-obtained products were separated using a centrifuge (Hermle Labortechnik Z326) and washed one time with distilled water and one time with ethanol. Finally, the collected powders were dried 70 °C for 12 h and calcined at 600°C for 5 h (heating rate of 1 °C/min).

Table 2.3: Sample composition and reagent amount used in the water-based ultrasonicator-assisted sol-gel procedure, using NH_4OH as catalyst

Name	Composition (%mol)	Reagents (g)		
		TEOS	$\text{Ca}(\text{NO}_3)_2 \cdot 4\text{H}_2\text{O}$	Therapeutic ion precursor
MBG_US_w_II_ SiO_2 /CaO	85 SiO_2 /15 CaO	28.20	5.64	/

2.3 Ammonia-catalysed water-based sol-gel synthesis (without sonication)

Based on the cost-analysis conducted by Nanolith, a Swedish partner of the MOZART project, the ultra-sonication step, introduced in the base-catalysed sol-gel synthesis described in section 2.2.2b, was removed and the procedure reported by Wu and co-authors [4] was carried out by incorporating specific amount of therapeutic ion to replace part of calcium in order to obtain ion-substituted nano-sized particles, as illustrated in Table 2.4.

Part of the work described in this chapter has been already published during the PhD period [5].

In this synthesis, the reagents were all purchased from Sigma-Aldrich and the samples were produced by following the same ammonia-catalysed water-based sol-gel procedure reported in section 2.2.2b without the sonication step.

Table 2.4: Sample composition and reagent amount used in the water-based sol-gel procedure, using NH_4OH as catalyst

Name	Composition (%mol)	Reagents (g)		
		TEOS	$Ca(NO_3)_2 \cdot 4H_2O$	Therapeutic ion precursor
MBG_SG_Cu0.5%	85 SiO ₂ /14.5 CaO/0.5 CuO	28.200	5.430	<u>CuCl₂</u> : 0.106
MBG_SG_Cu2%	85 SiO ₂ /13 CaO/2 CuO	28.200	4.880	<u>CuCl₂</u> : 0.428
MBG_SG_Ce1%	85 SiO ₂ /14 CaO/1 CeO	28.200	5.260	<u>Ce(NO₃)₃·6H₂O</u> : 0.691
MBG_SG_Ce2%	85 SiO ₂ /13 CaO/2 CeO	28.200	4.880	<u>Ce(NO₃)₃·6H₂O</u> : 1.383
MBG_SG_Ag0.1%	85 SiO ₂ /14.9 CaO/0.1 AgO	28.200	5.600	<u>AgNO₃</u> : 0.027
MBG_SG_Ag2%	85 SiO ₂ /13 CaO/2 AgO	28.200	4.880	<u>AgNO₃</u> : 0.541

2.4 Synthesis of micro-sized MBG particles assisted by spray-dryer

Among the explored routes, a procedure based on the aerosol assisted spray-drying approach was adopted with the final aim to obtain a water-based process under mild acidic conditions. By modifying a spray-drying method reported by Pontiroli et al. [6], MBG microspheres and ion-containing mesoporous silica microspheres (MSm) were synthesized. The aforementioned technique is very appealing for its scalability to an industrial environment and for its good repeatability.

Part of the work described in this chapter has been already published during the PhD period [5].

Briefly, 2.030 g of the non-ionic block copolymer Pluronic P123 (EO₂₀PO₇₀EO₂₀, average Mn ~5800 Da, Sigma-Aldrich) were dissolved in 85 g of double distilled water. In a separate batch, a solution of 10.73 g of TEOS was pre-

hydrolysed under acidic conditions using 5 g of an aqueous HCl solution at pH 2 until a transparent solution was obtained. The solution with TEOS was then poured drop by drop into the template solution and kept stirring for 1 h. Then, the amount of ion precursor and of $\text{Ca}(\text{NO}_3)_2 \cdot 4\text{H}_2\text{O}$, as reported in Table 2.5, were added.

The final solution was stirred for 15 min and then sprayed (Büchi, Mini Spray-Dryer B-290) using nitrogen as the atomizing gas with the following parameters: inlet temperature 220 °C, N_2 pressure 60 mmHg and feed rate 5 mL/min. The obtained powder was finally calcined at 600 °C in air for 5 h at a heating rate of 1 °C/min using a Carbolite 1300 CWF 15/5.

Table 2.5: Sample composition and reagent amount used in the spray-drying synthesis

Name	Composition (%mol)	Reagents (g)		
		TEOS	$\text{Ca}(\text{NO}_3)_2 \cdot 4\text{H}_2\text{O}$	Therapeutic ion precursor
MBG_SD_SiO ₂ /CaO	85 SiO ₂ /15 CaO	10.730	2.150	/
MBG_SD_Cu0.5%	85 SiO ₂ /14.5 CaO/0.5 CuO	10.730	2.070	<u>CuCl₂</u> :0.041
MBG_SD_Cu2%	85 SiO ₂ /13 CaO/2 CuO	10.730	1.860	<u>CuCl₂</u> : 0.163
MBG_SD_Sr1%	85 SiO ₂ /14 CaO/1 SrO	10.730	2.000	<u>SrCl₂ · 6H₂O</u> : 0.162
MBG_SD_CuSr2%	85 SiO ₂ /13 CaO/1 CuO/1 SrO	10.730	1.860	<u>CuCl₂</u> : 0.081 <u>SrCl₂ · 6H₂O</u> : 0.162
MBG_SD_Ce1%	85 SiO ₂ /14 CaO/1 CeO	10.730	2.000	<u>Ce(NO₃)₃ · 6H₂O</u> : 0.263
MBG_SD_Ce2%	85 SiO ₂ /13 CaO/2 CeO	10.730	1.860	<u>Ce(NO₃)₃ · 6H₂O</u> : 0.527
MBG_SD_Ag0.1%	85 SiO ₂ /14.9 CaO/0.1 AgO	10.730	2.130	<u>AgNO₃</u> : 0.010
MBG_SD_Ag2%	85 SiO ₂ /13 CaO/2 AgO	10.730	1.860	<u>AgNO₃</u> : 0.206
M _{Sm} _SD_Ce2%*	98 SiO ₂ /2 CeO	10.730	/	<u>Ce(NO₃)₃ · 6H₂O</u> : 0.456
M _{Sm} _SD_Ag2%*	98 SiO ₂ /2 AgO	10.730	/	<u>AgNO₃</u> : 0.178

2.5 Morphological, structural and compositional characterization

The analysis of the mesoporous nanomatrices developed through the different synthesis routes was performed in order to study the morphology, the particle size, the structural features and the composition of the as-synthesized samples. The data obtained through the characterization techniques, described in the following sections, allowed to verify the sample features and to select the best performing procedures.

These characterizations were used throughout the present research activity to investigate the properties of the prepared nanomatrices or to monitor their evolution during specific experiments (e.g. bioactivity test, ion release test...).

2.5.1 Morphological analysis: Field Emission Scanning Electron Microscopy (FE-SEM) and High-Resolution Transmission Electron Microscopy (HRTEM)

FE-SEM. The FE-SEM technique is a non-destructive characterization analysis adopted to investigate the morphological features, size and shape of the particles. The FE-SEM working principle consists in a high energy electron beam generated by an electron gun and focused at specimen surface, after being processed by magnetic lenses (Figure 2.2A). The interaction between the electron beam and the sample surface leads to the generation of a variety of signals.

In order to reduce the surface charging which can hinder the electron path, non-conductive specimens are generally coated with a very thin (~5-10 nm) layer of conductive heavy metal (such as gold, chromium or platinum).

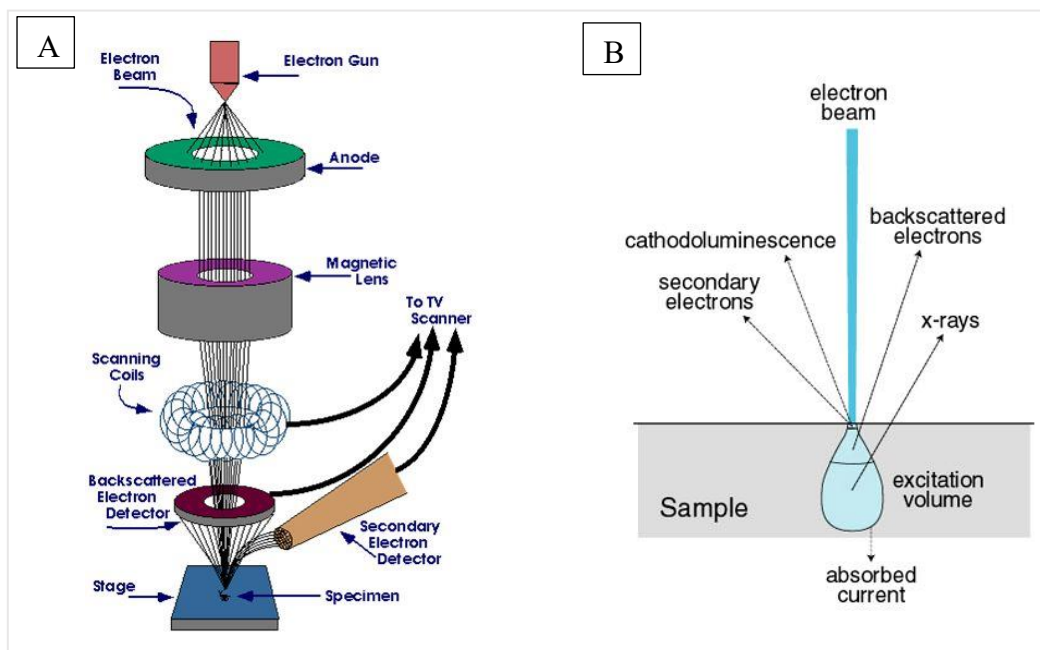


Figure 2.2: FE-SEM functioning (A) and interaction between the electron beam and the sample (B) [7]

In Figure 2.2A the FE-SEM functioning is displayed. In details, the electrons, generated by the electron gun and accelerated through a potential difference, pass through a system of lenses which deflects and focuses the beam on the specimen surface. The interaction between the beam and the sample gives rise to a generation of different signals (Figure 2.2B), which include secondary electrons (SE), backscattered electrons (BSE), photons (characteristic X-rays), visible light (cathodoluminescence-CL), diffracted backscattered electrons (EBSD), and heat. Among these signals, the SE and the BSE are exploited to obtain morphological and topographical information. In particular, SE are low energy electrons generated by inelastic scattering, with energy <math><50\text{ eV}</math>. Considering that only the SE produced by the surface are able to be collected by the detector, it follows that the SE signal provides a superficial topographical image. Differently, the BSE signal comes from deeper region of the sample due to the greater energy of BSE (>50 eV). The information obtained through this signal is closely linked to the chemical

composition of the specimen, since more primary electrons are scattered from higher average atomic number of the element in the sample, resulting in a brighter image [8,9].

Samples. The FE-SEM analysis was performed on all the nano- and micro-sized particles produced by all the synthesis routes. Moreover, the FE-SEM characterization was carried out on the samples after soaking in SBF to investigate the formation of HA layer (see section 2.7 for more details).

Pre-analysis preparation methods. Micro-sized samples produced by spray-drying technique were placed on sample holders using conductive carbon tape and coated with 10 nm of Cr layer.

At variance, in order to obtain a better dispersion of the nano-sized particles, the latter (~10 mg) were dispersed in 10 mL of isopropanol (Sigma-Aldrich) using an ultrasonic bath (Digitec DT 103H, Bandelin) for 5 min to create a stable suspension. Subsequently, 5 μ L of the as-obtained suspension were dropped on a carbon-coated copper grid and coated with Cr layer (10 nm).

The samples were analysed by a *ZEISS MERLIN* instrument.

HRTEM. The transmission electron microscope (TEM) represents a very powerful tool for analysing material. This technique uses the interaction between the source, represented by energetic electrons, with the sample to provide different types of information (*i.e.* morphological, compositional and crystallographic information). The functioning principle consists in an electron beam emitted from a filament which passes through a condenser lens system and an objective lens system and reaches the sample. In the HRTEM, both the transmitted and the scattered beams from the sample are used to create an interference image. The HRTEM provides data of crystal and internal structures.

Samples. MBG_US_m_Cu2% and MBG_US_m_Cu5% samples produced by methanol-based ultrasonicator-assisted sol-gel procedure were analysed by HRTEM technique in order to investigate the inner structure of the samples. Moreover, the EDS (Energy Dispersive Spectroscopy) mapping coupled to TEM allowed to explore the distribution of Cu ions and of the other elements within the particles.

Pre-analysis preparation methods. MBG_US_m_Cu2% and MBG_US_m_Cu5% nanomatrices were ultrasonically dispersed in n-butanol and placed on carbon-coated nickel grids.

HRTEM imaging and related local EDS were performed at the *Departamento de Química Inorgánica y Bioinorgánica, Universidad Complutense de Madrid, CIBER de Bioingeniería, Biomateriales y Nanomedicina (CIBER-BBN)* by the *Prof. Maria Vallet-Regí*'s research group. The instrument used to perform the analysis was the *JEOL JEM300FEG* electron microscope equipped with an *ISIS 300* X-ray microanalysis system (Oxford Instruments).

2.5.2 Compositional analysis: Energy Dispersive Spectroscopy (EDS), X-ray fluorescence spectroscopy (XRF), X-ray Photoelectron Spectroscopy (XPS) and Inductively Coupled Plasma Atomic Emission Spectrometry (ICP)

EDS. The Energy Dispersive Spectroscopy (EDS) allows to explore the elemental composition of the samples through the detection of the characteristic X-rays coming from the sample after the exposure to a high-energy electron beam. The energy of the generated X-rays depends on the atomic number of the element; thus, it can be used to obtain information about chemical composition. These X-rays, reaching the detector, cause the ionization in the detector and the production of an electrical charge which, after the analysis, allows the obtainment of a spectrum reporting the number of counts per channel as a function of the energy of the detected X-rays (keV). The detector and the related preamplifier are cooled with N₂ liquid at -192 °C to reduce the electronic noise [10].

Samples. The EDS investigation was carried out on all the nano- and micro-sized particles with the aim to study the chemical composition and the incorporation of the therapeutic ion.

Pre-analysis preparation methods. A small amount of powders was dispersed on the conductive carbon tape placed on the sample holders and the *Aztec EDS* equipment was used for the analysis.

XRF. The Energy dispersive X-ray fluorescence spectroscopy (XRF) is performed on the samples for qualitative and quantitative study of the elemental composition. During the process, the excitation of the specimen with a high energy primary X-rays causes the electrons of the inner orbital to be knocked. As a result, the electrons from the outer shells fill the resultant vacant spaces, by emitting X-rays fluorescence radiation characteristic of a specific material, which reaches the detector. The as-obtained spectrum shows the intensity of X-rays as a function of energy (keV) [11].

Samples. The XRF was adopted, as a non-routine technique, in order to analyse the elemental composition of MBG_US_m_Sr1% and MBG_SD_Sr1%. As described in detail in the following chapter, the overlapping of strontium and silicon peaks in the EDS spectrum and the low amount of the incorporated strontium led to the need of the XRF characterization technique.

Pre-analysis preparation methods. About 10 mg of the powders were pressed into pellets by using a die and applying a pressure of 2 t. The *Rigaku ZSX100E* instrument was used to perform the analysis.

XPS. Is one of the most widely used characterization technique for chemical surface analysis providing quantitative and chemical state information. In a typical spectrometer, the excitation of the sample surface with mono-energetic Al K α X-rays causes the emission of photoelectrons by the sample surface. The electron energy analyser measures the energy of the emitted photoelectrons. The elemental

identity, the amount and the chemical state of the specific detected element can be identified by the binding energy and the intensity of the resulting photoelectron peak. A typical analysis depth of an XPS instrument is less than 5 nm [12].

Samples. In order to investigate the nature of the copper species incorporated inside the MBG_US_m_Cu2% and MBG_US_m_Cu5% glass framework, XPS analyses were performed on these samples.

Methods. A *PHI 5000 Versaprobe II Scanning X-ray Photoelectron Spectrometer* (XPS), equipped with a monochromatic Al K-alpha X-ray source (1486.6 eV energy, 15 kV voltage and 1 mA anode current), was adopted to analyse sample surface chemical composition. The photoelectron signal for both the high resolution (HR) and the survey spectra were collected by using a spot size of 100 mm. Different pass energy values were exploited: 187.85 eV for survey spectra and 23.5 eV for HR peaks. The core level spectra were deconvoluted with a nonlinear iterative least squares Gaussian fitting procedure.

ICP. This analysis allows to determine the concentration (in ppb) of a specific chemical element in a water-dissolved sample. The functioning principle exploits the presence of argon plasma (which is a neutral conducting gas which contains the same amount of cations and electrons) generated in a stream of Ar. This Ar plasma, at high temperature (6000-10000 K), acts as excitation source for the sample electrons which emit energy at a specific wavelength, peculiar to its atomic environment, when they return to ground state. A peristaltic pump introduces the solution to the nebulizer chamber which produces a fine mist of liquid particles. Then, they pass through a torch which creates the plasma; in the torch, different processes occur, such as the evaporation of the solvent, the atomization and the excitation or ionization of the atoms. The plasma is continuously supplied by a radio-frequency generator which produces an oscillating magnetic field around the torch, causing the heating of the charged gas. Finally, the atoms leave the high temperature zone and relax by emitting specific photon which reaches the detector after the crossing of the monochromator that allows the separation of the wavelength.

Sample. With the aim to assess the released ion concentration from the nanomatrices, the ion released test were performed by following the procedures reported in section 2.6 and the as-obtained supernatant solution was analysed by ICP.

In addition, the ICP analysis was carried out on MBG_SD_CuSr2% and on MBG_US_m_CuSr2% with the purpose of investigating the capability of the nanomatrices to simultaneously incorporate two therapeutic ions.

Pre-analysis preparation methods. The supernatant solutions resulted from the ion release test were first diluted in order to reach a suitable concentration detectable by the ICP instrument and then analysed through this technique. The results, expressed as ppb and multiplied for the specific dilution factor, represent the concentration of the ion released by the sample.

The co-substituted Sr-Cu-containing samples were analysed by ICP after the dissolution of the powder by strongly acid medium (0.5 mL of HNO₃ and 2 mL of HF for 10 mg of powder).

The ICP-MS, Thermoscientific, ICAP Q was exploited to perform the analysis during this PhD work.

2.5.3 Textural properties: N₂ adsorption-desorption measurements

Textural features such as the pore size, pore shape, pore distribution, together with the specific surface area and pore volume were explored through N₂ adsorption-desorption measurements. This non-destructive technique is based on the physisorption phenomenon which occurs between an *adsorptive*, an adsorbable gas, and an *adsorbent*, the surface of a solid. The forces which are involved in this phenomenon are the intermolecular forces. The desorption, at variance, is the counterpart of the physisorption, where the amount of the adsorbed gas decreases. The not-perfect coincidence between the adsorption and desorption process gives rise to the hysteresis loop.

The isotherm obtained through this technique depicts the amount of gas adsorbed as a function of relative pressure (p/p_0). According to IUPAC classification [13,14], six types of isotherm are recognised, as visible in Figure 2.3:

- Type I isotherms: typical of microporous (pores <2 nm) solids. Two different types of isotherms belong to this category: Type I(a) and Type I(b). Type I(a) isotherms correspond to material with narrow micropores with < 1 nm; Type I(b) isotherms are obtained for materials with broader pore size distribution, ranging from micropores to narrow mesopores;
- Type II isotherms: characteristic of nonporous or macroporous (pores >50 nm) adsorbents; point B represents the completion of monolayer coverage;
- Type III isotherms: related to nonporous and macroporous materials where the interactions between the adsorbent-adsorbate are weak;
- Type IV isotherms: representative of mesoporous solids, where the adsorption phenomenon depends on the interaction between adsorbent-adsorptive, as well as between the molecules in the condensed state. The adsorption at very low p/p_0 corresponds to the monolayer-multilayer adsorption of N₂ on the walls of the mesopores, as already observed in Type II isotherm, but, in the mesoporous material, it is followed by the capillary condensation, indicating the condensation of a gas in the pore at a pressure < p_0 . Typically, the Type IV isotherms end with a plateau. As visible in Figure 2.3, two different isotherms belong to this category. Type IV(a) isotherms with its characteristic hysteresis loop in the capillary condensation region, represent materials with pores larger than a critical width (using nitrogen as adsorptive at 77K, it corresponds to 4 nm); the Type IV(b) isotherms, with the completely reversible process, are typical of adsorbents with smaller pore width;

- Type V isotherms: as Type III, they correspond to weak adsorbent–adsorbate interaction, with the addition of the hysteresis loop;
- Type VI isotherms: typical of highly uniform nonporous solids where a layer-by-layer adsorption is observed.

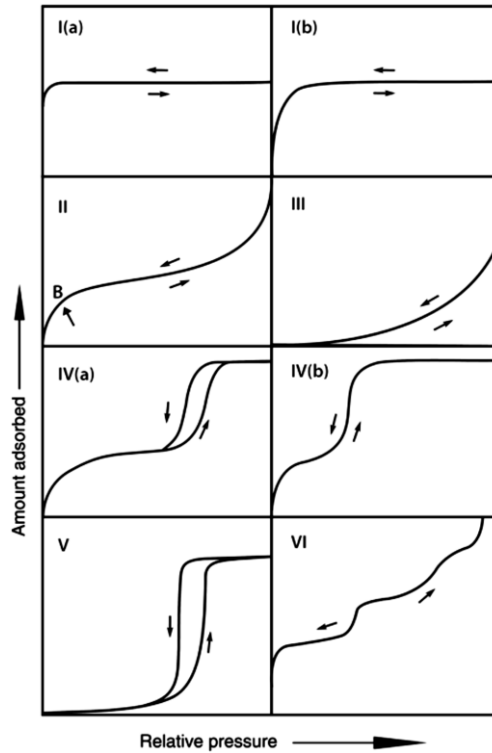


Figure 2.3: Physisorption isotherm classification [14]

Five types of hysteresis loops (from H1 to H5) are reported, depending on the pore structure and the specific adsorption mechanism (Figure 2.4). The Type H1 loop is typical in mesoporous material with narrow range of uniform mesopores; the Type H2 is usually associated to more complex pore features. Type H2(a), for example, could be ascribed to interconnected pores, where the evaporation occurs only from the pores directly connected to the surface; Type H2(b) loop is linked to the presence of pores with larger neck widths.

Type H3 occurs in presence of aggregates of plate-like particles; the H4 hysteresis loop is often associated to the elongated and narrow pore size. Finally, the Type H5 hysteresis loop is ascribed to solids containing both open and partially blocked pores [14].

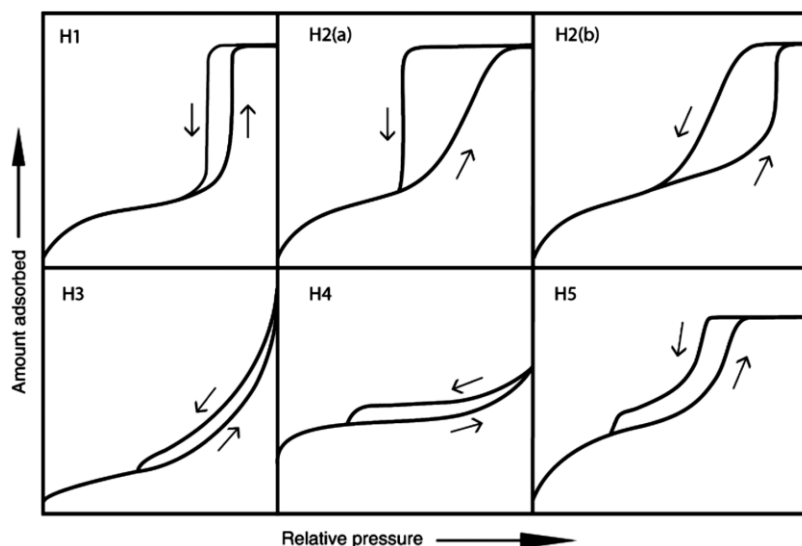


Figure 2.4: Hysteresis loop classification [14]

Among the data obtained through the N₂ adsorption-desorption measurements, the specific surface area (SSA) value represents the effective accessible area of the sample. One of the most widely adopted methods to calculate the SSA is the Brunauer–Emmett–Teller (BET) method [14]. This method is based on the theory that the adsorption enthalpy is constant during the multilayer formation.

The BET equation can be written as follows:

$$\frac{p}{V(p_0 - p)} = \frac{1}{V_m C} + \frac{C - 1}{V_m C} \frac{p}{p_0}$$

Where: p = equilibrium pressure (torr)

p₀ = saturation pressure at 77 K (torr)

V = adsorbed volume/g of solid

V_m = monolayer volume of N₂ (mL)

C = parameter associated to the energy of monolayer adsorption

By plotting $p/(V(p_0 - p))$ as a function of p/p_0 , a linear correlation in a limited range of p/p_0 (0.05 and 0.3) is obtained and the values of V_m and C can be calculated. Finally, the SSA value is determined by the following equation [14]:

$$SSA = \frac{\sigma V_m N_a}{v}$$

Where: SSA = specific surface area (m²/g)

σ = molecular cross-sectional area occupied by the adsorbate molecule in the monolayer, which corresponds to 13,5 Å for N₂

N_a = Avogadro number (6.02 · 10²³)

v = molar volume of the adsorbed gas (22414 mL/mol for N₂)

In addition to the SSA, the pore size distribution and the pore volume can be obtained through this characterization technique by means of different methods. Among them, one of the most exploited is the Non-Local-Density Functional

Theory (NLDFT) based methods. These methods, based on statistical mechanics, allow to calculate a series of theoretical isotherms (kernel), for a particular adsorptive/adsorbent system and for a given pore shape. The calculation of the pore size distribution function is obtained by solving an equation which correlates the isotherm kernel with the experimental isotherm [14].

Samples. After each synthesis, the as-produced samples were analysed through the N₂ adsorption/desorption measurements in order to investigate the mesoporous structure and the textural features.

Pre-analysis preparation methods. The samples were analysed through the ASAP2020 (Micromeritics) instrument, using nitrogen as adsorptive at -196 °C. The nanomatrices were outgassed at 150 °C for 5 h before analysis in order to remove gas adsorbed on the sample surface. After an overpressure of He, the samples were analysed through the administration of increasing amount of pressure.

2.5.4 Structural analyses: X-Ray Diffraction (XRD) and UV-visible Spectroscopy (UV-vis)

XRD. The X-ray diffraction (XRD) provides qualitative and quantitative information about the structure of the sample, with focus on the crystalline phases present. The analysis is based on the diffraction phenomenon of X-rays, peculiar to crystalline materials, by the crystal lattice of the analysed solid. The X-rays are high energy radiation with wavelength ranging between 0.01 and 10 nm and frequency in the range of $3 \cdot 10^{16}$ and $3 \cdot 10^{19}$ Hz. The wavelength of the X-rays is of the same order of d (Figure 2.5) that represents the distance between the parallel planes in which the atoms of a crystalline material are arranged.

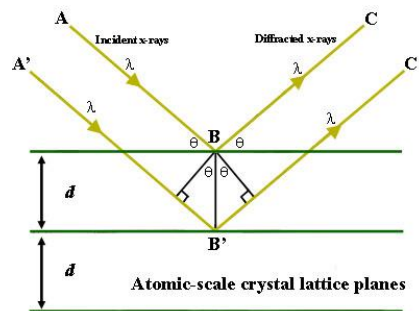


Figure 2.5: Diffraction phenomenon

Considering a monochromatic X-ray beam which reaches the crystalline material with λ as wavelength and an angle θ , the diffraction phenomenon occurs only when the distance travelled by the incident X-ray reflected from successive beam differs by a complete number n of wavelengths (Bragg's law, $n\lambda = 2d \sin\theta$). As visible in Figure 2.5, by varying the angle θ , different d -spacings satisfy the Bragg's law condition in polycrystalline solids. The resulting diffractogram, obtained by plotting the intensities of the diffracted X-rays as a function of the angular positions, is characteristic of the material.

A typical diffractometer is composed by a source of radiation, a monochromator to select the wavelength, some slits to tailor the shape of the beam and a detector.

The characteristic diffractogram of a crystalline material consists of sharp peaks, resulting from the diffracted beams arising from the different planes. Several data can be obtained from the diffractogram analysis such as the crystal cell symmetry and the type of phases. In particular, the quantitative composition can be derived from the intensity of the peak; whilst the peak shape gives information about the crystal dimension.

In the amorphous material, the diffractogram consists on a broad peak centred around the θ which shows a sharp peak in the diffractogram of the crystalline material with the same composition.

Samples. The micro- and nano-sized particles were analysed through XRD in order to investigate the structure of the sample and the presence of any segregated oxidic phases due to the incorporation of therapeutic metallic ions. Moreover, the powders after soaking in SBF (see section 2.7) were explored to confirm the bioactivity of the sample by searching the hydroxyapatite peaks.

Methods. The powders, prepared as plane surface, were placed on the sample holders and analysed through a wide-angle (2θ within 10° - 80°) X-ray diffraction (XRD, X'Pert PRO, PANalytical) diffractometer.

UV-vis. The UV-Visible Spectroscopy (UV-vis) can be employed to identify the metal ion coordination and the oxidation number of the species hosted in the mesoporous systems.

The basis of this spectroscopy technique is the absorption of monochromatic electromagnetic radiations in the ultraviolet (200-350 nm) and visible (350-700 nm) spectral region by species composed by specific functional groups, called chromophores. In detail, a chromophore is an atom or a group of atoms responsible for ultraviolet and/or visible radiation adsorption.

The absorption in the UV-visible region is associated with excitation of electrons from lower to higher energy levels by using excitation with precise amount of energy. Most of the molecules require very high energy radiation to be excited, thus the absorption of UV-visible light results only in the presence of atoms with non-bonding orbitals.

A typical UV-visible spectrometer is composed by a light source (which is a combination of tungsten/halogen and deuterium lamps), a monochromator and the detector. In brief, the light from the source reaches the monochromator which splits the light into its component colours of different wavelengths. After passing through the sample, the light reaches the detector which converts the intensity of the light in electric signal which undergoes to amplification and returns a diagram reporting the absorbance as a function of the wavelength.

Considering I the intensity of the incoming light in the sample and I_0 the resulting light after the absorption by the sample, the main considered phenomena are:

- Absorbance ($A = -\log(I/I_0)$)

- Reflectance

Through the application of the Lambert-Beer law, by knowing the absorbance, it is possible to obtain the concentration of a substance:

$$A = \varepsilon c d$$

Where: ε = molar extinction, which is peculiar for a substance ($\text{mol}^{-1} \text{L cm}^{-1}$)

d = optical path length

c = concentration of the solution (mol/L)

In some cases (*e.g.* powder sample), the scattering light phenomenon resulting from the shape of the analysed sample makes difficult to acquire directly the absorbance spectrum. By equipping the spectrometer with an integrating sphere covered by a highly reflecting material (usually MgO or BaSO₄), the diffuse reflectance light can be collected. Considering that absorbance and diffuse reflectance are strictly connected, through the diffuse reflectance phenomenon, information about the absorption phenomenon can be obtained.

Sample. Cerium- and silver-containing samples were analysed through diffuse reflectance UV-visible spectroscopy in order to investigate the oxidation state of the incorporated ion, since the ion clusters result in peaks in the visible region due to the plasmonic resonance.

Pre-analysis preparation methods. First, a baseline is recorded with reference disk covering the reflectance port, then, about 10 mg of powders were mounted over the port and the instrument *VARIAN CARY 5, Agilent* was used to obtain the diffuse reflectance UV-visible spectra of the samples.

2.6 Ion release tests

The capability of the ion-containing nanomatrices to release the incorporated therapeutic ion was explored by adopting different procedure and media, in order to study the influence of the experimental setups on the ion release kinetics. In this section, the detailed description of the followed procedures is reported.

Part of the work described in this chapter has been already published during the PhD period [2,5].

2.6.1 Ion release test performed in SBF

The first medium used to investigate the ion release from the nano- and micro-sized particles was SBF, prepared according to Kokubo recipe [15] in order to correlate the ion release property with the bioactive behaviour (see section 2.7) of the samples. In details, 30 mg of ion-substituted nanomatrices were placed in a plastic container with 30 mL of SBF (final concentration of 1 mg/mL of SBF). The samples were kept immersed for different times up to 14 days at 37 °C in an orbital shaker Excella E24 with an agitation rate of 150 rpm. At each time point (3 h, 24 h, 3 d, 7 d and 14 d), the suspension was centrifuged (Hermle Labortechnik Z326), and 1 mL of the supernatant solution was collected and analysed by ICP through

the ICP-MS, ThermoScientific, ICAP Q spectrometer. The experiment was carried out in triplicate. Table 2.6 listed a summary of the experimental setup.

Table 2.6: Experimental setup of ion release test in SBF

Medium	Concentration	Time point	Refill
SBF	1 mg/mL	3 h, 24 h, 3 d, 7 d, 14 d	No

2.6.2 Ion release test performed in DMEM

Dulbecco's modified eagle medium (DMEM) (Sigma-Aldrich), as a mimetic cell culture environment, was used in order to perform some experiments and to analyse the ion release kinetics in a more complex environment.

As in SBF medium, 30 mg of ion-containing powders were soaked in 30 mL of DMEM (final concentration of 1mg/mL) and placed in the orbital shaker (Excella E24) by setting 37 °C and 150 rpm as temperature and agitation rate, respectively. At each time point (3 h, 24 h, 3 d, 7 d and 14 d), the suspensions were centrifuged (Hermle Labortechnik Z326), and 1 mL of the DMEM solution was collected. The experiment was carried out in triplicate. The supernatant was analysed by ICP (ICP-MS, ThermoScientific, ICAP Q) in order to investigate the therapeutic ion concentration released in DMEM.

Compared to SBF medium, the DMEM required to be used in aseptic conditions under biological hood in order to avoid any contamination.

Table 2.7 listed a summary of the experimental setup.

Table 2.7: Experimental setup of ion release test in DMEM

Medium	Concentration	Time point	Refill
DMEM	1 mg/mL	3 h, 24 h, 3 d, 7 d, 14 d	No

2.6.3 Ion release test performed in Tris HCl

The samples were suspended in Tris HCl buffer (Tris(hydroxymethyl) aminomethane (Trizma) (Sigma-Aldrich) 0.1 M, pH 7.4) at a final concentration of 250 µg/mL, according to the protocol described by Shi et al. [3]. Specifically, 5 mg of the samples were kept immersed in 20 mL of buffer up to 14 days at 37 °C in an orbital shaker Excella E24 with an agitation rate of 150 rpm. At each predefined time point (3 h, 24 h, 3 d, 7 d and 14 d) the suspensions were centrifuged for 5 min at 10000 rpm (Hermle Labortechnik Z326), half of the supernatant was collected and replaced by the same amount of fresh buffer. Each experiment was carried out in triplicate. The concentration of ions was measured by ICP (ICP-MS, ThermoScientific, ICAPQ), after appropriate dilutions.

In Table 2.8 the followed experimental setup is summarized.

Table 2.8: Experimental setup of ion release test in Tris HCl

Medium	Concentration	Time point	Refill
Tris HCl	250 µg/mL	3 h, 24 h, 3 d, 7 d, 14 d	Half of medium replaced by fresh medium

By comparing this ion release procedure with the previous ones, the refill of the medium was introduced in order to better mimic the physiological conditions characterized by a continue liquid exchange. The refill of the medium, together with the lower concentration, allowed to avoid the saturation of the solution and hinder the ion release.

2.7 Bioactivity test

Part of the work described in this chapter has been already published during the PhD period [5].

Since the bioactivity of the MBGs is considered one of the main aspect of these materials, as largely reported in chapter 1, bioactivity test was performed on the MBG samples by following a methodology reported in ref [16], where a unified method for the evaluation of HA-forming ability of bioactive glasses in powder form is proposed. In particular, 30 mg of powders were soaked in 30 mL of SBF for 3 h, 24 h, 3, 7 and 14 days. The bottles were placed inside an orbital shaker (Excella E24) at a fixed temperature of 37 °C. At each selected time point, the powders were removed by centrifugation at 5000 rpm for 5 min, rinsed with double distilled water and dried in oven at 70 °C for 12 h. The pH of SBF was measured at each time point. The powders were analysed by FE-SEM, EDS and XRD to detect the HA phase formation.

2.8 Biological assessment

2.8.1 Biocompatibility test of ion-containing nanomatrices

The cytocompatibility test was performed on ion-containing nanomatrices with the aim to explore their effect on fibroblast L929 in view of the potential clinical applications. The biocompatibility test was performed by the group of *Dr. Marco Morra* at *Nobil Bio Ricerche Srl*, one of the industrial partners of the MOZART project involved in the biological assessment of the nanomatrices.

Sample. The optimized micro- and nano-sized samples were considered for the biocompatibility test. In details, the Cu- containing samples (both 0.5%mol and 2%mol concentrations) the Ce-containing samples (both 1%mol and 2%mol concentrations) and the Ag-substituted samples (0.1%mol and 2%mol concentrations) were analysed in order to investigate whether the incorporated metallic ions exert toxic effects on the cells.

Pre-analysis preparation methods. Fibroblasts L929 were used in the cell adhesion experiments. Experimental cell culture medium (Biochrom KG)

(Minimum Eagle's Medium without L-glutamine, 10 % fetal bovine serum, streptomycin (100 g/L), penicillin (100 U/mL), and 2 mmol/L of L-glutamine) was introduced in 250 mL plastic culture flask (Corning TM). The fibroblasts were cultured at 37 °C in a humidified incubator equilibrated with 5 % CO₂; subsequently, the fibroblasts L929 were harvested prior to confluence by means of a trypsin-EDTA solution (0.5 g/L trypsin, 0.2 g/L EDTA in normal phosphate buffered saline (PBS), pH 7.4), re-suspended in the experimental cell culture medium, and diluted in order to obtain 1 x 10⁵ cells/mL.

The biocompatibility was evaluated by means of two different assessments: a qualitative evaluation through direct observation using an inverted microscope, and the cell viability investigation through MTT assay in Transwell[®] membrane insert. The latter allows to take into account the role of the ion released by the nanomatrices, avoiding the direct contact of the particles with the cells. In order to perform the MTT assay, 1 mg/mL of ion-containing particles was placed into the Transwell[®], whilst the cells were seeded on polystyrene plate, under the insert. In addition, the effect of nanomatrices containing the highest amount of copper (2%mol) were also investigated using a lower concentration of particles (100 µg/mL). The cell viability was assessed after 72h of incubation. By evaluating the efficiency of the mitochondrial succinate dehydrogenase (SDH) enzyme, which is normally involved in the citric acid cycle, the MTT assay identifies any toxic effects of the tested material by analysing the decrease in the enzyme activity. The MTT test requires to incubate the cells with 1 mg/mL solution of soluble tetrazolium salt (specifically, 3-(4,5-dimethylthiazol – 2yl)-2,5 diphenyl tetrazolium bromide) at 37 °C for two hours, during which the succinate dehydrogenase enzyme causes the tetrazolium salts to be transformed into the formazan precipitate, a blue water-insoluble product. By quantifying the amount of precipitate, the degree of the enzyme activity and, consequently, the number of metabolically active cells can be deducted [17].

Finally, the formazan precipitate was dissolved in dimethylsulphoxide and measured spectrophotometrically at 570 nm, providing the optical density (OD) measurement. Cell growth on the polystyrene plate without any stimulus was used as a negative control.

2.8.2 Antibacterial tests

Ion-containing MBG nanomatrices underwent antibacterial *in vitro* tests in order to assess the effective antibacterial potential of the incorporated copper, cerium and silver ions. The tests described in sections 2.8.2.1 and 2.8.2.2 were performed in collaboration with the group of *Prof. Livia Visai (Molecular Medicine Department, Center for Health Technologies, UdR INSTM, University of Pavia)*; whereas, the *in vitro* antibacterial tests explained in sub-paragraphs 2.8.2.3 and 2.8.2.4 were carried out in collaboration with *Prof. Sheila MacNeil's* research group (*Department of Materials Science and Engineering, Kroto Research Institute, University of Sheffield*), one of the MOZART partners involved in the biological assessment of wound healing nanomatrices.

Part of the work described in this chapter has been already published during the PhD period [2].

2.8.2.1 Investigation of antibacterial effect of ion-containing sample on *E. Coli*, *S. epidermidis* and *S. Aureus* bacterial planktonic growth using MTT assay

The antibacterial properties of the copper-containing MBG synthesized by methanol-based ultrasonicator-assisted sol-gel method (MBG_US_m_Cu2%) and their ionic extracts were tested using *E. coli*, *S. epidermidis* and *S. aureus* bacterial strains.

The present antibacterial test was performed in collaboration with Prof. Livia Visai's research group (*Molecular Medicine Department, Center for Health Technologies, UdR INSTM, University of Pavia*).

Samples. Copper-containing sample produced by ultrasonicator-assisted sol-gel method (MBG_US_m_Cu2%) was used in order to confirm the antibacterial potential of copper [18]. The SiO₂/CaO sample synthesized through the same procedure (MBG_US_m_SiO₂/CaO) was investigated using the same antibacterial tests in order to ascribe the results to the presence of that specific therapeutic ion.

Methods. The microorganisms used in this study were *Escherichia coli* RB (*E. coli* RB), *Staphylococcus aureus* 8325-4 (*S. aureus* 8325-4) and *Staphylococcus epidermidis* (*S. epidermis* RP62A). *E. coli* RB was provided by the "Zooprofilattico Institute of Pavia" (Italy) whereas *S. aureus* 8325-4 and *S. epidermidis* RP62A were kindly supplied by Timothy J. Foster (*Department of Microbiology, Dublin, Ireland*). All bacteria strains were routinely grown in their culture medium overnight under aerobic conditions at 37 °C using a shaker incubator (New Brunswick Scientific Co., Edison): *E. coli* RB in Luria Bertani Broth (LB) (Difco), *S. aureus* 8325-4 in Brian Heart Infusion (BHI) (Difco) and *S. epidermidis* RP62A in tryptic soy broth (TSB, Difco). These cultures were statically incubated at 37 °C under aerobic conditions and reduced to a final density of 1x10¹⁰ cells/mL as determined by comparing the optical density (OD₆₀₀) of the sample with the standard curve relating OD₆₀₀ to cell number.

Two different experimental conditions were used to evaluate the antibacterial activity of un-doped (MBG_US_m_SiO₂/CaO) and copper-containing nanoparticles (MBG_US_m_Cu2%). For the first experimental condition, MBG_US_m_SiO₂/CaO or MBG_US_m_Cu2% suspensions in sterile PBS with a final concentration of 2 mg/mL were prepared, sonicated by using an ultrasonic bath (FALC Instruments) for 5 min at room temperature, and properly diluted to obtain concentrations of 31, 63, 125, 250, 500, 1000 and 2000 mg/mL. The obtained suspensions were further sonicated for 5 min at room temperature prior to the direct incubation with bacterial cells.

The second experimental condition was analogously performed, but in order to evaluate the antibacterial properties ascribable to the released Cu²⁺ ions from MBG_US_m_Cu2%, un-doped and MBG_US_m_Cu2% particles were dispersed in sterile PBS (2 mg/mL) and kept soaked for 3 h and 24 h, then centrifuged and

the supernatants collected for antibacterial activity tests. Bacterial strains were incubated without (control) or with increasing serial dilutions of the extracts collected after 3 h and 24 h from the MBG_US_m_SiO₂/CaO and MBG_US_m_Cu2% suspensions, respectively. The control samples of both the experimental conditions were performed by addition of the same volume of PBS. Each experiment condition was repeated three times.

For both experimental conditions, a predefined number (10^4 /mL) of *Gram negative* (*E. coli* RB) and *Gram positive* (*S. aureus* 8325-4 and *S. epidermidis* RP62A) cells were incubated in their culture broth at 37 °C in 96-well microtiter plates. For the first experimental condition, bacterial cells were untreated (control) or treated with nanoparticle suspensions at increasing concentrations, ranging from 31 up to 2000 mg/mL, for 1 and 3 days, respectively. For the second experimental condition, bacterial cells were untreated (control) or treated with increasing serial dilutions of extracts previously collected at 3 and 24 h from of MBG_US_m_SiO₂/CaO or MBG_US_m_Cu2% suspensions (2 mg/mL) and incubated for 1 day. For both experimental conditions, at fixed incubation times, the quantitative MTT assay was performed to assess the dehydrogenase activity, as an indicator of the metabolic state of cells, as previously described [17]. The bacterial viability was expressed as percentage related to the control set equal to 100%.

2.8.2.2 Investigation of antibacterial effect of ion-containing sample on *S. epidermidis* biofilm by metabolic activity evaluation

In recent years, the number of infections associated with antibiotic-resistant bacteria has greatly increased. Many of these infections are caused by microorganisms growing in biofilms, complex bacterial communities surrounded by a self-producing extracellular polymer matrix, able to resist both to antibiotic action and to human immune system [19]. The formation of biofilm is a peculiar characteristic of *S. aureus* and *S. epidermidis* [20] that quite frequently colonise medical devices, causing persistent body-related infections. Differently from planktonic populations, bacterial cells embedded in biofilms are characterized by intrinsic resistance to antibiotics due to several specific defence mechanisms given by the biofilm environment, including the inactivation of anti-microbial agents by exopolysaccharide (EPS), over expression of stress-responsive genes, oxygen gradients within the biofilm matrix and differentiation of a sub-population of biofilm cells into resistant dormant cells [21]. These aforementioned features of biofilms place them amongst the most serious problems currently faced by medicine and thus considerable efforts are devoted to identifying novel therapies to prevent or treat biofilms. To this purpose, a potentially promising treatment implies metal or metal oxide nanoparticles, showing antibacterial and antibiofilm activity [22].

In this frame, the biofilm antibacterial test was tested in collaboration with *Prof. Livia Visai's* research group (*Molecular Medicine Department, Center for Health Technologies, UdR INSTM, University of Pavia*).

Samples. To evaluate the antibacterial activity against staphylococcal biofilms, *S. epidermidis* cultures were incubated with MBG_US_m_SiO₂/CaO and MBG_US_m_Cu2% suspensions or with related extracts collected after 24 h of incubation, either during the biofilm formation or in the presence of pre-formed biofilm.

Methods. The experimental conditions adopted in the antibacterial effect evaluation against *S. aureus*, *S. epidermidis* and *E. coli* planktonic bacterial strains (see section 2.8.2.1), were also exploited in order to investigate the antibacterial potential of MBG_US_m_SiO₂/CaO and MBG_US_m_Cu2% nanoparticles (first experimental condition) and of MBG_US_m_SiO₂/CaO and MBG_US_m_Cu2% extracts collected after 24h of incubation (second experimental condition) against *S. epidermidis* RP62A biofilm.

For biofilm experiments, overnight culture of *S. epidermidis* RP62A was diluted in its broth culture medium with the addition of 0.25% glucose. Aliquots (100 µL) of the diluted bacterial suspensions were inoculated into 96-well flat-bottom sterile polystyrene microplates (Costar, Corning) as follows: *i.* without (control) or with a suspension of 2 mg/mL of MBG_US_m_SiO₂/CaO or MBG_US_m_Cu2% nanoparticles in PBS; *ii.* without (control) or with extracts collected after 24 h of incubation with MBG_US_m_SiO₂/CaO or MBG_US_m_Cu2% suspension (2 mg/mL) in PBS. In both cases (*i* and *ii*) the experiments were performed in two different types of settings: *a.* nanoparticle suspensions or nanoparticle extracts were contemporarily incubated with biofilm growing cultures in order to evaluate their effects during biofilm formation; *b.* nanoparticle suspensions or nanoparticle extracts were added after the biofilm formation, to assess their effects on the formed biofilms. After fixed incubation times, biofilms were washed twice with PBS to remove planktonic cells and loosely adhering bacteria [23]. Viability quantification of microbial cells inhabiting the biofilms was performed by MTT test, as described above.

In addition, the biofilm antibacterial effect of the samples was studied through morphological evaluation technique. In this frame, the biofilm untreated (control) or treated with nanoparticle suspensions or their extracts for both the experimental settings (as described above) were grown in plastic cell culture coverslip disks (Thermanox Plastic, Nalge Nunc International) seeded on the bottom of a 24-well culture plates and incubated for 24 h at 37 °C. Briefly, the disks were washed several times and then fixed for SEM with 2.5% glutaraldehyde in 0.1 M cacodylate buffer, pH 7.2 for 1 h at 4 °C. After additional washes, they were incubated with increasing concentrations of ethanol (25%, 50%, 75% and 96%) for 10 min each, dried to the critical point using an Emitech K-850 apparatus and placed on a mounting base. Finally, the disks were examined through SEM analysis (Zeiss EVO-MA10 scanning electron microscope), after a gold layer deposition.

2.8.2.3 Investigation of antibacterial effect of ion-containing samples on *S. Aureus* and *P. Aeruginosa* by viable count method

In order to explore the effect of the incorporated ion in presence of bacteria, the antibacterial studies were performed by using *in vitro* tests. Among the countless different types of antibacterial tests, the viable count method was selected with the aim to count the viable bacterial cell number after the treatment with the produced nanomatrices. In microbiology, a “viable” organism is defined as an organism able to multiply via binary fission under controlled conditions. The results are expressed as colony forming unit (CFU), since ascribing a bacterial colony to one cell or to one group of cells is considered almost impossible.

The viable count tests were performed at the *Department of Materials Science and Engineering (University of Sheffield)*, in the group of *Prof. Sheila MacNeil*, during my external research staying.

Samples. The optimized ion-containing micro- and nano-sized particles were tested by viable count method with the aim to explore the antibacterial potential of copper [18], cerium [24] and silver [25]. In details, the following samples were analysed: MBG_SG_Cu2%, MBG_SD_Cu2%, MBG_SG_Ce2%, MBG_SD_Ce2%, MBG_SG_Ag2% and MBG_SD_Ag2%.

Methods. The antibacterial properties of the ion-containing nanomatrices were tested against clinical isolate strains of *S. aureus* (S235) and *P. aeruginosa* (SOM1), representative of *Gram positive* and *Gram negative* bacteria, respectively. Both strains were cultured in BHI broth (Oxoid) at 37 °C overnight and stored at 4 °C on BHI agar (Sigma-Aldrich).

Two experimental conditions (Figure 2.6) were adopted in order to investigate the antibacterial effect exerted by the samples. In the first experimental condition (named “suspension”), the powders were suspended in PBS at a final concentration of 2 mg/mL, sonicated for 5 min and vortexed to obtain a stable suspension. Then, 50 µL of this suspension were incubated with 50 µL of the overnight suspension of bacteria for 24 h. The second experimental condition was carried out with the aim to study the antibacterial potential of the released ion. In this case, the powders were kept immersed in PBS for different time points (1, 3 and 8 days) at 37 °C in a static incubator to allow the particles to settle. At each time point, 50 µL of the supernatant were incubated with 50 µL of the overnight bacterial suspension for a further 24 h.

In both experimental conditions the control samples were obtained by adding 50 µL of PBS to the overnight bacterial suspension.

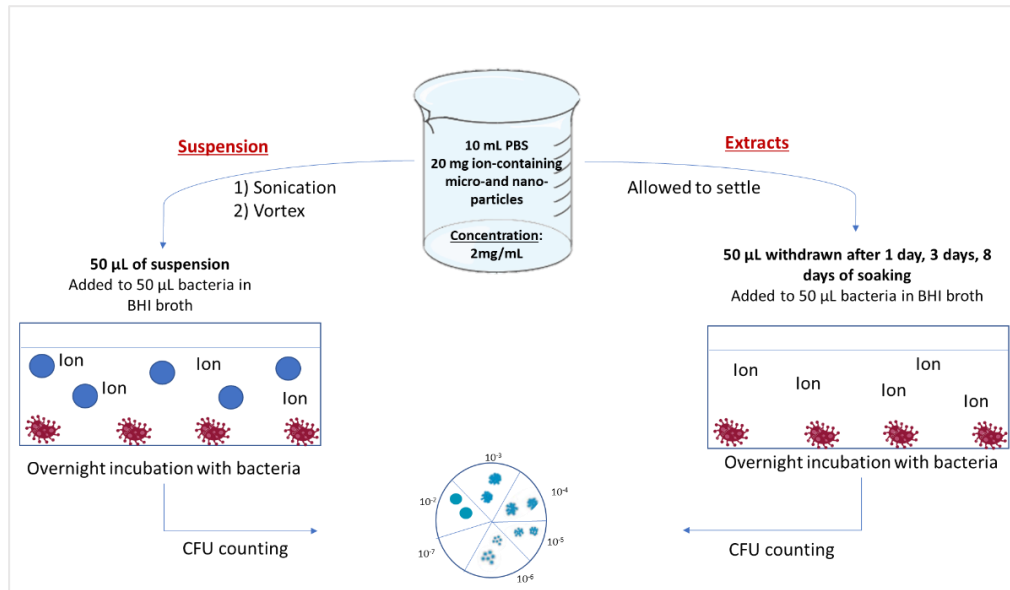


Figure 2.6: Viable count method experimental conditions

Following the 24h of incubation, serial dilutions of each suspension containing bacteria and tested samples were performed and viable colony count was carried out according to the standard Miles & Misra technique [26] by spotting out dilutions onto BHI agar plates and counting the numbers of CFU/mL after incubating plates for 24h at 37 °C.

The number of CFU/mL was calculated as follows: $\text{CFU/mL} = \text{number of colonies} \times \text{dilution factor} \times 100$

2.8.2.4 Investigation of antibacterial effect of ion-containing samples on *S. aureus* and *P. aeruginosa* biofilm through metabolic activity and biofilm mass evaluation

As evidenced previously, the bacterial biofilm represents one of the main issues in chronic infections. The bacterial biofilms are complex, heterogeneous 3D multi-layered bacteria communities embedded in a polysaccharide matrix. Traditional antimicrobials and treatments are not effective in reducing the bacterial biofilm [27] for several reasons, as extensively described earlier.

The as-synthesized nanomatrices could represent a valid alternative to the traditional drugs. In this context, antibacterial effect of the copper-containing nano-sized matrix was tested against *S. aureus* and *P. aeruginosa* biofilm, which commonly colonized chronic skin wounds [28]. This evaluation was carried out in collaboration with the *Department of Materials Science and Engineering (University of Sheffield)*, in the group of *Prof. Sheila MacNeil*.

Samples. The potential of copper-containing nano-sized particles (MBG_SG_Cu2%) to prevent the formation and to disrupt a pre-formed biofilm developed by SOM1 and S235 bacterial strain was investigated.

Methods. The antibacterial activity of the sample against prevention and disruption of bacterial biofilms was evaluated by two different techniques. Clinical isolates of *P. aeruginosa* (SOM1) and *S. aureus* (S235) were used to form 48h

biofilms in BHI broth (Oxoid). MBG_SG_Cu2% was suspended in PBS to a final concentration of 100 µg/mL.

To test the ability on preventing the biofilm formation, 1 mL of suspension was added at the same time of bacteria inoculation in BHI broth; whereas, the addition of the same amount of suspension occurred after 48h, to test the ability to disrupt the pre-formed biofilm. In the latter experiment, the sample was left incubated with the bacteria for 24h before performing assays.

In Figure 2.7, the experimental setup of antibacterial test against S235 and SOM1 bacterial biofilm is represented.

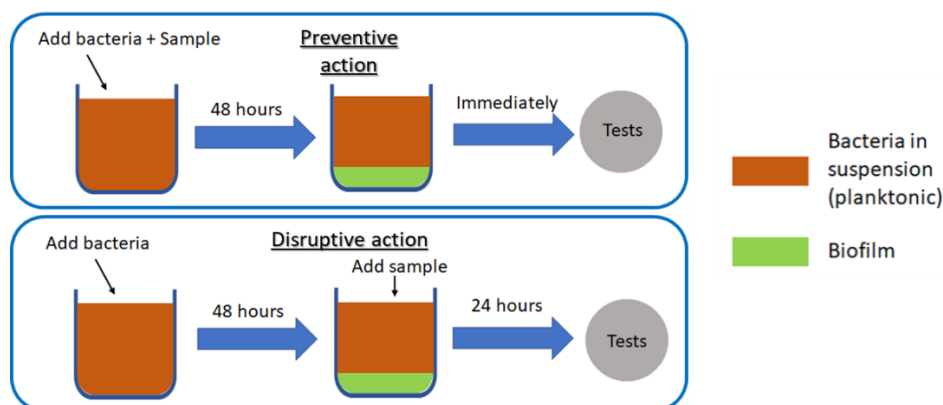


Figure 2.7: Experimental setup of antibacterial test against *S. aureus* and *P. aeruginosa* biofilm

In order to measure the antibacterial activity of the sample, the biofilm was assayed as follows:

i) Absorbance of the whole sample (planktonic and biofilm bacteria) was read at 600 nm to measure the entire biomass using the spectrophotometer (Tecan) equipped with Magellan software. Following this, planktonic bacteria were removed and absorbance at 600 nm was read in order to measure the biofilm mass alone

ii) PrestoBlue assays were carried out with the aim to measure the biofilm metabolic activity. Briefly, biofilms cultured in 12 well plates were incubated with 1 mL of PrestoBlue reagent (ThermoFisher) at 37 °C for 1 hour. The spectrophotometer (Tecan) was used to read the fluorescence with excitation/emission wavelengths of 560nm/590nm to obtain an evaluation of cell metabolism, indicating the cell viability.

2.8.3 Biological assessment on 3D tissue engineered skin model

The development and the use of reconstituted human tissue models is gaining increasing interest due to the presence of multiple cell types and naturally developed extracellular matrix which result in a more physiologically relevant environment to perform laboratory test (such as antibacterial, biocompatibility or anti-inflammatory tests) and for clinical application, such as graft substitutes [29,30].

In this context, the group of the *University of Sheffield (UK)*, under the supervision of *Prof. Sheila MacNeil* conducted the *in vivo*-like evaluation of the optimized ion-containing nanomatrices on the own-produced 3D skin model.

2.8.3.1 Production of 3D tissue engineered skin model

3D tissue engineered skin constructs were prepared as described previously [31]. Briefly, human dermal fibroblasts were isolated from split-thickness skin biopsies received from abdominoplasties and breast reductions performed at the Northern General Hospital (Sheffield, UK). Cells were maintained in DMEM high glucose (4500 mg/L glucose), 10% v/v foetal calf serum (FCS), 2 mM l-glutamine, 0.625 mg/mL amphotericin B, 100 IU/mL penicillin, and 100 mg/mL streptomycin. Research Ethics approval was obtained from the Sheffield Research Ethics Committee. Keratinocytes (HaCaT) cells were purchased from Promega and maintained in Greens' media (DMEM high glucose (4500 mg/L glucose) and Ham's F12 medium in a 3:1 ratio, 10% v/v FCS (UK), 10 ng/mL human recombinant epidermal growth factor, 0.4 mg/mL hydrocortisone, 10⁻¹⁰ M cholera toxin, 18 mM adenine, 5 mg/mL insulin, 5 mg/mL apo-transferrin, 20 mM 3,3,5-tri-iodothyronine, 2 mM glutamine, 0.625 mg/mL amphotericin B, 100 IU/mL penicillin, and 1000 mg/mL streptomycin). Decellularised dermis (DED), produced by removing cells using 1 M NaCl, as detailed in MacNeil et al. [31], from human cadaver skin (Euro Skin), was used as a base scaffold. Rings of DED (15 mm in diameter) were cut and placed within 12 mm tissue culture inserts with 4 mm pores in the base (Greiner). Inserts were suspended from the edges of 12-well plates into the wells. Greens' medium containing 10% foetal calf serum was added to the bottom of the wells in order to lap the DED under surface. Subsequently, 1x10⁵ fibroblasts and 5x10⁵ keratinocytes, each in 250 µL of 10% Greens' medium, were used to seed the DED. Again, after 24 h incubation at 37 °C, seeding medium was removed and replaced with fresh Greens' medium. After a further 24 h, medium was removed from the inside of the inserts to let the constructs to be at an air-liquid interface. Greens' medium in the tissue culture wells was replaced every 24 h. Finally, after 14 days at air-liquid interface, the constructs were used for the tests.

2.8.3.2 Biocompatibility test on the 3D tissue engineered skin model

Sample. Copper-containing nano-sized particles produced by the optimized sol-gel synthesis (MBG_SG_Cu2%) were used in order to assess the potential cytotoxic effect exerted by the sample on the 3D skin construct.

A 3D skin model without any type of treatment was used as control. Additionally, another 3D skin model was treated with a section (5x5 mm) of the commercially available standard silver-containing dressing Acticoat Flex 3[®] (Smith & Nephew).

Methods. The particles were suspended in PBS with a final concentration of 100 µg/mL prior to the test. 3D skin samples were incubated with 200 µL of the as-prepared suspension for 24h at 37 °C in an incubator equilibrated with 5 % CO₂.

The 3D construct was then tested for cell viability using PrestoBlue to investigate the metabolic activity of the cells. All media were removed and 100 μ L of a 1:10 dilution of PrestoBlue:DMEM was added for 2 hours. By using 560nm/590nm as excitation/emission wavelengths respectively, the resulting fluorescence was read using a spectrophotometer (Tecan) as an index of the cell metabolism, as well as of the cell vitality.

2.8.3.3 Investigation of antibacterial effect on *S. aureus* and *P. aeruginosa* biofilm on infected 3D tissue engineered skin model

Sample. With the aim to investigate the antibacterial potential of copper-containing nano-particles (MBG_SG_Cu2%) in a more biologically relevant environment, the 3D skin model produced by MacNeil's group was infected and treated with the sample suspension in PBS (100 μ g/mL). Since the Acticoat Flex 3[®] (Smith & Nephew) is considered a gold standard in the treatment of infected wound, other infected skin models were treated with the silver dressing as comparison.

Methods. First of all, the 3D skin models produced as described above were infected as follows.

Constructs were washed in antibiotic-free Greens' medium for 72 h prior to infection. They were then burnt using a surgical cauterizer for 8 s immediately prior to the infection in order to allow the bacteria to entry into the dermal tissue. Subsequently, 1×10^6 of *P. aeruginosa* or *S. aureus* bacteria, prepared as described in section 2.8.2.3, dispersed in 20 μ l of BHI broth per construct were placed into the inserts covering the epidermal surface. Finally, infected constructs were incubated at 37 °C in incubator equilibrated with 5% CO₂.

After infection, the constructs were adopted for testing the antibacterial effect exerted by the copper-containing MBG particles on the bacterial biofilm.

In brief, to analyse the disruptive biofilm forming ability of the sample, 200 μ L of the suspension at 100 μ g/mL was added simultaneously to the S235 and SOM1 bacteria and incubated for 24 hours before testing; whilst, the ability of the matrix to disrupt a pre-existing biofilm was explored by adding the same amount of suspension 24 h after infection. In both experiments, the skin models were left incubating at 37 °C/5%CO₂ for 24 h before surviving bacterial colony numbers were counted. At the testing point the tissue was weighed and homogenised in 1 mL of BHI broth. The viable counts of bacteria in the samples were performed on the resulting homogenates, after serial dilutions, using standard Miles & Misra methods, as described above.

References

- [1] A. El-Fiqi, T.H. Kim, M. Kim, M. Eltohamy, J.E. Won, E.J. Lee, H.W. Kim, Capacity of mesoporous bioactive glass nanoparticles to deliver therapeutic molecules, *Nanoscale*. 4 (2012) 7475. doi:10.1039/c2nr31775c.
- [2] A. Bari, N. Bloise, S. Fiorilli, G. Novajra, M. Vallet-Regí, G. Bruni, A. Torres-Pardo, J.M. González-Calbet, L. Visai, C. Vitale-Brovarone, Copper-containing mesoporous bioactive glass nanoparticles as multifunctional agent for bone regeneration, *Acta Biomater*. 55 (2017) 493–504. doi:10.1016/j.actbio.2017.04.012.
- [3] M. Shi, Z. Chen, S. Farnaghi, T. Friis, X. Mao, Y. Xiao, C. Wu, Copper-doped mesoporous silica nanospheres, a promising immunomodulatory agent for inducing osteogenesis, *Acta Biomater*. 30 (2016) 334–344. doi:10.1016/j.actbio.2015.11.033.
- [4] C. Wu, J. Chang, W. Fan, Bioactive mesoporous calcium-silicate nanoparticles with excellent mineralization ability, osteostimulation, drug-delivery and antibacterial properties for filling apex roots of teeth, *J. Mater. Chem*. 22 (2012) 16801–16809. doi:10.1039/c2jm33387b.
- [5] C. Pontremoli, M. Boffito, S. Fiorilli, R. Laurano, A. Torchio, A. Bari, C. Tonda-Turo, G. Ciardelli, C. Vitale-Brovarone, Hybrid injectable platforms for the in situ delivery of therapeutic ions from mesoporous glasses, *Chem. Eng. J*. 340 (2018) 103–113. doi:10.1016/j.cej.2018.01.073.
- [6] L. Pontiroli, M. Dadkhah, G. Novajra, I. Tcacencu, S. Fiorilli, C. Vitale-Brovarone, An aerosol-spray-assisted approach to produce mesoporous bioactive glass microspheres under mild acidic aqueous conditions, *Mater. Lett*. 190 (2017) 111–114. doi:10.1016/j.matlet.2016.12.125.
- [7] <https://www2.nau.edu/micro-analysis/wordpress/>, (n.d.).
- [8] A. Alyamani, O. Lemine, FE-SEM characterization of some nanomaterial, INTECH Open Access Publisher, Intech. (2012) 463–472. doi:10.5772/34361.
- [9] https://myscope.training/#/SEMlevel_3_3, (n.d.).
- [10] <https://cfamm.ucr.edu>, (n.d.).
- [11] <https://xrf-spectroscopy.com/>, (n.d.).
- [12] <https://www.phl.com/surface-analysis-techniques/xps-esca.html>, (n.d.).
- [13] K.S.W. Sing, D.H. Everett, R.A.W. Haul, L. Moscou, R.A. Pierotti, J. Rouquelon, T. Siemieniowska, Reporting physisorption data for gas/solid systems with special reference to the determination of surface area and porosity (Recommendations 1984), *Pure Appl. Chem*. 57 (1985) 603–619. doi:10.1351/pac198557040603.
- [14] M. Thommes, K. Kaneko, A. V. Neimark, J.P. Olivier, F. Rodriguez-Reinoso, J. Rouquerol, K.S.W. Sing, Physisorption of gases, with special reference to the evaluation of surface area and pore size distribution (IUPAC Technical Report), *Pure Appl. Chem*. 87 (2015) 1051–1069. doi:10.1515/pac-2014-1117.
- [15] T. Kokubo, H. Takadama, How useful is SBF in predicting in vivo bone bioactivity?, *Biomaterials*. 27 (2006) 2907–2915. doi:10.1016/j.biomaterials.2006.01.017.

- [16] A.L.B. Maçon, T.B. Kim, E.M. Valliant, K. Goetschius, R.K. Brow, D.E. Day, A. Hoppe, A.R. Boccaccini, I.Y. Kim, C. Ohtsuki, T. Kokubo, A. Osaka, M. Vallet-Regí, D. Arcos, L. Fraile, A.J. Salinas, A. V. Teixeira, Y. Vueva, R.M. Almeida, M. Miola, C. Vitale-Brovarone, E. Verné, W. Höland, J.R. Jones, A unified in vitro evaluation for apatite-forming ability of bioactive glasses and their variants, *J. Mater. Sci. Mater. Med.* 26 (2015) 1–10. doi:10.1007/s10856-015-5403-9.
- [17] H. Malekinejad, B. Bazargani-Gilani, A. Tukmechi, H. Ebrahimi, A cytotoxicity and comparative antibacterial study on the effect of *Zataria multiflora* Boiss, *Trachyspermum copticum* essential oils, and Enrofloxacin on *Aeromonas hydrophila*., *Avicenna J. Phytomedicine.* 2 (2012) 188–95.
- [18] C. Wu, Y. Zhou, M. Xu, P. Han, L. Chen, J. Chang, Y. Xiao, Copper-containing mesoporous bioactive glass scaffolds with multifunctional properties of angiogenesis capacity, osteostimulation and antibacterial activity, *Biomaterials.* 34 (2013) 422–433. doi:10.1016/j.biomaterials.2012.09.066.
- [19] J.W. Costerton, P.S. Stewart, E.P. Greenberg, Bacterial biofilms: A common cause of persistent infections, *Science.* 284 (1999) 1318–1322. doi:10.1126/science.284.5418.1318.
- [20] I. Armentano, C.R. Arciola, E. Fortunati, D. Ferrari, S. Mattioli, C.F. Amoroso, J. Rizzo, J.M. Kenny, M. Imbriani, L. Visai, The interaction of bacteria with engineered nanostructured polymeric materials: A review, *Sci. World J.* 2014 (2014). doi:10.1155/2014/410423.
- [21] I. Keren, N. Kaldalu, A. Spoering, Y. Wang, K. Lewis, Persister cells and tolerance to antimicrobials, *FEMS Microbiol. Lett.* 230 (2004) 13–18. doi:10.1016/S0378-1097(03)00856-5.
- [22] S.M. Dizaj, F. Lotfipour, M. Barzegar-Jalali, M.H. Zarrintan, K. Adibkia, Antimicrobial activity of the metals and metal oxide nanoparticles, *Mater. Sci. Eng. C.* 44 (2014) 278–284. doi:10.1016/j.msec.2014.08.031.
- [23] H.J. Busscher, H.C. Van Der Mei, Microbial adhesion in flow displacement systems, *Clin. Microbiol. Rev.* 19 (2006) 127–141. doi:10.1128/CMR.19.1.127-141.2006.
- [24] A. Chen, Q. Shi, Y. Ouyang, Y. Chen, Effect of Ce³⁺ on membrane permeability of *Escherichia coli* cell, *J. Rare Earths.* 30 (2012) 947–951. doi:10.1016/S1002-0721(12)60159-8.
- [25] M. Kawashita, S. Tsuneyama, F. Miyaji, T. Kokubo, H. Kozuka, K. Yamamoto, Antibacterial silver-containing silica glass prepared by sol-gel method, *Biomaterials.* 21 (2000) 393–398. doi:10.1016/S0142-9612(99)00201-X.
- [26] A.A. Miles, S.S. Misra, J.O. Irwin, The estimation of the bactericidal power of the blood, *J. Hyg. (Lond).* 38 (1938) 732–749. doi:10.1017/S002217240001158X.
- [27] H. Koo, R.N. Allan, R.P. Howlin, P. Stoodley, L. Hall-Stoodley, Targeting microbial biofilms: Current and prospective therapeutic strategies, *Nat. Rev. Microbiol.* 15 (2017) 740–755. doi:10.1038/nrmicro.2017.99.
- [28] R. Serra, R. Grande, L. Butrico, A. Rossi, U.F. Settimio, B. Caroleo, B. Amato, L. Gallelli, S. De Franciscis, Chronic wound infections: The role of *Pseudomonas aeruginosa* and *Staphylococcus aureus*, *Expert Rev. Anti. Infect. Ther.* 13 (2015) 605–613. doi:10.1586/14787210.2015.1023291.
- [29] S. MacNeil, Progress and opportunities for tissue-engineered skin, *Nature.* 445 (2007) 874–880. doi:10.1038/nature05664.

- [30] J. Shepherd, I. Douglas, S. Rimmer, L. Swanson, S. MacNeil, Development of Three-Dimensional Tissue-Engineered Models of Bacterial Infected Human Skin Wounds, *Tissue Eng. Part C Methods*. 15 (2009) 475–484. doi:10.1089/ten.tec.2008.0614.
- [31] S. MacNeil, J. Shepherd, L. Smith, Production of Tissue-Engineered Skin and Oral Mucosa for Clinical and Experimental Use, in: *3D Cell Cult.*, 2011: pp. 129–153. doi:10.1007/978-1-60761-984-0.

CHAPTER 3

Results and discussion

3.1 Introduction

With the final aim to produce a library of nanomatrices containing therapeutic ions to be used as multifunctional platform in the treatment of delayed bone healing and non-healing skin wounds, several ion-containing mesoporous inorganic systems were obtained by different synthesis approaches. With the general aim to obtain scalable nanomatrices and enhance the synthesis yield, several synthesis approaches were conducted, and the results related to the morphological, structural and chemical characterization of the obtained systems are presented.

In order to obtain particles in the range of 100-200 nm with pores ranging between 2 and 4 nm, an ultrasonicator-assisted method using methanol as solvent was originally adopted to produce different ion-containing MBGs, whose results are presented in paragraph 3.2.1. Besides the morphological, compositional and structural data, the paragraph reports the antibacterial results of the as-produced copper-containing nano-sized particles.

Despite the promising results of these nanomatrices, the involvement of a toxic solvent (methanol) caused the dismissal of this synthesis route and its replacement with ultrasonicator-assisted water-based sol-gel approaches. In paragraph 3.2.2, the results of the related characterization are described.

With the aim to attain the scalability of the process, since the ultrasonication represented an additional energy-consuming step, the efforts were devoted to optimise a water-based sol-gel procedure using ammonia as catalyst, without the application of ultrasounds. The related data are described in paragraph 3.3.1.

In section 3.3.2, the results concerning the nanomatrices obtained through an optimized water-based aerosol-assisted spray-drying approach are presented. This method, easily scalable at an industrial scale, allowed to obtain highly reproducible mesoporous nanomatrices in the form of microspheres with nanopores of around 8 nm.

3.2 Characterization of mesoporous nano-sized matrices produced by ultrasonicator-assisted synthesis

Different nano-sized matrices (MBG_US) were produced by an ultrasonicator assisted sol-gel method using methanol (see Table 3.1 for compositions) or water (see Table 3.7 for compositions) as solvent. In the latter instance, two different water-based approaches were used: the first at almost neutral pH with NH_4F as catalyst, and the second one involving the use of ammonia as catalyst with a final solution pH around 8.

In the following paragraphs, the results of morphological and structural characterization of the obtained nanomatrices are reported, by referring with the acronym MBG_US_m and MBG_US_w the samples produced by using methanol and water as solvent, respectively.

In the following paragraph, the description of morphological, compositional and structural features of the nanomatrices produced by the methanol-based sol-gel approach is presented. In particular, the results of mesoporous SiO_2 -CaO binary glass system without ions (named hereafter MBG_US_m SiO_2/CaO) will be presented in section 3.2.1.1. Subsequently, the characterization results of ion-containing samples, divided as copper-containing sample, strontium-containing sample and strontium-copper co-substituted sample will be explained.

Finally, the morphological, compositional and structural results of the nanomatrices synthesized through the water-based approaches will be presented in the paragraph 3.2.2. In this latter section, the samples coded as MBG_US_w_I represent the nanomatrices produced by the sol-gel procedure carried out at almost neutral pH with NH_4F as catalyst, and the nanomatrices coded as MBG_US_w_II identify the ones synthesized by the sol-gel route which involved the use of ammonia as catalyst.

3.2.1 Methanol-based synthesis results: MBG_US_m nanomatrices

Nanomatrices with different compositions, both in term of incorporated ions and of molar concentrations (Table 3.1), were produced through a modification of a procedure reported in the literature [1].

The results of the SiO_2 -CaO binary glass sample without ion (85 $\text{SiO}_2/15\text{CaO}$ %mol, named MBG_US_m SiO_2/CaO) will be presented as reference system. The ion-containing MBG particles were produced by substituting 1, 2, 5 % mol of CaO with specific ion precursors.

Table 3.1: List of MBG_US_m compositions

Name	Composition (%mol)
MBG_US_m_SiO ₂ /CaO	85 SiO ₂ /15 CaO
MBG_US_m_Cu2%	85 SiO ₂ /13 CaO/2 CuO
MBG_US_m_Cu5%	85 SiO ₂ /10 CaO/5 CuO
MBG_US_m_Sr1%	85 SiO ₂ /14 CaO/1 SrO
MBG_US_m_CuSr2%	85 SiO ₂ /13 CaO/1 CuO/1 SrO

3.2.1.1 MBG_US_m_SiO₂/CaO matrix

The sample, named in the following section MBG_US_m_SiO₂/CaO (85SiO₂/15CaO %mol), was used as reference system to study the influence of the different therapeutic ions on the morphology, chemical composition, bioactive response and on the structural features of the as-synthesized samples.

3.2.1.1a Morphological and structural characterization of MBG_US_m_SiO₂/CaO

The morphological and compositional information were obtained by FE-SEM and EDS technique, respectively. FE-SEM analysis revealed particles with size ranging between 40 and 80 nm, characterized by quite irregular spheroidal morphology (Figure 3.1) with a tendency to aggregate and form agglomerates. EDS characterization (Figure 3.1-inset) confirmed the theoretical composition; the detected Ca/Si molar ratio resulted very close to the nominal ratio.

The Cr peaks in the EDS spectrum are due to the chromium coating required to run the analysis, as described in the section 2.5.2 of “Materials and methods” chapter.

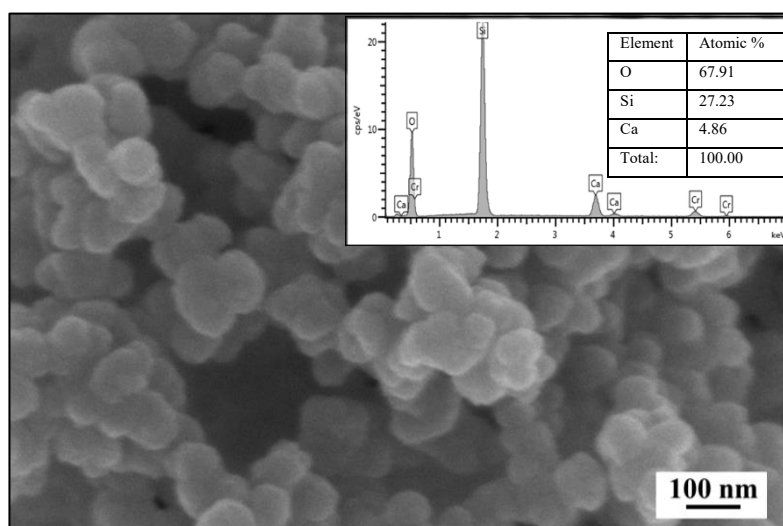


Figure 3.1: FE-SEM image, EDS spectrum and atomic % (inset) of MBG_US_m_SiO₂/CaO

The mesoporous structure of the sample was investigated by N₂ adsorption-desorption measurement. As shown in Figure 3.2 the isotherm confirmed the mesoporous structure of MBG_US_m_SiO₂/CaO with a IV type curve, typical of

mesoporous material, according to the IUPAC classification [2]. The presence of a step at $p/p_0 < 0.3$ represented the complete monolayer coverage and the beginning of the multilayer adsorption [2]. Related pore size distribution (inset in Figure 3.2) showed the presence of uniform mesopores with an average diameter of 2.9 nm, calculated through the DFT model, typical of CTAB templated system. The specific surface area (SSA) and pore volume, reported in Table 3.2 and equal to $621 \text{ m}^2/\text{g}$ and $1.05 \text{ cm}^3/\text{g}$ respectively, are remarkably higher than the non-templated bioactive glasses [3] and in fair agreement with systems produced using the same route [1].

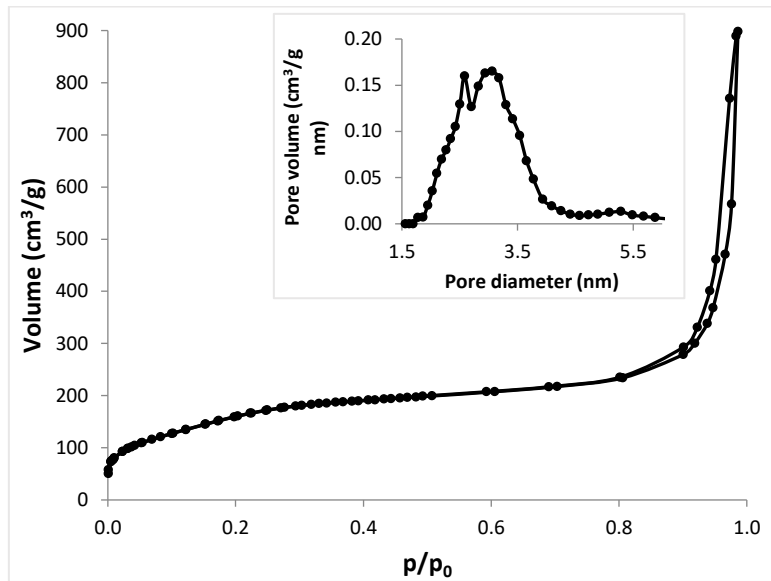


Figure 3.2: N_2 adsorption-desorption isotherm of MBG_US_m_SiO₂/CaO and related DFT pore size distribution (inset)

Table 3.2: Structural features of MBG_US_m_SiO₂/CaO

Name	Specific surface area (m ² /g)	Pore size (nm)	Volume (cm ³ /g)
MBG_US_m_SiO ₂ /CaO	621	2.9	1.05

The eventual presence of crystalline phases in the MBG_US_m_SiO₂/CaO sample was analysed by wide-angle XRD and the resulted pattern (Figure 3.3) confirmed the amorphous structure, with the broad peak between 20° and 30° (2θ values) attributed to amorphous silica, without peaks corresponding to the segregation of calcium oxide phases.

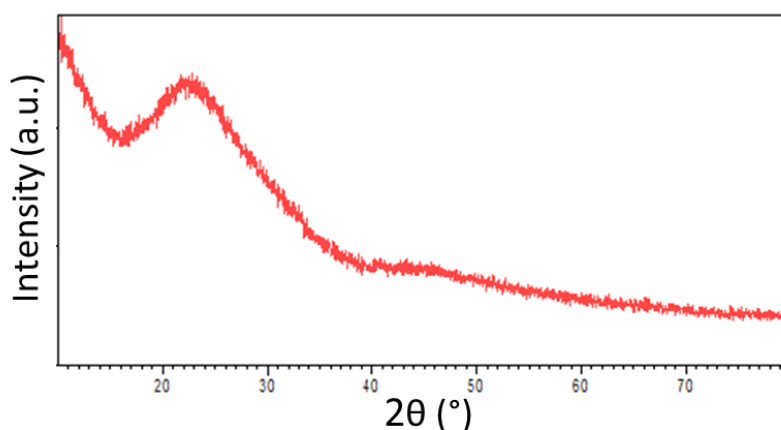


Figure 3.3: Wide-angle XRD spectrum of MBG_US_m_SiO₂/CaO

3.2.2.1b Bioactive behaviour of MBG_US_m_SiO₂/CaO in SBF

The bioactivity of the sample was assessed by soaking the powder in SBF using the procedure reported in reference [4], as described in section 2.7 of “Materials and methods” chapter, and was investigated by FE-SEM and EDS analyses.

As reported in Figure 3.4A, after only 1 day of soaking the sample MBG_US_m_SiO₂/CaO started to be covered by needle-like structure. After 7 days of immersion (Figure 3.4B), the needle-like structures assumed a flake-like shape, typical of hydroxyapatite (HA), and formed a homogeneous layer which made the particles difficult to discern.

The related EDS spectra (Figure 3.4C and 3.4D) evidenced the peak of phosphorus, not originally shown by the sample before soaking in SBF, which is attributed to the formation of the HA precipitates. The detected phase was characterized by Ca/P ratio equal to 1.38 after 1 day of incubation and equal to 1.79 after 7 days in SBF. As the soaking time increased, the Ca/P ratio became very close to the stoichiometric value of HA (1.67), as observed in several studies [5,6], highlighting the increase of PO₄³⁻ exchanges with SBF.

The monitoring of the pH confirmed that it remained in the physiological range of 7.4.

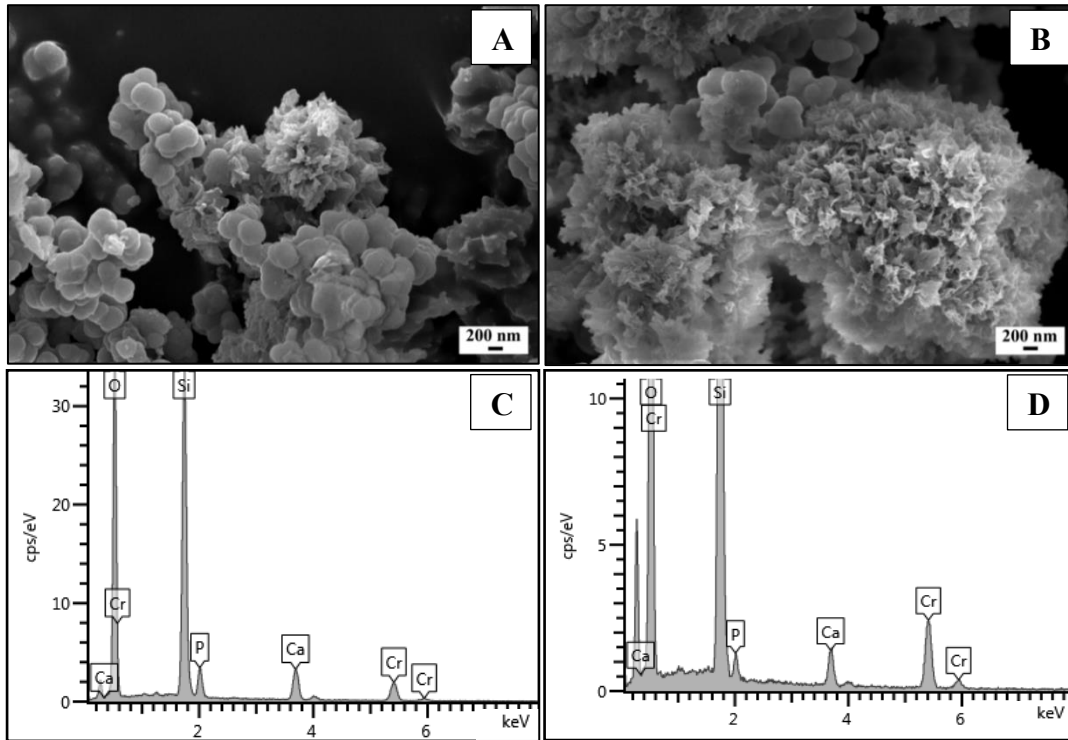


Figure 3.4: FE-SEM images of MBG_US_m_SiO₂/CaO after 1 day (A) and 7 days of soaking in SBF (B) and related EDS spectra (C, D)

3.2.1.2 Copper-containing MBG_US_m: MBG_US_m_Cu2%, MBG_US_m_Cu5%

The first ion selected to be incorporated into the SiO₂-CaO system produced by methanol-based ultrasonic-assisted sol-gel route was copper. As described in chapter “State of the art”, copper is largely studied for potential application in medical fields where antibacterial, pro-osteogenic and pro-angiogenic effects are needed [7].

Two different compositions of copper-containing MBG_US_m were produced by adding different amounts of copper chloride during the synthesis procedure.

The as-synthesized samples are named hereafter MBG_US_m_Cu2% (85SiO₂/13CaO/2CuO %mol) and MBG_US_m_Cu5% (85SiO₂/10CaO/5CuO %mol) and the related results are described in the following sub-chapters.

Part of the work described in this chapter has been already published by the candidate [8].

3.2.1.2a Morphological and structural characterization of copper-containing MBG_US_m samples

The FE-SEM images and related EDS characterization results are represented in Figure 3.5.

The FE-SEM image of MBG_US_m_Cu2% (Figure 3.5A) revealed particles with uniform spheroidal morphology, with size ranging between 170 and 200 nm. EDS analysis confirmed the incorporation of Cu into the framework: the detected Cu/Si molar ratio, as average of three measurements, resulted in fair agreement with the nominal ratio (Figure 3.5B). The investigation by TEM demonstrated the presence of mesopores throughout the nanoparticle inner structure, in the form of a worm-like system (Figure 3.5C). Quantitative analysis using EDS mapping, coupled to TEM, was used to explore the element distribution in the sample and showed that Cu ions, like the other elements, were evenly distributed within the whole of the particle (Figure 3.5D).

For what concerns the MBG_US_m_Cu5%, FE-SEM observation (Figure 3.5E) showed spheroidal particles whose size ranged between 180 and 230 nm, on average slightly larger than what was observed for MBG_US_m_Cu2%. The incorporation of copper, with a molar ratio (Cu/Si) very close to the theoretical one, was confirmed by EDS analysis, reported in the inset of Figure 3.5E.

TEM images of MBG_US_m_Cu5%, (Figure 3.5F) allowed discerning a core-shell morphology for this sample, with a shell characterized by a regular mesoporous structure and an internal core characterized by larger and irregular cavities. In this case, EDS mapping analysis evidenced different Si, Ca and Cu atomic percentages in the core and shell regions of the particles, showing, a higher concentration of Ca and Cu ions in the core ($\text{Ca/Si} = 0.13$ and $\text{Cu/Si} = 0.15$) compared to the outer shell ($\text{Ca/Si} = 0.05$ and $\text{Cu/Si} = 0.06$).

The TEM observation evidenced that the higher amount of doping cation had an evident impact on structural properties.

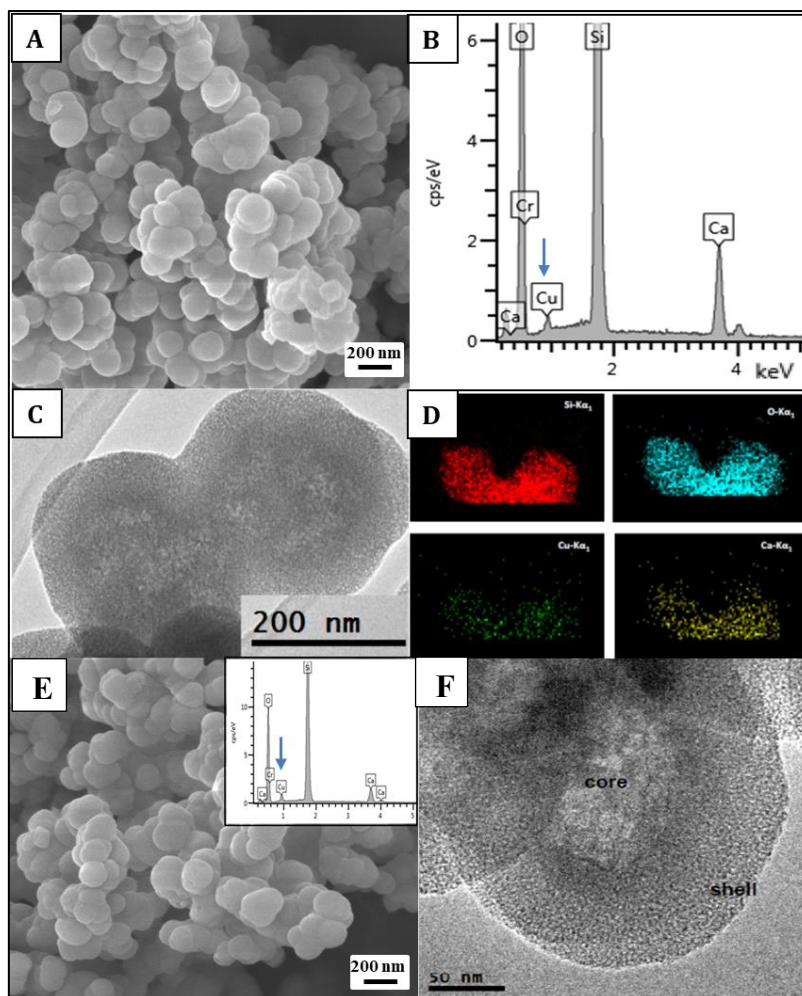


Figure 3.5: FE-SEM image of MBG_US_m_Cu2% (A), EDS spectrum (B), TEM image (C) and EDS mapping analysis of MBG_US_m_Cu2% (D); FE-SEM image of MBG_US_m_Cu5% (E), related EDS spectrum (inset), TEM image of MBG_US_m_Cu5% (F)

The mesoporous structure of Cu-modified MBG systems was confirmed by the N_2 adsorption-desorption isotherms (Figure 3.6), which revealed that the isotherm curves of MBG_US_m_Cu2% and MBG_US_m_Cu5% had type-IV isotherm with a well-defined step at relative pressure (p/p_0) below 0.3, indicative of the filling of uniform mesopores. The capillary condensation observed at higher relative pressures for MBG_US_m_Cu5% (green curve) is ascribable to intra-particle voids or to the disordered porosity located in the particle core, discernible from TEM images.

The values of BET specific surface area, mesopores volume and pore diameter for the investigated samples are reported in Table 3.3: a decrease of surface area and pore volume was found with the increase of the amount of copper ion. The mesopore diameter was approximately 2.6 nm in the Cu-containing samples, which is that typical of CTAB-templated systems.

Hence, the increase of copper amount in the synthesis had a negative effect, affecting the formation of the mesostructure and leading to a significant decrease of both exposed surface area and pore volume. These results confirmed that the

presence of an excess of metal ion species in the reaction plays a negative role on the condensation of the silica precursors and the assembly of the mesophase structure [9,10], leading to a significant decrease of the exposed surface area in the obtained nanomaterials.

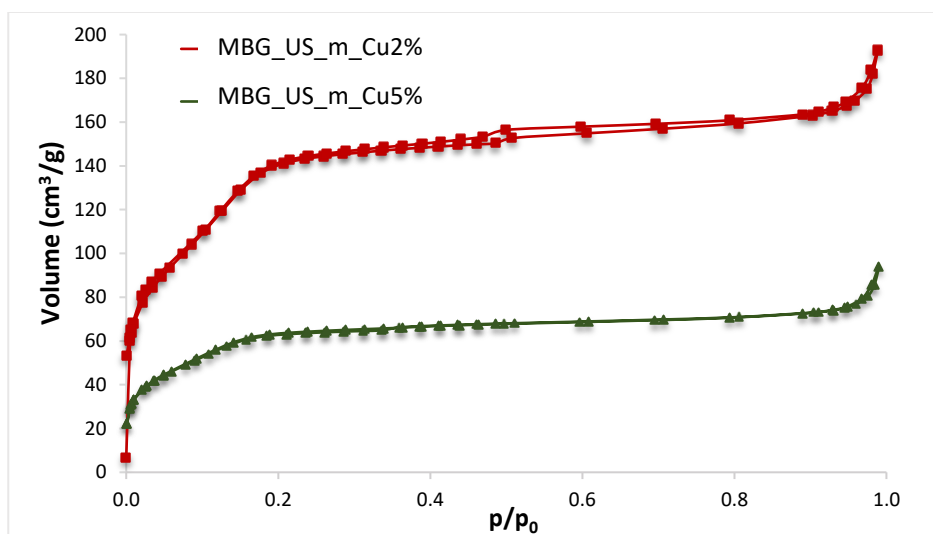


Figure 3.6: N_2 adsorption-desorption isotherms of MBG_US_m_Cu2% (red) and MBG_US_m_Cu5% (green)

Table 3.3: Structural features of copper-containing samples

Name	Specific surface area (m ² /g)	Pore size (nm)	Volume (cm ³ /g)
MBG_US_m_Cu2%	550	2.6	0.26
MBG_US_m_Cu5%	224	2.6	0.11

In the wide-angle XRD patterns (Figure 3.7), the broad peak at 23° corresponded to amorphous silica, and no diffraction peaks of copper oxide (CuOx) were observed in the samples, indicating that the incorporated copper does not form oxide crystals.

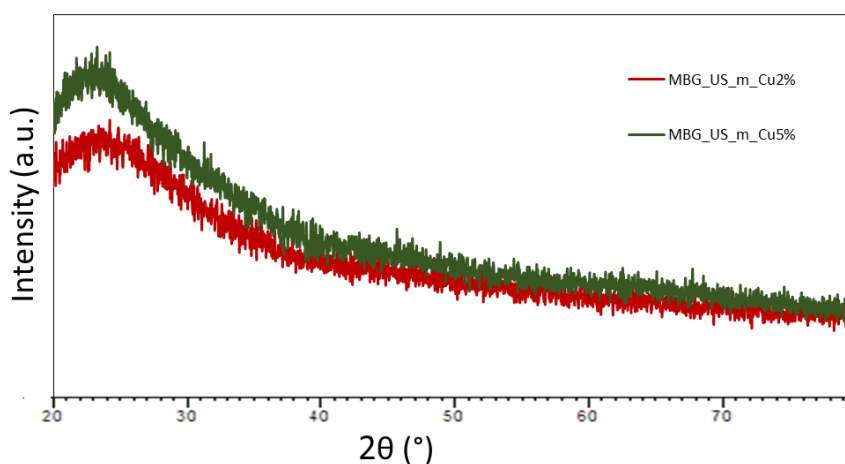


Figure 3.7: Wide-angle XRD spectrum of MBG_US_m_Cu2% (red) and MBG_US_m_Cu5% (green)

In order to investigate the nature of the copper species incorporated inside the glass framework, XPS spectra were recorded on MBG_US_m_Cu2% and

MBG_US_m_Cu5%. Figure 3.8 shows the deconvoluted XPS spectra of MBG_US_m_Cu2% and MBG_US_m_Cu5% in the Cu2p_{3/2} region. The components at 935.7 eV and 933.3 eV obtained through the deconvolution and their integrated peaks areas are reported in Table 3.4: an evident difference in the relative amount of the two components was found.

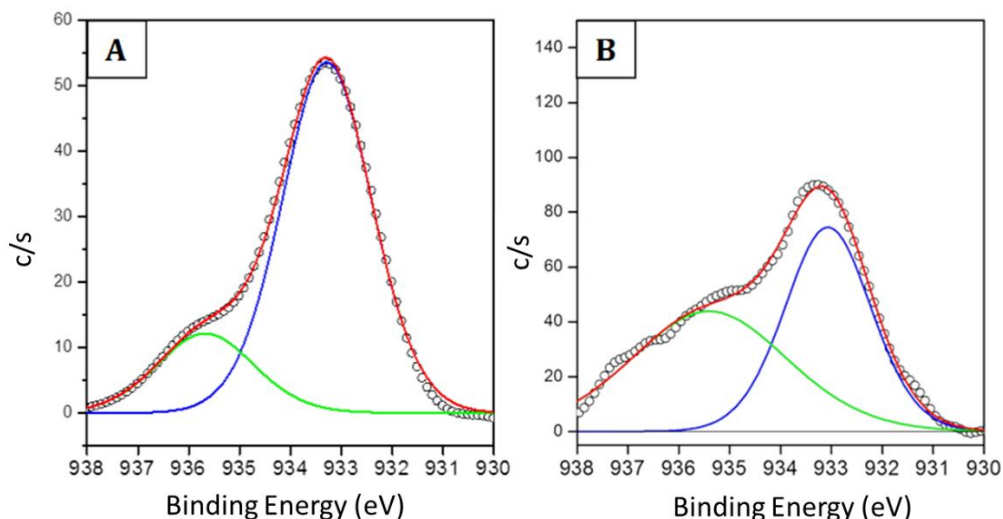


Figure 3.8: XPS deconvoluted spectra in the Cu2p_{3/2} region for MBG_US_m_Cu2% (A) and MBG_US_m_Cu5% (B)

The first component at lower binding energy (933.3 eV) was consistent with values ascribed in the literature to Cu²⁺ cations in extra-framework sites [11]. At variance, the component at higher binding energy, at ca 935.7 eV, much higher than that for pure CuO (ca 933.8 eV) [12], was attributed to copper species with a strong electronic interaction with the lattice, in analogy with results obtained for Cu-containing mesoporous silicas [13]. Specifically, for the MBG_US_m_Cu2% (Figure 3.8A) sample most of copper species were characterized by binding energy (933.3 eV) typical of extra-framework sites, with a limited contribution of species at higher values, whereas the MBG_US_m_Cu5% sample, as reported in Figure 3.8B, shows a significant higher amount of Cu²⁺ at higher binding energy (935.7 eV).

Table 3.4: Deconvoluted contributions of Cu2p core level and relative percentages

Name	Peak position (eV)	Peak area%	Peak position (eV)	Peak area%
MBG_US_m_Cu2%	933.3	80.3	935.7	19.7
MBG_US_m_Cu5%	933.3	48.5	935.7	51.5

3.2.1.2b Copper ion release from copper-containing MBG_US_m in SBF

The ionic concentrations (ppm) of Cu^{2+} species in SBF medium after 14 days of soaking are reported in Figure 3.9. In the case of MBG_US_m_Cu2%, a sustained release of Cu^{2+} is observed during the 7 days of soaking and the percentage released resulted approximately 90% respect to the incorporated amount. Furthermore, the EDS analysis of the sample after the release tests did not reveal the presence of residual copper, confirming the effective release of the functional ion. At variance, the release test carried out with MBG_US_m_Cu5% evidenced a very low percentage of released Cu^{2+} (around 10%), suggesting that copper ions are mostly inaccessible.

These different release behaviours could be ascribed to the different chemical environment of the incorporated copper species, resulting from XPS investigation. The MBG_US_m_Cu2% sample showed a sustained and almost complete release of the incorporated Cu^{2+} , which supports the assignment proposed for the component at 933.3 eV to species present as counter-ions in the silica framework, located at the mesopore surface and thus accessible for cation-exchange reactions when soaked in SBF. On the other hand, the unexpected profile observed for MBG_US_m_Cu5%, characterized by a very limited release of Cu^{2+} species, could be interpreted assuming the inaccessibility of mostly of the incorporated metal, as it was likely located in the particle cores or embedded into the silica walls.

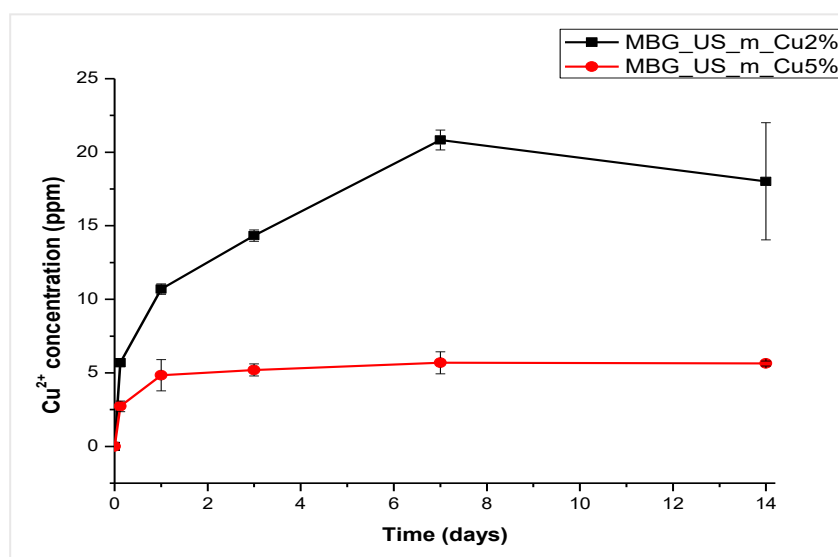


Figure 3.9: Cu^{2+} release profiles of MBG_US_m_Cu2% (black) and MBG_US_m_Cu5% (red) in SBF

3.2.1.2c Bioactive behaviour of MBG_US_m_Cu2% in SBF

Based on the obtained release kinetics for Cu^{2+} species, the investigation about the bioactive properties was uniquely performed on MBG_US_m_Cu2%. The sample showed a remarkable bioactivity when soaked in SBF. The precipitation of HA was assessed after only 3 h of immersion and a conspicuous amount of it could be easily detected after 24 h of soaking. Figure 3.10 shows FE-SEM images of

MBG_US_m_Cu2% nanoparticles after 3 (Figure 3.10A) and 7 days (Figure 3.10B) of SBF soaking, and related EDS spectra (Figure 3.10D' and D''): globe-shaped agglomerates are easily distinguishable on the nanoparticles surface. The phase nucleated after 3 h of soaking, as assessed by EDS analysis, can be identified as Ca-deficient HA (Ca/P = 1.51). The Ca content in the newly formed phase gradually rose as soaking time increased and after 7 days, a molar Ca/P ratio of 1.62 was detected, which was in the range of calcium-deficient biological apatite. The pH of SBF remained in the physiological range during particles soaking (between 7.4 and 7.5). The wide-angle XRD spectrum of MBG_US_m_Cu2% after 24 h of soaking in SBF is reported in Figure 3.10C. Marked peaks at 32° and 26° and other less intense reflections at about 40°, 47° and 49° were assigned to the (002), (211), (300), and (213) reflections of HA (external reference code 01-074-0565). The other narrow peaks are ascribable to calcite (external reference code 01-083-1762). The latter is often found when bioactive glasses with a high content of calcium (at least 30% mol of CaO) are soaked in SBF. These glasses, when in contact with water-based solutions, release immediately a high amount of Ca²⁺ ions, which, in the case of SBF, react with the carbonate ions present, leading to calcite precipitation within the very first hours of immersion [14–16]. Although the calcium content for MBG_US_m_Cu2% sample is not as high as reported in the literature, the very high exposed surface, due to the presence of the mesopores, is expected to allow a high release of calcium ions in terms of both the total amount and the kinetics. Calcite has been reported to be resorbable [17] and osteoconductive, even without the formation of a Ca-P-rich layer [18]. Therefore, the co-precipitation of apatite and calcite can be considered as an index of the mesoporous glass bioactivity [19].

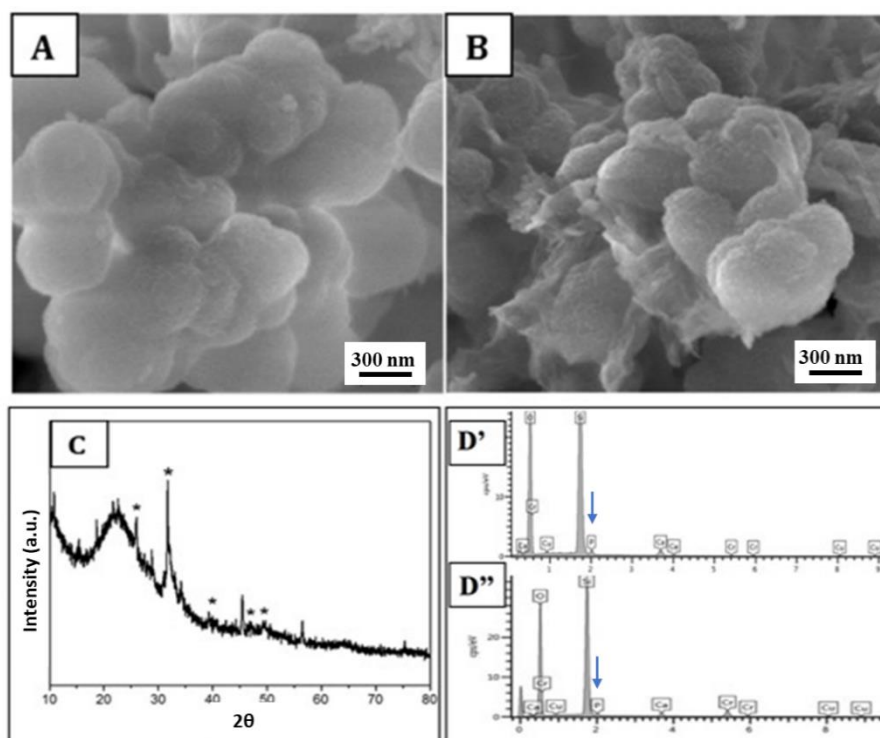


Figure 3.10: FE-SEM images of MBG_US_m_Cu2% after 3 days (A) and 7 days (B) of soaking in SBF and XRD pattern of MBG_US_m_Cu2% after soaking in SBF for 7 days (C); EDS spectra of MBG_US_m_Cu2% after 3 days (D') and 7 days (D'') of soaking in SBF

3.2.1.2d Antibacterial potential evaluation of MBG_US_m_Cu2%

Considering the MBG_US_m_Cu2% the best copper-containing candidate produced by methanol-based ultrasonicator-assisted sol-gel route, the antibacterial assessment was uniquely performed on this sample.

As described in the “Materials and methods” chapter, the microorganisms used to test this matrix were the following: the *Gram negative Escherichia coli RB* (E. coli RB) and two *Gram positive* bacteria *Staphylococcus aureus 8325-4* (S. aureus 8325-4) and *Staphylococcus epidermidis* (S. epidermis RP62A), being the later a strong biofilm-producing strain.

Two different experimental conditions were used to evaluate the antibacterial activity of MBG_US_m_Cu2%. The same experiments were carried out on the MBG_US_m_SiO₂/CaO as control, in order to be able to ascribe the antibacterial potential to the released copper species. As described in the chapter 2, the first experimental condition implied the use of particle suspension (named hereafter “suspension”), in order to take into account the nanoparticle effect, while the second one was conducted with the extracts of the nanoparticles in order to evaluate the antibacterial properties due only to the released Cu²⁺ ions from MBG_US_m_Cu2%.

Both experimental conditions were used in order to evaluate the antibacterial effect on bacterial planktonic growth and on *S. epidermidis* biofilms. In the latter, the effect of the nanoparticle suspensions and of the extracts was investigated in order to evaluate their effects during biofilm formation and on the formed biofilm.

Antibacterial property of MBG nanoparticles and their extracts on bacterial planktonic growth

The synthesized nanoparticles (first experimental condition) and their extracts (second experimental condition) were tested for their antibacterial activity against human pathogenic bacteria, namely, *E. coli RB*, *S. aureus 8325-4* and *S. epidermidis RP62A* (Figure 3.11 and 3.12).

For the first condition (Figure 3.11), all the bacterial strains were incubated with different concentrations of both MBG_US_m_SiO₂/CaO and MBG_US_m_Cu2% particles for 1 and 3 days of culture, respectively. The results in Figure 3.11 evidenced a similar trend on all bacteria cultures after the incubation with the MBG_US_m_Cu2% nanoparticles, showing that the bacterial growth suppression was clearly correlated to the presence of copper and its increasing availability for higher concentration. After 1 day of incubation with a concentration above 250 mg/mL, approximately 30–40% of growth inhibition was observed for all types of bacteria, in comparison to the control (cultures without nanoparticles). In particular, the obtained results showed that at longer incubation times (3 days) with the higher suspension concentration (2 mg/mL), the reduction of viability for both *E. coli RB* and *S. aureus 8325-4* cultures was 70–75%, and for *S. epidermidis* around 50%. Compared to MBG cultures both at short and long incubation times, *E. coli RB* and *S. aureus* showed a slightly lower cell viability using 2 mg/mL or 500 mg/mL of MBG_US_m_Cu2%, respectively. At variance, with *S. epidermidis*, the difference in cell viability was dose-dependent, starting from the lower concentrations and becoming more evident at the higher doses (Figure 3.11). Interestingly, the results showed that MBG_US_m_SiO₂/CaO, although not containing copper, exhibited a slight antibacterial effect against the *E. coli RB* and *S. aureus* (around 25%) remaining persistent at all the tested concentrations (not dose-dependent). On the contrary, with *S. epidermidis* cultures, the obtained results highlighted a clear effect related to copper, suggesting a different sensitivity of bacteria to the MBG composition and most likely a different antibacterial mechanism of action (Figure 3.11).

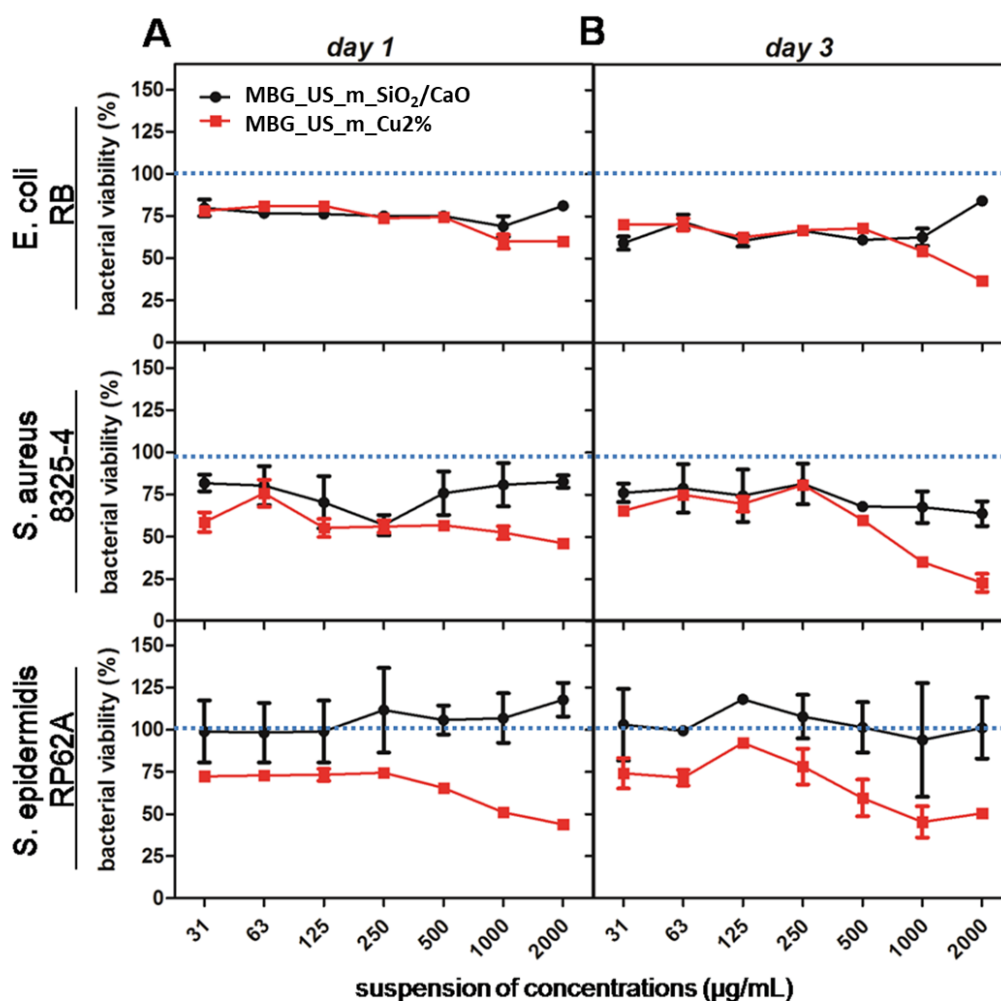


Figure 3.11: Dose-dependence viability of *E. coli* RB, *S. aureus* 8325-4 and *S. epidermidis* RP62A bacterial strains cultured with MBG_US_m_SiO₂/CaO and MBG_US_m_Cu2% suspensions

In order to evaluate the influence of the released copper on the antibacterial effect, the same experiments were performed in parallel with both MBG_US_m_SiO₂/CaO and MBG_US_m_Cu2% extracts (Figure 3.12). Overall, it was clear that there was a positive correlation between the extract concentrations and bacteria growth inhibition, showing the same trend observed in the experiments based on the direct contact with nanoparticles. Interestingly, in all bacteria cultures, a cell viability reduction was observed in the samples treated with extract of MBG_US_m_Cu2% collected after 24 h (Figure 3.12B), if compared with extracts from MBG_US_m_SiO₂/CaO, hence confirming the role of copper in the observed antibacterial activity. The same experiments carried out with extracts of MBG_US_m_Cu2% and MBG_US_m_SiO₂/CaO collected after 3 h revealed a rather varying trend in the bacterial viability for all the tested strains, which did not

allow a reliable interpretation of the data obtained for such short incubation times (Figure 3.12A).

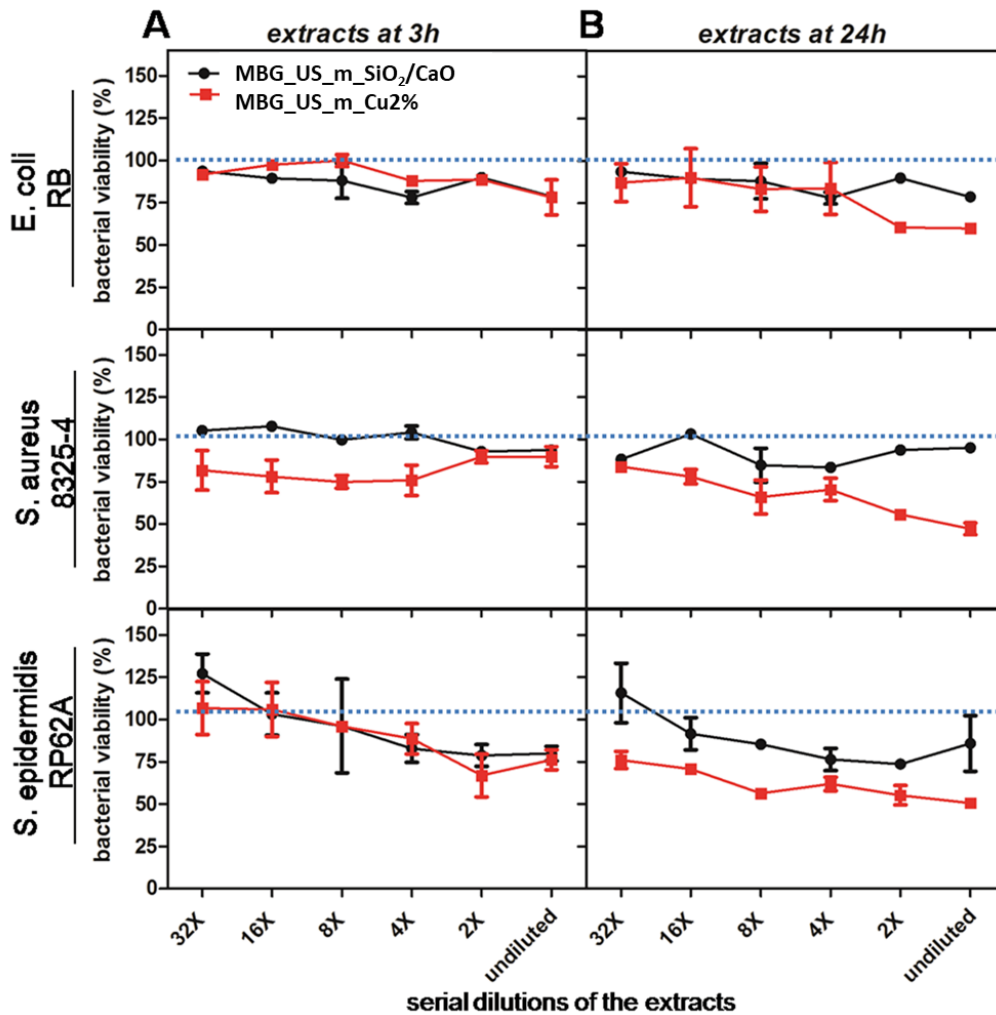


Figure 3.12: Dose-dependence viability of *E. coli* RB, *S. aureus* 8325-4 and *S. epidermidis* RP62A bacterial strains cultured with MBG_US_m_SiO₂/CaO and MBG_US_m_Cu2% extracts collected after 3h (A) and after 24h (B)

The antibacterial effect and the mechanism of action of copper on bacteria viability is not fully elucidated yet, however, it seems to be mainly associated to the pleiotropic effects of copper on bacterial cells, through multiple mechanisms of action. The results obtained in this work evidenced that Cu-containing glass nanoparticles showed antimicrobial effect, highly dependent upon the dose and bacterial strains. The remarkable difference might be attributed to the different properties of bacteria surfaces [20]. In *Gram positive* bacteria, the absence of an outer membrane and the presence of surface negatively charged teichuronic and lipoteichoic acids within a single lipid bilayer surrounded by a thick but porous layer of peptidoglycan (20–80 nm), make them attractive to positive charges [21]. Therefore, the inhibiting process is supposed to be most likely associated to the action of released metal ions, which might be easily moved inside the microbial cells or attached to the charged outer surfaces by electrostatic attraction, resulting

in cell apoptosis via protein denaturation and disruption of cell membrane [22]. By contrast, *Gram negative* bacteria expose a highly organized compact structure, which acts as a permeability barrier and prevents diffusion to the inner plasma membrane for high molecular weight compounds, making them less attractive to the metal cations. Moreover, the presence of copper tolerance mechanisms in *E. coli* [23], including the activation of copper export occurring from cytoplasm into the periplasmic space or into the extracellular milieu and the copper sequestration by metallothioneins, can further explain the requirement of a higher copper-containing MBG concentrations to inhibit *E. coli* cultures in comparison to the other bacterial strains. At variance in *E. coli* and *S. aureus* bacteria, the copper-containing MBG antibacterial effect seems not to be merely due to the release of metal ions in solution, but most likely also to the small size and the high surface-to-volume ratio of MBG_US_m_Cu2% particles that account for the activation of cell death mechanisms [24,25].

Antibacterial effect of nanoparticles and their extracts on *S. epidermidis*

S. epidermidis RP62A is known to produce considerable quantities of polysaccharide intercellular adhesions, inducing biofilm formation [26,27]. To evaluate the antibacterial activity on staphylococcal biofilms, *S. epidermidis* cultures were incubated with MBG_US_m_SiO₂/CaO and MBG_US_m_Cu2% suspensions (2 mg/mL) or with related extracts collected after 24 h of incubation, either during the biofilm formation or in the presence of pre-formed biofilms (Figure 3.13 and 3.14).

A significant reduction of biofilm growth was determined when the cultures were performed in the presence of MBG_US_m_Cu2% particles if compared to MBG_US_m_SiO₂/CaO (Figure 3.13A, indicated by ***) and untreated cultures (data not shown). Moreover, a significant difference in cell viability was obtained when a stable formed biofilm was treated with MBG_US_m_SiO₂/CaO or MBG_US_m_Cu2% nanoparticles (Figure 3.13C, indicated by **).

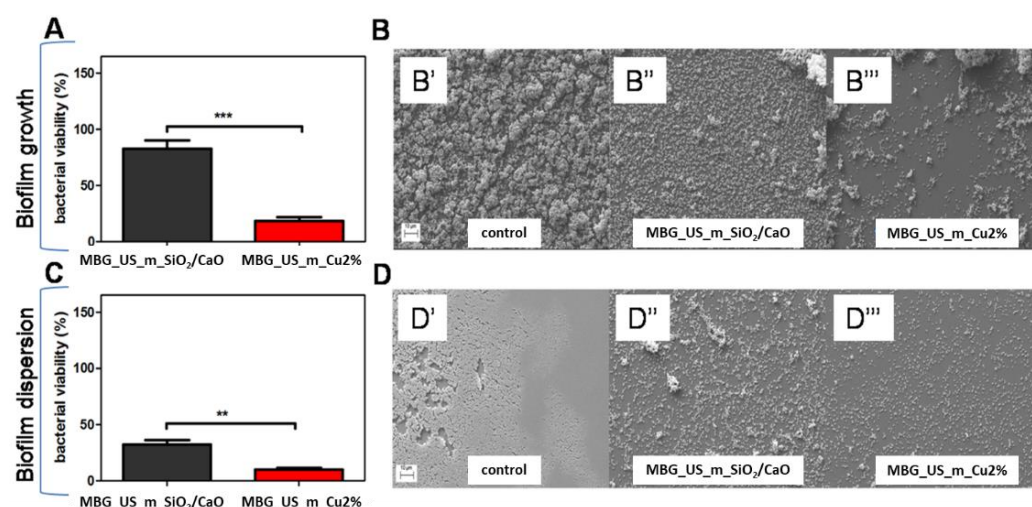


Figure 3.13: Bacterial viability and morphology of biofilms treated with MBG_US_m_SiO₂/CaO and MBG_US_m_Cu2% suspensions (2 mg/mL): effect on *S. epidermidis* RP62A biofilm formation cultures (A, B) and effect on the formation of a stable staphylococcal biofilm (C, D)

Conversely, these effects were less marked in the presence of only copper containing extracts (released by nanoparticles) when incubated during the biofilm formation (Figure 3.14A) or on the pre-formed biofilms (Figure 3.14C). Furthermore, in order to visualize the biofilms morphology after these treatments, SEM studies were carried out. As expected, large cellular aggregates were observed in the biofilms produced by *S. epidermidis* RP62A in all samples used as control (Figure 3.13B and D; Figure 3.14B and D). Conversely, the presence of nanoparticles during *S. epidermidis* biofilm formation prevented and reduced the number of adherent bacteria and cluster formation, more distinctly for MBG_US_m_Cu2% nanoparticles (Figure 13B’’). The addition of MBG_US_m_Cu2% suspension to an already formed staphylococcal biofilm, promoted a visible dispersion of biofilm aggregates (Figure 13D’’’) whereas the contact with MBG_US_m_SiO₂/CaO suspension produced a less noticeable influence on the biofilm morphology. Similar results were observed for biofilm growing cultures (Figure 14B’’’) or for formed biofilms (Figure 14D’’’) incubated with MBG_US_m_Cu2% extracts, although the bacterial reduction was less evident in comparison to biofilms treated with MBG_US_m_Cu2% suspensions.

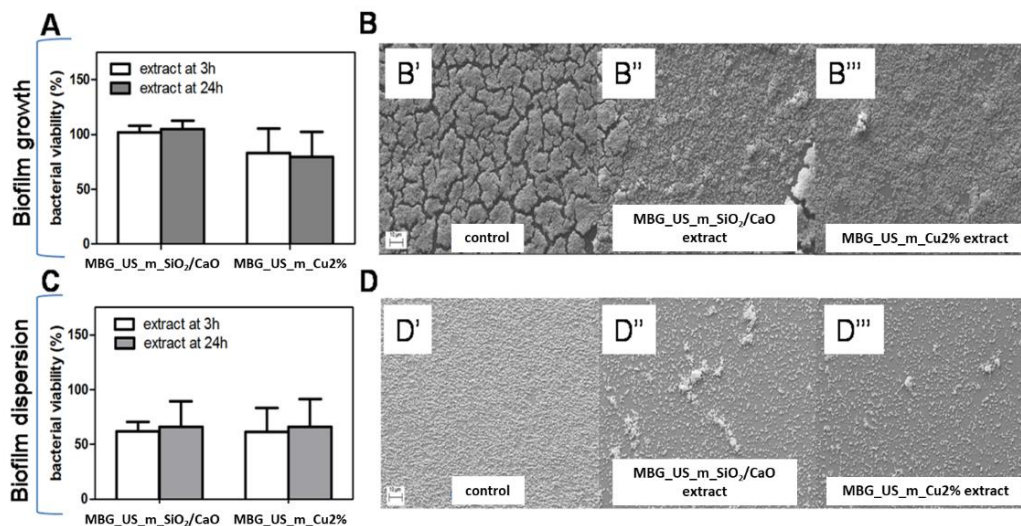


Figure 3.14: Bacterial viability and morphology of biofilms treated with extracts of MBG_US_m_SiO₂/CaO and MBG_US_m_Cu2%: effect of undiluted supernatants collected at 24 h on *S. epidermidis* RP62A biofilm growing cultures (A, B) and on the formation of a stable staphylococcal biofilm (C, D)

3.2.1.3 Strontium-containing MBG_US_m: MBG_US_m_Sr1%

Strontium was the second investigated ion due to its role in bone metabolism. In this context, strontium is gaining increasing attention thanks to the related osteoblast stimulation activity and the osteoclast inhibition property [28].

In this work, strontium-containing MBG nano-particles were produced through methanol-based ultrasonic-assisted sol-gel route by substituting a small amount of calcium with strontium. The obtained particles (85SiO₂/14CaO/1SrO %mol, named hereafter MBG_US_m_Sr1%) were studied in their morphology,

composition, structural features, ion release and bioactive properties. The results of the Sr-modified MBGs will be useful for interpreting those of the double-ion (strontium and copper) containing system that combined in a single matrix the antibacterial and the pro-osteogenic effect (see following section 3.2.1.4).

3.2.1.3a Morphological and structural characterization of MBG_US_m_Sr1%

First of all, the morphological investigation through FE-SEM analysis was performed.

As visible in Figure 3.15, the incorporation of the Sr therapeutic ion did not alter the morphology of the particles, as already evidenced in copper-containing MBGs, which appeared slightly aggregated, with a spheroidal shape and size ranging between 130 and 180 nm.

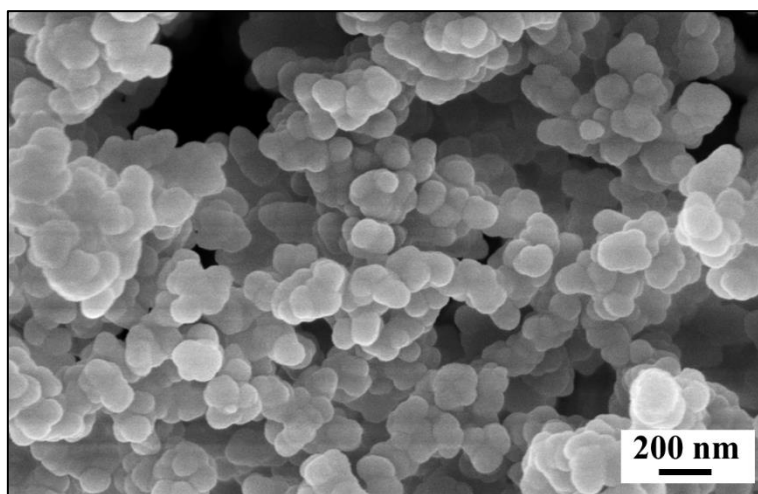


Figure 3.15: FE-SEM image of MBG_US_m_Sr1%

EDS investigation was conducted on Sr-containing powders to evaluate the chemical composition of the sample, however, due to the very close binding energy shown by Si and Sr elements, the corresponding peaks partly overlapped, and the evaluation of Sr content was unreliable (Figure 3.16).

The chromium peaks, as reported for the MBG_US_m_SiO₂/CaO, are ascribable to the coating deposited on the sample to make it conductive for the EDS investigation.

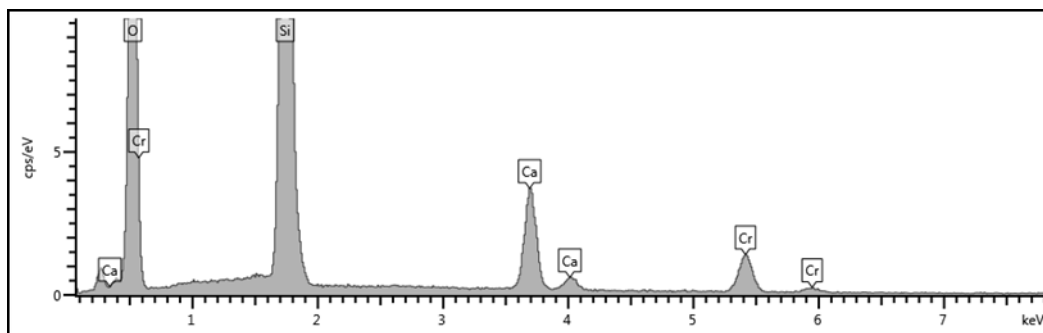


Figure 3.16: EDS spectrum of MBG_US_m_Sr1%

Hence, the incorporation of strontium was investigated by XRF spectroscopy which provided a molar ratio Sr/Si equal to 0.7 %mol, lower compared to the nominal value (1.18 %mol), highlighting a partial incorporation of the substituent ion. A similar discrepancy was reported in the literature in several strontium-containing systems [29–31] and was ascribed to the electronic properties of strontium. As the strontium ionic radius (1.16 Å) is larger than the calcium radius (0.94 Å), the strontium incorporation into the silica framework could be more difficult than the calcium one. Moreover, the lower charge density of strontium ion compared to calcium ion may determine weaker interactions between Sr²⁺ and the framework resulting in the observed lower Sr²⁺ incorporation efficiency.

The N₂ adsorption-desorption measurements were used to study the pore features. The curve in Figure 3.17 revealed a IV type isotherm associated with mesoporous structure, according to IUPAC [2]. The corresponding pore size distribution (inset graph of Figure 3.17) exhibited a narrow distribution centred in 2.5 nm. The ordered mesostructure and the high value of SSA (Table 3.5) are in agreement with SiO₂-CaO mesoporous nanoparticles obtained with the same procedure [1], further confirming that the incorporation of strontium occurred without hindering the mesoporous structure formation process.

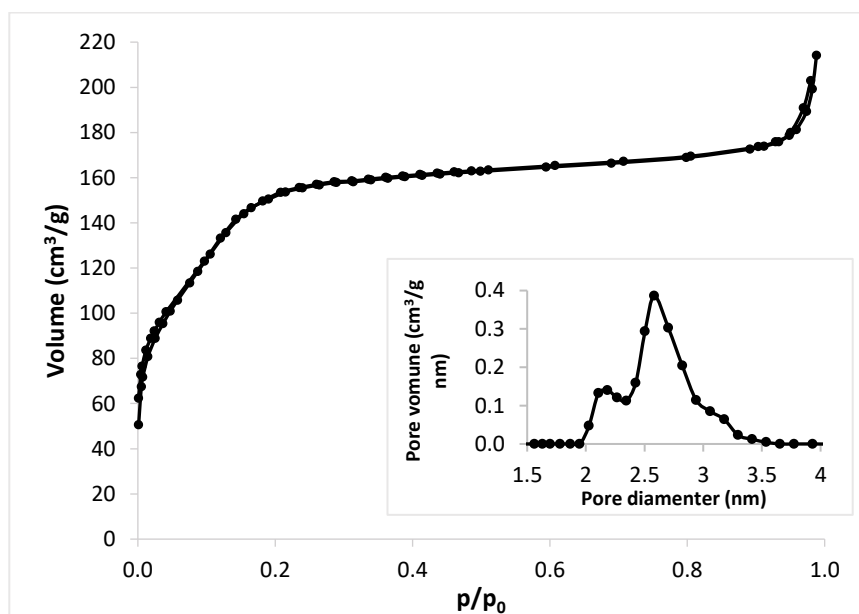


Figure 3.17: N₂ adsorption-desorption isotherm of MBG_US_m_Sr1% and related DFT pore size distribution (inset)

Table 3.5: Structural features of MBG_US_m_Sr1%

Name	Specific surface area (m ² /g)	Pore size (nm)	Volume (cm ³ /g)
MBG_US_m_Sr1%	470	2.5	0.23

3.2.1.3b Strontium ion release from MBG_US_m_Sr1% in SBF

The strontium release was tested in SBF following the procedure reported in section 2.6.1 of “Materials and methods”. The strontium release profile (Figure 3.18) showed a burst release within the first 3 h of soaking. The lower diffusion rate evidenced after 1 day of soaking was previously found in similar ion-modified systems [32,33] and it was ascribed to the partial occlusion of the mesopores caused by the dissolution of the silica framework. Other authors [34] found similar profile by studying the release from MCM-41 spheres which was attributed to the re-precipitation of the silica in the form of silica-gel at the pore entrance.

The MBG_US_m_Sr1% release trend tended to increase progressively: the released concentration after 14 days of incubation was 7 ppm and corresponded to 88% of the incorporated strontium amount, calculated by XRF analysis, suggesting the presence of a residual amount of strontium ion inside the network. Considering the curve slope at 14 days, it could be speculated that a further amount of ion might be released in a longer period.

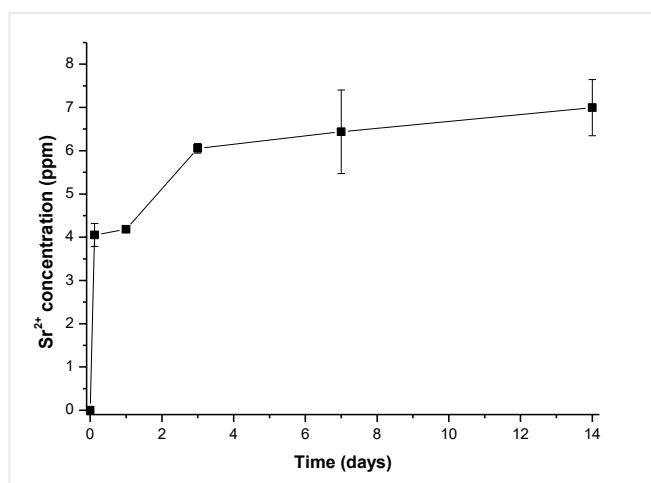


Figure 3.18: Sr²⁺ release profile of MBG_US_m_Sr1% in SBF

3.2.1.3c Bioactive behaviour of MBG_US_m_Sr1% in SBF

The bioactive behaviour of the strontium-containing mesoporous particles was analysed by soaking the sample in SBF for different time points up to 14 days. After 1 day of immersion, the particles did not show modification in their surface morphology and element composition. Needle-like structures, visible after 3 days of soaking, tended to cover all particles after 7 days (Figure 3.19). The influence of strontium on the bioactive response of glass is a controversial issue: different researches discovered that the substitution of Sr for Ca accelerated the HA deposition onto the bioactive glasses [35,36]. On the contrary, some other authors [37] found that the addition of strontium within glass composition represented an obstacle for the calcium phosphate nucleation sites, causing a delay in the hydroxyapatite precipitation rate.

In this work, the presence of strontium did not affect the bioactive response of the system whose ion exchange ability during soaking in SBF was confirmed by morphological observation.

Furthermore, from EDS measurements, the Ca/P ratio became similar to the Ca/P value characteristic of HA over the tested time. As stated in chapter “State of art”, the bioactive response of the material is composed by several surface ion exchange reactions which lead to the formation of the calcium phosphate layer [38]. According to the literature [31], the Ca/P ratio, starting from higher values during the first hours, becomes comparable to the stoichiometric value of hydroxyapatite (1.67) [5,6] over the time. In the present system, the same evidence was found: the detected Ca/P ratio, which was equal to 2.3 after 1 day of soaking, reached the value of 1.78 after 14 days of incubation in SBF.

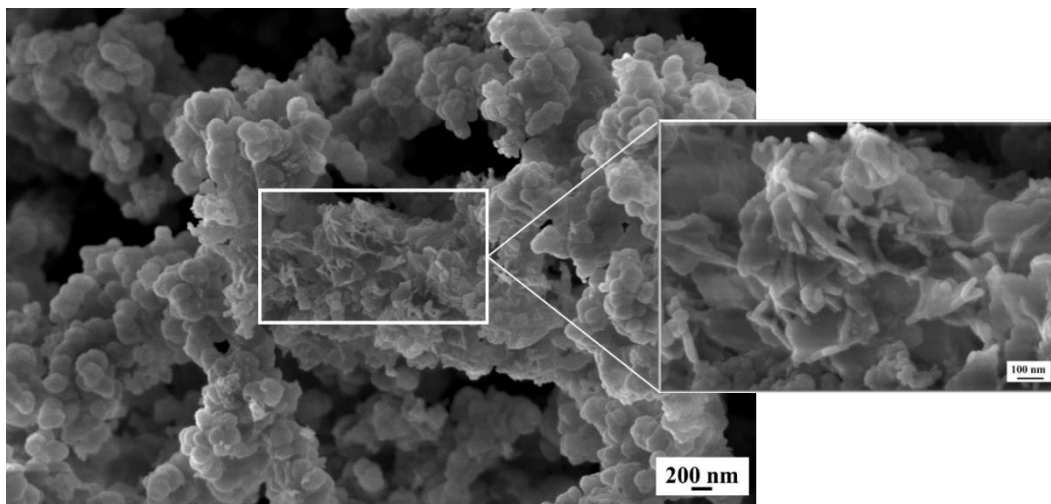


Figure 3.19: FE-SEM image of MBG_US_m_Sr1% after 7 days of soaking in SBF and its magnification

3.2.1.4 Strontium-copper co-containing MBG_US_m: MBG_US_m_CuSr2%

With the aim to obtain multifunctional biomaterials which synergistically combine the ability to promote bone formation and angiogenesis and to impart an antibacterial effect, double-ion co-substituted mesoporous bioactive particles were obtained by using strontium and copper as therapeutic species. The sample, named MBG_US_m_CuSr2%, was produced by modifying the composition as follows: 85SiO₂/13CaO/1SrO/1CuO %mol.

Part of the work described in this chapter has been already published by the candidate [33].

3.2.1.4a Morphological and structural characterization of MBG_US_m_CuSr2%

The FE-SEM analysis demonstrated that MBG_US_m_CuSr2% particles were spheroidal, slightly aggregated, with a size of about 100 nm (Figure 3.20). EDS analysis (inset of Figure 3.20) revealed a molar concentration in fair agreement with nominal ratio for what concerns copper ions, at variance with strontium, whose incorporation resulted less effective. However, as already reported for MBG_US_m_Sr1%, the EDS technique does not provide reliable results on the incorporated Sr amount, due to the overlapping of Sr and Si peaks and the relatively low amount of the strontium species.

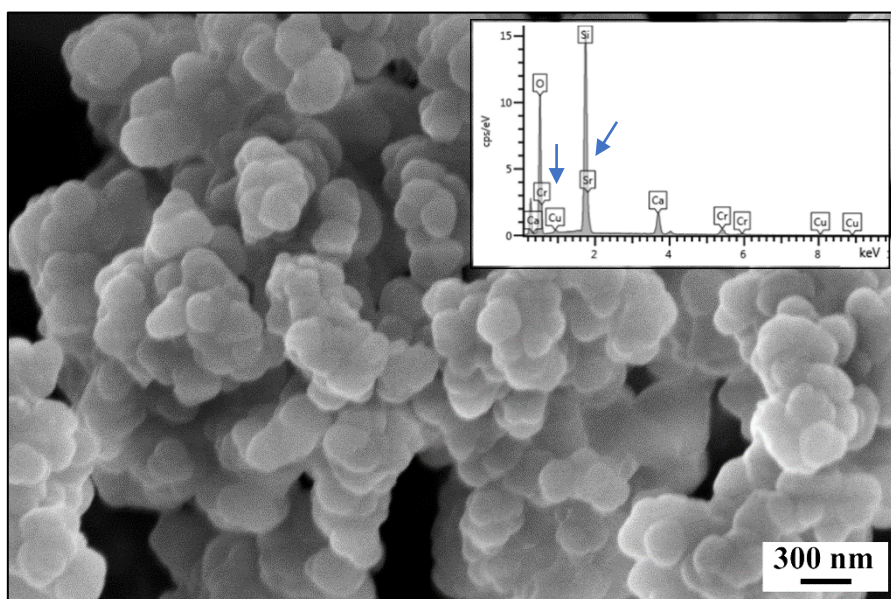


Figure 3.20: FE-SEM image of MBG_US_m_CuSr2% and related EDS spectrum (inset)

In this regard, a different compositional investigation was deemed necessary. Hence, the amount of incorporated ion was evaluated by dissolving the powder in a mixture of nitric and hydrofluoric acids (0.5 mL of HNO₃ and 2 mL of HF for 10 mg of powder) and the resulting solutions were analysed via ICP analysis, as described in the section 2.5.2 of “Materials and methods” chapter.

As already evidenced by EDS data, almost the 100% of copper added during the synthesis was incorporated within the glass network. The strontium loading, instead, corresponded to 50% of the amount added during the synthesis procedure. As reported above for MBG_US_m_Sr1% sample, the reason can be related to the slightly higher ionic radius and the lower charge/ionic radius (charge density) of Sr²⁺ compared to those of Ca²⁺, which account for the lower Sr²⁺ incorporation, as found in other works [30,39]. On the contrary, it can be speculated that the lower ionic radius of Cu²⁺ (0.71 Å) respect to that of Ca²⁺ allows the observed total incorporation of copper.

N₂ adsorption-desorption measurements showed IV type isotherm (Figure 3.21), confirming the mesoporous structure of the sample. MBG_US_m_CuSr2% curve exhibited a well-defined step between 0.1 and 0.2 p/p₀, indicative of the filling

of regular mesopores. The data reported in Table 3.6 highlighted that the ion co-substitution did not significantly affect the structural properties of the final powder that resulted only slightly different from Sr- or Cu-containing MBGs [8,30]. The DFT pore size distribution, reported in the inset of Figure 3.21, evidenced a narrow distribution around 2.6 nm, which is the same value of the one found in Sr- and Cu-containing sample.

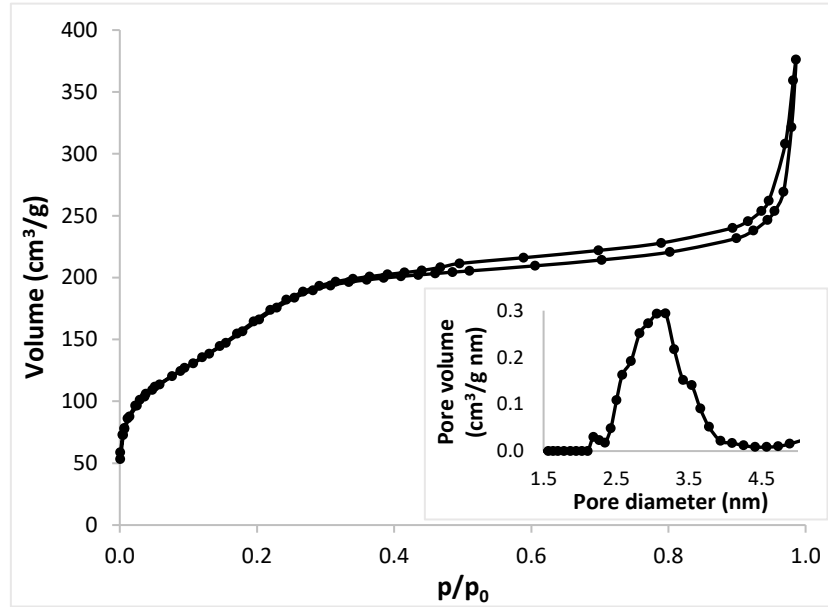


Figure 3.21: N_2 adsorption-desorption isotherm of MBG_US_m_CuSr2% and related DFT pore size distribution of (inset)

Table 3.6: Structural features of MBG_US_m_CuSr2%

Name	Specific surface area (m^2/g)	Pore size (nm)	Volume (cm^3/g)
MBG_US_m_CuSr2%	549	2.6	0.28

3.2.1.4b Strontium and copper ion release from MBG_US_m_CuSr2% in SBF

The incorporated Cu^{2+} and Sr^{2+} were successfully co-released in SBF by MBG_US_m_CuSr2% particles.

The curve profile (Figure 3.22) showed a burst release of both Cu^{2+} and Sr^{2+} ions within the first 3 h of incubation, reaching 9 and 11 ppm, respectively. After 1 day of soaking, a lower diffusion rate was observed and could be ascribed to the progressive occlusion of mesopores due to the dissolution of silica framework and its re-precipitation in the form of silica gel at the pore entrance [34]. Subsequently, after 7 days the constant release might be ascribed to the precipitation of HA (see the following section 3.2.1.4c) layer which could partially block the ion release. This aspect is more evident in the Cu^{2+} release profile than in that of Sr^{2+} , which showed higher released concentration for the entire test. This observation

suggests a higher accessibility and ion-exchange ability of Sr^{2+} within the silica framework compared to Cu^{2+} species, most likely due to its similarity with calcium as network modifier [28].

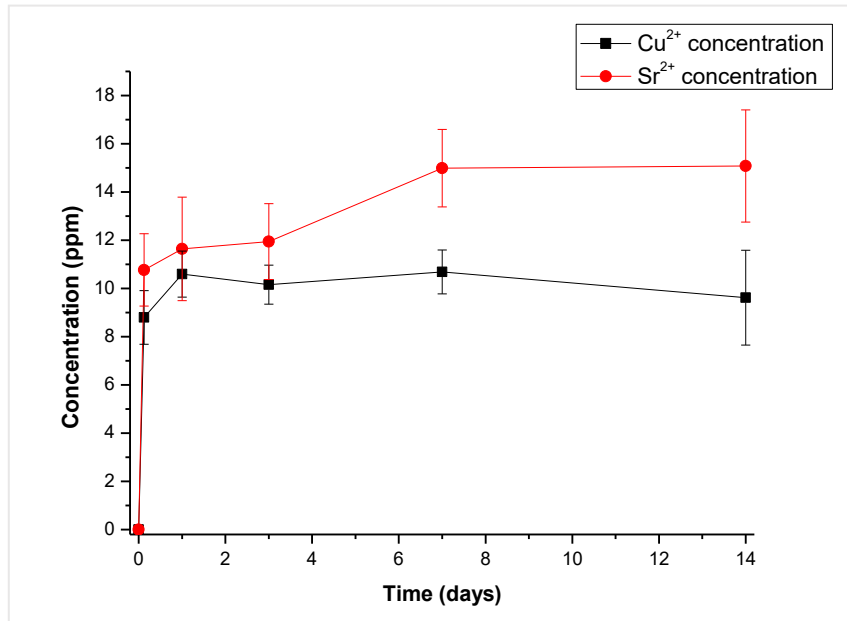


Figure 3.22: Ion release curve of MBG_US_m_CuSr2%

3.2.1.4c Bioactive behaviour of MBG_US_m_CuSr2% in SBF

In vitro bioactivity assessment highlighted that partial replacing of Ca with Cu and Sr ions did not significantly hamper the hydroxyapatite nucleation and deposition. After 1 day of soaking, the Ca/P ratio revealed by EDS analysis was 2.89 for MBG_US_m_CuSr2%. After 7 days of soaking in SBF the sample was fully covered by a layer of needle-like crystals (Figure 3.23) and the Ca/P ratio was in good accordance to the stoichiometric value of hydroxyapatite (1.67) [5,6].

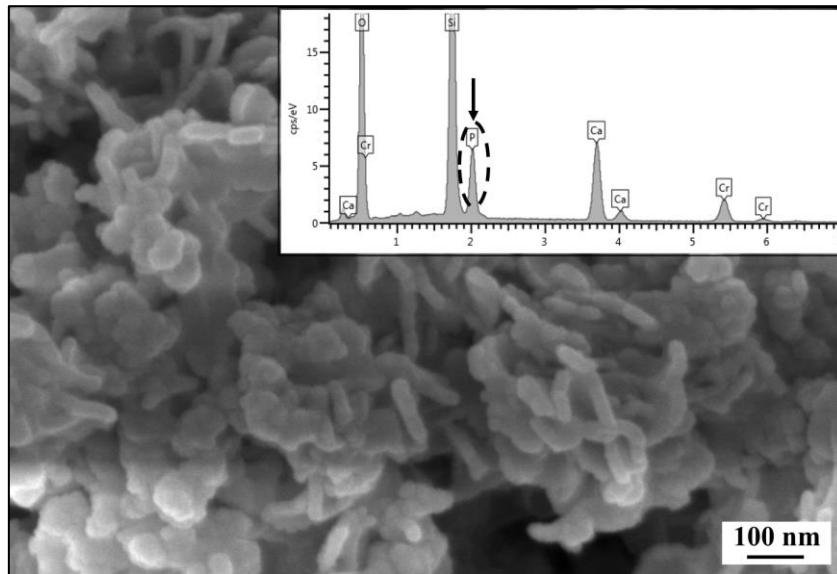


Figure 3.23: MBG_US_m_CuSr2% after 7 days of soaking in SBF with EDS spectrum (inset)

The formation of hydroxyapatite layer was also analysed by wide-angle XRD analysis. In Figure 3.24 the two spectra of MBG_US_m_CuSr2% before (Figure 3.24A) and after (Figure 3.24B) 7 days of soaking in SBF confirmed the bioactive response of the sample. In details, the spectrum of MBG_US_m_CuSr2% with the characteristic broad peak between 20° and 30° (2θ values) evidenced the amorphous structure of the sample. Figure 3.24B demonstrated the deposition of hydroxyapatite on the sample through the presence of new peaks which matched the hydroxyapatite external reference (00-001-1008).

The pH value of SBF was below 7.8 during the entire test, which is considered an optimal value for osteoblasts [40].

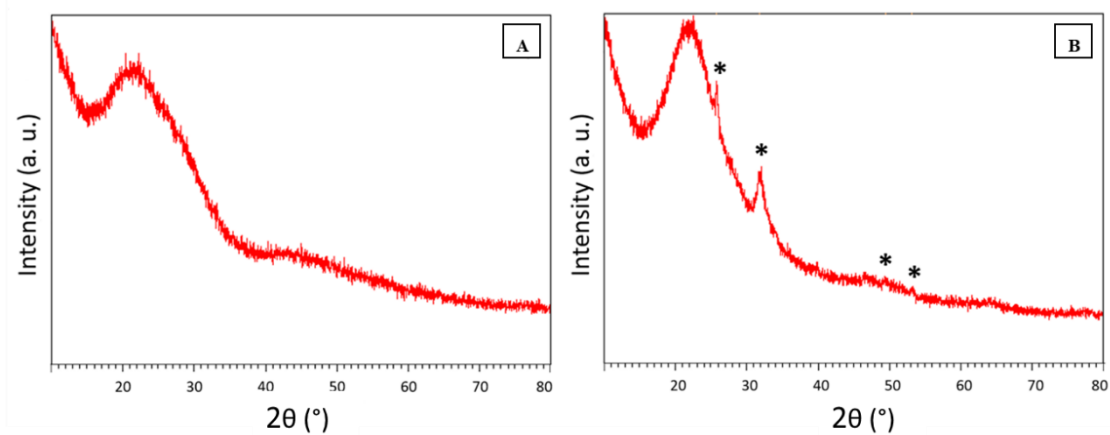


Figure 3.24: Wide-angle XRD spectra of MBG_US_m_CuSr2% before soaking in SBF(A) and MBG_US_m_CuSr2% after 7 days of soaking in SBF (B)

3.2.2 Water-based synthesis results: MBG_US_w nanomatrices

Despite the promising results in terms of morphology, composition, structural features, release and bioactive properties of the nanomatrices described in section 3.2.1 of the present chapter, alternative procedures were developed: in fact, water-based routes were considered more suitable for the ion-containing matrix up-scaling compared to the previous procedures which involved the use of a toxic solvent (methanol).

In details, two different water-based ultrasonicator-assisted synthesis were carried out in order to obtain particles in the range of 100-200 nm with pores ranging between 2 and 4 nm.

In details, the first water-based procedure, using NH_4F as catalyst, was adopted by modifying a synthesis method reported by Shi et al. [9]. The as-synthesized samples, indicated with the acronym MBG_US_w_I followed by the %mol of the substituent species, were produced by adding different types of therapeutic ion (Table 3.7). In addition, two samples, indicated with the * in Table 3.7, were obtained with the same synthesis route, without the addition of calcium, resulting in ion-containing mesoporous silica nanoparticles (MSn).

The second water-based procedure, involving the use of ammonia as catalyst, was used to produce the sample MBG_US_w_II_SiO₂/CaO by adding the ultrasonication step to a procedure already reported in the literature [41].

Table 3.7: Composition of samples produced by water-based ultrasonicator-assisted sol-gel routes

Name	Composition (%mol)
MBG_US_w_I_Cu2%	85 SiO ₂ /13 CaO/2 CuO
MSn_US_w_I_Ag2%*	98 SiO ₂ /2 AgO
MSn_US_w_I_Ce2%*	98 SiO ₂ /2 CeO
MBG_US_w_II_SiO ₂ /CaO	85 SiO ₂ /15 CaO

3.2.2.1 Copper-containing MBG_US_w_I: MBG_US_w_I_Cu2%

MBG nanoparticles were produced by adapting a water-based sol-gel procedure reported by Shi et al. [9] through the addition of CaNO_3 and the ultrasonication step during the synthesis.

As reported above, the copper was chosen in view of the obtainment of MBG matrix with antibacterial, pro-angiogenic and pro-osteogenic potential [7] for tissue applications. The sample, named hereafter MBG_US_w_I_Cu2%, was synthesized with the following molar composition: 85SiO₂/13CaO/2CuO %mol.

3.2.2.1a Morphological and structural characterization of MBG_US_w_I_Cu2%

The FE-SEM investigation (Figure 3.25) showed agglomerated particles with smaller size and irregular shape and size compared to the methanol-based samples described in section 3.2.1.

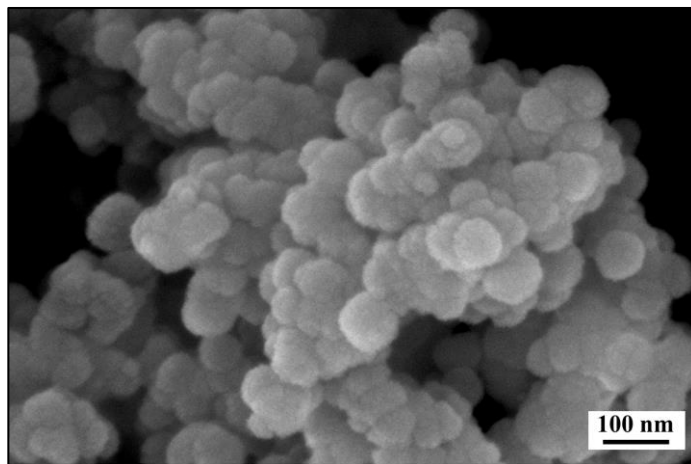


Figure 3.25: FE-SEM image of MBG_US_w_I_Cu2%

The EDS analysis (Figure 3.26) evidenced the presence of fluoride (blue arrow in Figure 3.26) on this sample ascribed to residual fluoride species of NH_4F used as catalyst during the synthesis procedure. It could be speculated that the fluoride have formed a very stable compound with elements of the framework (*e.g.* with calcium to form calcium fluoride) which remained as contaminant even after several washing steps.

In addition, the atomic percentage data, resulting from EDS characterization, showed a not uniform distribution of the calcium element: the detected Ca/Si ratio, as average of three different measurements, was three times higher than the theoretical ratio. Differently, the Cu/Si ratio was very close to the theoretical one.

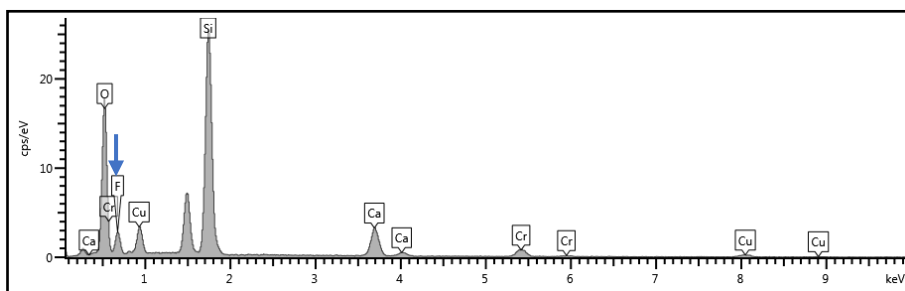


Figure 3.26: EDS spectrum of MBG_US_w_I_Cu2%

The same evidence resulted from the EDS mapping analysis coupled with STEM technique. As shown in Figure 3.27, Cu and Si elements were homogeneously distributed (blue and yellow signal, respectively). At variance, the calcium signal was not detected in the area marked in red. Calcium ions were

detected only in the area marked in blue where the powder seemed to form a disorganized phase which can be tentatively ascribed to calcium fluoride salt.

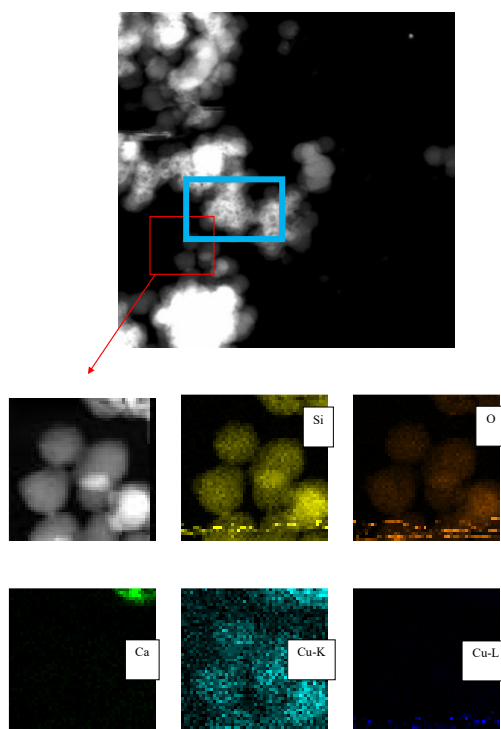


Figure 3.27: EDS mapping of MBG_US_w_I_Cu2%

The issues encountered in the calcium distribution might be attributed to the sol-gel procedure carried out at almost neutral pH (~ 6). As stated in the “State of the art” chapter, the pH is a process influencing factor during the hydrolysis and condensation sol-gel phases. In details, with the increase of pH, the hydrolysis stage proceeds slowly, while the condensation is more rapid [42]. Valliant et al. [42] conducted a study on the role of pH on the silica network formation and calcium incorporation inside the sol-gel bioactive glasses. By synthesizing sol-gel glasses from sols at different pH, they found that at pH 5.1 the gelation stage took only 30s and resulted in a more disordered network. In the present work, it might be assumed that the fast gelation stage resulted in uneven incorporation of calcium inside the MBG_US_w_I_Cu2% framework.

The mesopore structure was confirmed by N_2 adsorption-desorption measurements. The isotherm (Figure 3.28) revealed a IV type curve with a well-defined step between 0.2-0.4 p/p_0 indicative of the order of the mesostructure. The pore size distribution was centred around 4 nm (Figure 3.28-inset), bigger than the analogous mesoporous nanosphere silica system [9]. The SSA and the pore volume are reported in Table 3.8.

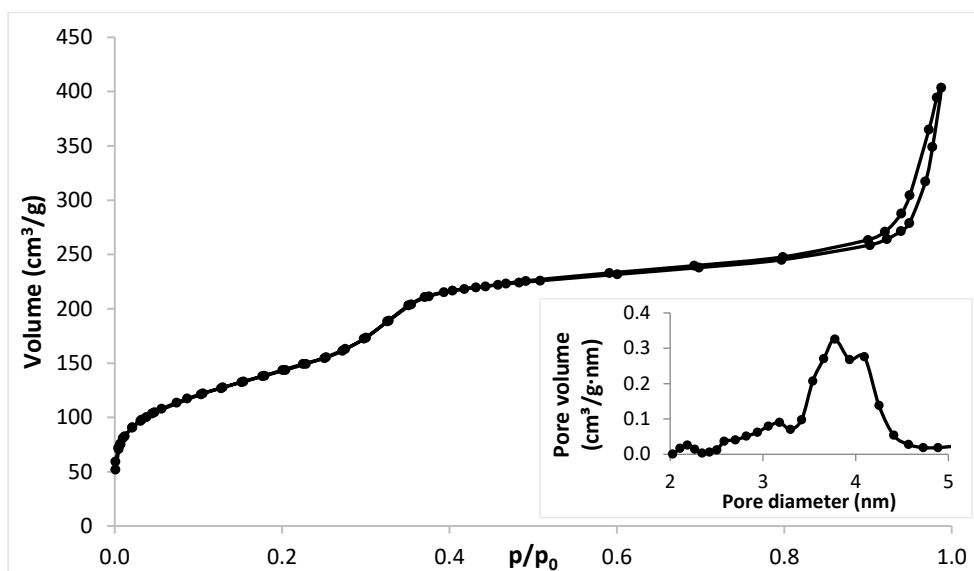


Figure 3.28: N₂ adsorption-desorption isotherm of MBG_US_w_I_Cu2% and DFT pore size distribution of MBG_US_w_I_Cu2% (inset)

Table 3.8: Structural features of MBG_US_w_I_Cu2%

Name	Specific surface area (m ² /g)	Pore size (nm)	Volume (cm ³ /g)
MBG_US_w_I_Cu2%	518	3.7 - 4	0.53

3.2.2.1b Copper ion release from MBG_US_w_I_Cu2% in DMEM

The copper release from MBG_US_w_I_Cu2% was assessed in DMEM following the procedure described in section 2.6.2 of the “Materials and methods” chapter. As stated in that chapter, the DMEM medium was selected since it represents a mimetic cell culture environment suitable for the *in vitro* biological assessment.

The release kinetics is shown in Figure 3.29. The profile evidenced a burst release within the first 3 h of incubation in DMEM, followed by a slower release kinetics. After 7 days of soaking, the released copper concentration reached the maximum of 7.8 ppm, corresponding to 40% of the theoretical incorporated amount. The partial release of copper species could be ascribed to the complex composition of DMEM solution. Other authors [9,43], in fact, speculated that the species contained in that medium may interfere with the bioactive response and the release kinetics of the sample.

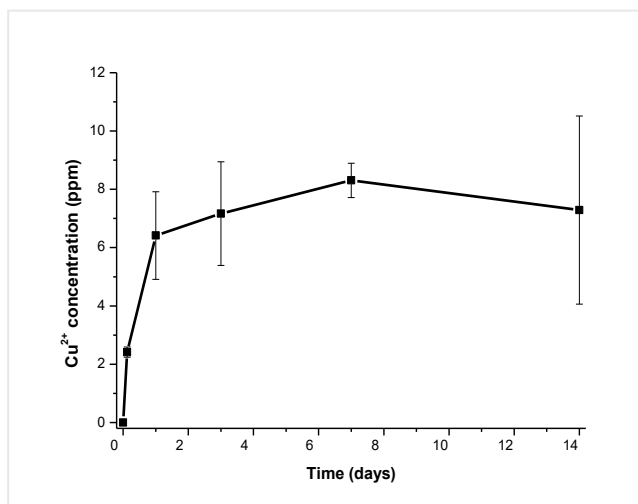


Figure 3.29: Cu^{2+} release profile of MBG_US_w_I_Cu2% in DMEM

3.2.2.2 Silver-containing MSn: MSn_US_w_I_Ag2%*

The mesoporous silicas show the same well-known advantages of the MBG (*i.e.* large surface area, high pore volume, tunable pore size, huge amount of silanol groups on the surface) [44], but they are characterized by very slow bioactive response [45]. Since the fast bioactivity is not demanded in wound healing application, silver-containing MSn (98SiO₂/2AgO %mol, named hereafter MSn_US_w_I_Ag2%*) was investigated as promising agent to be used in infected wound, due to the antibacterial effect of silver ion [46].

3.2.2.2a Morphological and structural characterization of MSn_US_w_I_Ag2%*

The FE-SEM image in Figure 3.30 showed spherical particles with size ranging from 20 to 100 nm. The rough appearance, widely visible in the FE-SEM image, was ascribed to the conductive Cr coating covering the powder. The incorporation of the therapeutic ion was confirmed by the EDS analysis (inset in Figure 3.30). Moreover, the Cu and Al peaks visible in the spectrum (blue arrows) are attributed to the copper-coated carbon grid and the stub used for the EDS investigation, respectively.

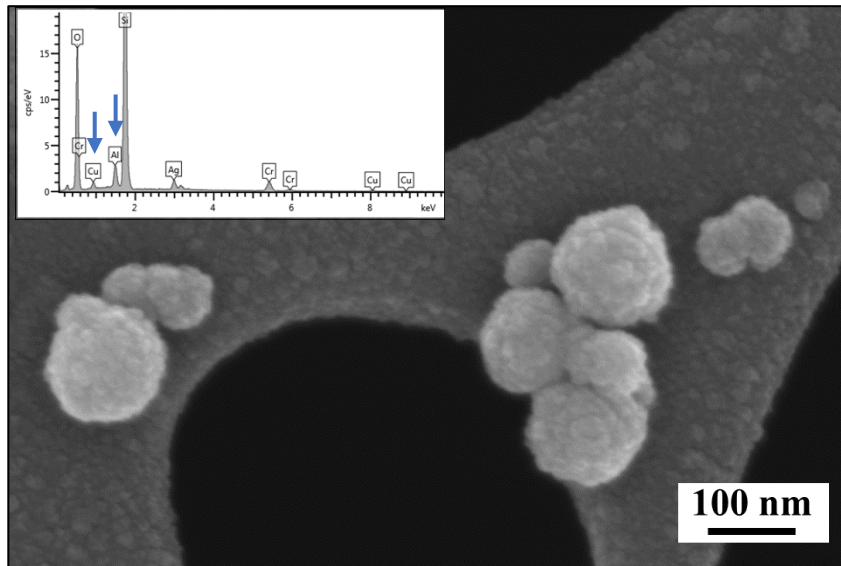


Figure 3.30: FE-SEM image of $MSn_US_w_I_Ag2\%^*$ and related EDS spectrum

The IV type isotherm (Figure 3.31) confirmed the mesoporosity of the sample, according to the IUPAC classification [2]. The lack of hysteresis is typical of mesoporous materials with pore size lower than a critical width, which, for nitrogen adsorption system at 77 K, corresponds to 4 nm [47]. Moreover, the step between 0.2 and 0.4 p/p_0 indicated the filling of uniform mesopores.

The DFT pore size distribution reported in the inset of the graph in Figure 3.31 evidenced a pore mean diameter of about 3.8 nm. The SSA and pore volume, listed in Table 3.9, were comparable to the un-doped mesoporous silica nanoparticles as reported in the literature [9].

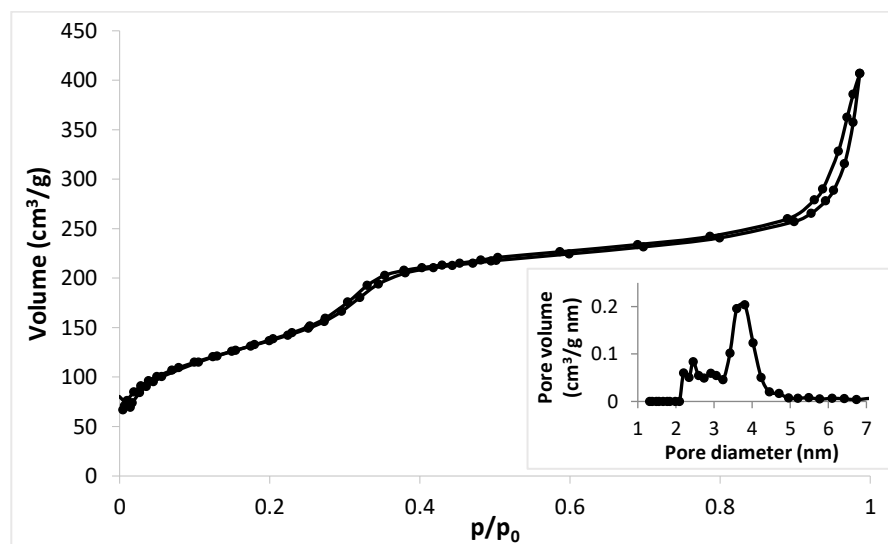


Figure 3.31: N_2 adsorption-desorption isotherm of $MSn_US_w_I_Ag2\%^*$ and related DFT pore size distribution (inset)

Table 3.9: Structural features of $MSn_US_w_I_Ag2\%^*$

Name	Specific surface area (m^2/g)	Pore size (nm)	Volume (cm^3/g)
$MSn_US_w_I_Ag2\%^*$	517	3.8	0.49

The UV-visible analysis was used to identify the oxidation states of silver species in the silica matrix.

In Figure 3.32, the UV-visible spectrum of MSn_US_w_I_Ag2%* showed the absence of peaks in the visible region, typically attributed to silver metallic particles [48]. In the ultraviolet region, the major peak at around 250 nm was assigned to $4d^{10}$ to $4d^9 5s^1$ transition of Ag^+ ions [48]. The shoulder around 300 nm can be tentatively attributed to small Ag_n^{m+} clusters [49].

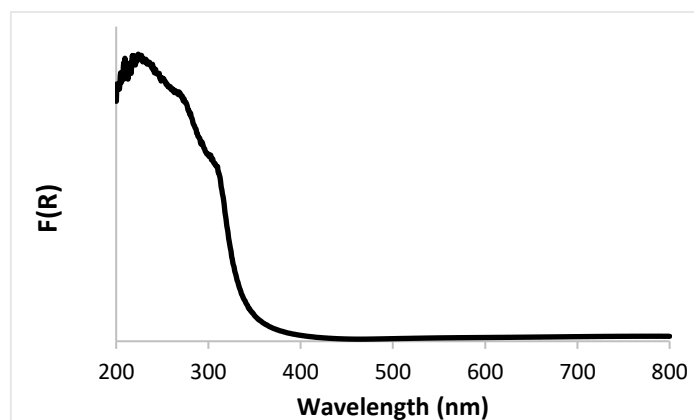


Figure 3.32: Diffuse reflectance UV-vis spectrum of MSn_US_w_I_Ag2%*

The UV-visible observations were supported by wide-angle XRD characterization. As shown in Figure 3.33, the spectrum of MSn_US_w_I_Ag2%* is characterized by the typical broad peak between 20° and 30° (2θ values) characteristic of amorphous silicas. The peaks centred in 26.74, 30.97, 44.36, 52.61, 55.08, 64.54 and 73.29° 2θ values represented the contribution of small crystalline clusters and are matched by silver bromide (external reference 01-079-0149). Probably, the bromide present in the CTAB surfactant reacted with Ag^+ ions in the synthesis medium to form AgBr clusters [50].

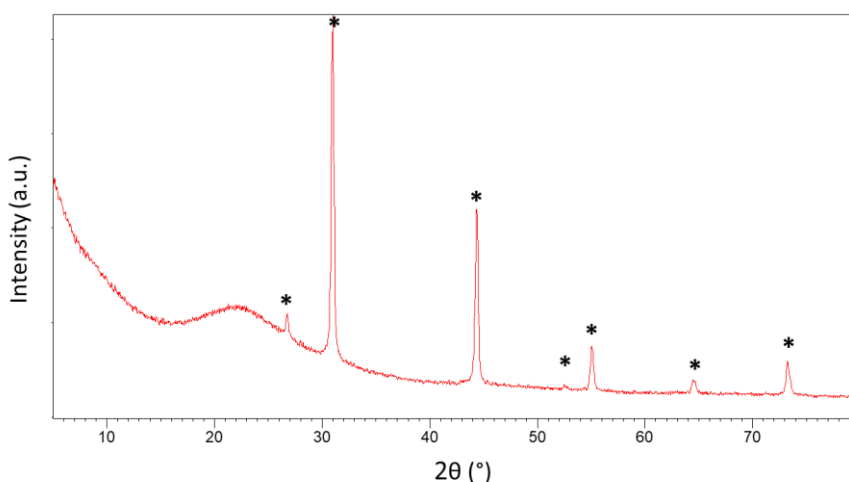


Figure 3.33: Wide-angle XRD spectrum of MSn_US_w_I_Ag2%*

3.2.2.2b Silver ion release from MSn_US_w_I_Ag2%* in DMEM

In order to assess the silver release from MSn_US_w_I_Ag2%*, the powders were soaked in DMEM following the procedure reported in section 2.6.2.

As depicted in Figure 3.34, after reaching the maximum at 3 days of soaking (equal to 3.9 ppm), the release profile curve started to decrease over the remaining time. A similar behaviour was found in other silver-containing MBG systems [51] and it was ascribed to the tendency of silver to react with chlorides present in the DMEM medium, forming insoluble AgCl salts which precipitate.

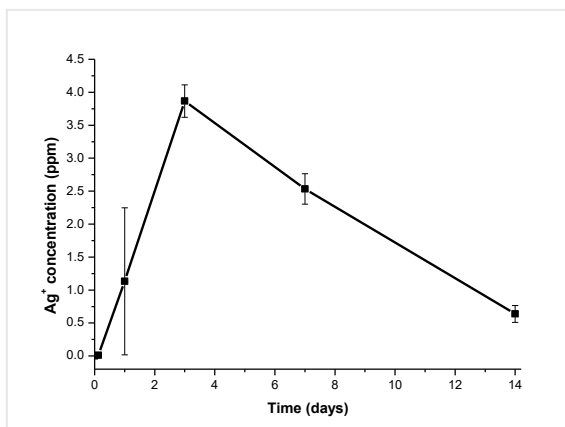


Figure 3.34: Ag⁺ release profile of MSn_US_w_I_Ag2%* in DMEM

3.2.2.3 Cerium-containing MSn_US_w_I: MSn_US_w_I_Ce2%*

By following the same water-based ultrasonicator assisted procedure, Ce-substituting nanoparticles (named hereafter MSn_US_w_I_Ce2%*) were produced with the molar composition of 98SiO₂/2CeO %mol.

This cerium-containing mesoporous silica matrix was produced pursuing the same objective of silver-containing MSn, which consisted in creating nanomatrices for wound healing application. As silver-containing samples, cerium-modifying systems are studied for the antibacterial effect imparted by cerium [52].

3.2.2.3a Morphological and structural characterization of MSn_US_w_I_Ce2%*

The morphological and compositional characterizations were performed by FE-SEM and EDS analysis.

MSn_US_w_I_Ce2%* particles were spheroidal with dimension mostly around 100 nm, as visible in Figure 3.35. EDS analysis (data not shown) confirmed the incorporation of cerium with a Ce/Si molar ratio, calculated as average of three measurements, in fair agreement with the theoretical one.

Furthermore, the EDS characterization showed the presence of fluoride peaks, as already noticed in MBG_US_w_I_Cu2%, most likely due to the NH₄F used as catalyst which remained as contaminant despite the washing steps.

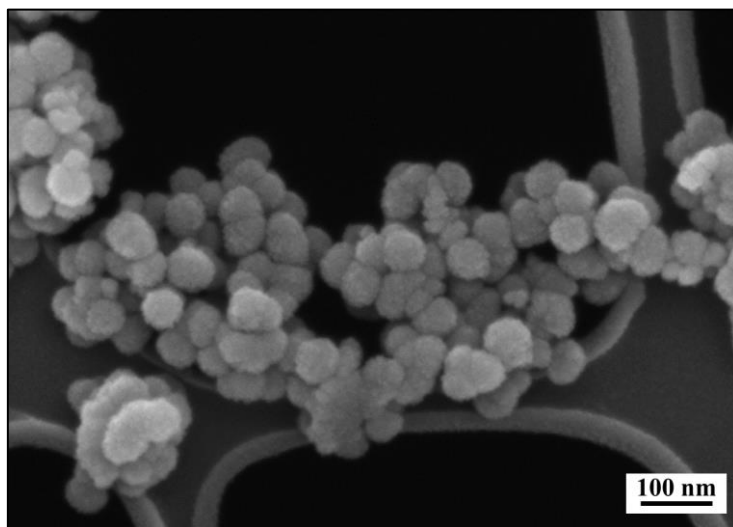


Figure 3.35 FE-SEM image of MSn_US_w_I_Ce2%*

N₂ adsorption-desorption measurements were performed on the powder in order to characterize the textural features of MSn_US_w_I_Ce2%*.

The IV type isotherm in Figure 3.36 is typical of mesoporous material with the step around 0.3 p/p₀. The capillary condensation, represented by the hysteresis loop in the multilayer range [2], is attributed to intra-particles voids. The narrow pore size distribution (inset of Figure 3.36), centred at 3.6 nm, was calculated by DFT method. The extremely high values of the SSA (763 m²/g) and pore volume (0.98 cm³/g), reported in Table 3.10, are only slightly lower respect to non-doped mesoporous silica systems [45].

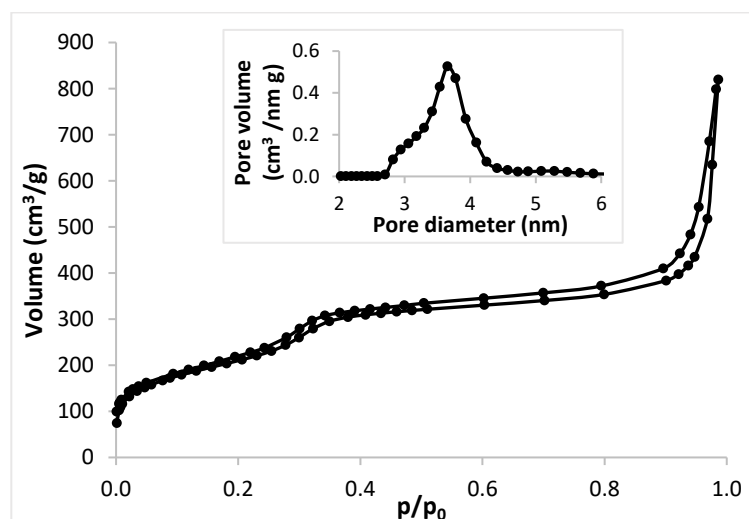


Figure 3.36: N₂ adsorption-desorption isotherm of MSn_US_w_I_Ce2%* and related DFT pore size distribution (inset)

Table 3.10: Structural features of MSn_US_w_I_Ce2%*

Name	Specific surface area (m ² /g)	Pore size (nm)	Volume (cm ³ /g)
MSn_US_w_I_Ce2%*	763	3.6	0.98

As cerium is highly sensitive to the change of oxidation state [53], UV-visible analysis was used to obtain qualitative data about the oxidation state of cerium in the MNs_US_w_I_Ce2%* and the spectrum is reported in Figure 3.37. The peak around 297 nm corresponded to Ce³⁺ inter-configurational transitions (4f to 5d) [54].

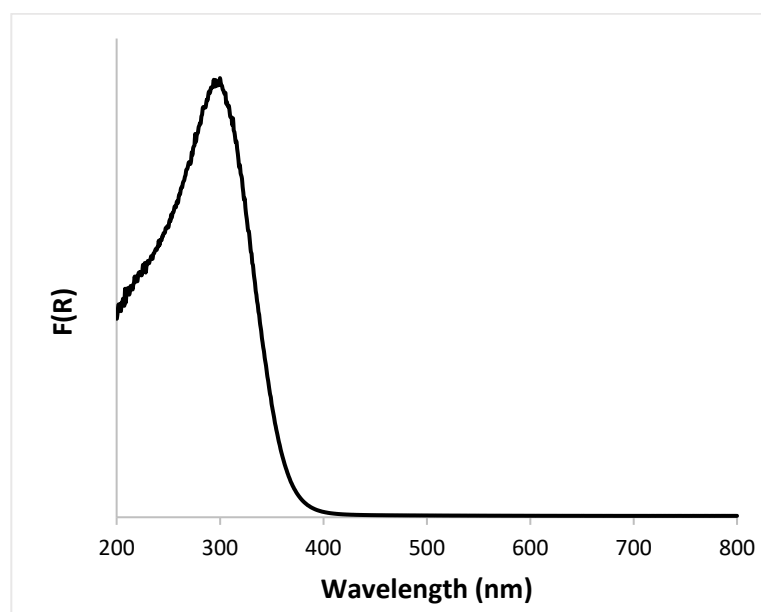


Figure 3.37: Diffuse reflectance UV-vis spectrum of MSn_US_w_I_Ce2%*

The phase composition of MSn_US_w_I_Ce2%* was analysed by wide-angle XRD technique. As visible in Figure 3.38, the presence of several peaks at 28.41, 33.02, 47.19, 56.21, 58.92, 69.19 and 76.60 2 θ degrees suggested the formation of crystalline phases within the amorphous matrix, represented by the broad peak around 20° (2 θ values). The aforesaid peaks were in agreement with the CeO₂ external reference (01-081-0792). The broadening of these peaks can be due to the nanometer size of the cerium oxide clusters [55].

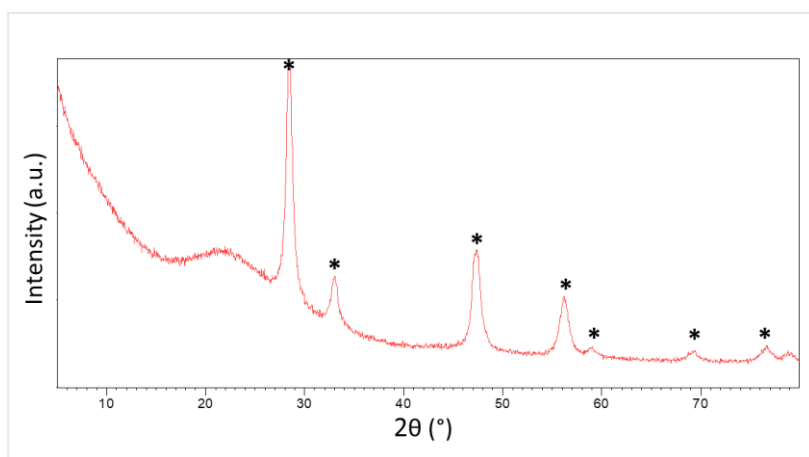


Figure 3.38: Wide-angle XRD spectrum of MSn_US_w_I_Ce2%*

3.2.2.2b Cerium ion release from MSn_US_w_I_Ce2%* in DMEM

The capability of MSn_US_w_I_Ce2%* to release cerium ions was tested in DMEM solution. As visible in Figure 3.39, the cerium released amount was almost negligible during the entire duration of the test. This reduced released amount may be related to the high stability of the formed cerium oxide clusters. In this regard, several cerium-containing MBGs with a cerium content up to 3.5 %mol demonstrated a scarce ability to release cerium ion in SBF [10], with a maximum released concentration of 0.05 ppm after 8 days of soaking.

Moreover, as already mentioned, the use of DMEM medium slowed down the dissolution process of the system causing a delay to the ion release, as previously observed in different ion-containing biomaterials [9,56].

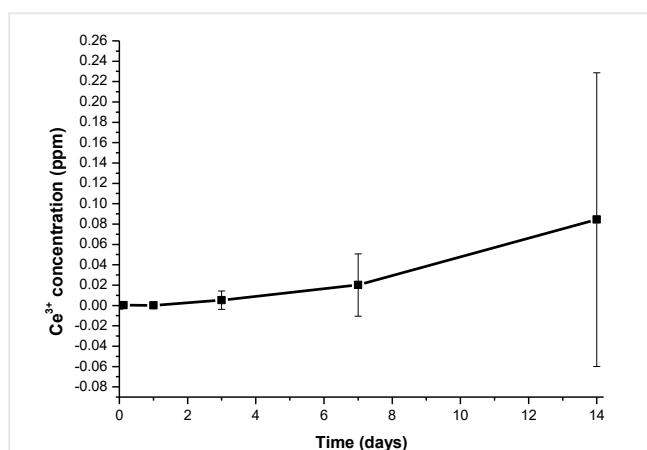


Figure 3.39: Ce³⁺ release profile of MSn_US_w_I_Ce2%* in DMEM

3.2.2.4 Un-doped MBG_US_w_II: MBG_US_w_II_SiO₂/CaO

Considering that the samples produced by the water-based ultrasonicator-assisted sol-gel route with NH₄F as catalyst showed high amount of fluorine-based contaminants, the formation of clusters and the poor release properties, an alternative different water-based route was explored.

In details, the sample with 85SiO₂/15CaO %mol molar composition, named hereafter MBG_US_w_II_SiO₂/CaO, was produced by adding the ultrasonication step to a base-catalysed sol-gel procedure already reported in the literature [41], as described in the related section in chapter 2.

3.2.2.4a Morphological and structural characterization of MBG_US_w_II_SiO₂/CaO

The as-synthesized sample was characterized in its morphology, composition and structural properties.

In Figure 3.40, the FE-SEM technique showed dispersed particles, spherical shaped with size of about 100 nm. The chemical composition, analysed by EDS (inset graph in Figure 3.40), confirmed the presence of the Si and Ca with a nominal ratio (Ca/Si=0.17) equal to the theoretical one. Moreover, the EDS analysis did not reveal the presence of contaminants. The not assigned peaks in the EDS spectrum are attributed to Cu and Al due to the copper-coated grid and aluminium stub used during the FE-SEM/EDS investigation, respectively, and the Cr peaks are ascribable to the coating layer.

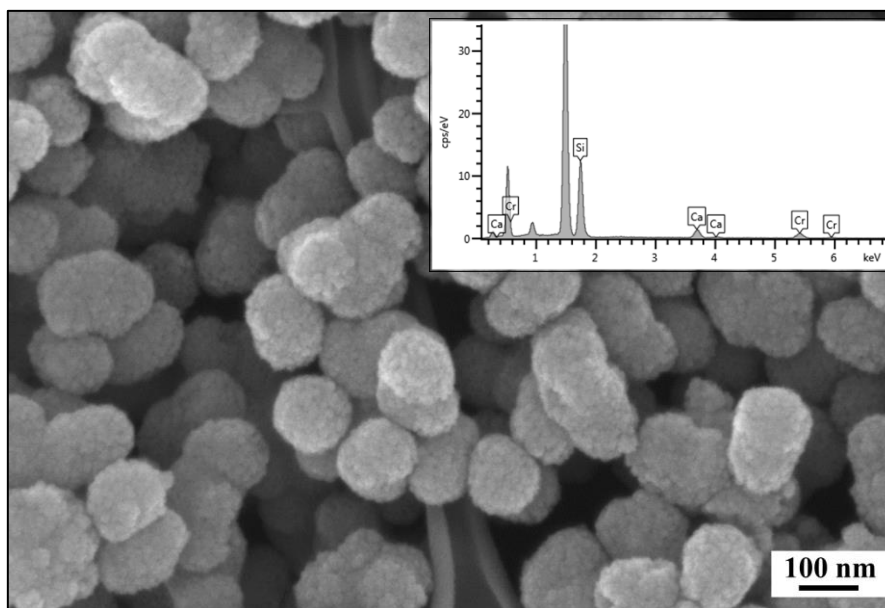


Figure 3.40: FE-SEM image of MBG_US_w_II_SiO₂/CaO and related EDS spectrum

The structural features of the sample were studied by N₂ adsorption-desorption measurements. Comparing the textural feature results (Table 3.11) with those obtained by Wu et al. [41], it seems that the use of the high frequency ultrasonication step enhanced the exposed surface area and accessible pore volume. Nevertheless, the isotherm (Figure 3.41) and the pore size distribution (inset in Figure 3.41) did not reveal the formation of an ordered mesostructure. The pore size distribution obtained through the DFT method showed a broad distribution, with diameter ranging between 3 and 11 nm.

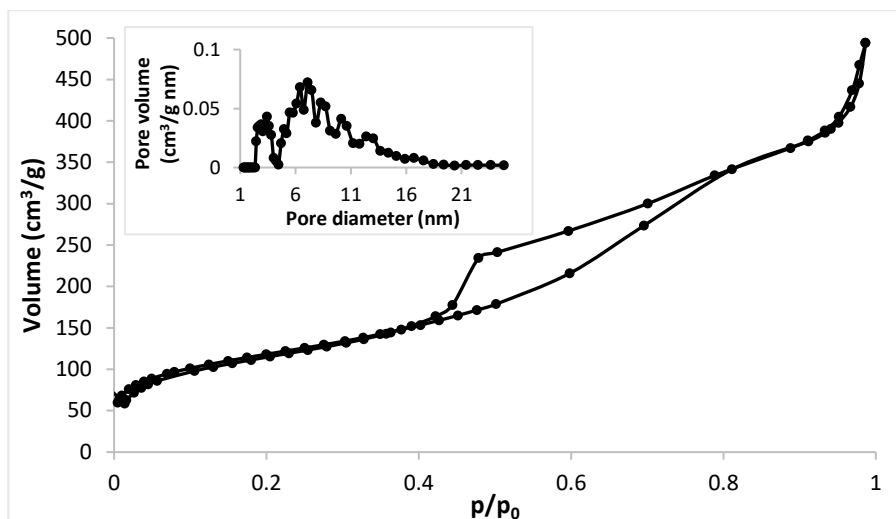


Figure 3.41: N₂ adsorption-desorption isotherm of MBG_US_w_II_SiO₂/CaO and DFT pore size distribution of MBG_US_w_II_SiO₂/CaO (inset)

Table 3.11: Structural features of MBG_US_w_II_SiO₂/CaO

Name	Specific surface area (m ² /g)	Pore size (nm)	Volume (cm ³ /g)
MBG_US_w_II_SiO ₂ /CaO	418	3-11	0.65

Hence, it is possible to speculate that the use of ultrasounds disturbed the mesophase assembly, leading to a disorganized porous structure.

As the ultrasonication step was identified as the main influencing step on the mesostructure formation and is also an energy-consuming phase, a different synthesis procedure was developed, and the related results are presented in the following section.

3.3 Morphological and structural characterization of optimized sol-gel nanomatrices

Following the aim to obtain scalable nanomatrices without using inflammable organic solvents and several synthesis steps, the selection process led to the optimization of two routes: a water-based sol-gel procedure using ammonia as catalyst to produce nano-sized MBG particles (see the following section 3.3.1) and an aerosol-assisted spray-drying approach in order to obtain micro-sized MBG spheres (see the following section 3.3.2).

3.3.1 Morphological and structural characterization of base-catalysed sol-gel nanomatrices

The nano-sized MBG particles with pores of about 4 nm were finally produced by using a base-catalysed water-based sol-gel route by incorporating different amounts and types of therapeutic ions in a SiO₂-CaO framework. Since the ultrasonication treatment (section 3.2.2.4) represented an energy-consuming step and accounted for not-fully satisfying results, the nano-sized matrices were produced by using the same sol-gel synthesis approach [41], avoiding the ultrasound step. In details, the as-synthesized samples are listed in Table 3.12.

Table 3.12: List of MBG_SG compositions

Name	Composition (%mol)
MBG_SG_Cu2%	85 SiO ₂ /13 CaO/2 CuO
MBG_SG_Ce1%	85 SiO ₂ /14 CaO/1 CeO
MBG_SG_Ce2%	85 SiO ₂ /13 CaO/2 CeO
MBG_SG_Ag0.1%	85 SiO ₂ /14.9 CaO/0.1 AgO
MBG_SG_Ag2%	85 SiO ₂ /13 CaO/2 AgO

3.3.1.1 Copper-containing MBG_SG: MBG_SG_Cu2%

In addition to the antibacterial property, the therapeutic potential of copper is also related to the induction of a pro-angiogenic and pro-osteogenic effect, which make copper a promising agent in wound and bone healing applications [7].

In this section, the results concerning the copper-containing nano-sized particles (85SiO₂/13CaO/2CuO %mol, named hereafter MBG_SG_Cu2%) are shown.

Part of the work described in this chapter has been previously published in [32].

3.3.1.1a Morphological and structural characterization of MBG_SG_Cu2%

FE-SEM image of MBG_SG_Cu2% (Figure 3.42A) showed particles with a uniform spherical morphology, with size ranging between 150 and 200 nm. EDS mapping analysis revealed a homogeneous distribution of silicon (yellow) and calcium (red) throughout the analysed particles (Figure 3.42B), at variance the analysis of copper was not reliable due to presence of the element in the sample holder. EDS spectrum of the powder dispersed on carbon tape (Figure 3.42C) confirmed the incorporation of copper inside the framework, with a Cu/Si molar ratio, as average of three measurements, in fair agreement with the nominal ratio.

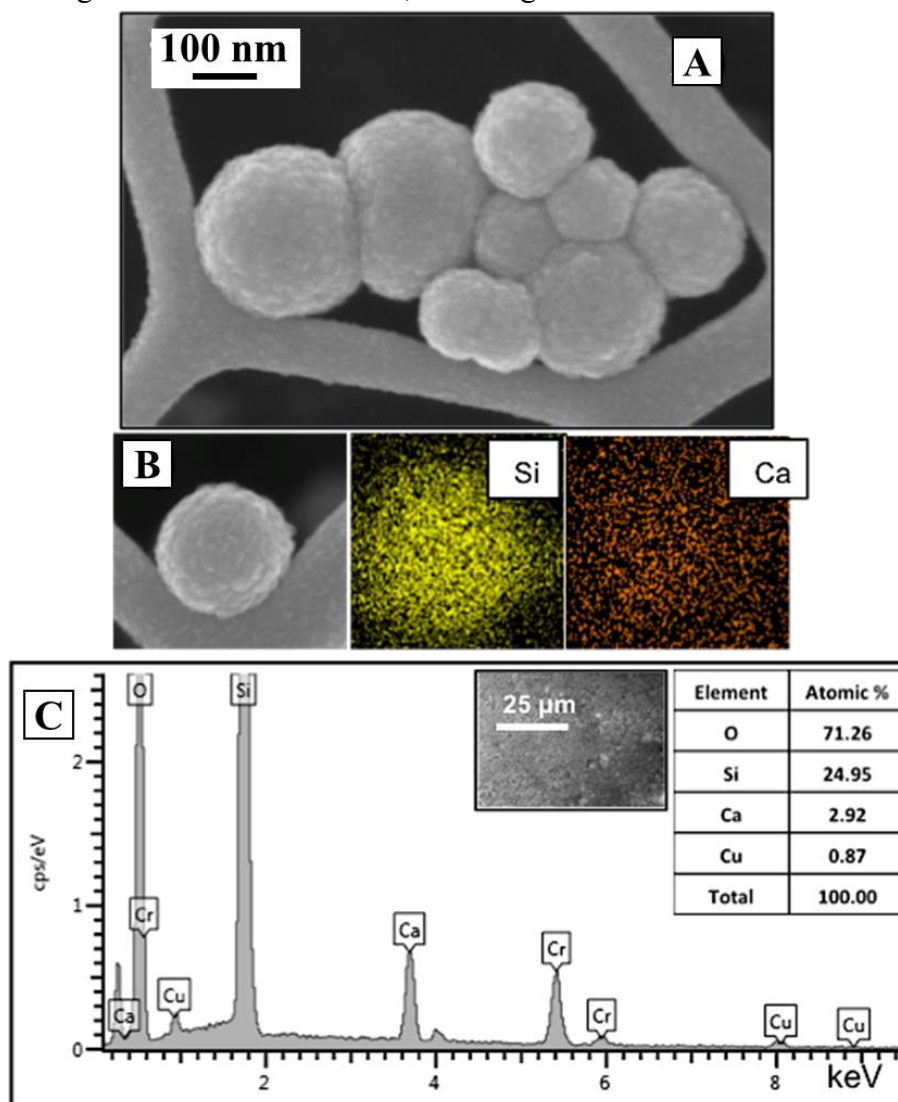


Figure 3.42: FE-SEM image of MBG_SG_Cu2% (A), EDS mapping analysis of MBG_SG_Cu2% single particle (B), EDS spectrum of MBG_SG_Cu2% (C)

Wide-angle XRD (Figure 3.43) confirmed that copper did not form segregated oxide clusters after calcination treatment, as assessed by the absence of crystalline oxide-based phases.

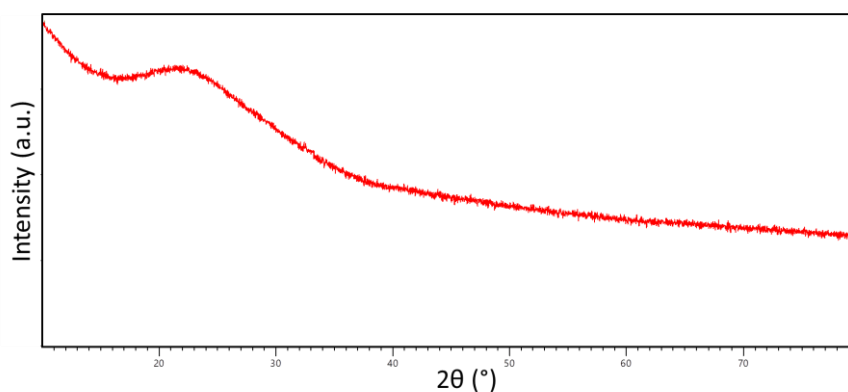


Figure 3.43: Wide-angle XRD spectrum of MBG_SG_Cu2%

The N₂ adsorption-desorption isotherm confirmed the mesoporous structure (Figure 3.44): the type IV isotherm curve showed a well-defined step around 0.4 (p/p₀), indicative of the filling of uniform mesopores. Related DFT pore size distribution (inset in Figure 3.44) confirmed the presence of uniform mesopores with a mean diameter centred at around 4 nm. The BET SSA and pore volume (reported in Table 3.13) resulted remarkably high, slightly lower than those reported for similar systems without copper [1].

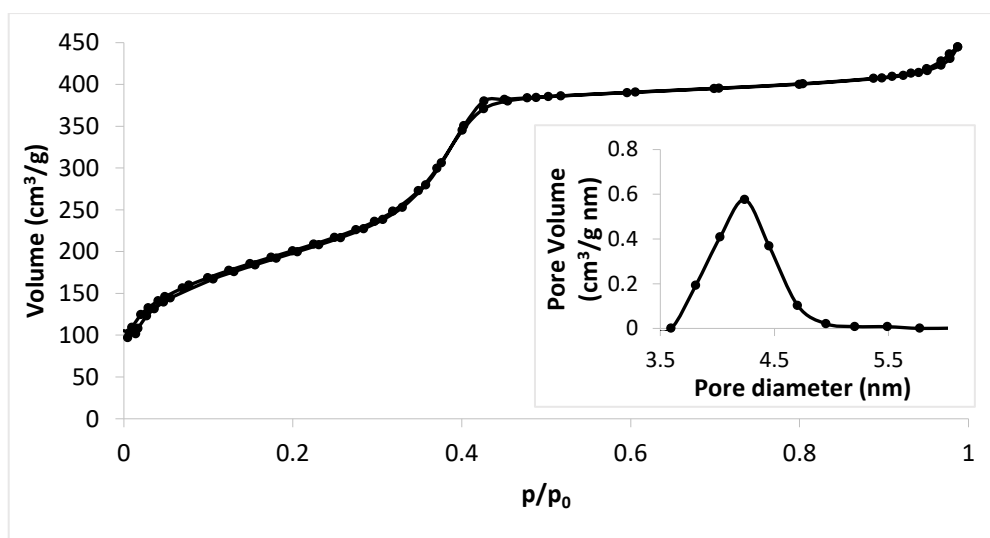


Figure 3.44: N₂ adsorption-desorption isotherm of MBG_SG_Cu2% and related DFT pore size distribution (inset)

Table 3.13: Structural features of MBG_SG_Cu2%

Name	Specific surface area (m ² /g)	Pore size (nm)	Volume (cm ³ /g)
MBG_SG_Cu2%	740	4	0.65

3.3.1.1b Copper ion release from MBG_SG_Cu2% in Tris HCl

The ionic concentration (ppm) of Cu^{2+} species from MBG_SG_Cu2% powder in Tris HCl medium is reported in Figure 3.45: almost the total amount of incorporated copper was released within the first 3 h of incubation with a final released concentration of about 4.7 ppm. After the first hours of soaking, the copper released concentration remained constant till the end of the test (14 days).

The slightly decreasing trend after 3 days of soaking could be ascribed to the deposition of HA (see section 3.3.1.1c) which partially bothers the Cu^{2+} release.

The fast ion release kinetics of MBG_SG_Cu2% can be ascribed to the remarkably high surface area and the small particle size (short diffusion paths), which allow fast ion diffusion inside the porous structure.

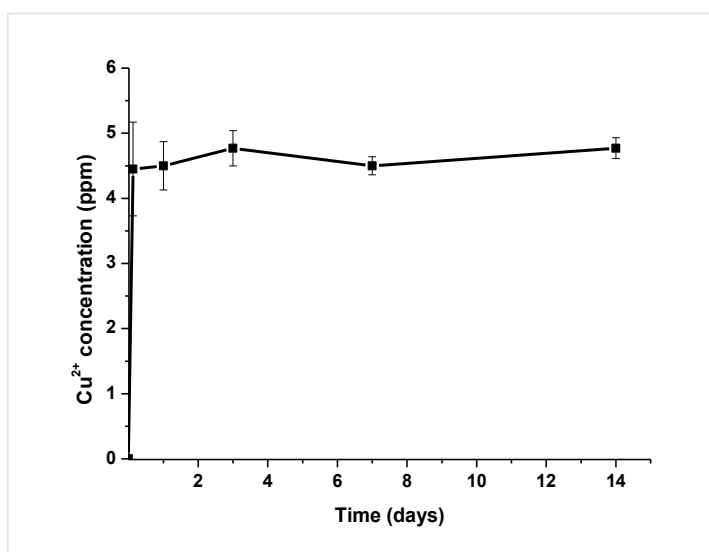


Figure 3.45: Cu^{2+} release curve of MBG_SG_Cu2% in Tris HCl

3.3.1.1c Bioactive behaviour of MBG_SG_Cu2% in SBF

The bioactive response of the MBG_SG_Cu2% was tested by soaking the particles in SBF up to 14 days.

New HA crystals appeared after 3 days of soaking, making the particle surface rough, which confirms the rapid bioactive response of the sample for Cu-containing systems. After 7 days of soaking (Figure 3.46), the deposition of HA became even more extended.

From EDS investigation, new peak, ascribed to phosphorous, appeared, further suggesting the deposition of HA.

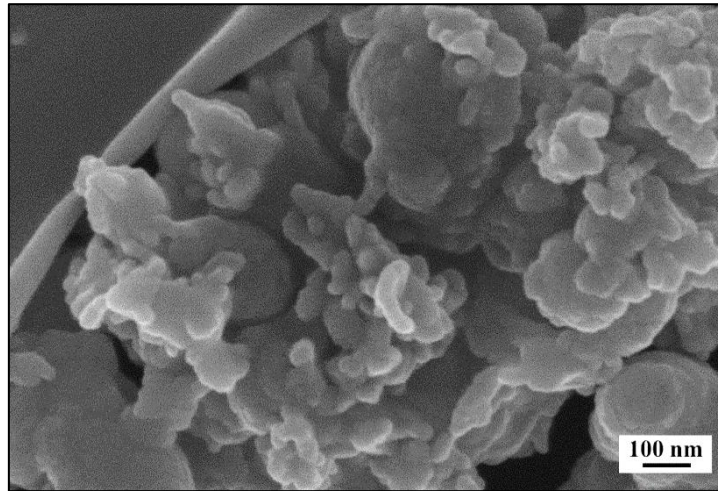


Figure 3.46: FE-SEM image of MBG_SG_Cu2% after 7 days of soaking in SBF

Based on the wide-angle XRD analysis, a further confirmation of the formation of HA cluster was provided. The pattern obtained by analysing the powder after 7 days of soaking (Figure 3.47) showed the presence of new peaks at 25.84, 29.32 and 32.13 2θ degrees that matched those of HA (external reference 01-086-0740).

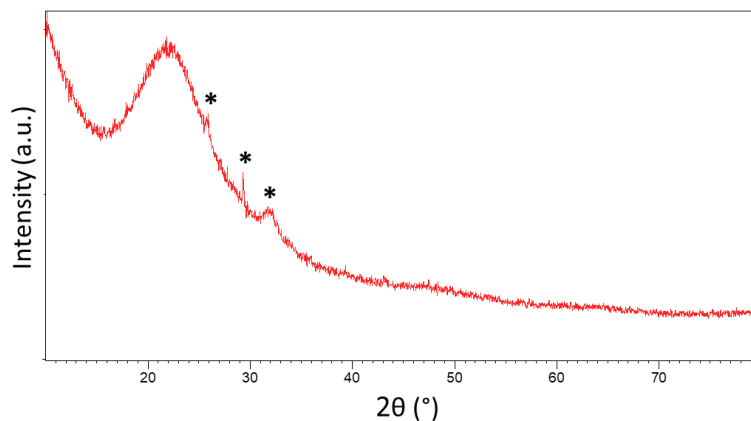


Figure 3.47: Wide-angle XRD of MBG_SG_Cu2% after 7 days of soaking in SBF

3.3.1.2 Cerium-containing MBG_SG: MBG_SG_Ce1% and MBG_SG_Ce2%

Two different cerium-containing nanomatrices were produced by adding different amounts of cerium precursor during synthesis [41], in order to analyse the effects of substituting small amounts (1 or 2 %mol) of cerium to the MBG particles. The as-produced samples are called MBG_SG_Ce1% (with composition 85SiO₂/14CaO/1CeO %mol) and MBG_SG_Ce2% (with composition 85SiO₂/13CaO/2CeO %mol). The cerium was used as therapeutic ion due to the pro-osteogenic and antibacterial properties, as described in chapter 1 [57].

3.2.1.2a Morphological and structural characterization of cerium-containing MBG_SG samples

Both cerium-containing samples were analysed in their morphology, composition and structural property.

Figure 3.48 depicts the FE-SEM images of both samples. The incorporation of different amounts of cerium did not affect the spherical morphology of both samples. For what concerns the size, the diameter of the particles was in the range of 100 nm in MBG_SG_Ce1% particles (Figure 3.48A), slightly bigger than MBG_SG_Ce2% spheres (Figure 3.48B).

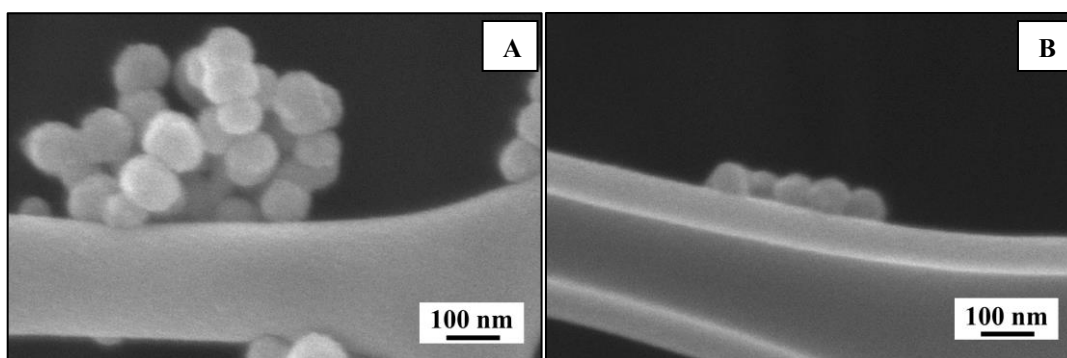


Figure 3.48: FE-SEM images of MBG_SG_Ce1% (A) and MBG_SG_Ce2% (B)

The elemental composition of the samples was investigated by EDS analysis. The EDS spectra (data not shown) confirmed the incorporation of the therapeutic ion. Nevertheless, the analysis showed an uneven distribution of the substituent element, especially for the sample with the highest concentration.

In addition, the increase of cerium content corresponded to a partial deterioration of the mesoporous structure order, as assessed by N₂ adsorption-desorption measurements. Both samples showed a IV type isotherm (Figure 3.49A and 3.49B), typical of mesoporous material [2]. Nevertheless, the MBG_SG_Ce2% hysteresis loop in Figure 3.49B indicated a broad pore size distribution confirmed also by Figure 3.49D. Whilst, the MBG_SG_Ce1% particles showed a single-mode pore size distribution centred at 4 nm, as shown in Figure 3.49C. In MBG_SG_Ce2%, the contribution of the pore family with size centred around 2 nm is higher respect the one of MBG_SG_Ce1%, suggesting the formation of microporosity with the increase of Ce amount.

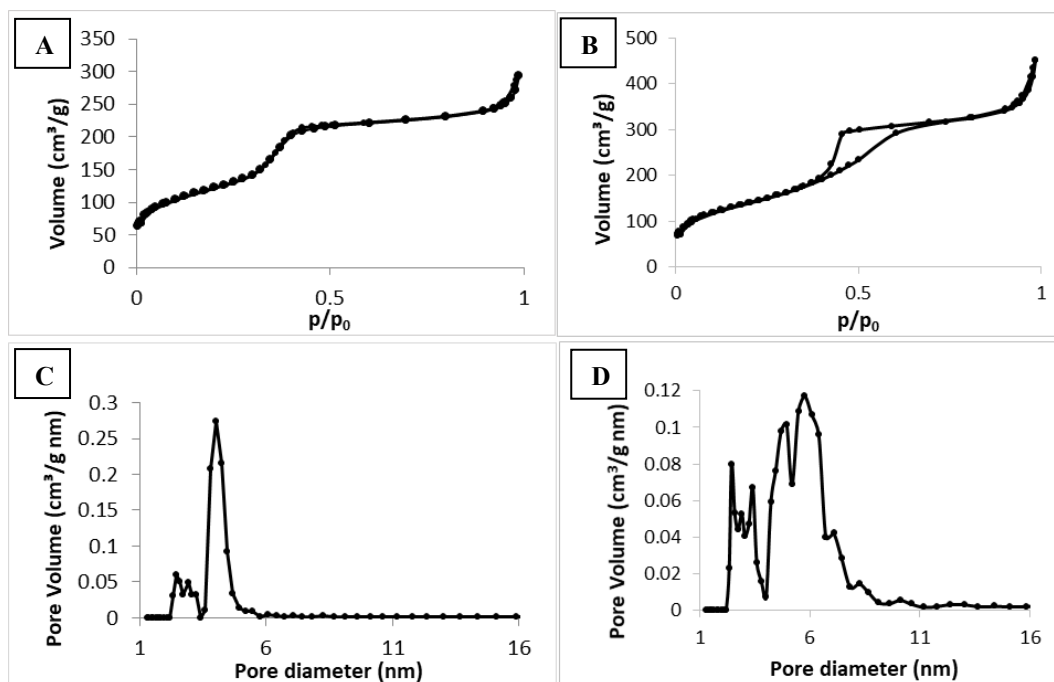


Figure 3.49: N_2 adsorption-desorption isotherm of MBG_SG_Ce1% (A) and MBG_SG_Ce2% (B); DFT pore size distribution of MBG_SG_Ce1% (C) and MBG_SG_Ce2% (D)

The structural parameters are reported in Table 3.14. The values of specific surface area and the pore volume are slightly bigger in MBG_SG_Ce2% compared to the sample with lower amount of cerium. This behaviour can be ascribed to the above mentioned microporosity and the smaller size of MBG_SG_Ce2% particles compared to MBG_SG_Ce1% ones, as already found in cerium-substituted hydroxyapatite nanoparticles [58].

Table 3.14: Structural features of cerium-containing of MBG_SG

Name	Specific surface area (m^2/g)	Pore size (nm)	Volume (cm^3/g)
MBG_SG_Ce1%	440	4	0.39
MBG_SG_Ce2%	505	2-6	0.58

Based on wide-angle XRD spectra of both samples (data not shown), the introduction of cerium in two different concentrations did not induce the formation of crystalline phases. The characteristic peak of silica-based between 20° and 30° (2θ values) was evidenced.

3.3.1.2b Cerium ion release from cerium-containing MBG_SG samples in Tris HCl

The ionic concentration of Ce^{3+} species released by both cerium-containing MBG nanoparticles is reported in Figure 3.50.

MBG_SG_Ce1% curve (Figure 3.50A) showed an increase in the released amount till 3 days of soaking in Tris HCl, followed by a plateau until the end of the test (14 days). On the other hand, the Ce^{3+} released from MBG_SG_Ce2% (Figure 3.50B) was almost negligible overtime. This behaviour was already evidenced in literature by several authors [59,60] who found that the increase in cerium content in different types of bioactive glasses was reflected in an improved chemical stability and in a delay in the degradation process. Furthermore, Salinas et al. [10] demonstrated that the cerium concentration released in the medium from the analysed MBGs was very low, irrespective of the amount of cerium added (up to 3.5 %mol.).

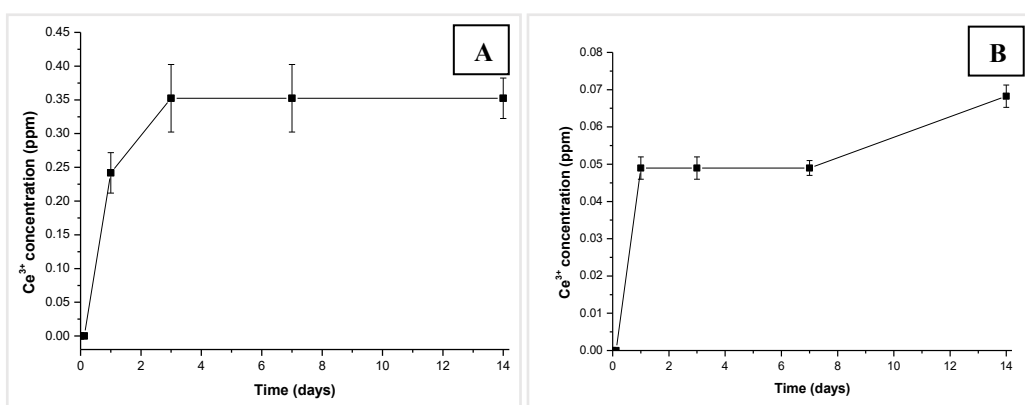


Figure 3.50: Ce^{3+} release profiles of MBG_SG_Ce1% (A) and MBG_SG_Ce2% (B)

3.3.1.2c Bioactive behaviour of cerium-containing MBG_SG samples in SBF

The bioactive response of cerium-containing samples was tested by soaking powders in SBF for different times, up to 14 days. The FE-SEM and EDS investigations (data not shown) were not significantly different from those before soaking. Moreover, the wide-angle XRD diagrams at 14 days of incubation did not present the typical peaks of HA.

The poor bioactive response was noticed in other cerium-containing glasses [59,60] which demonstrated to be covered by crystalline HA only after 30 days of soaking in SBF. This behaviour was ascribed to the higher chemical stability due to the presence of cerium which resulted in a lower ion exchange ability and dissolution degree of the framework.

3.3.1.3 Silver-containing MBG_SG: MBG_SG_Ag0.1% and MBG_SG_Ag2%

Silver-containing nano-sized particles were produced by water-based sol-gel route using ammonia as catalyst, by adding two different amounts of $AgNO_3$ during the synthesis reported by Wu et al. [41]. As stated above, silver was selected with the aim to impart an antimicrobial effect [46]. The choice of the molar concentration (listed in Table 3.15) was due to the known cytotoxicity of silver ions [61].

Table 3.15: Silver-containing MBG_SG nanoparticles

Name	Composition (%mol)
MBG_SG_Ag0.1%	85 SiO ₂ /14.9 CaO/0.1 AgO
MBG_SG_Ag2%	85 SiO ₂ /13 CaO/2 AgO

3.3.1.3a Morphological and structural characterization of silver-containing MBG_SG samples

As evidenced by FE-SEM investigations (Figure 3.51), the perfect rounded nano-spheres were not influenced in their morphology by the introduction of AgNO₃ during the synthesis. By increasing the amount of the substituent, the particles became bigger, but always in the range of hundreds of nanometres (around 150 nm and 100 nm for MBG_SG_Ag0.1% particles and for MBG_SG_Ag2% spheres, respectively).

The EDS spectrum of MBG_SG_Ag0.1% (data not shown) did not present the peaks corresponding to the silver element likely for the low amount of silver which is below the detection range of the EDS equipment.

As far as MBG_SG_Ag2% is concerned, the EDS element analysis (data not shown) showed the incorporation of silver.

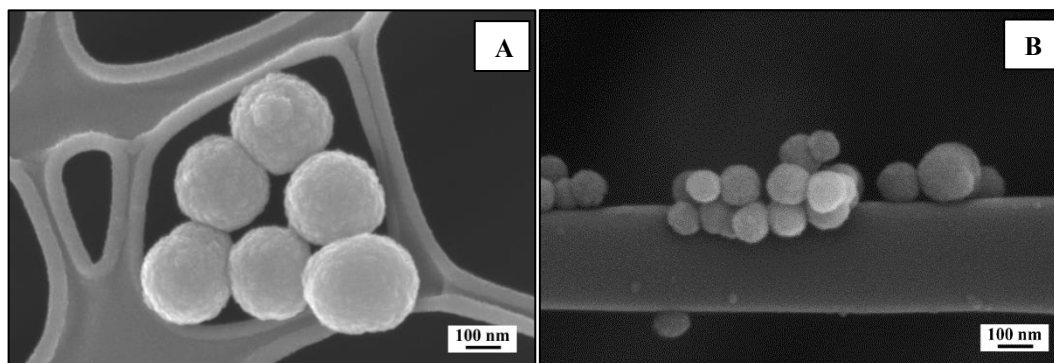


Figure 3.51: FE-SEM images of MBG_SG_Ag0.1% (A) and MBG_SG_Ag2%

The textural features of the silver-containing samples were evaluated by N₂ adsorption-desorption measurements. The surface area values, calculated by the BET equation, decreased with the increase of the silver amount (Table 3.16), confirming previous data found in the literature for different ion substituents [10]. In spite this slight decrease, the mesoporous structures were confirmed for both samples by the IV type isotherm (Figure 3.52A and B) and the narrow pore size distributions centred at 4.2 nm (Figure 3.52C and D).

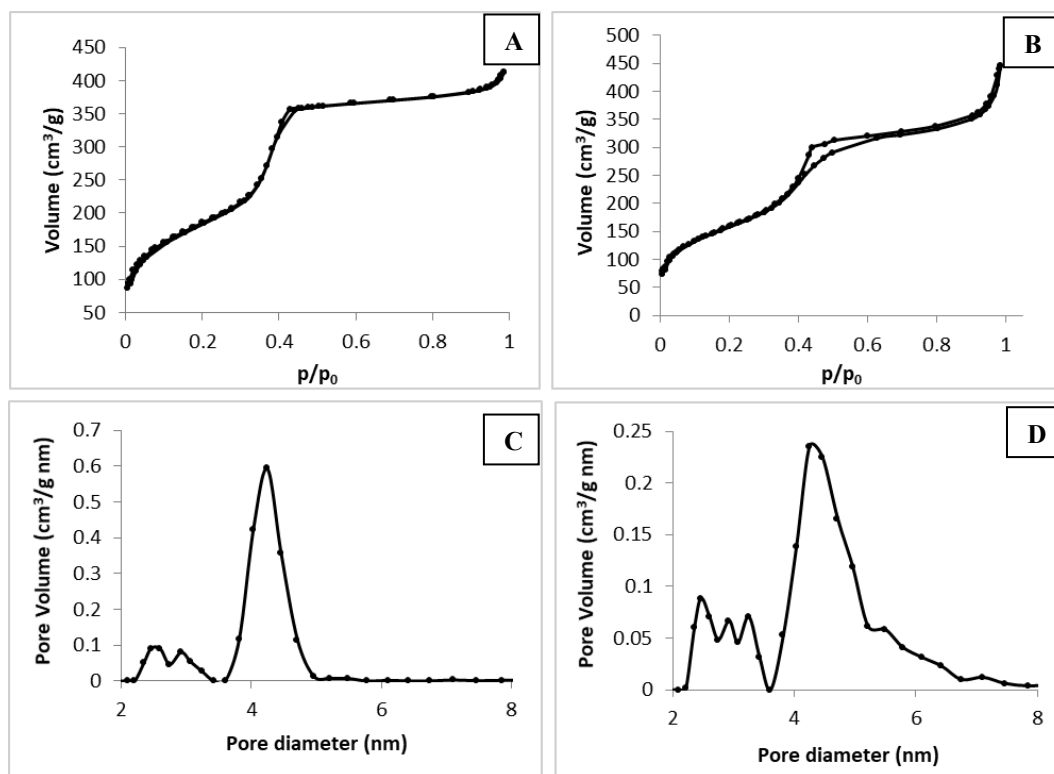


Figure 3.52: N_2 adsorption-desorption isotherm of MBG_SG_Ag0.1% (A) and MBG_SG_Ag2% (B); DFT pore size distribution of MBG_SG_Ag0.1% (C) and MBG_SG_Ag2% (D)

Table 3.16: Structural features of silver-containing MBG_SG

Name	Specific surface area (m^2/g)	Pore size (nm)	Volume (cm^3/g)
MBG_SG_Ag0.1%	674	4.2	0.6
MBG_SG_Ag2%	577	4.2	0.6

Wide-angle XRD patterns revealed, besides the broad reflection typical of amorphous silica-based systems, several peaks, which, based on reference 01-079-0149, are referred to silver bromide clusters resulting from the reaction between the bromide present in CTAB surfactant and the $AgNO_3$.

Since in MBG_SG_Ag2% pattern (Figure 3.53B) the AgBr peaks are more evident over the amorphous alone respect those in MBG_SG_Ag0.1% diffractogram (Figure 3.53A), it is reasonable to state that the silver in MBG_SG_Ag2% formed higher amount of crystalline clusters compared to the ones in MBG_SG_Ag0.1%.

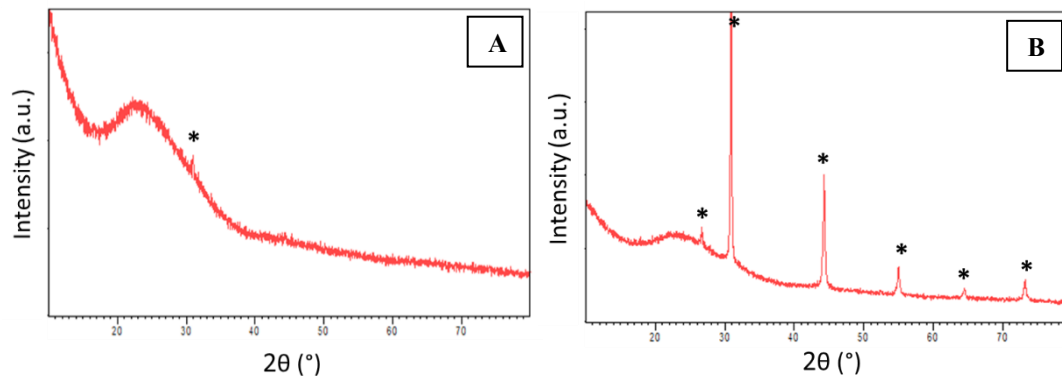


Figure 3.53: Wide-angle XRD spectrum of MBG_SG_Ag0.1% (A) and MBG_SG_Ag2% (B)

3.3.1.3b Silver ion release from silver-containing MBG_SG samples in Tris HCl

The silver release of the nanoparticles was assessed in Tris HCl following the procedure described in section 2.6.3.

MBG_SG_Ag0.1% (Figure 3.54A) showed a sharply increase in the silver released concentration during the first day of soaking followed by a very slow release until the end of the test.

In Figure 3.54B, the release kinetics of MBG_SG_Ag2% is shown. The profile curve evidenced a sustained release of silver ions within 14 days. Furthermore, the slope of the curve after 14 days suggested the capability of the nanoparticles to release a further amount of silver ions. Similar trend was already found in the literature with analogous systems [62].

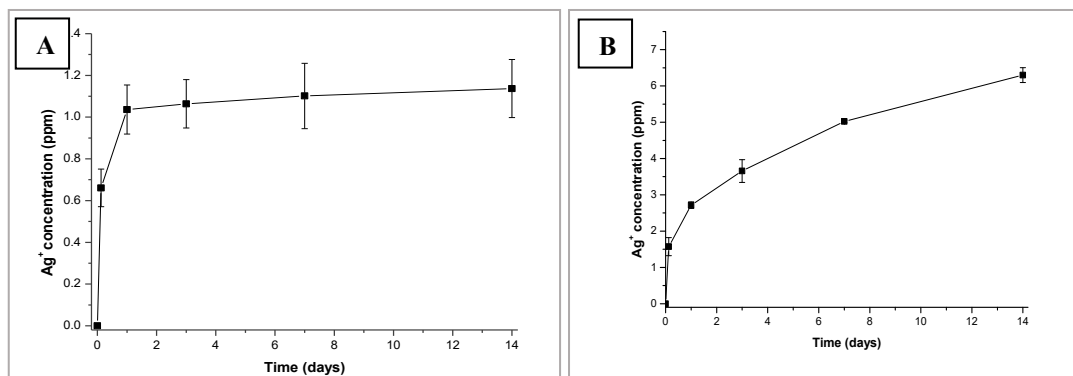


Figure 3.54: Silver ion release from MBG_SG_Ag0.1% (A) and from MBG_SG_Ag2% (B)

3.3.2 Morphological and structural characterization of aerosol-assisted spray-drying nanomatrices

In this section the results related to micro-sized MBGs produced by an aerosol-assisted spray-drying approach are reported. As stated in the “Thesis goals” chapter, one of the key points of the present work was the optimization of a potentially scalable manufacturing approach for MBG preparation. To this aim, a water-based spray-drying procedure carried out under mild acidic conditions represents a very promising solution due to its scalability and automatization in an industrial environment. Several ion-containing MBGs were synthesized and are listed in Table 3.17. Moreover, a mesoporous SiO₂-CaO binary glass system without substituting ion (as reference sample) was produced by following the procedure already reported by Pontiroli et al. [63]. In addition, two mesoporous silica micro-sized (MSm) particles were produced by following the same procedure, without the addition of the calcium precursor.

Table 3.17: List of MBG_SD compositions

Name	Composition (%mol)
MBG_SD_SiO ₂ /CaO	85 SiO ₂ /15 CaO
MBG_SD_Cu2%	85 SiO ₂ /13 CaO/2 CuO
MBG_SD_Sr1%	85 SiO ₂ /14 CaO/1 SrO
MBG_SD_CuSr2%	85 SiO ₂ /13 CaO/1 CuO/1 SrO
MBG_SD_Ce1%	85 SiO ₂ /14 CaO/1 CeO
MBG_SD_Ce2%	85 SiO ₂ /13 CaO/2 CeO
MBG_SD_Ag0.1%	85 SiO ₂ /14.9 CaO/0.1 AgO
MBG_SD_Ag2%	85 SiO ₂ /13 CaO/2 AgO
MSm_SD_Ce2%*	98 SiO ₂ /2 CeO
MSm_SD_Ag2%*	98 SiO ₂ /2 AgO

3.3.2.1 Un-doped MBG_SD: MBG_SD_SiO₂/CaO

Before the ion incorporation, micro-sized particles without ions (85SiO₂/15CaO, named hereafter MBG_SD_SiO₂/CaO) were produced by spray-drying approach through the replication of the procedure reported in [63].

3.3.2.1a Morphological and structural characterization of MBG_SD_SiO₂/CaO

The main results of MBG_SD_SiO₂/CaO regarding its morphology, composition and structural features are summarized in this section.

The FE-SEM image (Figure 3.55) of MBG_SD_SiO₂/CaO showed particles with spherical morphology, mostly ranging between 500 nm and 5 μm. The chemical composition analysed by EDS (data not shown) confirmed the presence of silica and calcium, with a Ca/Si ratio corresponding to the theoretical one.

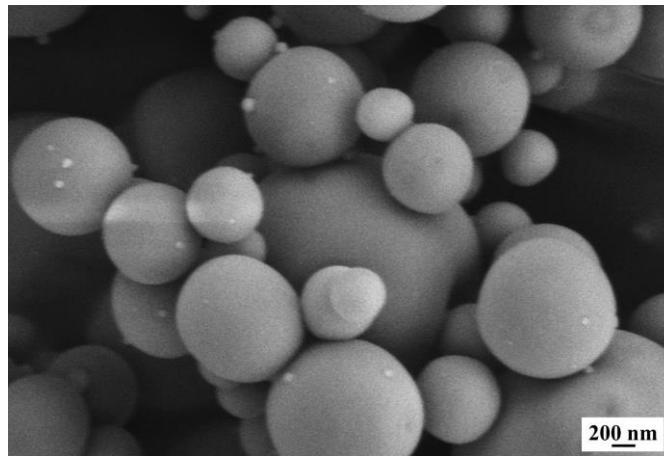


Figure 3.55: FE-SEM image of MBG_SD_SiO₂/CaO

Nitrogen adsorption-desorption measurements on MBG_SD_SiO₂/CaO revealed the mesoporous structure of the sample. The isotherm reported in Figure 3.56 is a IV type curve with a hysteresis loop characteristic of mesoporous material with regular pores bigger than 4 nm [2]. In Table 3.18 the corresponding textural features of the samples are summarized. The BET SSA and pore volume are in fair agreement with the similar system [63]. The pore size distribution calculated by DFT method and centred at 8 nm is reported as insert in Figure 3.56.

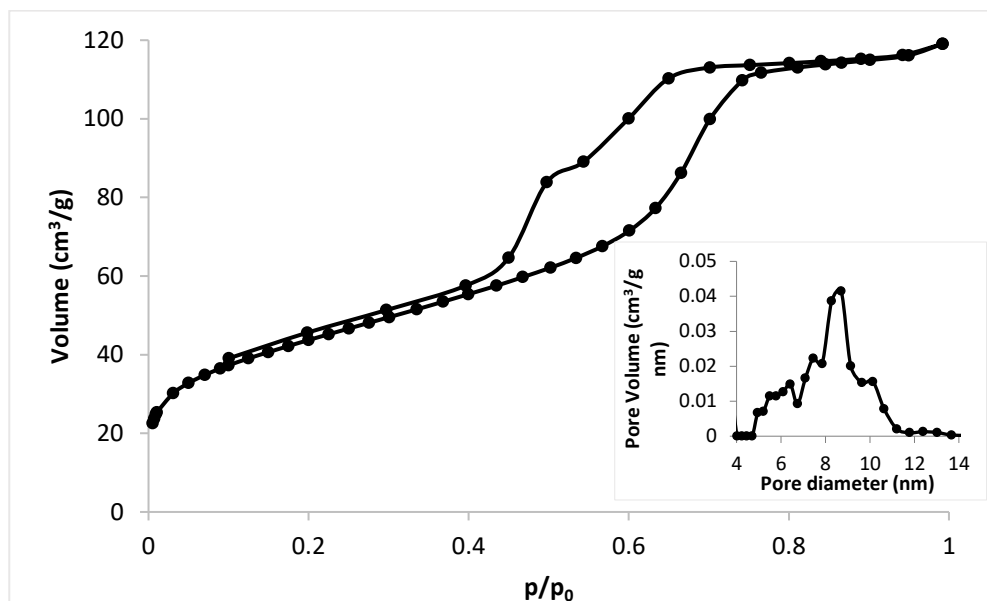


Figure 3.56: N_2 adsorption-desorption isotherm of MBG_SG_SiO₂/CaO and related DFT pore size distribution

Table 3.18: Structural features of MBG_SD_SiO₂/CaO

Name	Specific surface area (m ² /g)	Pore size (nm)	Volume (cm ³ /g)
MBG_SD_SiO ₂ /CaO	156	8.7	0.17

The amorphous structure of the MBG_SD_SiO₂/CaO glass particles was investigated by the wide-angle XRD analysis and the corresponding spectrum is depicted in Figure 3.57. As expected, the only visible broad peak between 20° and 30° corresponded to the amorphous structure of the sample.

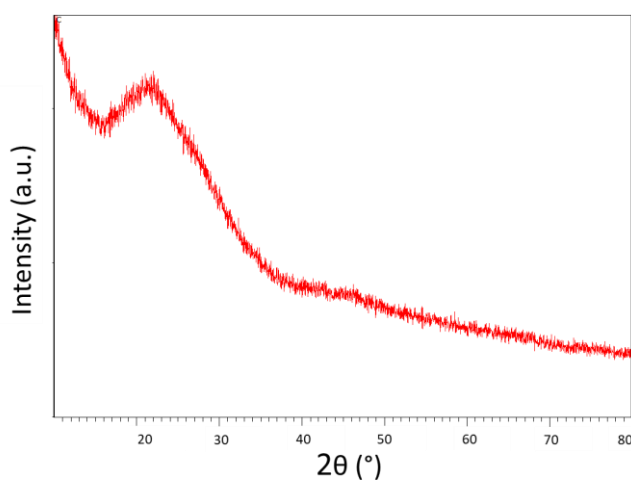


Figure 3.57: Wide-angle XRD analysis of MBG_SD_SiO₂/CaO

3.3.2.1b Bioactive behaviour of MBG_SD_SiO₂/CaO in SBF

The bioactive response of micro-sized MBG_SD_SiO₂/CaO was studied by soaking the particles in SBF by following the procedure described in section 2.7.

The formation of hydroxyapatite started after 1 day of soaking. With the increase of incubation time, the micro-sized particles became fully covered by a rough layer reminiscent of hydroxyapatite formation. In Figure 3.58A, the FE-SEM characterization performed on particles after 7 days of soaking showed a layer of cauliflower formations. The presence of HA was also confirmed by EDS analysis (Figure 3.58B) which showed the P peak and a Ca/P ratio very close to the theoretical one (1.67) after 3 days of soaking. The wide-angle XRD spectrum (data not reported) further demonstrated the formation of hydroxyapatite with the corresponding major peak at 32°, confirming the already noticed high bioactive response of these types of systems [63].

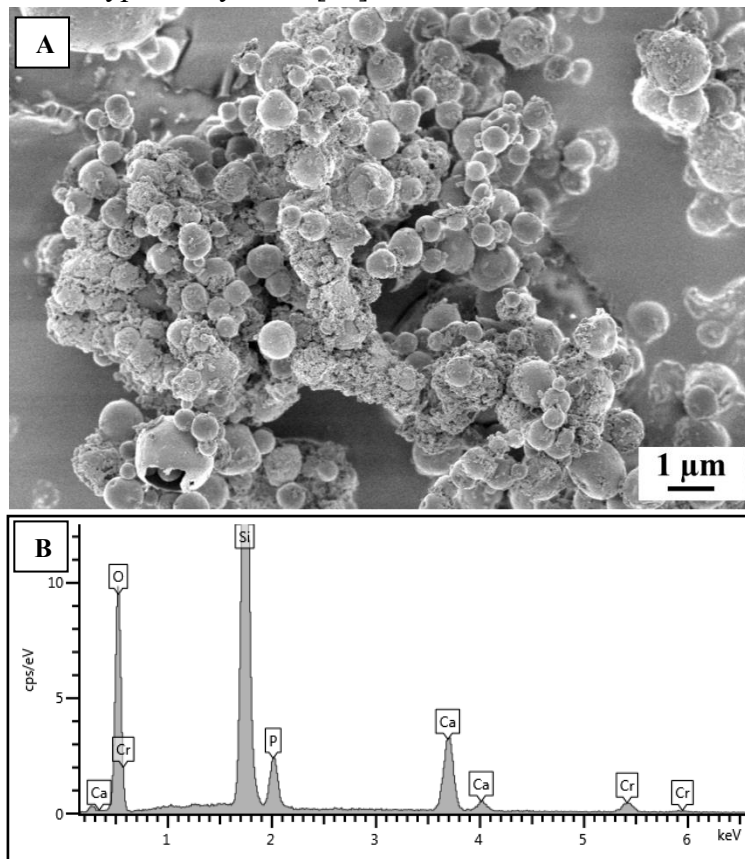


Figure 3.58: FE-SEM (A) and EDS spectrum (B) of MBG_SD_SiO₂/CaO after 7 days of soaking in SBF

3.3.2.2 Copper-containing MBG_SD: MBG_SD_Cu2%

The first ion chosen for the incorporation into the calcium silicate MBG micro-particles was copper, due to its recognised therapeutic effect [7].

The copper-containing micro-sized particles (85SiO₂/13CaO/2CuO %mol, named hereafter MBG_SD_Cu2%) were produced by modifying the procedure reported by Pontiroli et al. [63].

Part of the work described in this chapter has been previously published in [32].

3.3.2.2a Morphological and structural characterization of MBG_SD_Cu2%

As shown in Figure 3.59A, the sample consisted of microspheres with size mostly in the range of 1–5 μm, showing silicon (yellow), calcium (green) and copper (light blue) homogeneously distributed into the framework, as revealed by the compositional mapping EDS analysis carried out on a single sphere (Figure 3.59B). EDS spectrum (Figure 3.59C) of the powder supported on the carbon-based tape revealed the incorporation of copper with a molar concentration very close to the nominal ratio.

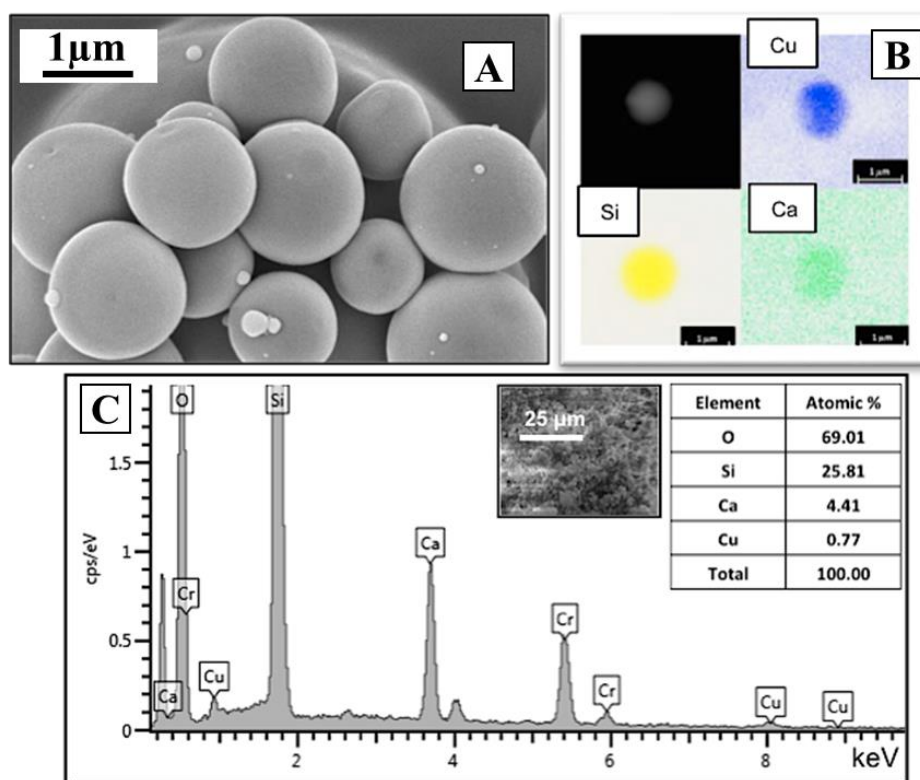


Figure 3.59: FE-SEM image of MBG_SD_Cu2% (A), EDS mapping analysis of MBG_SD_Cu2% single particle (B), EDS spectrum of MBG_SD_Cu2% (C)

Based on wide-angle XRD spectrum (Figure 3.60), copper did not form segregated oxide clusters after calcination treatment, as assessed by the absence of crystalline oxide-based phases.

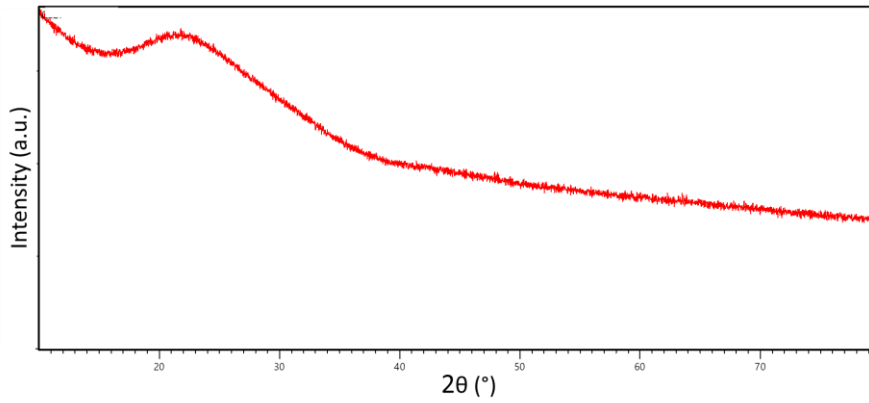


Figure 3.60: Wide-angle XRD analysis of MBG_SD_Cu2%

The mesoporous structure was confirmed by N₂ adsorption-desorption measurement. The isotherm of the sample obtained by aerosol-assisted procedure also confirmed its mesoporous structure. The isotherm (Figure 3.61) is a IV type curve, with H1 hysteresis loop, typical of mesoporous material with pores larger than 4 nm [2]. The pore size distribution showed multi-sized pores with broad distribution, ranging between 8 and 11 nm (inset in Figure 3.61). The BET SSA of MBG_SD_Cu2% of 226 m²/g, although lower than the one shown by MBG_SG_Cu 2% (Table 3.13), is still very high compared to values typical of not-templated sol-gel glasses (few m²/g), which confers a high reactivity to MBGs in the biological environment [64].

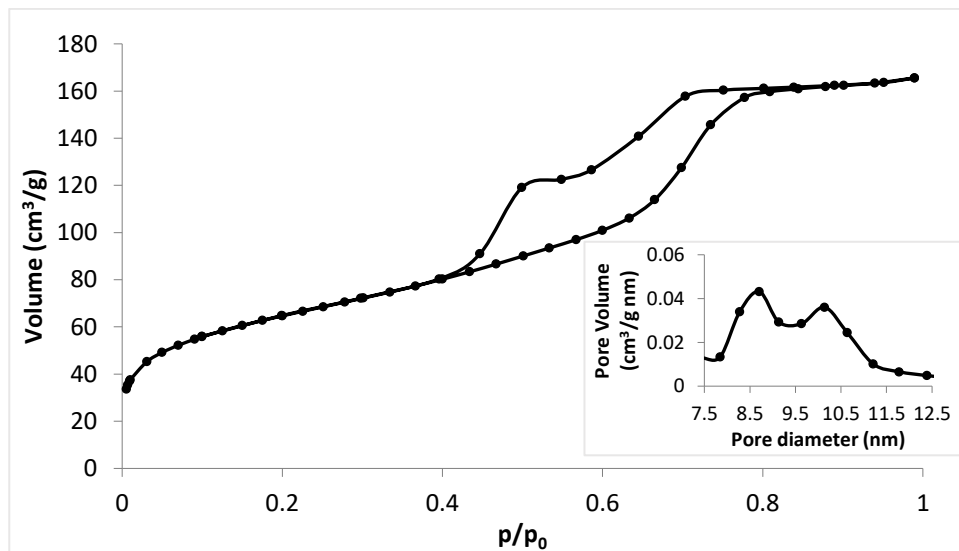


Figure 3.61: N₂ adsorption-desorption isotherm of MBG_SD_Cu2% and related DFT pore size distribution (inset)

Table 3.19: Structural features of MBG_SD_Cu2%

Name	Specific surface area (m ² /g)	Pore size (nm)	Volume (cm ³ /g)
MBG_SD_Cu2%	226	8-11	0.24

3.3.2.2b Copper ion release from MBG_SD_Cu2% in Tris HCl

The Cu²⁺ release profile from MBG_SD_Cu2% particles (Figure 3.62), assessed in Tris HCl, showed a burst effect in the first 3 h, followed by a sustained release of copper ions overtime. The observed release kinetics suggested that the diffusion of Cu²⁺ out of the mesopores is probably hindered or even blocked after the first hours (2–3 h) of incubation. A similar release profile has been already observed from silica-based mesoporous spheres [34] and was ascribed to the progressive occlusion of mesopores due to the dissolution of the silica framework and its reprecipitation as silica gel at the pore mouth [65,66]. The final concentration of released copper species from MBG_SD_Cu2% was about 2.5 ppm, and corresponded to approximately the 60% of incorporated copper, suggesting the presence of a residual amount of copper into the MBG framework or re-precipitation phenomena.

It is also worth mentioning that, since MBG_SD_Cu 2% particles are produced by an aerosol-assisted spray-drying process, where a rapid evaporation of the solvent takes place, the resulting powder is expected to show a less condensed framework compared to MBG_SG samples and thus much higher reactivity toward surface dissolution/re-precipitation reactions. This major tendency to the re-precipitation phenomena could explain the difference between MBG_SD_Cu2% and MBG_SG_Cu2% ion release property: as described in section 3.3.1.1b, the final released concentration of MBG_SG_Cu2% (4.7 ppm) was almost twice compared the final concentration of MBG_SD_Cu2%.

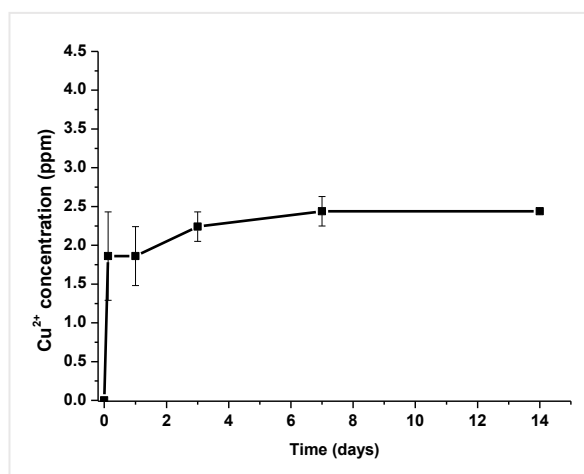


Figure 3.62: Cu²⁺ release curve of MBG_SD_Cu2% in Tris HCl

3.3.2.2c Bioactive behaviour of MBG_SD_Cu2% in SBF

The remarkable bioactivity of MBG_SD_Cu2% when soaked in SBF was clearly revealed by FE-SEM observations (Figure 3.63). After only 1 day of soaking, the particles started to be covered by a rough layer of globular agglomerates of Ca-deficient HA phase (Ca/P=1.51), as shown by EDS analysis (data not shown). After 14 days, MBG particles were almost fully covered by a compact layer of needle-like nanocrystals, composed by calcium and phosphorus. Figure 3.63 shows MBG_SD_Cu2% after soaking for 14 days. EDS analysis performed on powders evidenced a Ca/P ratio of 1.7, typical of HA [5,6].

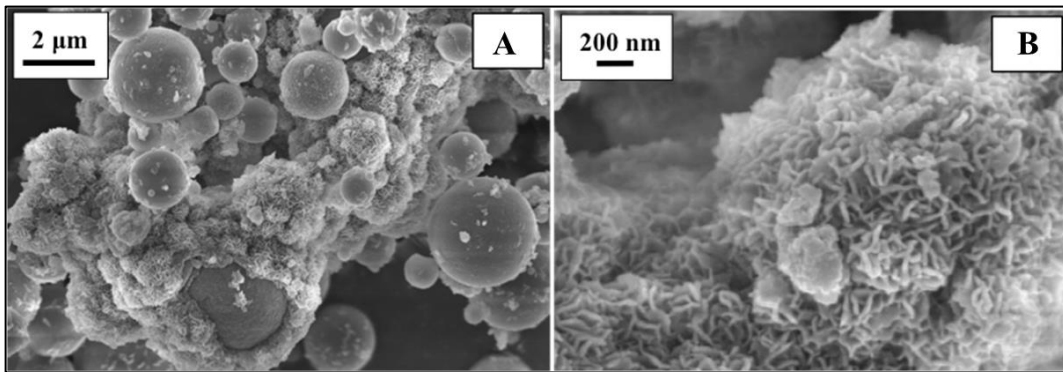


Figure 3.63: FE-SEM of MBG_SD_Cu 2% after 14 day of soaking in SBF (A) and high magnification of A image (B)

Wide-angle XRD analysis performed on the MBG particles after the bioactivity test confirmed the formation of crystalline HA (Figure 3.64): marked peaks appeared at 25.87° and 31.73° (2θ value) and other less intense reflections at 49.39° and 53.17° (2θ value) matched by hydroxyapatite reference (01-089-6440).

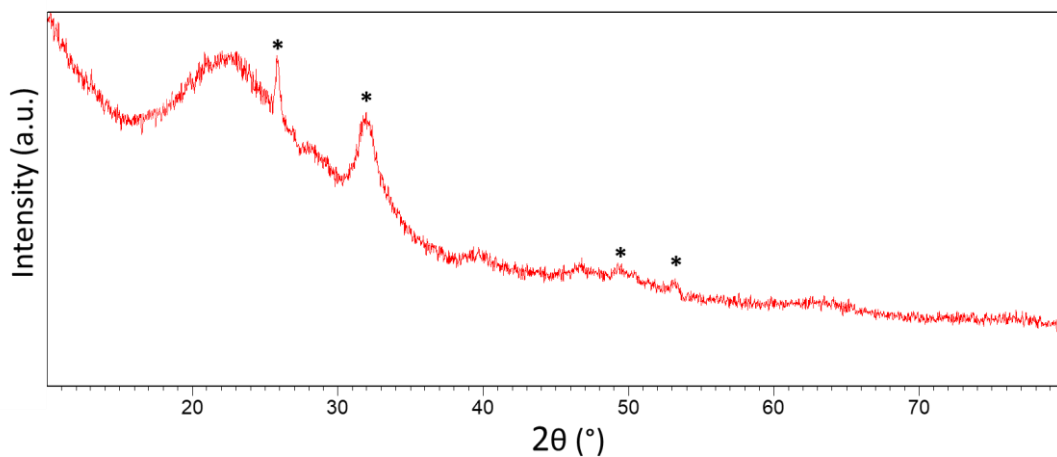


Figure 3.64: Wide-angle XRD analysis of MBG_SD_Cu2%

3.3.2.3 Strontium-containing MBG_SD: MBG_SD_Sr1%

In order to obtain advanced devices for bone healing application, strontium was incorporated into the micro-sized MBG particles, due to its ability to impart pro-osteogenic effect, through osteoblast stimulation and osteoclast inhibition [28].

The results of the Sr-modified MBGs (85SiO₂/14CaO/1SrO %mol, named hereafter MBG_SD_Sr1%) will be useful for interpreting those of the double-ion (strontium and copper) containing system (see following section 3.3.2.4).

Part of the work described in this chapter has been previously published in [29].

3.3.2.3a Morphological and structural characterization of MBG_SD_Sr1%

Figure 3.65 shows a representative FE-SEM image of the MBG_SD_Sr1% particles which were spherically shaped with size ranging from 0.4 to 5 μm. The morphological features of sprayed MBG_SD_Sr1% powders were comparable to those obtained for samples produced by similar approach [63,67], thereby confirming the high reproducibility and versatility of this method.

As previously discussed, the EDS analysis (inset in Figure 3.65) of MBG_SD_Sr1% revealed a lower value of Sr/Si ratio (0.85 mol%) compared to the nominal one (1.18 mol%), suggesting that strontium precursor is only partially incorporated within the glass network.

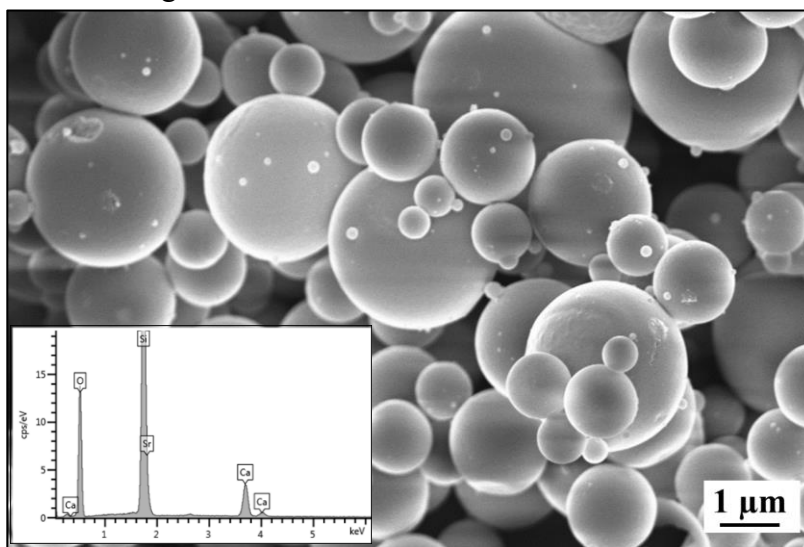


Figure 3.65: FE-SEM image of MBG_SD_Sr1% and related EDS spectrum

Since the detection of strontium through EDS could be unreliable because of the overlapping of Si and Sr peaks, MBG_SD_Sr1% was also analysed through XRF spectroscopy which confirmed the partial incorporation of strontium (Sr/Si = 0.77 mol%). As stated above, this discrepancy may be likely due to the larger ionic radius of strontium (1.16 Å) compared to calcium (0.94 Å) [39], which can limit its incorporation into the network during silica polymerization. Furthermore, the larger ionic radius of Sr²⁺ implies a lower charge-to-size ratio compared to Ca²⁺, with consequent less effective ionic interactions with the oxygen atoms of the network

[39]. Compositional mapping obtained with EDS technique revealed that all the elements were uniformly distributed in the powder (Figure 3.66): the colour maps of a particle, in fact, show homogeneous intensities for silicon (yellow), calcium (blue) and strontium (red).

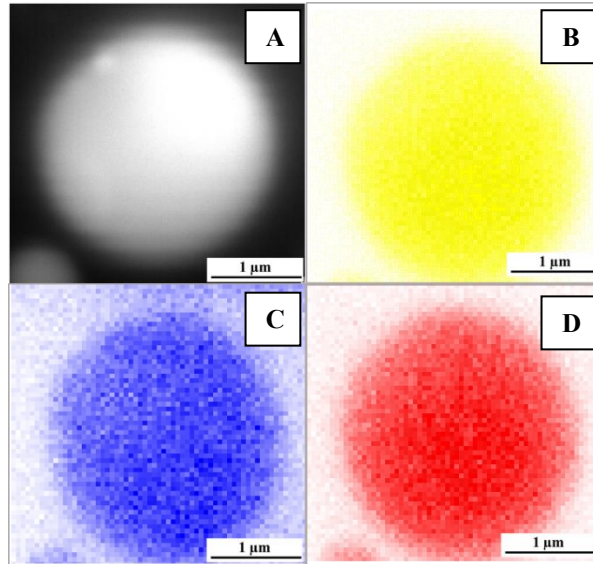


Figure 3.66: Elemental mapping of MBG_SD_Sr1% particle: SEM image of the analysis area (A), and distribution of silicon (B), calcium (C) and strontium (D)

Nitrogen adsorption-desorption measurements confirmed the mesoporous structure of the spray-dried material: a IV type isotherm with H1 hysteresis loop, typical of mesoporous materials with pores larger than 4 nm, is shown in Figure 3.67 [2]. The pore size distribution obtained through the DFT method (inset in Figure 3.67) confirmed that the pore size of MBG_SD_Sr1% ranged between 4 and 10 nm. The SSA calculated through the BET method was 152.9 m²/g (Table 3.20), a very high value which conferred high reactivity to MBGs in the biological environment [64].

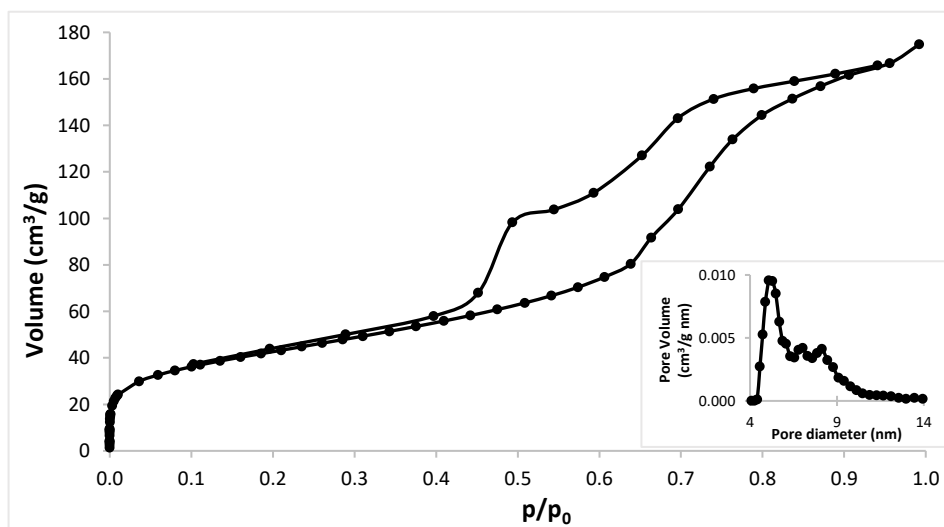


Figure 3.67: N₂ adsorption-desorption isotherm of MBG_SD_Sr1% and related DFT pore size distribution (inset)

Table 3.20: Structural features of MBG_SD_Sr1%

Name	Specific surface area (m ² /g)	Pore size (nm)	Volume (cm ³ /g)
MBG_SD_Sr1%	153	5.5	0.25

3.3.2.3b Strontium ion release from MBG_SD_Sr1% in SBF

Strontium release profile from MBG_SD_Sr1% was assessed by soaking the powders in SBF (Figure 3.68). The curve revealed a burst release of Sr ions after the first 3 h of soaking, consisting of about the 80% of the strontium released during the whole test. The fast release kinetics suggested high accessibility and availability to ion exchange reactions of Sr²⁺ species throughout the framework. After 3 h, the release reached a plateau, settling on the final concentration of 11 µg/mL, value that, according to the literature data [28], allows cell survival and could stimulate the biological response of pre-osteoblastic cells. In order to assess the amount of non-released strontium after 14 days of soaking in SBF, ICP analysis was performed on the sample after its complete dissolution in acidic environment. The analysis revealed the presence of 0.3 wt% of residual strontium and, based on the measured initial strontium content (ca 1 wt%), the overall released percentage was approximately 70%.

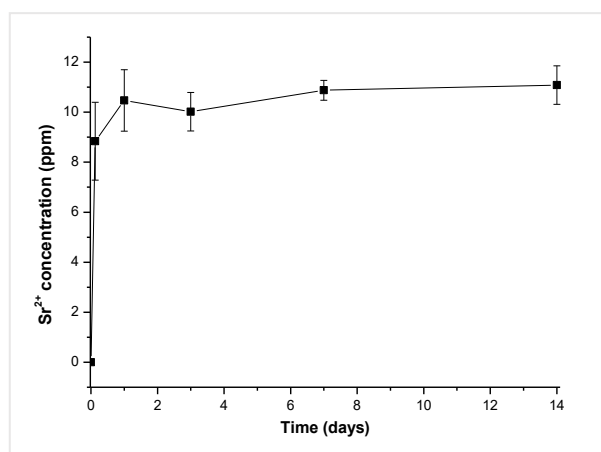


Figure 3.68: Sr²⁺ release curve of MBG_SD_Sr1% in SBF

3.3.2.3c Bioactive behaviour of MBG_SD_Sr1% in SBF

The peculiar characteristic of MBGs is their ability to quickly form a surface apatite layer as a result of a series of ionic exchanges with body fluids, where the ion calcium plays a crucial role. In this regard, the substitution of calcium with strontium in the glass composition did not alter the fast bioactive behaviour of MBGs. In fact, the bioactivity test revealed the presence of numerous calcium phosphate deposits on the surface of Sr-containing powder just after 1 day of immersion in SBF (Figure 3.69A). After 1 week, these deposits covered completely the particles and had the typical “cauliflower” morphology of nano-crystalline HA (Figure 3.69B). Phosphorous peaks appeared in the EDS spectrum of the sample

after 7 days of immersion in SBF (data not shown): since P was not present in the original composition of MBG_SD_Sr1%, its detection could be attributed to the formation of a new phase, *i.e.* HA. The Ca/P atomic ratio of this newly formed phase, extrapolated from EDS data, was in good accordance with the stoichiometric value of hydroxyapatite (1.67) [5,6].

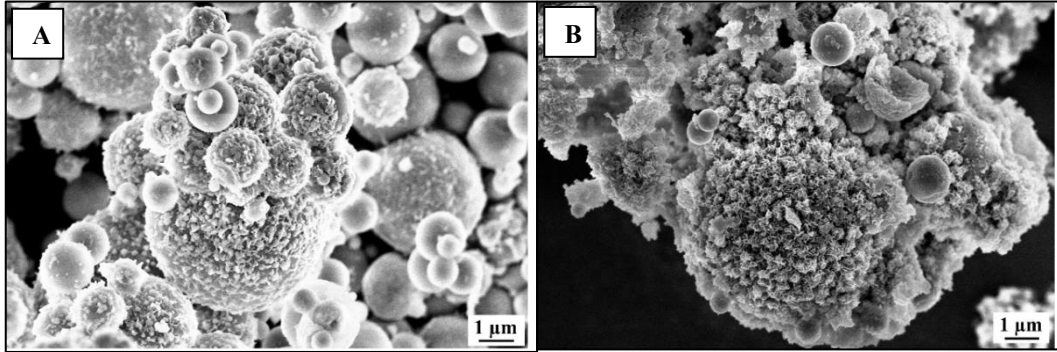


Figure 3.69: FE-SEM images of MBG_SD_Sr1% after 1 day (A) and 7 days (B) of soaking in SBF

XRD analysis performed on the MBG powder after the bioactivity test (Figure 3.70) further confirmed the formation of crystalline HA: new peaks appeared at 25.68, 31.99, 39.85, 46.53 and 49.36 2θ degrees and were matched by hydroxyapatite reference (00-001-1008). During the test, the pH of SBF remained always below 7.8, which is considered the threshold value for allowing osteoblasts to maintain their physiological activity [68]. The pronounced bioactive behaviour of these mesoporous glasses, despite their high silica content (85 mol%) was the result of their large SSA (above 150 m^2/g) which increases their reactivity in the body fluid. The fast deposition of the HA crystals, which can obstruct the entrance of the pores, can account for the incomplete release of the strontium ions, as evidenced for other previously described samples.

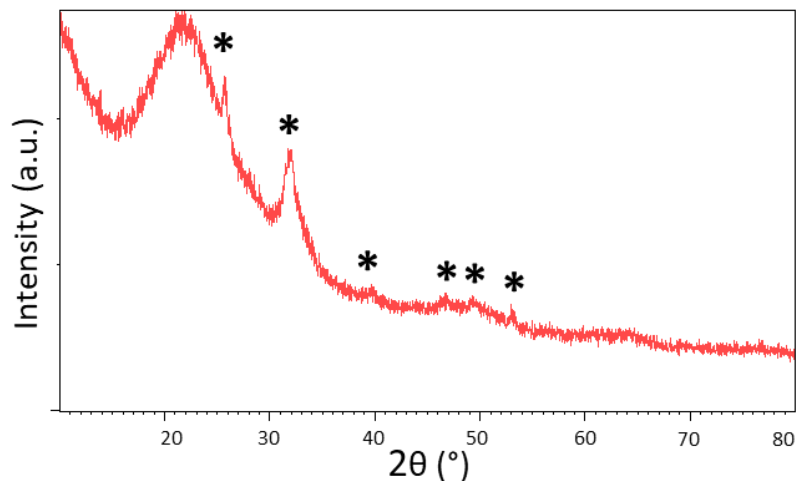


Figure 3.70: Wide-angle XRD analysis of MBG_SD_Sr1% after 7 days of soaking in SBF

3.3.2.4 Strontium-copper co-containing MBG_SD: MBG_SD_CuSr2%

With the aim to obtain multifunctional biomaterials combining the ability to promote bone formation and angiogenesis and to impart an antibacterial effect, double-ion co-substituted mesoporous bioactive micro-particles were obtained by incorporating strontium and copper ions. The co-modified system, produced by aerosol-assisted spray-drying approach, was called MBG_SD_CuSr2% (85SiO₂/13CaO/1SrO/1CuO %mol).

Part of the work described in this chapter has been previously published in [33].

3.3.2.4a Morphological and structural characterization of MBG_SD_CuSr2%

The Sr-Cu co-containing micro-sized particles were investigated in their morphology, composition and structural properties.

MBG_SD_CuSr2% showed spherical particles ranging between 500 nm and 5 μ m, as depicted in Figure 3.71. The EDS spectrum (inset in Figure 3.71) revealed that the incorporation occurred for both ions. Since the EDS analysis was considered unreliable to know the exact concentration of Sr²⁺ ions, as already pointed out for all the Sr-containing systems, the incorporated ion concentration was analysed by ICP after dissolution in acidic environment (as described in section 2.5.2). The detected ion content corresponded to 95% and 70% for the copper and strontium ion, respectively. Hence, as previously noticed, the incomplete incorporation of strontium could be ascribed to the electronic properties of the strontium [30,39].

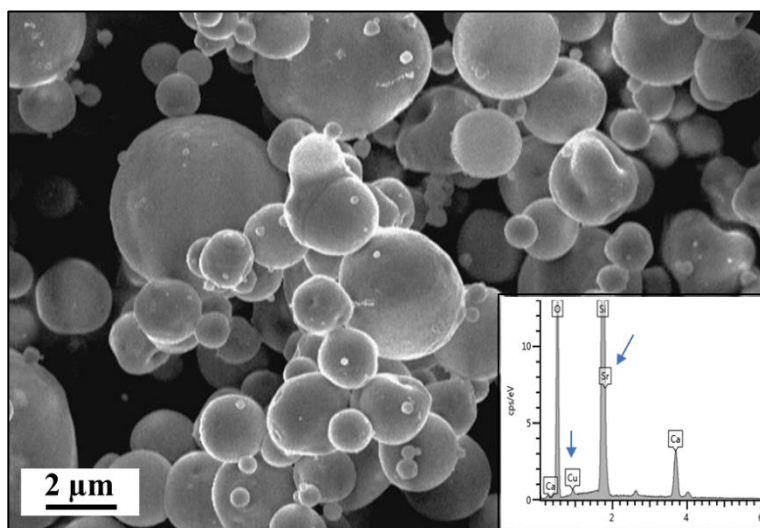


Figure 3.71: FE-SEM image of MBG_SD_CuSr2% with related EDS spectrum (inset)

N₂ adsorption-desorption measurements showed IV type isotherm (Figure 3.72) which confirmed the mesoporous structure of the sample. The presence of H1 hysteresis loop is ascribable to the filling of ordered mesopores with diameter bigger than 4 nm. The inset in Figure 3.72 revealed a single-mode pore size distribution with an average pore diameter of 5 nm.

As already noticed for MBG_US_m_CuSr2% sample, the obtained results evidenced that the incorporation of two types of ions did not significantly affect the formation of an ordered structure and the textural features (Table 3.21) of the final powder resulted only slightly different from Sr- or Cu-containing MBGs [8,29].

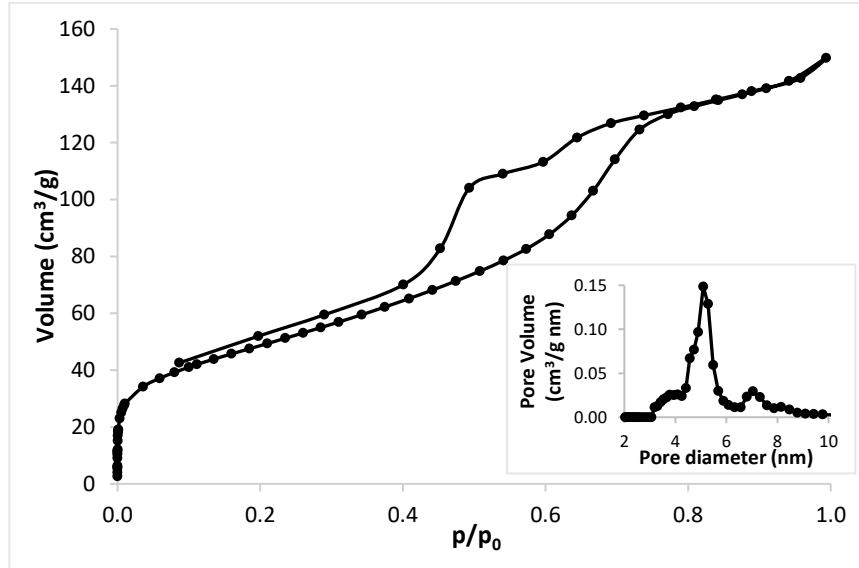


Figure 3.72: N_2 adsorption-desorption isotherm of MBG_SD_CuSr2% and related DFT pore size distribution (inset)

Table 3.21: Structural features of MBG_SD_CuSr2%

Name	Specific surface area (m^2/g)	Pore size (nm)	Volume (cm^3/g)
MBG_SD_CuSr2%	176	5	0.21

3.3.2.4b Strontium and copper ion release from MBG_SD_CuSr2% in SBF

The ion release capability of MBG_SD_CuSr2% was assessed by soaking the sample in SBF up to 14 days.

The incorporated Cu^{2+} and Sr^{2+} were successfully co-released by the micro-sized MBG particles (Figure 3.73). A burst release within the first hours was observed for both Cu^{2+} and Sr^{2+} ions which reached 6 and 11 ppm, respectively. Then a slower increase in the released concentration (9 and 13 ppm for Cu^{2+} and Sr^{2+} ions, respectively) was shown. After 3 days of incubation, the trend of the curve suggested that the precipitation of a HA layer could partially hamper further ion release. The higher release of Sr^{2+} compared to Cu^{2+} suggests a higher accessibility and ion-exchange ability of Sr^{2+} within the MBG framework compared to the incorporated copper species, most likely due to its similarity with calcium as network modifier [28].

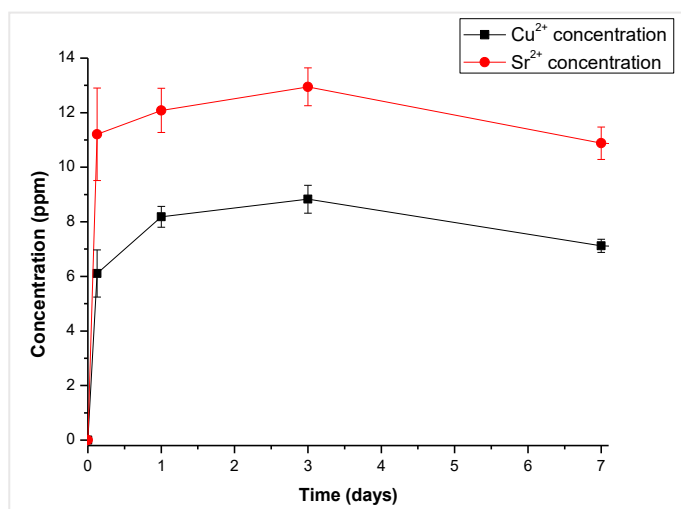


Figure 3.73: Ion release curve of MBG_SD_CuSr2%

3.3.2.4c Bioactive behaviour of MBG_SD_CuSr2% in SBF

In vitro bioactivity assessment highlighted that partial replacing of Ca with Cu and Sr ions did not significantly hinder the hydroxyapatite nucleation and deposition. After 1 day of soaking, the Ca/P ratio revealed by EDS analysis was 1.63. After 7 days of soaking in SBF the particles were fully covered by a layer of needle-like crystals (Figure 3.74) and the Ca/P ratio was in good accordance to the stoichiometric value of hydroxyapatite (1.67) [5,6].

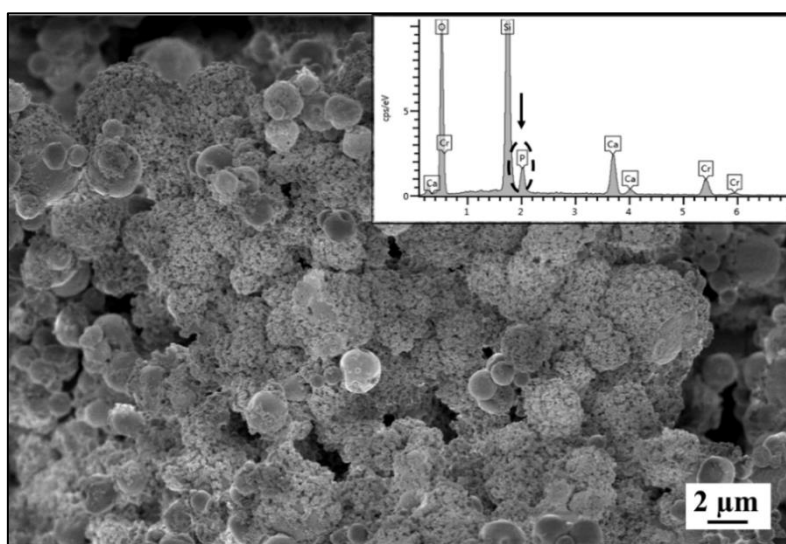


Figure 3.74: MBG_SD_CuSr2% after 7 days of soaking in SBF with EDS spectrum (inset).

The formation of HA layer was confirmed by wide-angle XRD analysis (Figure 3.75). The diffractogram in Figure 3.75B revealed the presence of new peaks which were matched by crystalline hydroxyapatite (external reference 00- 001-1008), not detected in the wide-angle XRD pattern performed on MBG_SD_CuSr2% before soaking (Figure 3.75A).

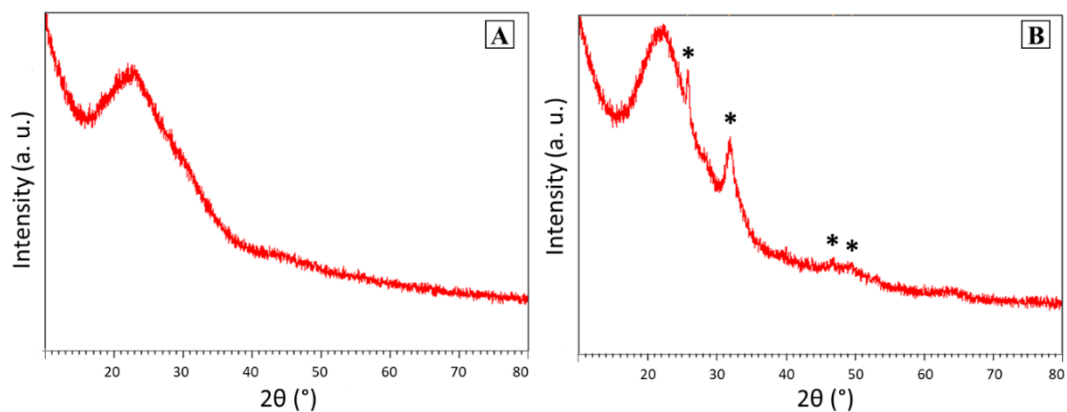


Figure 3.75: MBG_SD_CuSr2% before soaking in SBF (A) and MBG_SD_CuSr2% after 7 days of soaking in SBF (B)

3.3.2.5 Cerium-containing MBG_SD: MBG_SD_Ce1% and MBG_SD_Ce2%

Aerosol-assisted spray-drying procedure was adopted in order to produce cerium-containing micro-sized particles in the following molar concentrations: 85SiO₂/14CaO/1CeO %mol (named hereafter MBG_SD_Ce1%) and 85SiO₂/13CaO/2CeO %mol (called MBG_SD_Ce2%).

Cerium was selected as therapeutic ion due to its osteoconductive and antibacterial properties [57].

3.3.2.5a Morphological and structural characterization of cerium-containing MBG_SD

The two different compositions of cerium-containing micro-sized samples were fully characterized in order to investigate the influence of the substituent ion.

The FE-SEM images (Figure 3.76) revealed spherical particles with size ranging between 500 nm and 4 μm, in analogy with results found in the literature [30]. The FE-SEM characterization demonstrated that the presence of the double amount of cerium ion did not affect significantly the morphology of the samples.

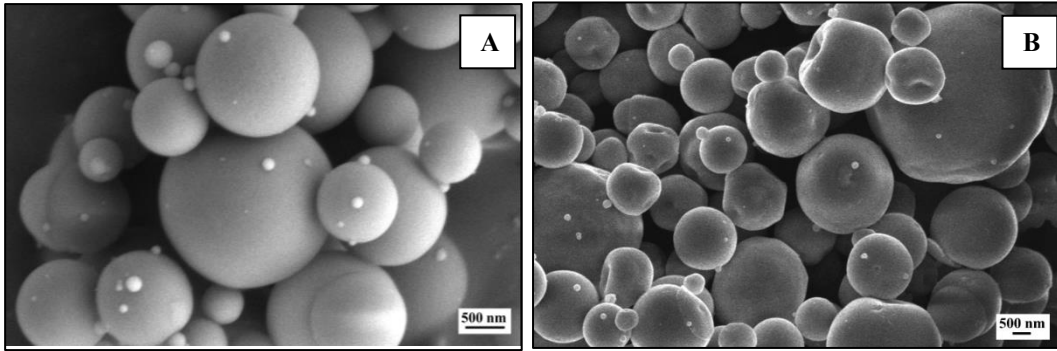


Figure 3.76: FE-SEM image of MBG_SD_Ce1% (A) and MBG_SD_Ce2% (B)

The average of three measurements obtained by EDS investigation confirmed the presence of the cerium ion with Ce/Si ratio in fair agreement with the theoretical ratio. Moreover, it was possible to observe a uniform distribution of the substituent into the silica framework. These data demonstrated that the substitution of cerium for calcium did not affect the ion incorporation process.

Both samples showed a IV type isotherm with a H1 hysteresis loop ranging between 0.4 and 0.8 p/p_0 (Figure 3.77A and B) indicating the presence of cylindrical pores [2]. The pore size distributions obtained through DFT method are reported in Figure 3.77C and Figure 3.77D for MBG_SD_Ce1% and MBG_SD_Ce2%, respectively. As visible, both samples showed two families of mesopores, the first around 2 nm and the second around 8 nm. Considering the use of P123 as surfactant, the first family could be due to the presence of microporosity in the silica framework. According to Arcos et al. [69], in fact, P123-templated systems are usually characterized by pore size around 8 nm.

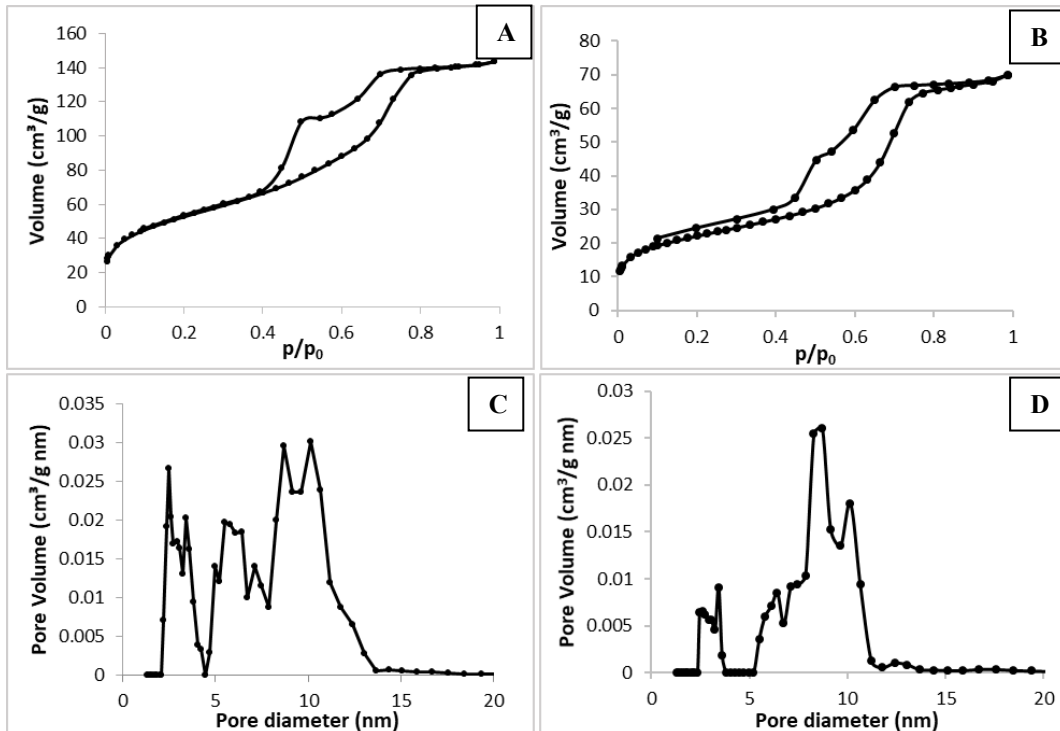


Figure 3.77: N_2 adsorption-desorption isotherm of MBG_SD_Ce1% (A) and MBG_SD_Ce2% (B); DFT pore size distribution of MBG_SD_Ce1% (C) and MBG_SD_Ce2% (D)

In Table 3.22, the textural parameters of the cerium-containing micro-particles are listed. As expected, the specific surface area values and pore volume decreased as the cerium content increased. The same evidence is reported in the literature both in cerium-doped system as well as in other metallic ion-doped matrices [10,30].

Table 3.22: Structural features of cerium-containing of MBG_SD

Name	Specific surface area (m ² /g)	Pore size (nm)	Volume (cm ³ /g)
MBG_SD_Ce1%	187	~ 2 nm ~ 8 nm	0.21
MBG_SD_Ce2%	77	~ 2 nm ~ 8 nm	0.10

Based on wide-angle XRD analysis (data not shown), the absence of peaks confirmed that the incorporated cerium did not form any crystalline phases.

3.3.2.5b Cerium ion release from MBG_SD_Ce1% and from MBG_SD_Ce2% in Tris HCl

The cerium release profile in Tris HCl of both samples is reported in Figure 3.78. As expected, the released amount of Ce³⁺ is dependent on cerium concentration: higher cerium substitution resulted in higher released concentration in Tris HCl. Both cerium-containing samples showed an increasing trend up to a maximum settled at 0.33 ppm for MBG_SD_Ce1% and 1.21 ppm for MBG_SD_Ce2%. Then both curves presented a decreasing trend. It stands to reason that the curve of MBG_SD_Ce2% has the same trend of MBG_SD_Ce1%, only slightly delayed. As already evidenced in 3.3.1.2b, an improved chemical stability and a delay in the degradation process was found with the increase in cerium content in different types of bioactive glasses [59,60].

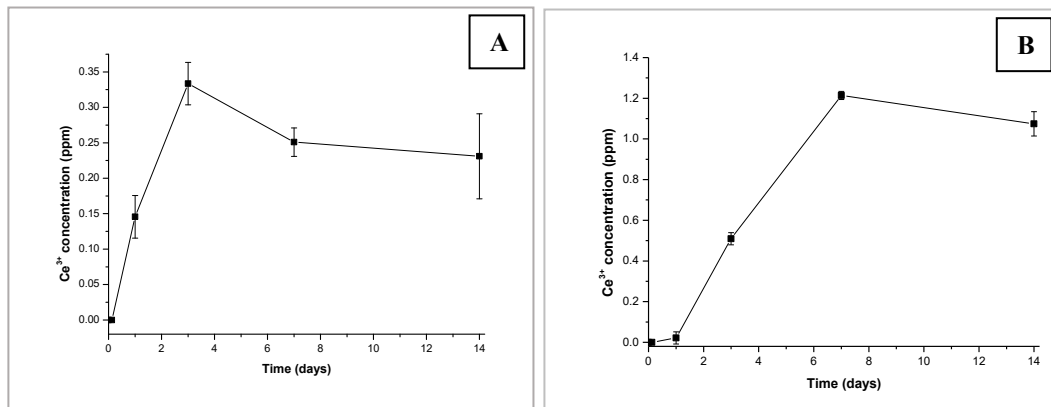


Figure 3.78: Ce³⁺ release profiles of MBG_SD_Ce1% (A) and MBG_SD_Ce2% (B)

3.3.2.5c Bioactive behaviour of cerium-containing MBG_SD samples in SBF

Considering the MBG_SD_Ce2% more promising than the MBG_SD_Ce1% in terms of cerium release property (Figure 3.78) and assuming that the ion exchange capability of MBG_SD_Ce2% was better than MBG_SD_Ce1%, the bioactivity test was uniquely performed with MBG_SD_Ce2% sample.

Based on wide-angle XRD investigation, the formation of crystalline HA phase was particularly discernible after 14 days of soaking (Figure 3.79) highlighting the bioactive behaviour of the cerium-containing micro-sized sample.

Compared to MBG_SD particles (see section 3.3.2.1b), however, the MBG_SD_Ce2% showed a delay in the deposition of HA. As already evidenced in cerium-containing nano-sized particles (see section 3.3.1.2) and in other works [59,60], the presence of cerium slowed down the ion release kinetics and exchange of the MBG systems. At variance with cerium-containing nano-sized particles whose bioactive response was negligible after 14 days of soaking, the formation of HA layer in micro-sized MBG particles was due to the different synthesis process which, as asserted before, resulted in a less polymerized silica framework.

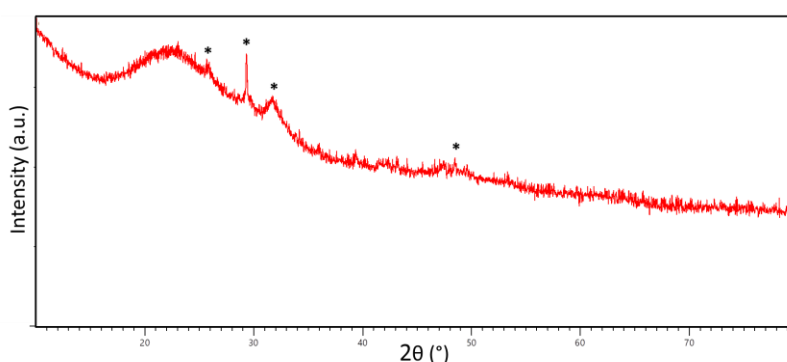


Figure 3.79: Wide-angle XRD analysis of MBG_SD_Ce2% after 14 days of soaking in SBF

3.3.2.6 Silver-containing MBG_SD: MBG_SD_Ag0.1% and MBG_SD_Ag2%

Silver-containing materials were considered due to the well-known antibacterial effect of silver [20,70]. In order to synthesize Ag-modified micro-sized particles, spray-drying route was used and CaNO_3 was partially substituted with two different concentrations of AgNO_3 . In details, the as-synthesized samples are the following: MBG_SD_Ag0.1%, with the $85\text{SiO}_2/14.9\text{CaO}/0.1\text{AgO}$ %mol and MBG_SD_Ag2%, with the $85\text{SiO}_2/13\text{CaO}/2\text{AgO}$ %mol.

3.3.2.6a Morphological and structural characterization of silver-containing MBG_SD samples

MBG_SD_Ag0.1% and MBG_SD_Ag2% were studied in their morphology, composition and structural properties.

The morphological characterization in Figure 3.80 showed the spherical particles with size ranging between 300 nm and 5 μm , confirming the potentiality of the nanomatrices to incorporate silver ions without affecting the morphology.

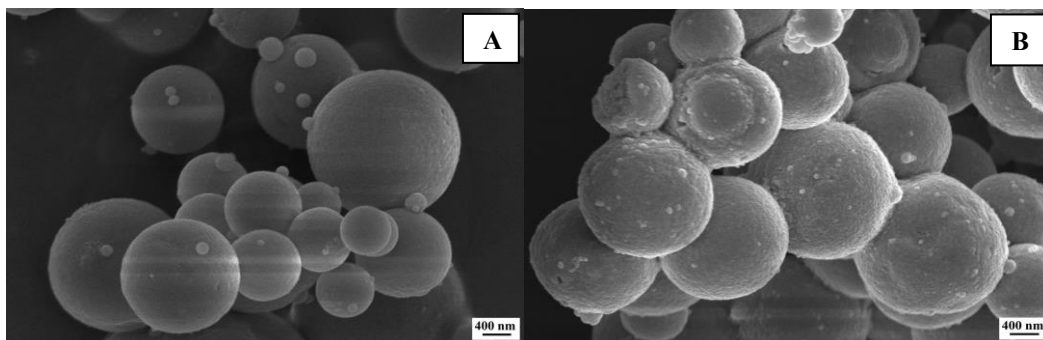


Figure 3.80: FE-SEM images of MBG_SD_Ag0.1% (A) and MBG_SD_Ag2% (B)

The EDS technique, used to obtain compositional information, was not useful for the 0.1%mol-containing silver because of the too low concentration of the element. Based on the EDS analysis of MBG_SD_Ag2%, calculated as average of three measurements, the distribution of silver resulted not homogeneous.

MBG_SD_Ag0.1% isotherm (Figure 3.81A) evidenced the mesoporous structure of the sample with a IV type isotherm and a H1 hysteresis loop. The IV type curve of MBG_SD_Ag2% in Figure 3.81B confirmed the mesoporosity and its H3 hysteresis loop, according to IUPAC classification [2], is associated to slit-shaped pores.

The pore size distribution obtained through DFT method is reported in Figure 3.81C and 3.81D. Both samples showed not uniform pore size distribution. Most of the pores are characterized by dimension in the range of 11-12 nm. The other relevant peak centred around 3 nm could be associated to the internal voids of particle aggregates.

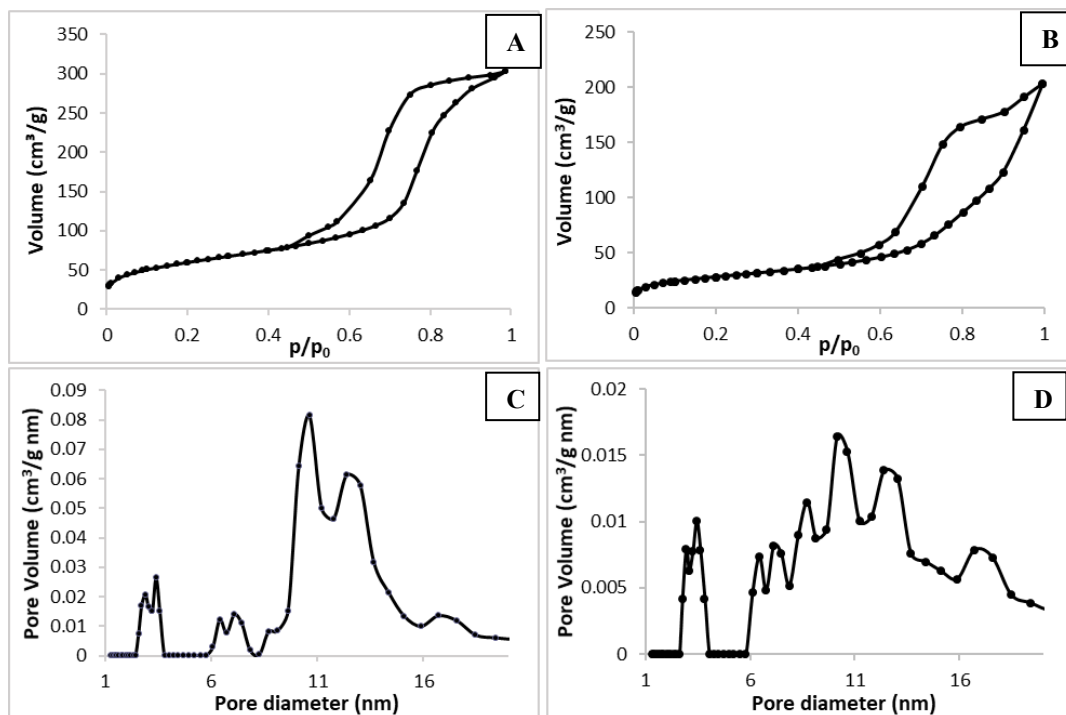


Figure 3.81: N₂ adsorption-desorption isotherm of MBG_SD_Ag0.1% (A) and MBG_SD_Ag2% (B); DFT pore size distribution of MBG_SD_Ag0.1% (C) and MBG_SD_Ag2% (D)

The structural features of Ag-substituted MBG_SD are listed in Table 3.23. The specific surface area and pore volume values decreased by increasing the silver amount, as already observed with other ion-containing mesoporous materials [10]. Besides, the disordered mesoporous structure revealed by the isotherm of MBG_SD_Ag2% is reflected also in these values which were quite low if compared with analogous ion-containing systems [29,30,32,33].

Table 3.23: Structural features of silver-containing MBG_SD

Name	Specific surface area (m ² /g)	Pore size (nm)	Volume (cm ³ /g)
MBG_SD_Ag0.1%	211	10.6	0.45
MBG_SD_Ag2%	99	10-12	0.27

In order to investigate the formation of crystalline phases due to the presence of silver, both samples were analysed by wide-angle XRD. The patterns depicted in Figure 3.82 showed a peak ascribed to silver oxide (external reference code 00-065-3289) over the amorphous alone.

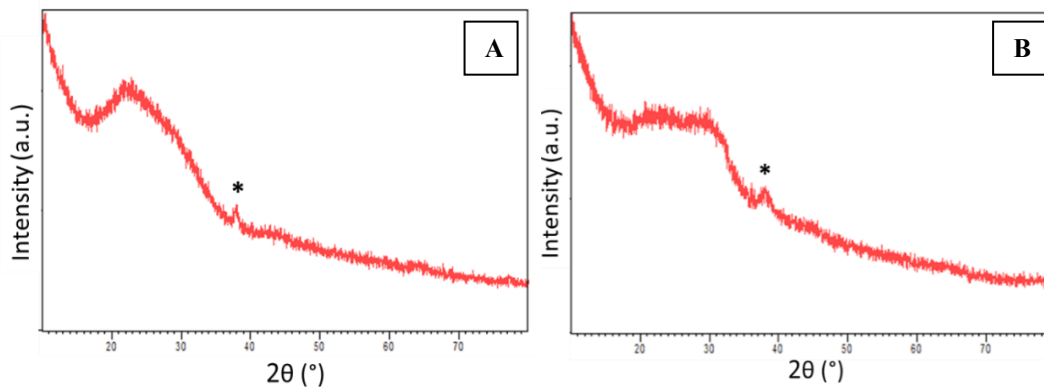


Figure 3.82: Wide-angle XRD spectra of MBG_SD_Ag0.1% (A) and MBG_SD_Ag2% (B)

3.3.2.6b Silver ion release from MBG_SD_Ag0.1% and MBG_SD_Ag2% in Tris HCl

Silver ion release from MBG_SD_Ag0.1% and from MBG_SD_Ag2% was assessed by soaking the samples in Tris HCl for different time points, up to 14 days.

For what concerns the MBG_SD_Ag0.1% (Figure 3.83A), silver released concentration reached a plateau after 3 days of soaking and remained at 1.3 ppm overtime. As expected, the higher substituent concentration led to a higher amount of released ion concentration in the medium. The MBG_SD_Ag2%, in fact, released 7.53 ppm after 14 days of soaking. Furthermore, the ascending trend of the curve suggested the presence of residual amount of silver which could be still released.

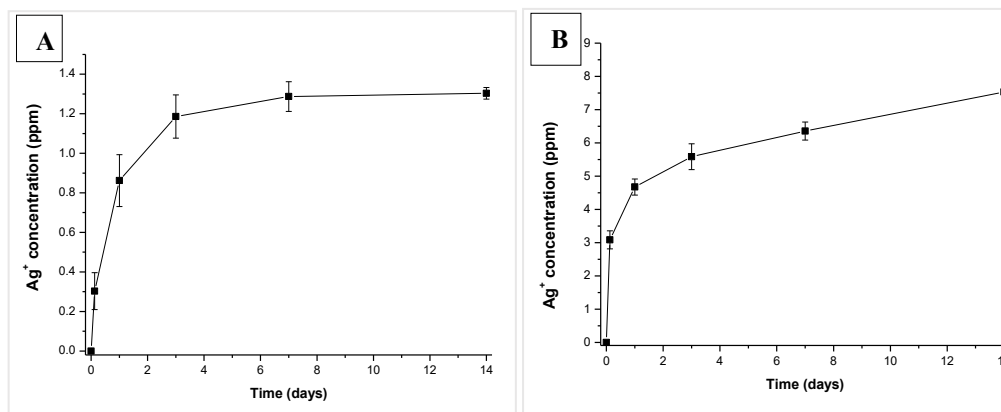


Figure 3.83: Ag^+ release profiles of MBG_SD_Ag0.1% (A) and MBG_SD_Ag2% (B)

3.3.2.7 Cerium-containing silica SD: MSm_SD_Ce2%*

In view of the potential use in wound healing application where the bioactive response, mainly associated to calcium ions, is not a required property, cerium-containing silica in form of micro-particles were produced by spray-drying assisted sol-gel route. In particular, MSm_SD_Ce2%* ($98SiO_2/2CeO$) was obtained by removing calcium precursor and adding cerium precursor in the aerosol-assisted spray-drying approach [63].

3.3.2.7a Morphological and structural characterization of MSm_SD_Ce2%*

MSm_SD_Ce2% particles showed a morphology very close to the other spray-drying MBG samples, with diameters ranging from 500 nm to 5 μm (Figure 3.84).

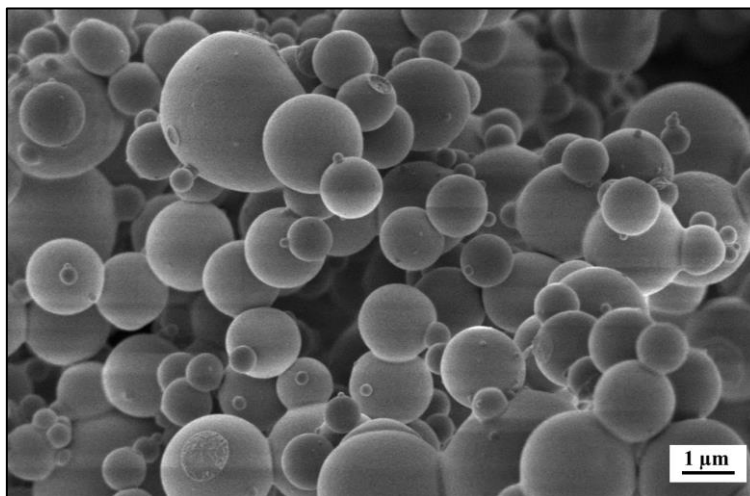


Figure 3.84: FE-SEM image of MSm_SD_Ce2%*

The detected Ce/Si ratio obtained through EDS analysis (Figure 3.85) and calculated as average of three measurements confirmed the incorporation of cerium ions in a ratio very close to the theoretical one. The chromium peak was ascribed to the layer used to make conductive the sample for the analysis.

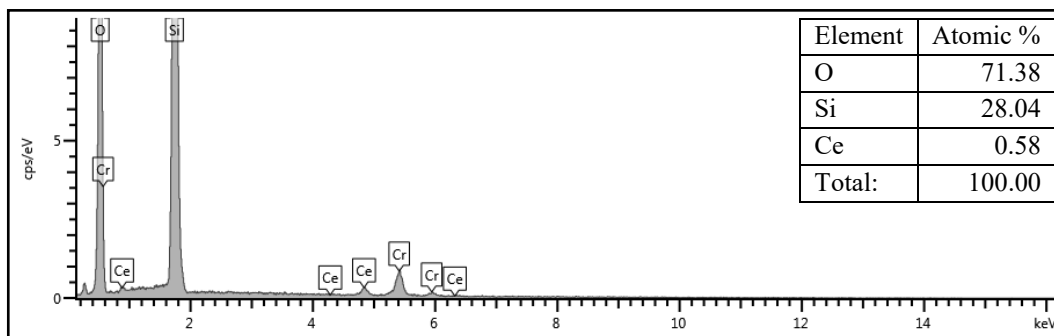


Figure 3.85: EDS spectrum of MSm_SD_Ce2%*

Graphs in Figure 3.86 depict the adsorption-desorption isotherm and the related DFT pore size distribution. The H1 large hysteresis loop between 0.4-0.9 p/p_0 observed in the IV type isotherm meant a mesoporous material with uniform pores larger than 4 nm, according to IUPAC classification [2].

The structural features listed in Table 3.24 highlight that the incorporation of cerium into silica framework did not interfere with the formation of an ordered structure which exhibited an excellent surface area value.

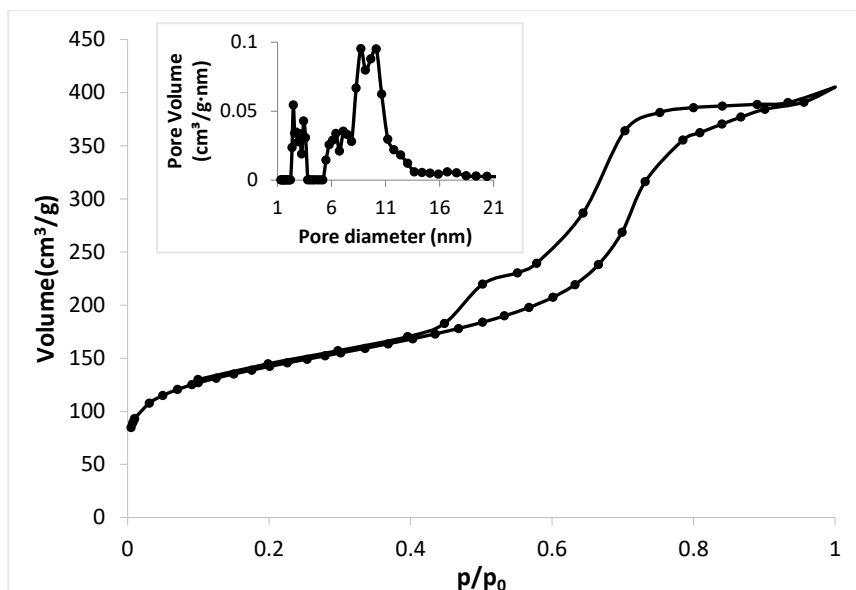


Figure 3.86: N_2 adsorption-desorption isotherm of $MSm_SD_Ce2\%^*$ and related DFT pore size distribution (inset)

Table 3.24: Structural features of $MSm_SD_Ce2\%^*$

Name	Specific surface area (m^2/g)	Pore size (nm)	Volume (cm^3/g)
$MSm_SD_Ce2\%^*$	479	9	0.59

In order to identify the oxidic phases formed by cerium, diffuse reflectance UV-vis spectroscopy was performed on the powder. The spectrum in Figure 3.87 shows the absence of peaks in the visible region characteristic of ceria in +4 oxidation state [71], thus excluding the presence of cerium in the oxidic phase.

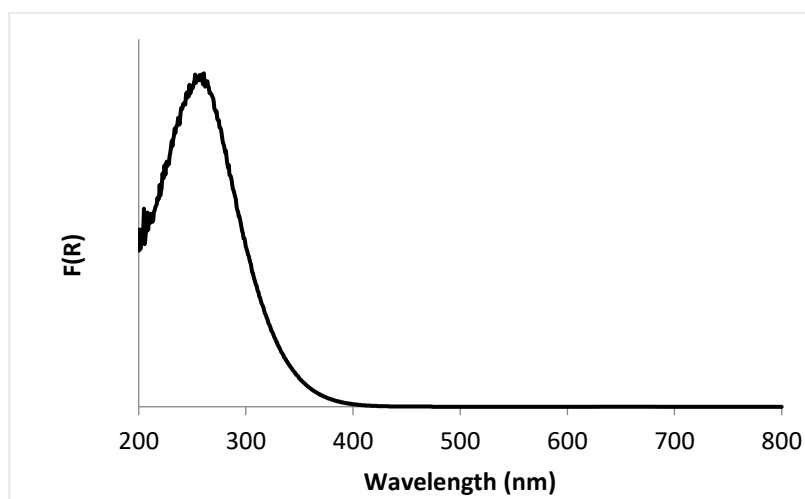


Figure 3.87: Diffuse reflectance UV-vis spectrum of $MSm_SD_Ce2\%^*$

In order to further exclude the formation of cerium oxidic phases, wide-angle XRD investigation was carried out and the pattern is depicted in Figure 3.88. The absence of relevant sharp peak characterized by high intensity confirmed the amorphous nature of the silica mesoporous micro-particles, with its characteristic broad peak between 20° and 30°.

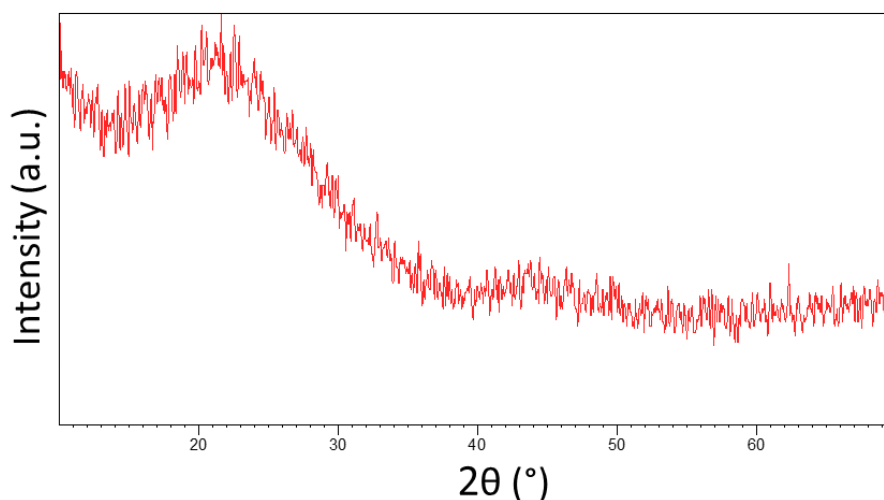


Figure 3.88: Wide-angle XRD spectrum of MSm_SD_Ce2%*

3.3.2.7b Cerium ion release from MSm_SD_Ce2%* in DMEM

Cerium release profile from mesoporous silica micro-particles in DMEM further confirmed the observations about the use of DMEM and about cerium ion reported previously in this chapter.

In details, the release kinetics is shown in Figure 3.89. In spite of the increasing trend of the curve, the ion released concentration, reached after 14 days of soaking, was 0.0025 ppm. The Ce^{3+} release properties still represent an open issue in the literature. Guangjian et al. [72] found some evidences about the formation of hydrogen bonds between hydrated Ce^{3+} and -OH on the surface of zirconium phosphate. Hence, it is reasonable to assume that the formation of bonds between the silica surface and cerium, in combination with the already observed negative influence of DMEM medium hampered the Ce^{3+} ion release from the cerium-containing micro-particles.

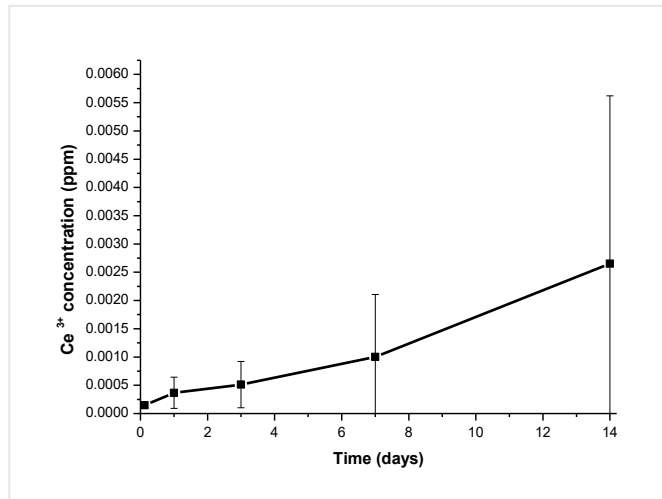


Figure 3.89: Ce³⁺ release profile of MSm_SD_Ce2%* in DMEM

3.3.2.8 Silver-containing silica SD: MSm_SD_Ag2%*

To the same purpose of MSm_SD_Ce2%*, Ag-substituted mesoporous silica micro-sized particles (98SiO₂/2AgO, named hereafter MSm_SD_Ag2%*) were synthesized by spray-drying approach in order to produce an agent for non-healing wound infected by bacteria [48].

3.3.2.8a Morphological and structural characterization of MSm_SD_Ag2%*

The morphology of the sample was not affected by both the addition of the substituent and the removal of calcium during the synthesis. The spherical particles shown in Figure 3.90 were in the range of 500 nm-5 μm.

Furthermore, the EDS investigation (Figure 3.91) revealed the silver incorporation with a molar ratio very close to the theoretical one.

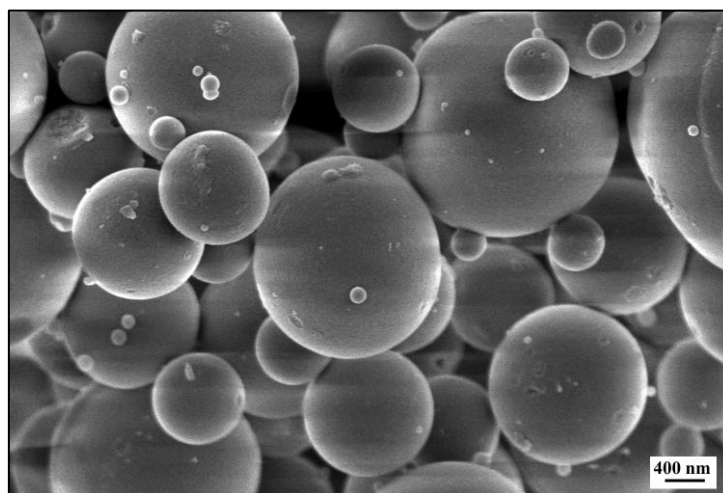


Figure 3.90: FE-SEM image of MSm_SD_Ag2%*

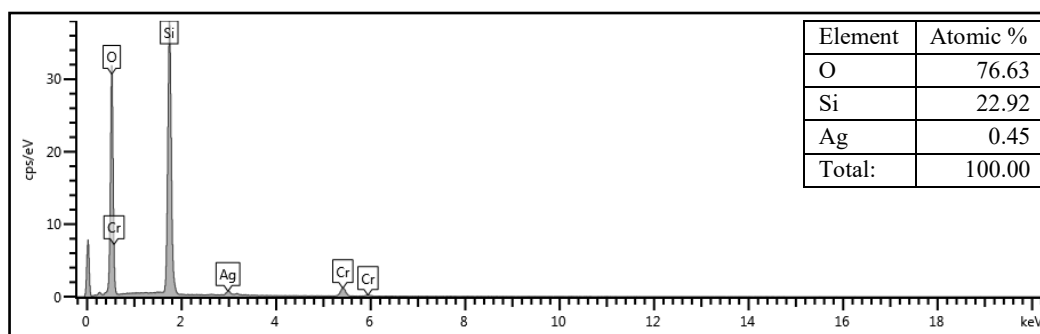


Figure 3.91: EDS spectrum of MSm_SD_Ag2%* and related element atomic %

N₂ adsorption-desorption measurements were used to identify the presence of an ordered mesoporous structure. As shown in Figure 3.92, a IV type isotherm was observed for this sample. Furthermore, the H1 hysteresis loop is discernible and is linked to the presence of pore larger than 4 nm. A further confirmation to this was given by the pore size distribution obtained through DFT method (inset in Figure 3.92), which showed a single-mode pore diameter curve of about 7.4 nm.

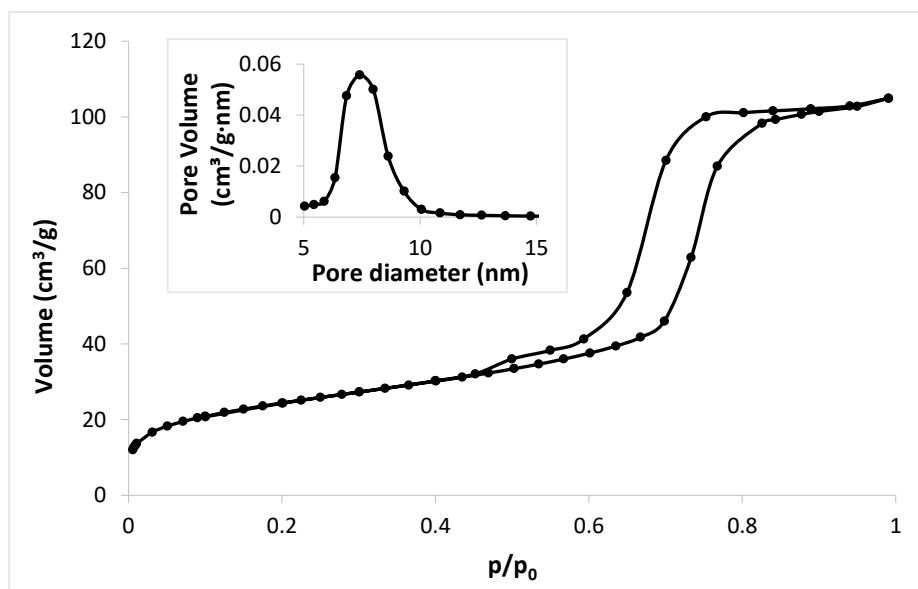


Figure 3.92: N₂ adsorption-desorption isotherm of MSm_SD_Ag2%* and related DFT pore size distribution (inset)

The structural parameters obtained through this technique are listed in Table 3.25. The specific surface area value calculated through the BET model was smaller compared to the un-doped mesoporous silica systems [73], as expected. In addition, this value is rather low, if compared to SiO₂-CaO matrices containing metallic ion and synthesized by aerosol-assisted spray-drying route [30,32,33].

Table 3.25: Structural features of MSm_SD_Ag2%*

Name	Specific surface area (m ² /g)	Pore size (nm)	Volume (cm ³ /g)
MSm_SD_Ag2%*	96	7.4	0.15

As already done for the Ag-containing mesoporous silica nano-sized particles (see paragraph 3.2.2.2a), the UV-visible technique was used in order to investigate the formation of oxidic phases within the silica framework. Figure 3.93 displayed the diffuse reflectance UV-vis spectrum of MSm_SD_Ag2%*. The broad peak in the visible band (around 420 nm) was assigned to the surface plasmon resonance of silver metallic particles. A first evidence of the presence of silver in oxide form could be derived from the colour of the powder after calcination, which showed slightly grey colour. The same correlation and observation were previously reported by others [48].

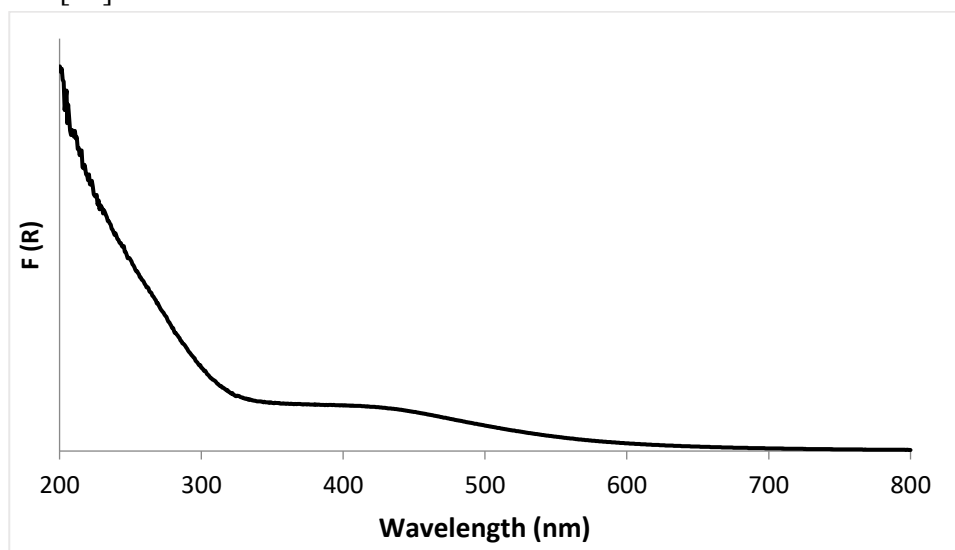


Figure 3.93: Diffuse reflectance UV-vis spectrum of MSm_SD_Ag2%*

The presence of several peaks in the wide-angle XRD pattern (Figure 3.94) suggested the formation of segregated oxidic phase, which matched by the crystalline form of silver silicate (external reference 01-076-0385).

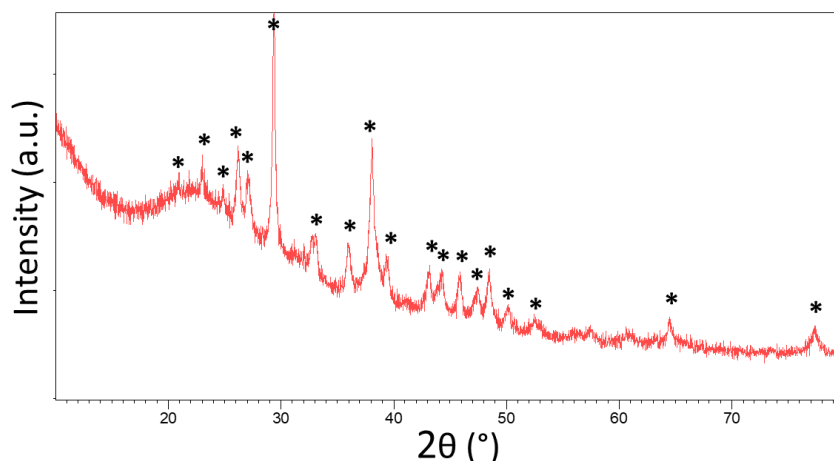


Figure 3.94: Wide-angle XRD spectrum of MSm_SD_Ag2%*

3.3.2.8b Silver ion release from MSm_SD_Ag2%* in DMEM

The release curve (Figure 3.95) reached the maximum (1.4 ppm) after 1 day of soaking, followed by a decreasing trend till the end of the test. As highlighted previously in this chapter and observed in the literature, this behaviour could be ascribed to the DMEM which may interact with the materials and hinder the ion exchange and the bioactive response more widely than SBF or PBS [9,43]. Furthermore, the decreasing release rate observed after the first day of soaking can be tentatively linked to the formation of AgCl insoluble salt due to the reaction of Ag^+ released from the micro-particles and the chloride present in DMEM solution [51].

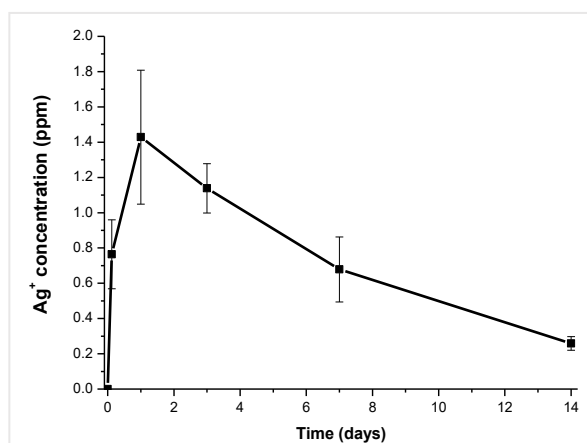


Figure 3.95: Ag⁺ release profile of MSm_SD_Ag2%* in DMEM

3.4 Final considerations

Several compositions of both micro- and nano-sized particles were successfully produced by aerosol-assisted spray-drying method and base-catalysed water-based

sol-gel route, respectively. These two complementary approaches allowed to produce a wide and versatile library of nanomatrices with different morphology, size, structural features and ion release kinetics in order to develop systems for tissue applications.

As far as morphology is concerned, the base-catalysed water-based sol-gel route allowed to obtain particles with quite uniform size ranging between 100 and 200 nm, with a spheroidal shape and slightly aggregated. The spray-drying route, instead, produced spherical, well dispersed particles with size mostly ranging between 500 nm and 5µm.

Both types of synthesis procedure enabled the formation of mesoporous structure with pores of about 4 nm for CTAB-templated system (MBG_SG samples) and around 8 nm for P123-templated nanomatrices (MBG_SD samples). The related specific surface area and pore volume, especially for MBG_SG samples, were higher compared to the not-templated conventional sol-gel glasses [74] and in line with similar ion-containing MBG particles [30,75].

The ion incorporation inside the silica framework was assessed in all nanomatrices. As a general trend, based on the compositional analysis, the ion incorporation yield was superior for spray-dried samples and might be attributed to the very fast kinetics of the process, which forces the incorporation of the ions into the silica framework during its polymerization.

Based on the obtained results, the ion release property of the nanomatrices was influenced more by the chemical composition (*i.e.* type of ion) rather than the synthesis approach.

In particular, the cerium-containing samples in both concentrations and produced by both synthesis approaches demonstrated a very low amount of released ion, confirming previous results reported in the literature [10]. The reason could be ascribed to the formation of stronger chemical bonds between Ce^{3+} and siloxanes present on the glass surface which slow down the cerium release kinetics. The same result was previously obtained by others [59,60] who found an improved chemical stability and a delay in the degradation process with the increase of cerium content in several bioactive glass compositions.

As far as the bioactive response is concerned, both MBG_SG and MBG_SD samples showed a good reactivity after soaking in SBF and they started to be covered by a rough layer composed by structures which resembled hydroxyapatite. The bioactivity test confirmed that the incorporation of different metallic ion did not hamper the ion exchange with the SBF which led to the deposition of the CaP formation, except for cerium-containing systems which showed very low bioactive response.

As a general conclusion, Cu-containing nanomatrices were evaluated as the most promising agents in terms of reproducibility for the potential applications in the tissue regeneration field.

References

- [1] A. El-Fiqi, T.H. Kim, M. Kim, M. Eltohamy, J.E. Won, E.J. Lee, H.W. Kim, Capacity of mesoporous bioactive glass nanoparticles to deliver therapeutic molecules, *Nanoscale*. 4 (2012) 7475. doi:10.1039/c2nr31775c.
- [2] K.S.W. Sing, D.H. Everett, R.A.W. Haul, L. Moscou, R.A. Pierotti, J. Rouquelon, T. Siemieniowska, Reporting physisorption data for gas/solid systems with special reference to the determination of surface area and porosity (Recommendations 1984), *Pure Appl. Chem.* 57 (1985) 603–619. doi:10.1351/pac198557040603.
- [3] I. Izquierdo-Barba, M. Vallet-Regí, Mesoporous bioactive glasses: Relevance of their porous structure compared to that of classical bioglasses, *Biomed. Glas.* 1 (2015) 140–150. doi:10.1515/bglass-2015-0014.
- [4] A.L.B. Maçon, T.B. Kim, E.M. Valliant, K. Goetschius, R.K. Brow, D.E. Day, A. Hoppe, A.R. Boccaccini, I.Y. Kim, C. Ohtsuki, T. Kokubo, A. Osaka, M. Vallet-Regí, D. Arcos, L. Fraile, A.J. Salinas, A. V. Teixeira, Y. Vueva, R.M. Almeida, M. Miola, C. Vitale-Brovarone, E. Verné, W. Höland, J.R. Jones, A unified in vitro evaluation for apatite-forming ability of bioactive glasses and their variants, *J. Mater. Sci. Mater. Med.* 26 (2015) 1–10. doi:10.1007/s10856-015-5403-9.
- [5] V. Uskoković, D.P. Uskoković, Nanosized hydroxyapatite and other calcium phosphates: Chemistry of formation and application as drug and gene delivery agents, *J. Biomed. Mater. Res. - Part B Appl. Biomater.* 96 B (2011) 152–191. doi:10.1002/jbm.b.31746.
- [6] K. Lin, C. Wu, J. Chang, Advances in synthesis of calcium phosphate crystals with controlled size and shape, *Acta Biomater.* 10 (2014) 4071–4102. doi:10.1016/j.actbio.2014.06.017.
- [7] C. Wu, Y. Zhou, M. Xu, P. Han, L. Chen, J. Chang, Y. Xiao, Copper-containing mesoporous bioactive glass scaffolds with multifunctional properties of angiogenesis capacity, osteostimulation and antibacterial activity, *Biomaterials*. 34 (2013) 422–433. doi:10.1016/j.biomaterials.2012.09.066.
- [8] A. Bari, N. Bloise, S. Fiorilli, G. Novajra, M. Vallet-Regí, G. Bruni, A. Torres-Pardo, J.M. González-Calbet, L. Visai, C. Vitale-Brovarone, Copper-containing mesoporous bioactive glass nanoparticles as multifunctional agent for bone regeneration, *Acta Biomater.* 55 (2017) 493–504. doi:10.1016/j.actbio.2017.04.012.
- [9] M. Shi, Z. Chen, S. Farnaghi, T. Friis, X. Mao, Y. Xiao, C. Wu, Copper-doped mesoporous silica nanospheres, a promising immunomodulatory agent for inducing osteogenesis, *Acta Biomater.* 30 (2016) 334–344. doi:10.1016/j.actbio.2015.11.033.
- [10] A.J. Salinas, S. Shruti, G. Malavasi, L. Menabue, M. Vallet-Regí, Substitutions of cerium, gallium and zinc in ordered mesoporous bioactive glasses, *Acta Biomater.* 7 (2011) 3452–3458. doi:10.1016/j.actbio.2011.05.033.
- [11] F.E. López-Suárez, S. Parres-Esclapez, A. Bueno-López, M.J. Illán-Gómez, B. Ura, J. Trawczynski, Role of surface and lattice copper species in copper-containing (Mg/Sr)TiO₃ perovskite catalysts for soot combustion, *Appl.*

- Catal. B Environ. 93 (2009) 82–89. doi:10.1016/j.apcatb.2009.09.015.
- [12] B.E. Goodby, J.E. Pemberton, XPS characterization of a commercial Cu / ZnO / Al₂O₃ catalyst: Effects of oxidation, reduction, and the steam reformation of methanol, 42 (1988) 754–760.
- [13] H. Zhang, C. Tang, Y. Lv, C. Sun, F. Gao, L. Dong, Y. Chen, Synthesis, characterization, and catalytic performance of copper-containing SBA-15 in the phenol hydroxylation, J. Colloid Interface Sci. 380 (2012) 16–24. doi:10.1016/j.jcis.2012.04.059.
- [14] M. Mozafari, F. Moztarzadeh, M. Tahriri, Investigation of the physico-chemical reactivity of a mesoporous bioactive SiO₂-CaO-P₂O₅ glass in simulated body fluid, J. Non. Cryst. Solids. 356 (2010) 1470–1478. doi:10.1016/j.jnoncrysol.2010.04.040.
- [15] P. Siriphannon, Y. Kameshima, A. Yasumori, Formation of hydroxyapatite on CaSiO₃ powders in simulated body fluid, J. Eur. Ceram. Soc. 22 (2002) 511–520. doi:10.1016/s0955-2219(01)00301-6.
- [16] A. Martínez, I. Izquierdo-Barba, M. Vallet-Regí, Bioactivity of a CaO–SiO₂ Binary Glasses System, Chem. Mater. 12 (2000) 3080–3088. doi:10.1021/cm001107o.
- [17] H. Ohgushi, M. Okumura, T. Yoshikawa, K. Inoue, N. Senpuku, S. Tamai, Bone formation process in porous calcium carbonate and hydroxyapatite, J. Biomed. Mater. Res. 26 (1992) 885–895. doi:10.1002/jbm.820260705.
- [18] Y. Fujita, T. Yamamuro, T. Nakamura, S. Kotani, C. Ohtsuki, T. Kokubo, The bonding behavior of calcite to bone, J. Biomed. Mater. Res. 25 (1991) 991–1003. doi:10.1002/jbm.820250806.
- [19] M. Mami, A. Lucas-Girot, H. Oudadesse, R. Dorbez-Sridi, F. Mezahi, E. Dietrich, Investigation of the surface reactivity of a sol-gel derived glass in the ternary system SiO₂-CaO-P₂O₅, Appl. Surf. Sci. 254 (2008) 7386–7393. doi:10.1016/j.apsusc.2008.05.340.
- [20] S. Shrivastava, T. Bera, A. Roy, G. Singh, P. Ramachandrarao, D. Dash, Characterization of enhanced antibacterial effects of novel silver nanoparticles, Nanotechnology. 18 (2007) 225103. doi:10.1088/0957-4484/18/22/225103.
- [21] H. Li, Q. Chen, J. Zhao, K. Urmila, Enhancing the antimicrobial activity of natural extraction using the synthetic ultrasmall metal nanoparticles, Sci. Rep. 5 (2015) 1–13. doi:10.1038/srep11033.
- [22] Y.S.E. Lin, R.D. Vidic, J.E. Stout, C.A. McCartney, V.L. Yu, Inactivation of Mycobacterium avium by copper and silver ions, Water Res. 32 (1998) 1997–2000. doi:10.1016/S0043-1354(97)00460-0.
- [23] E. Ladomersky, M.J. Petris, Copper tolerance and virulence in bacteria, Metallomics. 7 (2015) 957–964. doi:10.1039/c4mt00327f.
- [24] S. Hu, J. Chang, L. Mingqiu, C. Ning, Study on antibacterial effect of 45S5 Bioglass, J. Mater. Sci. Mater. Med. 20 (2009) 281–286. doi:10.1007/s10856-008-3564-5.
- [25] V. Mortazavi, M. Mehdikhani Nahrkhalaji, M.H. Fathi, S.B. Mousavi, B. Nasr Esfahani, Antibacterial effects of sol-gel-derived bioactive glass nanoparticle on aerobic bacteria, J. Biomed. Mater. Res. - Part A. 94 (2010) 160–168. doi:10.1002/jbm.a.32678.
- [26] A. Cochis, B. Azzimonti, R. Sorrentino, C. Della Valle, E. De Giglio, N. Bloise, L. Visai, G. Bruni, S. Cometa, D. Pezzoli, G. Candiani, L. Rimondini, R. Chiesa, Data in support of Gallium (Ga³⁺) antibacterial activities to

- counteract *E. coli* and *S. epidermidis* biofilm formation onto osteointegrative titanium surfaces, *Data Br.* 6 (2016) 758–762. doi:10.1016/j.dib.2016.01.024.
- [27] M.S. Sbarra, C.R. Arciola, A. Di Poto, E. Saino, H. Rohde, P. Speziale, L. Visai, The photodynamic effect of tetra-substituted N-methyl-pyridyl-porphine combined with the action of vancomycin or host defense mechanisms disrupts *Staphylococcus epidermidis* biofilms, *Int. J. Artif. Organs.* 32 (2009) 574–583. doi:10.1177/039139880903200906.
- [28] E. Gentleman, Y.C. Fredholm, G. Jell, N. Lotfibakhshaiesh, M.D. O'Donnell, R.G. Hill, M.M. Stevens, The effects of strontium-substituted bioactive glasses on osteoblasts and osteoclasts in vitro, *Biomaterials.* 31 (2010) 3949–3956. doi:10.1016/j.biomaterials.2010.01.121.
- [29] G. Molino, A. Bari, F. Baino, S. Fiorilli, C. Vitale-Brovarone, Electrophoretic deposition of spray-dried Sr-containing mesoporous bioactive glass spheres on glass–ceramic scaffolds for bone tissue regeneration, *J. Mater. Sci.* 52 (2017) 9103–9114. doi:10.1007/s10853-017-1026-5.
- [30] S. Fiorilli, G. Molino, C. Pontremoli, G. Iviglia, E. Torre, C. Cassinelli, M. Morra, C. Vitale-Brovarone, The incorporation of strontium to improve bone-regeneration ability of mesoporous bioactive glasses, *Materials (Basel).* 11 (2018). doi:10.3390/ma11050678.
- [31] J. Lao, E. Jallot, J.M. Nedelec, Strontium-delivering glasses with enhanced bioactivity: A new biomaterial for antiosteoporotic applications?, *Chem. Mater.* 20 (2008) 4969–4973. doi:10.1021/cm800993s.
- [32] C. Pontremoli, M. Boffito, S. Fiorilli, R. Laurano, A. Torchio, A. Bari, C. Tonda-Turo, G. Ciardelli, C. Vitale-Brovarone, Hybrid injectable platforms for the in situ delivery of therapeutic ions from mesoporous glasses, *Chem. Eng. J.* 340 (2018) 103–113. doi:10.1016/j.cej.2018.01.073.
- [33] A. Bari, G. Molino, S. Fiorilli, C. Vitale-Brovarone, Novel multifunctional strontium-copper co-substituted mesoporous bioactive particles, *Mater. Lett.* 223 (2018) 37–40. doi:10.1016/j.matlet.2018.04.006.
- [34] R. Mortera, S. Fiorilli, E. Garrone, E. Verné, B. Onida, Pores occlusion in MCM-41 spheres immersed in SBF and the effect on ibuprofen delivery kinetics: A quantitative model, *Chem. Eng. J.* 156 (2010) 184–192. doi:10.1016/j.cej.2009.10.018.
- [35] Y.C. Fredholm, N. Karpukhina, D.S. Brauer, J.R. Jones, R. V Law, G. Hill, Y.C. Fredholm, N. Karpukhina, D.S. Brauer, Influence of strontium for calcium substitution in bioactive glasses on degradation, ion release and apatite formation, *J. R. Soc. Interface.* 9 (2011) 880–889. doi:10.1098/rsif.2011.0387.
- [36] S. Taherkhani, F. Moztarzadeh, Influence of strontium on the structure and biological properties of sol–gel-derived mesoporous bioactive glass (MBG) powder, *J. Sol-Gel Sci. Technol.* 78 (2016) 539–549. doi:10.1007/s10971-016-3995-2.
- [37] S. Hesaraki, M. Gholami, S. Vazehrad, S. Shahrabi, The effect of Sr concentration on bioactivity and biocompatibility of sol-gel derived glasses based on CaO–SrO–SiO₂–P₂O₅ quaternary system, *Mater. Sci. Eng. C.* 30 (2010) 383–390. doi:10.1016/j.msec.2009.12.001.
- [38] L.L. Hench, N. Roki, M.B. Fenn, Bioactive glasses: Importance of structure and properties in bone regeneration, *J. Mol. Struct.* 1073 (2014) 24–30. doi:10.1016/j.molstruc.2014.03.066.

- [39] Y.C. Fredholm, N. Karpukhina, R. V. Law, R.G. Hill, Strontium containing bioactive glasses: Glass structure and physical properties, *J. Non. Cryst. Solids.* 356 (2010) 2546–2551. doi:10.1016/j.jnoncrysol.2010.06.078.
- [40] J.E. Gough, J.R. Jones, L.L. Hench, Nodule formation and mineralisation of human primary osteoblasts cultured on a porous bioactive glass scaffold, *Biomaterials.* 25 (2004) 2039–2046. doi:10.1016/j.biomaterials.2003.07.001.
- [41] C. Wu, J. Chang, W. Fan, Bioactive mesoporous calcium-silicate nanoparticles with excellent mineralization ability, osteostimulation, drug-delivery and antibacterial properties for filling apex roots of teeth, *J. Mater. Chem.* 22 (2012) 16801–16809. doi:10.1039/c2jm33387b.
- [42] E.M. Valliant, C.A. Turdean-Ionescu, J. V. Hanna, M.E. Smith, J.R. Jones, Role of pH and temperature on silica network formation and calcium incorporation into sol-gel derived bioactive glasses, *J. Mater. Chem.* 22 (2012) 1613–1619. doi:10.1039/c1jm13225c.
- [43] G. Lutišánová, M.T. Palou, J. Kozánková, Mechanism of bioactivity of LS2-FA glass-ceramics in SBF and DMEM medium, *Ceram. - Silikaty.* 56 (2012) 229–237.
- [44] Y. Wang, Q. Zhao, N. Han, L. Bai, J. Li, J. Liu, E. Che, L. Hu, Q. Zhang, T. Jiang, S. Wang, Mesoporous silica nanoparticles in drug delivery and biomedical applications, *Nanomedicine Nanotechnology, Biol. Med.* 11 (2015) 313–327. doi:10.1016/j.nano.2014.09.014.
- [45] I. Izquierdo-Barba, L. Ruiz-González, J.C. Doadrio, J.M. González-Calbet, M. Vallet-Regí, Tissue regeneration: A new property of mesoporous materials, *Solid State Sci.* 7 (2005) 983–989. doi:10.1016/j.solidstatesciences.2005.04.003.
- [46] M. Kawashita, S. Tsuneyama, F. Miyaji, T. Kokubo, H. Kozuka, K. Yamamoto, Antibacterial silver-containing silica glass prepared by sol-gel method, *Biomaterials.* 21 (2000) 393–398. doi:10.1016/S0142-9612(99)00201-X.
- [47] M. Thommes, K. Kaneko, A. V. Neimark, J.P. Olivier, F. Rodriguez-Reinoso, J. Rouquerol, K.S.W. Sing, Physisorption of gases, with special reference to the evaluation of surface area and pore size distribution (IUPAC Technical Report), *Pure Appl. Chem.* 87 (2015) 1051–1069. doi:10.1515/pac-2014-1117.
- [48] C.R. Mariappan, N. Ranga, Influence of silver on the structure, dielectric and antibacterial effect of silver doped bioglass-ceramic nanoparticles, *Ceram. Int.* 43 (2017) 2196–2201. doi:10.1016/j.ceramint.2016.11.003.
- [49] N. Bogdanchikova, F.C. Meunier, M. Avalos-Borja, J.P. Breen, A. Pestryakov, On the nature of the silver phases of Ag/Al₂O₃ catalysts for reactions involving nitric oxide, *Appl. Catal. B-Environmental.* 36 (2002) 287–297. doi:10.1016/S0926-3373(01)00286-7.
- [50] Z. Fang, S. Li, Y. Gong, W. Liao, S. Tian, C. Shan, C. He, Comparison of catalytic activity of carbon-based AgBr nanocomposites for conversion of CO₂ under visible light, *J. Saudi Chem. Soc.* 18 (2014) 299–307. doi:10.1016/j.jscs.2013.08.003.
- [51] N. Gargiulo, A.M. Cusano, F. Causa, D. Caputo, P.A. Netti, Silver-containing mesoporous bioactive glass with improved antibacterial properties, *J. Mater. Sci. Mater. Med.* 24 (2013) 2129–2135. doi:10.1007/s10856-013-4968-4.

- [52] Y. Lin, Z. Yang, J. Cheng, Preparation, characterization and antibacterial property of cerium substituted hydroxyapatite nanoparticles, *J. Rare Earths*. 25 (2007) 452–456. doi:10.1016/S1002-0721(07)60455-4.
- [53] C. Xu, X. Qu, Cerium oxide nanoparticle: A remarkably versatile rare earth nanomaterial for biological applications, *NPG Asia Mater.* 6 (2014) e90. doi:10.1038/am.2013.88.
- [54] Z. Assefa, R.G. Haire, D.L. Caulder, D.K. Shuh, Correlation of the oxidation state of cerium in sol-gel glasses as a function of thermal treatment via optical spectroscopy and XANES studies, *Spectrochim. Acta - Part A Mol. Biomol. Spectrosc.* 60 (2004) 1873–1881. doi:10.1016/j.saa.2003.10.005.
- [55] K.K. Babitha, A. Sreedevi, K.P. Priyanka, B. Sabu, T. Varghese, Structural characterization and optical studies of CeO₂ nanoparticles synthesized by chemical precipitation, *Indian J. Pure Appl. Phys.* 53 (2015) 596–603.
- [56] V. Aina, G. Malavasi, A. Fiorio Pla, L. Munaron, C. Morterra, Zinc-containing bioactive glasses: Surface reactivity and behaviour towards endothelial cells, *Acta Biomater.* 5 (2009) 1211–1222. doi:10.1016/j.actbio.2008.10.020.
- [57] D.S. Morais, S. Fernandes, P.S. Gomes, M.H. Fernandes, P. Sampaio, M.P. Ferraz, J.D. Santos, M.A. Lopes, N. Sooraj Hussain, Novel cerium doped glass-reinforced hydroxyapatite with antibacterial and osteoconductive properties for bone tissue regeneration, *Biomed. Mater.* 10 (2015) 55008. doi:10.1088/1748-6041/10/5/055008.
- [58] G. Ciobanu, A. Maria Bargan, C. Luca, New cerium(IV)-substituted hydroxyapatite nanoparticles: Preparation and characterization, *Ceram. Int.* 41 (2014) 12192–12201. doi:10.1016/j.ceramint.2015.06.040.
- [59] A.M. Deliormanlı, Synthesis and characterization of cerium- and gallium-containing borate bioactive glass scaffolds for bone tissue engineering, *J. Mater. Sci. Mater. Med.* 26 (2015) 1–13. doi:10.1007/s10856-014-5368-0.
- [60] S. Shruti, A.J. Salinas, G. Malavasi, G. Lusvardi, L. Menabue, C. Ferrara, P. Mustarelli, M. Vallet-Regí, Structural and in vitro study of cerium, gallium and zinc containing sol-gel bioactive glasses, *J. Mater. Chem.* 22 (2012) 13698–13706. doi:10.1039/c2jm31767b.
- [61] C. Marambio-Jones, E.M.V. Hoek, A review of the antibacterial effects of silver nanomaterials and potential implications for human health and the environment, *J. Nanoparticle Res.* 12 (2010) 1531–1551. doi:10.1007/s11051-010-9900-y.
- [62] A.M. El-Kady, A.F. Ali, R.A. Rizk, M.M. Ahmed, Synthesis, characterization and microbiological response of silver doped bioactive glass nanoparticles, *Ceram. Int.* 38 (2012) 177–188. doi:10.1016/j.ceramint.2011.05.158.
- [63] L. Pontiroli, M. Dadkhah, G. Novajra, I. Tcacencu, S. Fiorilli, C. Vitale-Brovarone, An aerosol-spray-assisted approach to produce mesoporous bioactive glass microspheres under mild acidic aqueous conditions, *Mater. Lett.* 190 (2017) 111–114. doi:10.1016/j.matlet.2016.12.125.
- [64] A. López-Noriega, D. Arcos, I. Izquierdo-Barba, Y. Sakamoto, O. Terasaki, M. Vallet-Regí, Ordered mesoporous bioactive glasses for bone tissue regeneration, *Chem. Mater.* 18 (2006) 3137–3144. doi:10.1021/cm060488o.
- [65] P. Li, I. Kangasniemi, K. de Groot, T. Kokubo, A.U. Yli-Urpo, Apatite crystallization from metastable calcium phosphate solution on sol-gel-prepared silica, *J. Non. Cryst. Solids.* 168 (1994) 281–286. doi:10.1016/0022-3093(94)90340-9.

- [66] P. Li, K. Nakanishi, T. Kokubo, K. de Groot, Induction and morphology of hydroxyapatite, precipitated from metastable simulated body fluids on sol-gel prepared silica, *Biomaterials*. 14 (1993) 963–968. doi:10.1016/0142-9612(93)90186-6.
- [67] S. Fiorilli, F. Tallia, L. Pontiroli, C. Vitale-Brovarone, B. Onida, Spray-dried mesoporous silica spheres functionalized with carboxylic groups, *Mater. Lett.* 108 (2013) 118–121. doi:10.1016/j.matlet.2013.06.040.
- [68] K.K. Kaysinger, W.K. Ramp, Extracellular pH modulates the activity of cultured human osteoblasts., *J. Cell. Biochem.* 68 (1998) 83–89. doi:10.1002/(SICI)1097-4644(19980101)68:1<83::AID-JCB8>3.0.CO;2-S.
- [69] D. Arcos, A. López-Noriega, E. Ruiz-Hernández, O. Terasaki, M. Vallet-Regí, Ordered mesoporous microspheres for bone grafting and drug delivery, *Chem. Mater.* 21 (2009) 1000–1009. doi:10.1021/cm801649z.
- [70] K.J. Woo, C.K. Hye, W.K. Ki, S. Shin, H.K. So, H.P. Yong, Antibacterial activity and mechanism of action of the silver ion in *Staphylococcus aureus* and *Escherichia coli*, *Appl. Environ. Microbiol.* 74 (2008) 2171–2178. doi:10.1128/AEM.02001-07.
- [71] Y.F. Goh, A.Z. Alshemary, M. Akram, M.R. Abdul Kadir, R. Hussain, In-vitro characterization of antibacterial bioactive glass containing ceria, *Ceram. Int.* 40 (2014) 729–737. doi:10.1016/j.ceramint.2013.06.062.
- [72] G. Dai, A. Yu, X. Cai, Q. Shi, Y. Ouyang, S. Tan, Synthesis, characterization and antimicrobial activity of zinc and cerium co-doped α -zirconium phosphate, *J. Rare Earths*. 30 (2012) 820–825. doi:10.1016/S1002-0721(12)60137-9.
- [73] I.I. Slowing, J.L. Vivero-Escoto, C.W. Wu, V.S.Y. Lin, Mesoporous silica nanoparticles as controlled release drug delivery and gene transfection carriers, *Adv. Drug Deliv. Rev.* 60 (2008) 1278–1288. doi:10.1016/j.addr.2008.03.012.
- [74] S. Midha, T.B. Kim, W. Van Den Bergh, P.D. Lee, J.R. Jones, C.A. Mitchell, Preconditioned 70S30C bioactive glass foams promote osteogenesis in vivo, *Acta Biomater.* 9 (2013) 9169–9182. doi:10.1016/j.actbio.2013.07.014.
- [75] L.B. Romero-Sánchez, M. Mari-Beffa, P. Carrillo, M.Á. Medina, A. Díaz-Cuenca, Copper-containing mesoporous bioactive glass promotes angiogenesis in an in vivo zebrafish model, *Acta Biomater.* 68 (2018) 272–285. doi:10.1016/j.actbio.2017.12.032.
- [76] S.P. Fricker, The therapeutic application of lanthanides, *Chem. Soc. Rev.* 35 (2006) 524–533. doi:10.1039/b509608c.
- [77] C.A. Barta, K. Sachs-Barrable, J. Jia, K.H. Thompson, K.M. Wasan, C. Orvig, Lanthanide containing compounds for therapeutic care in bone resorption disorders, *Dalt. Trans.* (2007) 5019–5030. doi:10.1039/b705123a.
- [78] K. Wang, R. Li, Y. Cheng, B. Zhu, Lanthanides - The future drugs?, *Coord. Chem. Rev.* 190–192 (1999) 297–308. doi:10.1016/S0010-8545(99)00072-7.

CHAPTER 4

Antibacterial tests of ion-substituted nano- and micro-sized MBGs

4.1 Introduction

The nano- and micro-sized, referred as MBG_{SG} and MBG_{SD}, respectively, containing ions with recognized antibacterial property (copper, cerium and silver) were also tested through antibacterial assays. The tests were carried out against clinical isolates of *Staphylococcus aureus* (S235) and *Pseudomonas aeruginosa* (SOM1), representative of *Gram positive* and *Gram negative* bacteria, respectively, which commonly cause infection in both chronic skin wounds and bone fractures [1,2].

As already described in the “Materials and Methods” chapter, the antibacterial tests were initially attempted using standard MIC (minimum inhibitory concentration) tests in 96 well plates. The MIC is the lowest concentration of antimicrobial agent able to inhibit the bacterial growth. Since the bacterial growth leads to the cloudiness of the medium, the MIC is identified by evaluating the clarity of this medium by visual inspection.

However, this method has proved to be unsuitable for the tested samples since the broth resulted cloudy even in the absence of microorganisms due to the presence of dispersed MBG particles.

Subsequently, MIC test was attempted by placing the particles within transwell inserts (transwell-96 well, 0.4 μm pore sizes) in order to allow the diffusion of ions into broth containing the bacteria. Nevertheless, the smallest particles were able to go through the transwell pores, as well, causing the broth to turn cloudy even in absence of bacteria strains.

Considering the issues related to MIC assay with the MBG nanomatrices, this standard bacterial viability test was replaced by the counting colony forming units (CFU) test. In microbiology, a “viable” organism is defined as an organism able to multiply via binary fission under controlled conditions.

Two different experimental conditions were used to evaluate the antibacterial activity of ion-containing nanomatrices, as described in the “Material and methods” section. In details, the antibacterial potential of suspended nanomatrices (named hereafter “suspension”) and the antibacterial efficacy of the released ion extracts (named hereafter “extract”) were tested in order to ascribe the therapeutic effect to the particle itself or to the action of specific ion, or to a combination of both effects. The results are presented as reduction of viable bacteria compared to the control (bacterial samples incubated with PBS without the particles) using the following equation:

$$(\text{CFU sample} \times 100) / \text{CFU control}$$

4.2 Antibacterial property of MBG_SD_Cu2% and MBG_SG_Cu2% against planktonic bacteria

The sensitivity of S235 and SOM1 against copper-containing micro- and nano-sized particles and the related extracts are displayed in Figure 4.1 and Figure 4.2, respectively.

The results shown in Figure 4.1 evidenced high antibacterial efficacy of both copper-containing particles (suspension) and the copper ion released from the samples (extracts). Both the experimental conditions demonstrated a reduction of the survival rate of S235 up to almost zero. After 1 day of soaking, MBG_SD_Cu2% did not cause relevant decrease in the bacteria viability. At variance, MBG_SG_Cu2% after 1 day of soaking provoked a 99% of reduction, as can be deduced by the absence of orange columns in Figure 4.1. This difference could be linked to the ion release property of the tested samples (Table 4.1): as shown in chapter 3, almost the total amount of incorporated copper in MBG_SG_Cu2% (see section 3.3.1.1b) was released within the first 3 h of incubation; while it was demonstrated that the diffusion of copper ions from MBG_SD_Cu2% (see section 3.3.2.2b) was blocked during the first hours of soaking most likely due to faster hydroxyapatite deposition.

Table 4.1: Summary of Cu²⁺ released in Tris HCl

Sample	3h of soaking (ppm)	1d of soaking (ppm)	3d of soaking (ppm)	7d of soaking (ppm)	14d of soaking (ppm)
MBG_SG_Cu2%	4.45	4.50	4.77	4.50	4.77
MBG_SD_Cu2%	1.86	1.86	2.24	2.44	2.44

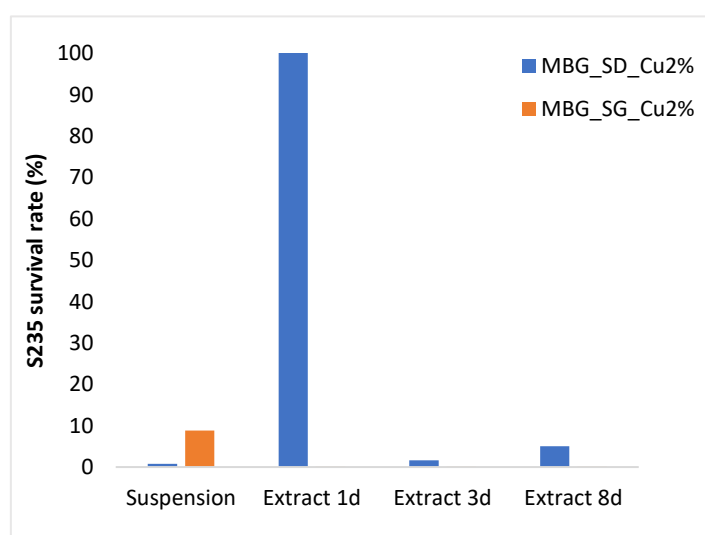


Figure 4.1: Survival rate of S235 after exposure to MBG_SD_Cu2%, MBG_SG_Cu2% and related extracts after 1 day, 3 days and the 8 days of soaking

Antibacterial potential of copper-containing samples and copper ion released from the samples was tested against SOM1, as representative of *Gram negative* bacteria strain. Figure 4.2 depicts the results of both experimental conditions

(suspension and extracts). Although after 3 days of soaking, the ion released amount provoked a high reduction of survival rate (20%), the other columns in the graph show high percentage of viable bacteria colonies, highlighting the different mode of action of the sample against *Gram positive* (Figure 4.1) and *Gram negative* (Figure 4.2) bacteria.

The different S235 and SOM1 bacteria sensitivity to copper-containing samples, attributed to the different bacteria structure of *Gram positive* and *Gram negative* bacteria strains, was already evidenced in ref. [3] using the MBG_US_m_Cu2%, as antimicrobial agent, and the related results are explained in the paragraph 3.2.1.2d.

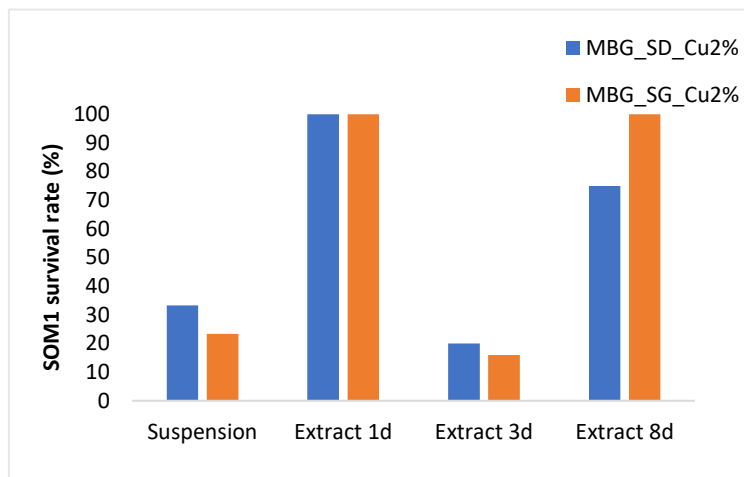


Figure 4.2: Survival rate of SOM1 after exposure to MBG_SD_Cu2%, MBG_SG_Cu2% and related extracts after 1 day, 3 days and 8 days of soaking

4.3 Antibacterial property of MBG_SD_Ce2% and MBG_SG_Ce2% against planktonic bacteria

The antibacterial activity of cerium-containing particles was tested against S235 and SOM1 and the results of the viable count method are shown in Figure 4.3 and Figure 4.4.

The suspension columns of both graphs evidenced a scarce antibacterial potential related to the particles themselves (first experimental condition). Differently, the survival rate of S235 (Figure 4.3) after contact with cerium-compound extracts showed a marked reduction of viable colonies with longer incubation times (8 days). The effect of cerium ions on different bacteria strains was investigated by Morais et al. [4] by studying the antibacterial potential of cerium-containing hydroxyapatite composite. They speculated that the cerium ions may influence the bacteria metabolism and that the uptake of cerium into cytoplasm could block the cellular respiration.

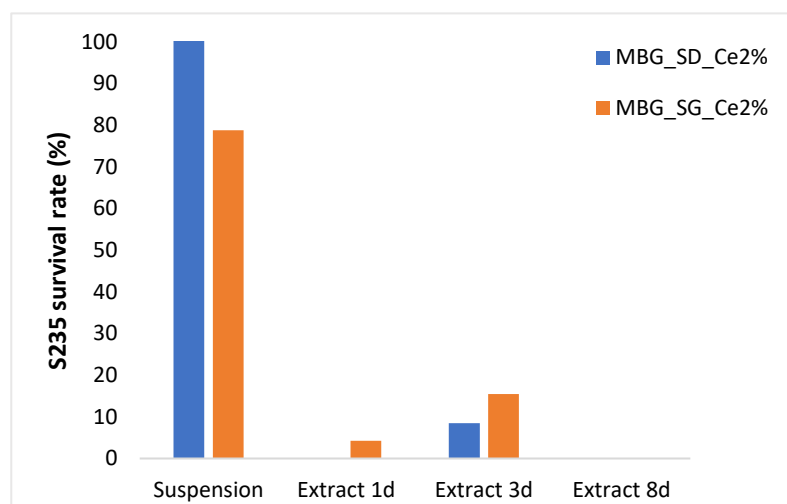


Figure 4.3: Survival rate of S235 after exposure to MBG_SD_Ce2%, MBG_SG_Ce2% and related extracts after 1 day, 3 days and the 8 days of soaking

As far as SOM1 sensitivity is concerned, the MBG_SD_Ce2% demonstrated different antibacterial activity respect to MBG_SG_Ce2%. The micro-sized particles (first experimental condition) led to a reduction of 60% of the survival rate. By comparison, no SOM1 viable reduction was encountered with the nano-sized particles. Considering that the chemical composition of the samples is the same, the different behaviour could be attributed to the different size and the associated particle dispersion. Since the spray-dried micro-particles give a more stable suspension, evaluated by DLS measurements (data not shown) compared to the nano-sized particles, it is expected a more effective particle-bacteria interaction with higher antibacterial efficacy.

The effect of the extracts from MBG_SD_Ce2% demonstrated a decrease of viable SOM1 as the soaking time increased. At variance, the antibacterial effect of Ce ions from MBG_SG_Ce2% showed the opposite trend: by increasing the incubation time of particles in PBS, the effect of the released ions became not sufficient to kill the bacteria. Considering that no refresh of the PBS solution containing the sample was performed during the entire test, the trend of MBG_SG_Ce2% shown in Figure 4.4 could be tentatively ascribed to the formation of cerium phosphate aggregates which subtracted Ce ions from the solution. The hypothesis of the formation of a mixed phase composed by cerium and calcium phosphate was already made by Shruti et al. [5] when evaluating the *in vitro* bioactive response of cerium substituted sol-gel bioactive glass.

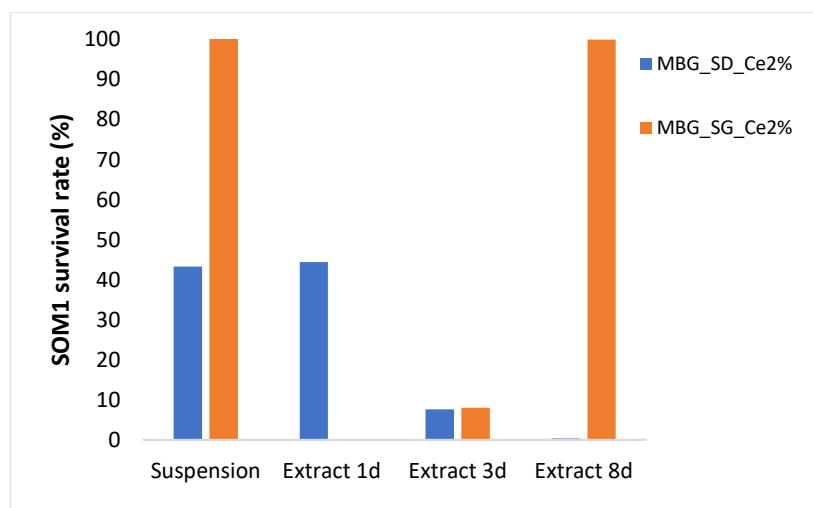


Figure 4.4: Survival rate of SOM1 after exposure to MBG_SD_Ce2%, MBG_SG_Ce2% and related extracts after 1 day, 3 days and the 8 days of soaking

4.4 Antibacterial property of MBG_SD_Ag2% and MBG_SG_Ag2% against planktonic bacteria

The antibacterial properties of silver-containing compounds were proved following the viable count method explained in “Materials and methods” section and Figure 4.5 and Figure 4.6 showed the results concerning the S235 and SOM1 survival rate, respectively.

The first experimental condition using both micro- and nano-sized Ag-substituted MBGs showed a reduction of >99% of both bacteria strains.

After 1 day of incubation, the silver released from MBG_SD_Ag2% allowed the reduction of S235 survival rate to 10%, differently from MBG_SG_Ag2% at the same time point in accordance with the ion release kinetics (see paragraphs 3.3.1.3b and 3.3.2.6b). The Ag-modified systems, in fact, showed a higher ion released concentration (Table 4.2) from MBG_SD_Ag2% compared to the nano-sized particles at the same time point (see Figure 3.54B and Figure 3.83B).

Table 4.2: Summary of Ag⁺ release in Tris HCl

Sample	3h of soaking (ppm)	1d of soaking (ppm)	3d of soaking (ppm)	7d of soaking (ppm)	14d of soaking (ppm)
MBG_SG_Ag2%	1.57	2.71	3.65	5.02	6.29
MBG_SD_Ag2%	3.08	4.67	5.58	6.36	7.53

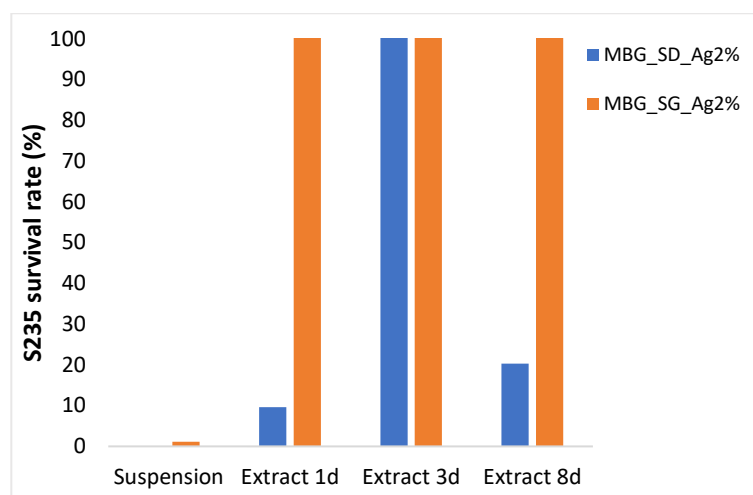


Figure 4.5: Survival rate of S235 after exposure to MBG_SD_Ag2%, MBG_SG_Ag2% and related extracts after 1 day, 3 days and the 8 days of soaking

As far as SOM1 is concerned, the results are reported in Figure 4.6.

As already noticed with S235, the antibacterial effect of silver-containing particles (first experimental condition) was more effective in reducing the bacteria viable colonies compared to the extracts. The results related to the second experimental condition showed a decreasing antibacterial effect with the increase of the soaking time for both samples. Considering that the second experimental condition was carried out without the refresh or the replace of PBS medium, the decreasing effect of the silver ion released could be ascribed to the formation of not soluble silver-aggregates (*e.g.* silver phosphates) through reaction between Ag^+ released and phosphate ions from PBS.

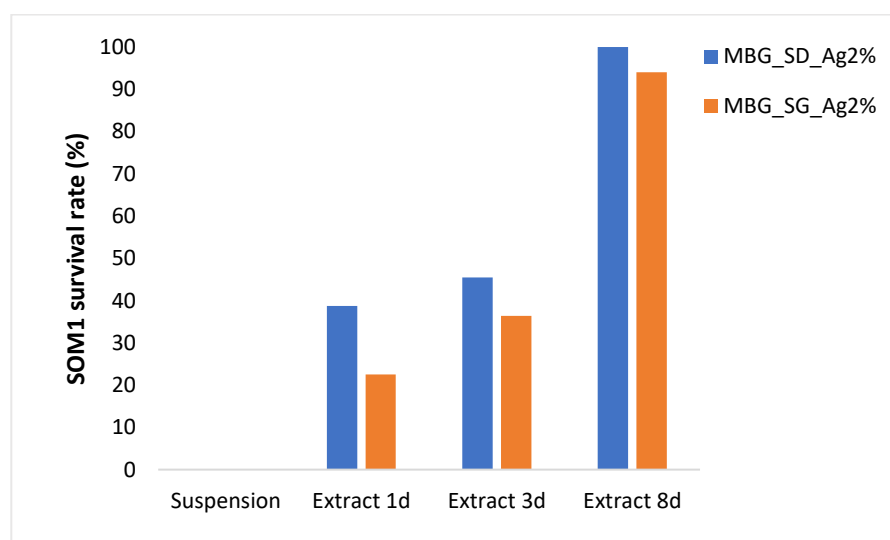


Figure 4.6: Survival rate of SOM1 after exposure to MBG_SD_Ag2%, MBG_SG_Ag2% and related extracts after 1 day, 3 days and the 8 days of soaking

The evident difference between the two experimental conditions might be ascribed to the presence of Ag compounds, as described in chapter 3: the wide-angle XRD spectra, reported in section 3.3.2.6a and 3.3.1.3a, evidenced the

formation of AgBr and AgO₂ clusters in MBG_SG_Ag2% and in MBG_SD_Ag2% respectively.

Several studies investigated the antimicrobial potential of silver-containing materials [6–8]. Never the less, the mechanism by which the silver affects the bacteria viability is not well understood and, moreover, the difference between the bactericidal activity of the silver nanoparticles and of the silver in ionic form still represents an open issue [9,10]. Several authors speculated that the presence of metallic silver cluster embedded in a matrix (*e.g.* silica glass [6,10]) showed remarkable antibacterial activity through the release of Ag⁺ from the clusters. In this frame, Ruparelia et al. [9] asserted that the antibacterial results of silver nanoparticles against both *Gram positive* and *Gram negative* bacteria strains were ascribed to the double effect of the nanoparticles themselves and the Ag⁺ released from the nanoparticles. It seems that the nanoparticles caused rupture of the plasma membrane and represented a continue source of silver ions which, by attaching to the negatively charged bacterial wall, led to the protein inactivation and bacteria death [9,10].

Since AgO₂ clusters were revealed in the MBG_SD_Ag2%, the same explanation could be done for the antibacterial results of MBG_SD_Ag2% assuming that the AgO₂ clusters are whether on the particle surface or in an area accessible to the medium allowing the ion diffusion.

Concerning the MBG_SG_Ag2%, the good antibacterial results of the first experimental condition could be ascribed to the presence of silver bromide clusters formed during the synthesis due to the reaction between the bromide present in CTAB surfactant and the AgNO₃. Previously Sambhy and co-authors [11] realized silver bromide nanoparticles/polymer composites with the aim to produce an antibacterial material. The use of silver bromide in place of elemental silver and soluble silver salt should increase the long-lasting release of Ag⁺ ions. We can conclude that, in our study, the presence of silver bromide clusters induced the generation of active silver ions which provoked the reduction of SOM1 and S235 viable species.

References

- [1] M.E. Olson, A.R. Horswill, Staphylococcus aureus osteomyelitis: Bad to the bone, *Cell Host Microbe*. 13 (2013) 629–631. doi:10.1016/j.chom.2013.05.015.
- [2] R. Serra, R. Grande, L. Butrico, A. Rossi, U.F. Settimio, B. Caroleo, B. Amato, L. Gallelli, S. De Franciscis, Chronic wound infections: The role of *Pseudomonas aeruginosa* and *Staphylococcus aureus*, *Expert Rev. Anti. Infect. Ther.* 13 (2015) 605–613. doi:10.1586/14787210.2015.1023291.
- [3] A. Bari, N. Bloise, S. Fiorilli, G. Novajra, M. Vallet-Regí, G. Bruni, A. Torres-Pardo, J.M. González-Calbet, L. Visai, C. Vitale-Brovarone, Copper-containing mesoporous bioactive glass nanoparticles as multifunctional agent for bone regeneration, *Acta Biomater.* 55 (2017) 493–504. doi:10.1016/j.actbio.2017.04.012.
- [4] D.S. Morais, S. Fernandes, P.S. Gomes, M.H. Fernandes, P. Sampaio, M.P. Ferraz, J.D. Santos, M.A. Lopes, N. Sooraj Hussain, Novel cerium doped glass-reinforced hydroxyapatite with antibacterial and osteoconductive properties for bone tissue regeneration, *Biomed. Mater.* 10 (2015) 55008. doi:10.1088/1748-6041/10/5/055008.
- [5] S. Shruti, A.J. Salinas, G. Malavasi, G. Lusvardi, L. Menabue, C. Ferrara, P. Mustarelli, M. Vallet-Regí, Structural and in vitro study of cerium, gallium and zinc containing sol-gel bioactive glasses, *J. Mater. Chem.* 22 (2012) 13698–13706. doi:10.1039/c2jm31767b.
- [6] M. Kawashita, S. Tsuneyama, F. Miyaji, T. Kokubo, H. Kozuka, K. Yamamoto, Antibacterial silver-containing silica glass prepared by sol-gel method, *Biomaterials.* 21 (2000) 393–398. doi:10.1016/S0142-9612(99)00201-X.
- [7] C. Marambio-Jones, E.M.V. Hoek, A review of the antibacterial effects of silver nanomaterials and potential implications for human health and the environment, *J. Nanoparticle Res.* 12 (2010) 1531–1551. doi:10.1007/s11051-010-9900-y.
- [8] C. Dai, Y. Yuan, C. Liu, J. Wei, H. Hong, X. Li, X. Pan, Degradable, antibacterial silver exchanged mesoporous silica spheres for hemorrhage control, *Biomaterials.* 30 (2009) 5364–5375. doi:10.1016/j.biomaterials.2009.06.052.
- [9] J.P. Ruparelia, A.K. Chatterjee, S.P. Duttagupta, S. Mukherji, Strain specificity in antimicrobial activity of silver and copper nanoparticles, *Acta Biomater.* 4 (2008) 707–716. doi:10.1016/j.actbio.2007.11.006.
- [10] N. Gargiulo, A.M. Cusano, F. Causa, D. Caputo, P.A. Netti, Silver-containing mesoporous bioactive glass with improved antibacterial properties, *J. Mater. Sci. Mater. Med.* 24 (2013) 2129–2135. doi:10.1007/s10856-013-4968-4.
- [11] A. Sambhy, Varun; MacBride, MM; Peterson, BR; Sen, Silver bromide nanoparticle/polymer composites: Dual action tunable antimicrobial materials, *J Am Chem Soc.* 128 (2006) 9798–9808. doi:10.1021/ja061442z.

CHAPTER 5

Biological assessment of optimized ion-containing nanomatrices

5.1 Introduction

After the optimization of the synthesis procedures and the confirmation of the ion incorporation and the related release properties, the optimized nanomatrices were tested in order to assess their biological effect. As stated in section 2.8 of the “Materials and methods” chapter, different assays were performed to investigate the effect on cell viability and the antibacterial properties of the ion-substituted MBGs.

To this purpose, the biocompatibility assays, which involved both a qualitatively and a quantitatively evaluation, were carried out at *Nobil Bio Ricerche Srl*. As widely explained in “Materials and methods” chapter, the cytocompatibility of copper, cerium and silver containing nanomatrices was studied through the direct observation under the inverted microscope and MTT measurement using fibroblast L929 cells. Specifically, in this chapter, sub-paragraphs 5.1.1.1a, 5.1.1.2, 5.1.2 and 5.1.3 report the *in vitro* biocompatibility results obtained for the Cu-containing, Ce-containing and Ag-containing nanomatrices, respectively.

Based on the overall results in term of morphology, structural features, bioactivity, ion release properties and biocompatibility, the Cu-containing (2% mol) systems in the form of nanoparticles were further tested by means of different antibacterial assays and cytocompatibility test using an alternative more advanced model, based on a 3D skin construct. These tests, whose results are discussed in the subsections of 5.1.1 paragraph, were performed at the *Department of Materials Science and Engineering* of the *University of Sheffield* by *Prof. Sheila MacNeil*’s research group.

5.1.1 Biological assessment of Cu-containing nano- and micro-sized MBGs

Cu-substituted systems (MBG_SG_Cu2%, MBG_SD_Cu2%, MBG_SG_Cu0.5% and MBG_SD_Cu0.5%) were tested through the evaluation of the cell viability using fibroblast L929 cells (see the following section 5.1.1.1a and 5.1.1.2).

In addition, considering the promising ion release properties (see section 3.3.1.1b) and the evidenced antibacterial potential (section 4.2) of the MBG_SG_Cu2%, the latter was selected to investigate the antibacterial action against the formation and the disruption of the bacterial biofilms, and the related results are described in the paragraph 5.1.1.2.

Finally, the biological effect of this system was also investigated using a 3D skin model in order to analyse the biocompatibility and the antibacterial potential thought a more advanced biological model.

Due to the biocompatibility issues related to MBG_SG_Cu2% and MBG_SD_Cu2% samples, the particles containing lower amount of copper (0.5% mol) were produced and their biocompatibility was tested (section 5.1.1.2).

5.1.1.1a Biocompatibility of MBG_SG_Cu2% and MBG_SD_Cu2%

The biocompatibility evaluation was performed both through MTT assay and visual inspection, and the related results are shown in Figure 5.1.

As stated in “Materials and methods” chapter, the biocompatibility assessment was first carried out using a particle suspension at 1 mg/mL concentration through a Transwell[®] membrane insert. This concentration was selected in accordance to the *ISO 10993-5: 2009, Biological Evaluation of Medical Devices Tests for In vitro cytotoxicity*, which requires to evaluate the material performance in the worst case. At this concentration, the particles resulted cytotoxic on the L929, which evidenced a round morphology indicating the suffering and the death of the cells (data not shown).

Therefore, further tests with a reduced (100 µg/mL) suspension concentration were performed in order to target the therapeutic window of released copper ions.

By comparing the morphology of the fibroblast cells on polystyrene plate (image on the left in Figure 5.1B) with the fibroblast shape after the treatment with Cu-containing nanomatrices (middle and right images in Figure 5.1B), it could be asserted that negligible morphological changes occurred. MTT assay results, depicted in Figure 5.1A, confirmed the evidences of the optical image. The negligible cell viability reduction allowed to consider both MBG_SG_Cu2% and MBG_SD_Cu2% biocompatible at 100 µg/mL suspension concentration. The minimum value of cell viability to consider a material biocompatible is 70% [1], which is considerably smaller than the fibroblast viability percentages reached by contact with Cu-containing matrices.

An important consideration resulted from these results is that the biocompatibility response of copper-containing biomaterial is strongly dependent

on the Cu^{2+} released amount and on the condition used during the test (e.g. the sample concentration used for the test) [2,3]. To support this consideration, the same type of MBG particles containing strontium as therapeutic ion showed excellent biocompatibility using a concentration of 1 mg/mL, suggesting that the toxic response described above is linked to the substituting ion rather than to the particles themselves [1].

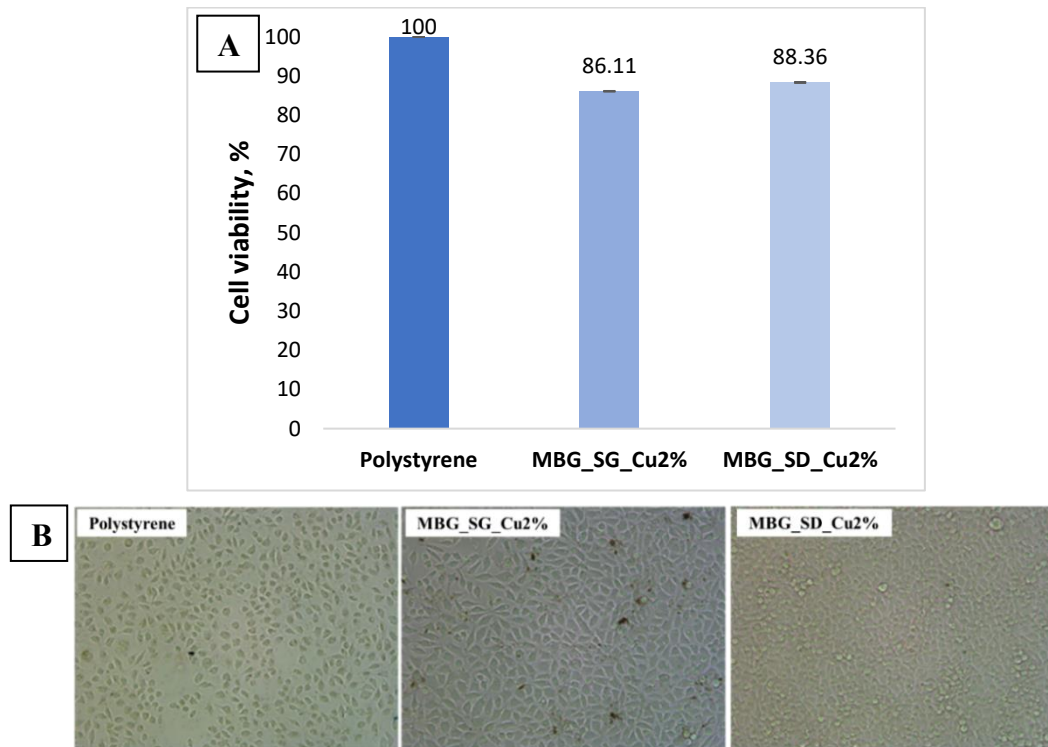


Figure 5.1: Quantification of cell viability through MTT assay for MBG_SG_Cu2% and MBG_SD_Cu2% compared with polystyrene (negative control) (A); optical images of cells after 72 h of incubation with MBG_SG_Cu2% and MBG_SD_Cu2% at concentration of 100 $\mu\text{g}/\text{mL}$, compared to cells seeded on polystyrene plate (B)

5.1.1.1b Antibacterial activity of MBG_SG_Cu2% against bacterial biofilms

S. aureus S235 and *P. aeruginosa* SOM1 were selected as bacterial strains to evaluate the antibacterial biofilm activity since they are the main biofilm developers [4].

As stated in “Materials and methods” chapter, the prevention of the biofilm formation and the disruption of the pre-formed biofilm were evaluated by incubating MBG_SG_Cu2% both at the same time of bacteria inoculum and after 48h. In both experiments the antibacterial potential was assessed through the evaluation of the bacteria metabolic activity (to investigate the level of living bacteria) and the measurement of the optical density (to study the biofilm mass).

Figure 5.2A and 5.2C depict the measurements of the metabolic activity and of the optical density in preventing biofilm formation experiment; whereas, Figure 5.2B and 5.2D display the investigation of the potential in disrupting bacterial

biofilm through metabolic activity and optical density. In both experiments, the controls were represented by bacteria inoculum.

Overall, the results suggest that the MBG_SG_Cu2% was highly effective against *P. aeruginosa* SOM1 in both preventive and disruptive bacterial biofilm, whilst the *S. aureus* S235 bacterial biofilm appears to be less affected by the presence of the Cu-containing particles.

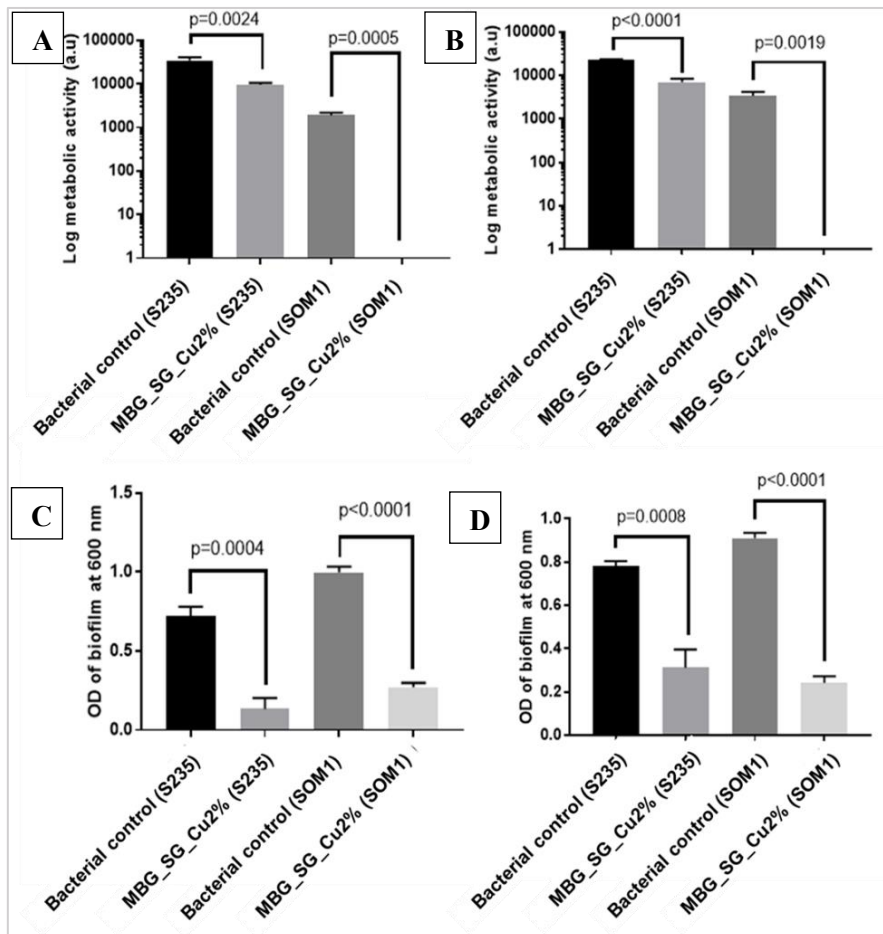


Figure 5.2: MBG_SG_Cu2% preventive action on the formation of biofilms using the measure of bacterial metabolic activity (A) MBG_SG_Cu2% ability to disrupt pre-existing biofilms using the measure of bacterial metabolic activity (B) MBG_SG_Cu2% preventive action on the formation of biofilms using the measure of optical density of the biofilm with higher values indicating greater biofilm formation (C) MBG_SG_Cu2% ability to disrupt pre-existing biofilms using the measure of optical density of the biofilm with higher values indicating biofilm formation to larger extent (D). n=3, error bars = SEM, ANOVA statistics

The different antibacterial effect of MBG_SG_Cu2% against S235 and SOM1 could be tentatively ascribed to an increase in *S. aureus* cell density [5] which provokes a higher resistance to killing. In this regard, further investigations are needed in order to fully explain the mechanisms involved in the antibacterial biofilm activity.

5.1.1.1c Biological assessment of MBG_SG_Cu2% on 3D skin models

The biocompatibility of MBG_SG_Cu2% was further tested on 3D skin construct, prepared according to the procedure described by MacNeil et al. [6] in order to assess the potential cytotoxicity in a more physiologically relevant 3D model.

As reported in “Material and methods”, 3D skin model was incubated with 200 μ L of MBG_SG_Cu2% dispersed in PBS (concentration of 100 μ g/ml) for 24h. Incubation of 3D skin model with 5x5 mm section of Acticoat Flex 3[®] (the gold standard in the treatment of infected wound) was also conducted and results used as comparison.

Figure 5.3 confirms the cytocompatibility of Cu-substituted system which causes only a slight decrease in cell metabolism compared to the untreated 3D skin construct. At variance, the commercially available Ag-containing dressing demonstrated high toxic effect on the cell metabolism using the 3D tissue engineered skin construct.

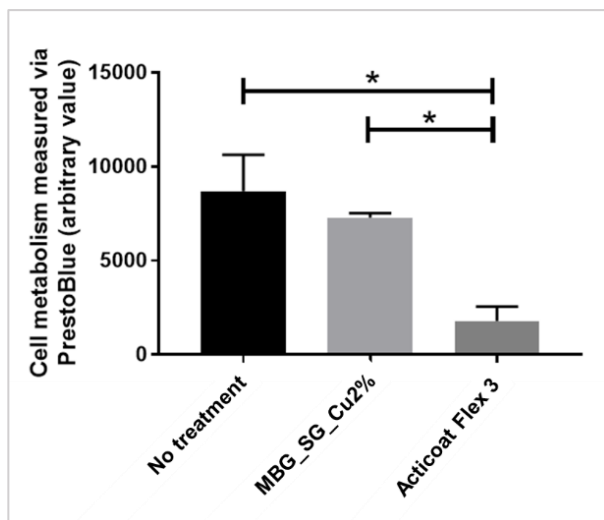


Figure 5.3: Cytotoxicity of MBG_SG_Cu2% sample and industrial standard Acticoat Flex 3[®] after 24 h of incubation with the tissue engineered skin models

After confirming the cytocompatibility of the MBG_SG_Cu2% in 3D skin construct, its antibacterial potential (see section 5.1.1.1b) was explored in infected 3D skin model. As reported in section 2.8.3.3, the 3D skin models were artificially infected by SOM1 and S235 bacteria strains prior to the viable count test.

Figure 5.4 displays the bacteria CFU per gram of tissue after the treatment with the sample and the Acticoat Flex 3[®]. In particular, Figure 5.4A shows the ability of the matrix to prevent biofilm formation, Figure 5.4B, instead, the one to disrupt a pre-existing bacterial biofilm.

In contrast to the previous results shown in section 5.1.1.1b, the impact of MBG_SG_Cu2% against SOM1 biofilm was less pronounced than against S235 biofilm. As depicted in Figure 5.4, no significant differences were found between SOM1 bacteria control and the treated samples, both in preventive and disruptive biofilm experiments. The commercial standard Acticoat Flex 3[®], instead, showed

better results in both SOM1 biofilm experiments compared to the Cu-containing sample. Whilst, the MBG_SG_Cu2% resulted to be as effective as the Acticoat Flex 3[®] against S235 biofilm formation and disruption.

The similar effect against S235 and the better results against SOM1 of the commercially available Acticoat Flex 3[®] with respect to MBG_SG_Cu2% has to be evaluated considering the above biocompatibility results shown in Figure 5.3. In addition to better antibacterial properties, the silver ion dressing resulted also more toxic than the tested Cu-containing sample.

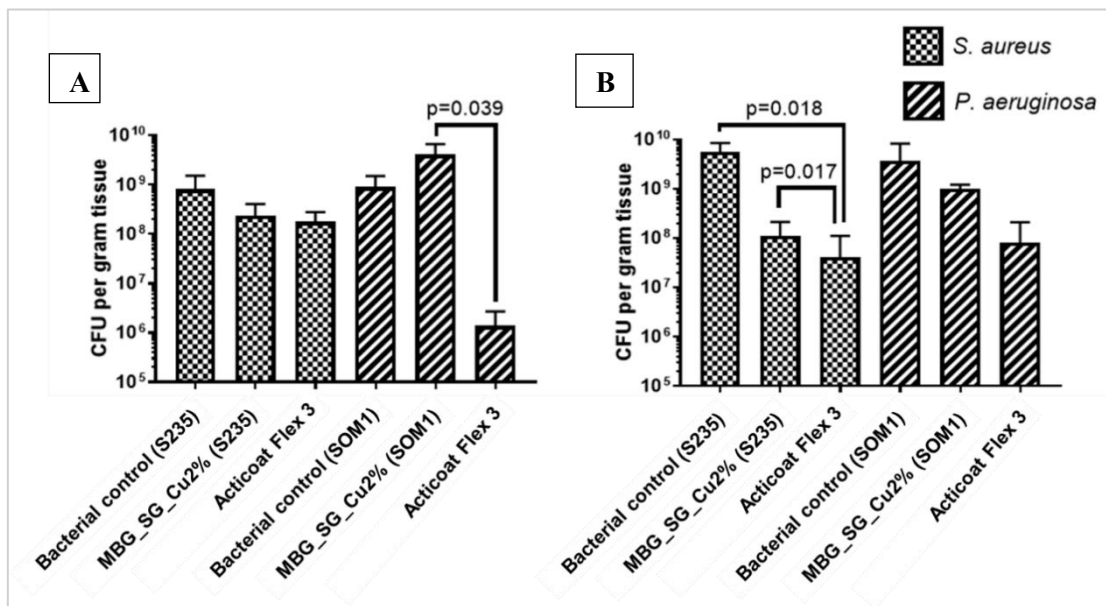


Figure 5.4: MBG_SG_Cu2% preventive action on the formation of biofilms on the infected 3D skin model (A) and MBG_SG_Cu2% ability to disrupt pre-existing biofilms on the infected 3D skin model (B). $n = 3$, plotting mean \pm standard deviation, ANOVA statistics used

In contrast to the obtained antibacterial result in 2D model, the increased resistance to treatment showed by *P. aeruginosa* in the 3D skin model may be associated to the deeper penetration of the *P. aeruginosa* into the dermal layers of the tissue engineered skin, as previously observed by Shepherd et al. [7], which accounted for a weaker antibacterial action played by the Cu-containing nanomaterials.

5.1.1.2 Biocompatibility test results of MBG_SG_Cu0.5% and MBG_SD_Cu0.5%

Due to the biocompatibility issues related to copper (2% mol) containing nanomaterials, the particles containing lower amount of copper (0.5% mol) were analysed in accordance to the *ISO 10993-5: 2009, Biological Evaluation of Medical Devices Tests for In vitro cytotoxicity*.

The first qualitative investigation using an inverted microscope (data not shown) demonstrated that nanomaterials containing lower amount of incorporated copper resulted more biocompatible, thus allowing to use a major amount of powder (1 mg/mL) without showing a toxic effect.

5.1.2 Biocompatibility test results of Ce-containing nanomatrices

The same quantitative and qualitative investigations were performed on cerium-containing particles at the facilities of *Nobil Bio Ricerche Srl*.

In Figure 5.5B the healthy status of fibroblast L929 cells in contact with 1 mg/mL of 1% and 2% mol of Ce-containing MBG_SG and SD was confirmed by the cell morphology. By comparing the L929 shape deposited on polystyrene plates with the L929 morphology after the treatment with the Ce-containing nanomatrices, no relevant differences were observed.

These data were confirmed by MTT test (Figure 5.5A) where 1% and 2% mol of Ce-modified systems demonstrated excellent biocompatibility: compared to polystyrene controls, the Ce-substituted systems seem to stimulate fibroblast proliferation.

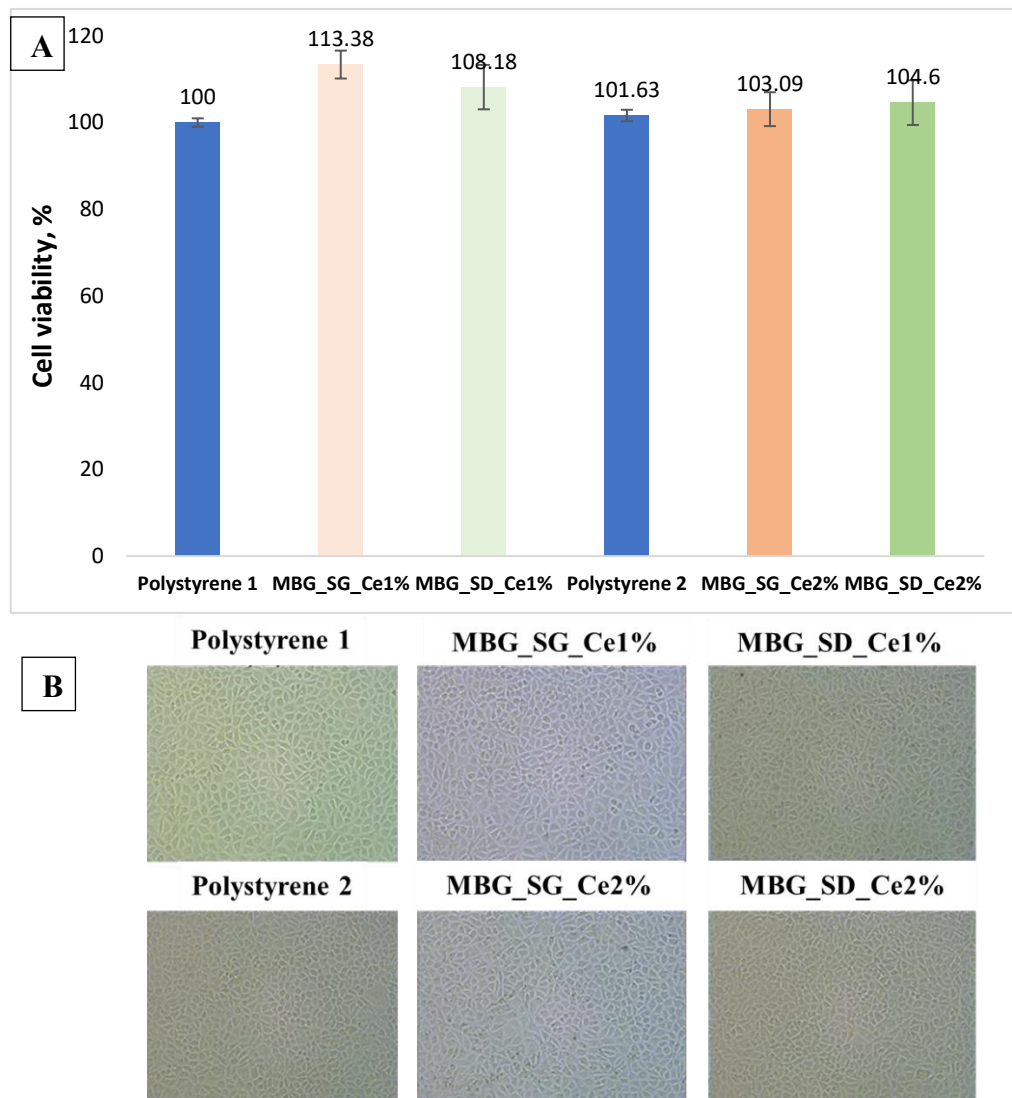


Figure 5.5: Quantification of cell viability through MTT assay for MBG_SG_Ce1%, MBG_SD_Ce1%, MBG_SG_Ce2% and MBG_SD_Ce2% compared with polystyrene (negative control) (A); optical images of cells after 72 h of incubation with MBG_SG_Ce1%, MBG_SD_Ce1%, MBG_SG_Ce2% and MBG_SD_Ce2% at concentration of 1 mg/mL, compared to cells seeded on polystyrene plates (B)

Although the promising data on biocompatibility, Ce-containing matrices were not further investigated in terms of antibacterial tests, due to the scarce ion release properties of all the Ce-modified systems. Besides, in the literature, the best approach to obtain antibacterial effect in Ce-containing systems consists in the incorporation of ceria particles instead of cerium in ionic form within the MBG glass framework [10–12]. In this regard, further studies need to be considered.

5.1.3 Biocompatibility test results of Ag-containing nanomaterials

As already presented for the Cu-containing and Ce-containing samples, the first test performed on nanomaterials containing 0.1% mol and 2% mol of silver was the biocompatibility assay using fibroblast L929.

Ag-containing systems showed strong cytotoxicity effect both in the form of micro- and nano-particles. The visual inspection using the inverted microscope (Figure 5.6) evidenced fibroblast cells with round shape completely detached from the plate, demonstrating the suffering state of the cells after the contact with MBG_SG_Ag_2%.

Moreover, the MTT assay (Figure 5.7) confirmed the high toxicity of the particles: less than 20% of cell viability was encountered with MBG_SG_Ag_2%.

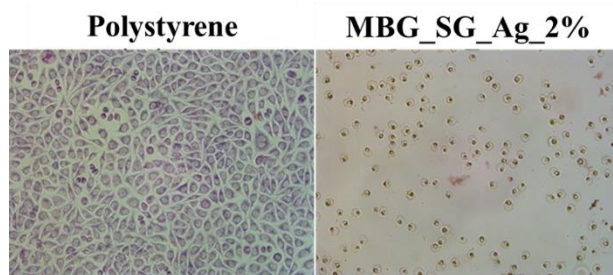


Figure 5.6: Optical images of cells after 72 h of incubation with MBG_SG_Ag_2%, at concentration of 1 mg/mL, compared to cells seeded on polystyrene plates

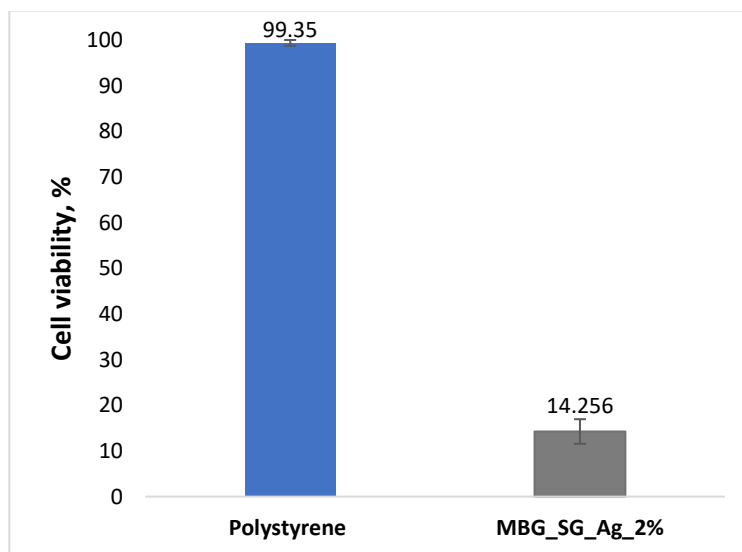


Figure 5.7: Quantification of cell viability through MTT assay for MBG_SG_Ag2% compared with polystyrene (negative control)

Since the biocompatibility is considered a key aspect for any biomedical application, no further tests were performed using the silver-containing samples.

5.2 Final considerations

The biological assessment performed on the optimized ion-containing nanomatrices leads to the following considerations:

- The cytotoxicity of MBG_SG_Cu2% and MBG_SD_Cu2% at 1 mg/mL suspension concentration and the biocompatible response of the same nanomatrices at 100 µg/mL suspension concentration allowed to conclude that the biocompatibility response of Cu-containing MBGs is strongly dependent on the concentration used during the test and on the Cu²⁺ released amount;
- The MBG_SG_Cu2% was highly effective against *P. aeruginosa* SOM1 in both preventive and disruptive bacterial biofilm;
- The tests conducted using a 3D skin construct further confirmed the biocompatibility of MBG_SG_Cu2% (100 µg/ml) and its antibacterial effect;
- The biocompatibility showed by the particles containing lower amount of copper (0.5% mol) at 1 mg/mL suspension concentration suggested the possibility to tailor the biological response of the Cu-containing nanomatrices by incorporating different amount of therapeutic ion;
- Ce-containing nanomatrices demonstrated excellent biocompatibility but, due to the poor ion release properties, they were not tested by means of antibacterial tests;
- Ag-containing systems evidenced strong cytotoxicity.

In conclusion, the Cu-containing nanomatrices are the most promising systems due to the possibility to find a proper therapeutic window within which they resulted both biocompatible and antibacterial.

Among the Cu-containing nanomatrices, the MBG_SG_Cu0.5% and MBG_SD_Cu0.5%, providing the best results in terms of biocompatibility, deserve to be taken into account for further investigations, especially in terms of multifunctional systems able to release both therapeutic ion and specific drugs.

In fact, since mesoporous matrices could be used as drug delivery systems [8,9], the possibility to use a major amount of powder (1 mg/mL) without showing a toxic effect, could be considered in view of potential drug loading inside the matrices, since a higher amount of powder, corresponding to a higher amount of drug.

References

- [1] S. Fiorilli, G. Molino, C. Pontremoli, G. Iviglia, E. Torre, C. Cassinelli, M. Morra, C. Vitale-Brovarone, The incorporation of strontium to improve bone-regeneration ability of mesoporous bioactive glasses, *Materials (Basel)*. 11 (2018). doi:10.3390/ma11050678.
- [2] R. Koohkan, T. Hooshmand, M. Tahriri, D. Mohebbi-Kalhari, Synthesis, characterization and in vitro bioactivity of mesoporous copper silicate bioactive glasses, *Ceram. Int.* 44 (2018) 2390–2399. doi:10.1016/j.ceramint.2017.10.208.
- [3] X. Wang, F. Cheng, J. Liu, J.H. Smatt, D. Gepperth, M. Lastusaari, C. Xu, L. Hupa, Biocomposites of copper-containing mesoporous bioactive glass and nanofibrillated cellulose: Biocompatibility and angiogenic promotion in chronic wound healing application, *Acta Biomater.* 46 (2016) 286–298. doi:10.1016/j.actbio.2016.09.021.
- [4] L. Drago, M. Toscano, M. Bottagisio, Recent evidence on bioactive glass antimicrobial and antibiofilm activity: A mini-review, *Materials (Basel)*. 11 (2018) 1–11. doi:10.3390/ma11020326.
- [5] A.M.Y.L. Spoering, K.I.M. Lewis, Biofilms and planktonic cells of *Pseudomonas aeruginosa* have similar resistance to killing by antimicrobials, *J. Bacteriol.* 183 (2001) 6746–6751. doi:10.1128/JB.183.23.6746.
- [6] S. MacNeil, J. Shepherd, L. Smith, Production of Tissue-Engineered Skin and Oral Mucosa for Clinical and Experimental Use, in: *3D Cell Cult.*, 2011: pp. 129–153. doi:10.1007/978-1-60761-984-0.
- [7] J. Shepherd, I. Douglas, S. Rimmer, L. Swanson, S. MacNeil, Development of Three-Dimensional Tissue-Engineered Models of Bacterial Infected Human Skin Wounds, *Tissue Eng. Part C Methods*. 15 (2009) 475–484. doi:10.1089/ten.tec.2008.0614.
- [8] E. Peretti, I. Miletto, B. Stella, F. Rocco, G. Berlier, S. Arpicco, Strategies to Obtain Encapsulation and Controlled Release of Pentamidine in Mesoporous Silica Nanoparticles, *Pharmaceutics*. 10 (2018) 195. doi:10.3390/pharmaceutics10040195.
- [9] I. Izquierdo-Barba, M. Vallet-Regi, Mesoporous bioactive glasses: Relevance of their porous structure compared to that of classical bioglasses, *Biomed. Glas.* 1 (2015) 140–150. doi:10.1515/bglass-2015-0014.
- [10] O. Zeyons, A. Thill, F. Chauvat, N. Menguy, C. Cassier-Chauvat, C. ORéAR, J. Daraspe, M. Auffan, J. Rose, O. Spalla, Direct and indirect CeO₂ nanoparticles toxicity for *Escherichia coli* and *Synechocystis*, *Nanotoxicology*. 3 (2009) 284–295. doi:10.3109/17435390903305260.
- [11] S. Das, S. Singh, J.M. Dowding, S. Oommen, A. Kumar, T.X.T. Sayle, S. Saraf, C.R. Patra, N.E. Vlahakis, D.C. Sayle, W.T. Self, S. Seal, The induction of angiogenesis by cerium oxide nanoparticles through the modulation of oxygen in intracellular environments, *Biomaterials*. 33 (2012) 7746–7755. doi:10.1016/j.biomaterials.2012.07.019.
- [12] C. Xu, X. Qu, Cerium oxide nanoparticle: A remarkably versatile rare earth nanomaterial for biological applications, *NPG Asia Mater.* 6 (2014) e90. doi:10.1038/am.2013.88.

CHAPTER 6

Conclusions and perspectives

The activities conducted during the present PhD work were mainly aimed to produce a library of mesoporous inorganic nanomatrices containing therapeutic ions for biomedical applications.

In particular, the first aim of this PhD thesis was to produce mesoporous bioactive glass (MBG) particles based on silica-calcium oxide composition and containing different amount of therapeutic ions for the design of advanced biomedical devices for tissue regeneration (*i.e.* delayed bone healing and non-healing skin wounds).

The second aim was to find the best synthesis procedures in terms of materials properties, scalability, safety and cost-efficiency.

The third objective was to investigate the therapeutic potential of these nanomatrices through different *in vitro* biological assessments, including biocompatibility assays and antibacterial tests.

Specifically, MBGs in the binary system ($\text{SiO}_2\text{-CaO}$) were produced by using different synthesis routes, in order to obtain nanomatrices with high specific surface area (in the range of hundreds m^2/g) and accessible pore volume, characterised by different pore size and particle size/morphology. In details, a selection process of the synthesis procedures was performed in order to identify the best routes in terms of morphology, composition, ion release properties and scalability for obtaining micro- and nano-sized particles.

In particular, with the aim to produce particles in the range of 100-200 nm with pores ranging between 2 and 4 nm, different routes were tested, and the selection process led to identify a water-based ammonia-catalysed sol-gel procedure as the most promising route in terms of reproducibility, structural results and final chemical composition. Moreover, a water-based spray-drying procedure carried out under mild acidic conditions was adopted to produce microspheres with pores of around 8 nm due to its easiness of scalability to an industrial environment.

On the basis of the obtained results, it can be affirmed that the substitution of small amount (1%, 2% or 5% mol) of CaO with specific ion precursors (i.e. copper, cerium and silver) did not significantly affect the MBG morphology and the textural properties. Moreover, the inclusion of different metallic ions did not hamper the deposition of HA layer.

In details, the selection process of the synthesis routes started by adapting a method described in the literature by Kim and co-workers which consisted of an ultrasonicator-assisted sol-gel procedure using methanol solution as solvent. This first synthesis route allowed to obtain spherical ion-containing particles with size ranging between 100-200 nm and pores around 3 nm characterized by high specific surface area values and pore volume. Subsequently, the water-based sol-gel procedures were found to be more suitable for the up-scaling and represented a valid alternative route to the methanol-based procedure. Moreover, during the optimization process, it was proved that the ultrasonicator, introduced on the basis of the literature, represented a further energy-consuming step without providing substantial positive results in terms of morphological, textural and bioactive properties.

Based on these findings, the final selection of the synthesis routes led to the optimization of the following two procedures:

- The base-catalysed water-based sol-gel route to obtain mesoporous spheroidal particles with quite uniform size ranging between 100 and 200 nm, pores of about 4 nm and excellent specific surface area values;
- The spray-drying route produced spherical, well dispersed mesoporous particles with size mostly ranging between 500 nm and 5 μ m and pores around 8 nm.

The structural/morphological characterization, the ion release and the bioactivity tests performed on the produced nanomatrices drove to the following conclusions:

- The ion incorporation was successful in all the nanomatrices, with superior ion incorporation yield for spray-dried samples;
- The ion release properties of the samples tested in different media (SBF, DMEM and Tris HCl) demonstrated that the species contained in DMEM medium (NaHCO₃, glucose, HEPES, sodium pyruvate) may interfere with the surface ion-exchange reactions, slowing down the ion release kinetics.

Among all the produced compositions, the most promising nanomatrices in terms of ion release capability and reproducibility are the copper-substituted MBGs both in the form of micro- and nano-sized particles. At variance, the Ce-containing samples (with two different cerium concentrations) demonstrated a very low amount of released ion and the reason of this behaviour was ascribed to the incorporation of cerium within the silica framework through the formation of strong chemical bonds with siloxanes, which improved the chemical stability of the resulting glass and can be accounted for the negligible release properties.

The biological assessment performed on the optimized ion-containing nanomatrices evidenced that the cytocompatibility depends on the specific therapeutic ion and the suspension concentration used during the test. In details, the Cu-containing nanomatrices resulted biocompatible at 100 µg/mL suspension concentration, the Ce-containing nanomatrices demonstrated excellent biocompatibility, the Ag-containing systems evidenced, instead, strong cytotoxicity.

Among the Cu-containing nanomatrices, the MBG_SG_Cu0.5% and MBG_SD_Cu0.5%, providing the best results in terms of biocompatibility, deserve to be taken into account for further investigations, especially in terms of multifunctional systems able to release both therapeutic ion and specific drugs.

Furthermore, the optimized nanomatrices containing ion with recognised antibacterial properties were investigated through the antibacterial viable count test using two different experimental conditions. In detail, the antibacterial potential of suspended nanomatrices (named “suspension”) and the antibacterial efficacy of the released ion extracts (named “extract”) were tested in order to ascribe the therapeutic effect to the particle itself or to the action of specific ion, or to a combination of both effects.

In details, the copper-containing samples evidenced remarkable differences in the results of the antibacterial test performed against *Gram positive* and *Gram negative* bacteria strains with a reduction of the survival rate of *S. Aureus* (*Gram positive*) up to almost zero and a less effectiveness against *P. Aeruginosa* (*Gram negative*). The different sensitivity shown by the bacteria strains was attributed to the differences in the bacteria structure and surfaces.

Concerning the cerium-containing nanomatrices, although the antibacterial test demonstrated a reduction of both *Gram positive* and *Gram negative* bacteria strains, it was not possible to find a clear correlation between the results, the experimental conditions and the bacteria structure.

Finally, the silver-containing nanomatrices showed a strong correlation between the antibacterial results and the specific experimental condition, evidencing that the antibacterial effect of silver-containing particles (suspension) was more effective in reducing the bacteria viable colonies compared to the extracts. The antibacterial effect of the particles was ascribed to the presence of insoluble and accessible metal Ag compounds which, through the direct contact and the formation of interactions between silver and the sulfhydryl groups of the bacterial wall, led to the reduction of *Gram positive* and *Gram negative* viable species by blocking their respiration.

The combination of biocompatibility and antibacterial results further confirmed that the Cu-containing nanomatrices are the most promising systems due to the possibility to find a proper therapeutic window within which they resulted both biocompatible and antibacterial.

The high amount of silanol groups, the excellent specific surface area, the high pore volume and the opportunity to tailor the pore size further widen the possible applications of these biomaterials through the incorporation of specific drugs.

Besides, the possibility to disperse these nanomatrices in materials of different nature, without the risk to lose the aforementioned advantages, paves the way to the creation of several hybrid formulations.

In this context, the incorporation of the produced nanomatrices in an injectable gel could lead to the development of a new formulation able to release *in situ* and keep in place the therapeutic ions through a non-invasive procedure.

The combination of these inorganic bioactive phases, as well as of other inorganic fillers (i.e. hydroxyapatite or calcium phosphate) with various polymeric matrices (i.e. natural and synthetic hydrogels) could be exploited in order to design composite scaffolds to be used in different biomedical applications. These hybrid materials could combine the flexibility of the polymer matrix with the stiffness and the bioactive property of the inorganic phase. Moreover, the possibility to incorporate and deliver both therapeutic ions and drugs makes these composites versatile agents. Considering the MBG key role in the bioactive response, the application in bone tissue engineering is certainly one of the most promising field of action of these new materials. Among the bone tissue engineering, the use in non-load-bearing bone applications (such as in dentin pulp regeneration) deserves special attention and further investigations.

Apart from the bone tissue application, the bioactive inorganic/organic composites could represent a substantial innovation also in soft tissue application (i.e. diabetic wound healing). Due to the potentiality to induce angiogenesis, to impart antibacterial activity and to tailor the mechanical properties, these composites represent excellent candidates as wound dressings able to promote a healthy wound healing process.

Due to the essential requirement of resembling the extracellular matrix pattern of both hard and soft tissue application, the innovative additive manufacturing techniques represent one of the most interesting fabrication routes to tailor the proportion of the organic/inorganic phases and to design specific structures able to better mimic the natural ones.

In conclusion, the ion-containing MBGs could be exploited in order to enrich specific formulations and create hybrid systems to be used in several kinds of tissue treatments: the combination with different materials leads to the creation of versatile complex structures which resemble the natural ones.

Ringraziamenti

Ho trascorso tutti i mesi della tesi magistrale con la voglia di scrivere i ringraziamenti. Ora mi ritrovo a dover scrivere la stessa parte con la stessa voglia ma con più paura. Forse perché sono le uniche righe scritte in italiano.

Ringrazio prima di tutto le mie supervisors, Chiara Vitale Brovarone e Sonia Fiorilli per questi anni, per l'opportunità che mi hanno dato, per le cose che ho imparato e l'esperienza che ho maturato.

Ringrazio inoltre tutti i partner del progetto Mozart per i meeting, gli scambi di e-mail e di idee che ha permesso di sviluppare i materiali di cui ho tanto parlato nelle pagine precedenti. Ringrazio in particolare la Prof. Sheila MacNeil e il suo gruppo per l'ospitalità e per la l'opportunità di crescita.

Desidero ringraziare tutte le persone con cui ho collaborato strettamente e che hanno permesso di aggiungere dati significativi al lavoro di tesi, in particolar modo Giorgio Iviglia, Elisa Torre e Marco Morra (NBR Ricerche), Anthony Bullock e Joey Shepherd (Sheffield University) e Emma Bjork (Nanolith).

Un ringraziamento pieno di amore va ai miei genitori e a mio fratello, coloro che hanno visto, capito e percepito ogni mio stato d'animo, ogni mia delusione, ogni mia gioia. Coloro che mi hanno fatto nascere e crescere, che sono stati presenti in ogni cambiamento profondo sia della mia vita che del mio carattere. Che mi amavano per la bambina capricciosa, testarda e piagnucolosa che ero e che mi amano per la donna forte, solare ma sempre testarda che sono diventata. Lo sapevo già, ma ora ne sono ancora più convinta, voi mi appoggerete e sosterrete sempre, con tutto l'amore possibile, in qualsiasi mia scelta, qualunque essa sia.

Grazie a tutta la mia famiglia e ai miei nonni, perché solo con delle radici salde si può crescere bene ed andare oltre. Grazie a voi, nonni miei, perché ho sempre fatto della vostra umiltà la mia più grande dote, perché voi siete stati sempre la mia roccia, anche ora con tanti acciacchi e poca memoria. Grazie nonno Gigi e zio Mario, il tempo passa ma voi siete sempre lì, impressi nella mia memoria e nel mio cuore, consapevole che oggi avreste pianto di felicità ancora una volta per me.

Grazie alla mia nuova piccola famiglia, Denise, colei che "sa di casa", che mi coccola e mi rimprovera in modo unico, che mi vizia e che cerca affetto come solo le sorelle sanno fare. Sì, tu sei la sorella che non ho mai avuto. Ti ho voluto bene dal primo giorno, con il tuo modo di essere così vicino al mio. Così riservata e rispettosa, così divertente e bambina. Ti voglio bene Deni, e se dico che "una coinquilina è per sempre" è proprio perché ho incontrato te.

Grazie alle mie compagne di avventura e al nostro principe azzurro (Giorgia, Giulia, Giorgia, Carlotta, Stefania, Maria Chiara, Enrico e Federica) per questi

indimenticabili anni. Questo gruppo che ho visto nascere è cresciuto e cambiato nel tempo ma ognuno di noi è stato bravo a ristabilire l'equilibrio, sempre diverso, necessario quando si passano tutte queste ore insieme. Voglio ringraziarvi uno ad uno, perché ve lo meritate.

Grazie Mamy per gli insegnamenti che mi hai dato, per le tue conoscenze e per la tua praticità. Grazie per aver sempre nascosto nervosismi ed ansie, grazie per la preziosa guida che hai rappresentato per me.

Grazie Giuli per essere stata la mia prima tesista e per avermi insegnato ed aiutato tanto. Grazie per esserci sempre stata per me, grazie per aver gioito davvero con il cuore per me e per aver sofferto con me. Grazie per avermi dimostrato un bene inimmaginabile.

Grazie Piccola Lordina per il tuo ritmo che tanto ho preso in giro ma altrettanto ho invidiato, per la tua grazia e la tua finezza che tanto sono lontane da me. Grazie per i momenti in cui hai abbandonato la tua finezza e mi hai fatto credere che la mia vicinanza ti avesse influenzato.

Grazie Carlottina per le lezioni di chimica, gli insegnamenti e le gaffe che hanno caratterizzato questi nostri anni insieme. Grazie per le ansie e le gioie condivise insieme. Grazie per i successi e gli insuccessi vissuti fianco a fianco.

Grazie Stefi, mia autista preferita. Vederti ogni mattina, a bordo della freccia bianca mi ha dato la forza di affrontare alcune delle giornate più brutte ed infinite passate qui dentro. Le nostre risate fino alle lacrime, le lacrime vere e proprie, i discorsi senza senso e quelli fin troppo profondi hanno permesso che tu entrassi a far parte della cerchia di persone che mai dimenticherò e sempre vorrò vicine a me.

Grazie Maria Chiara per i tuoi rimproveri inaspettati ma sempre giusti, per il tuo saper cambiare faccia e atteggiamento in modo repentino, per la tua serietà così lontana dalla mia stupidità ma che mi fa sentire tanto vicina a te.

Grazie Fede per tutta quella dolcezza e sensibilità che si nasconde dietro al tuo essere mascolino e finto aggressivo.

Grazie Enri, ex collega ma grande amico, confidente, consigliere. Grazie per tutto quello che mi hai dato in così poco tempo. Mi hai ascoltato, aiutato e compreso come solo i fratelli sanno fare. Mi hai fatto ridere fino alle lacrime e mi hai fatto ragionare offrendomi sempre un punto di vista completamente diverso. Mi hai "costretto" a conoscere il tuo mondo che ti rende così sensibile e che ora fa parte anche un po' di me.

Grazie Cri, Marti, Vero, Gian e Dlp, che avete fatto parte del mio inizio in questi laboratori, che mi avete fatto ridere e fatto sentire parte di un gruppo, che mi avete aiutato e supportato/sopportato.

Grazie alle mie amiche storiche, le Spice che sono sempre state presenti, che hanno sopportato ogni mio cambiamento di umore e soprattutto che mi sono state vicine nonostante i miei tanti periodi no, i miei periodi di mutismo. Grazie perché voi mi avete aspettato, perché mi avete dato modo e spazio per cambiare e non avete mai preteso spiegazioni. Grazie per i lunghi messaggi e le sporadiche uscite, per gli abbracci e per le serate. Grazie per rappresentare un punto saldo e fermo nella mia vita nonostante la distanza.

Grazie Betta, Giuli e Ale. Voi, in modo completamente diverso l'una dall'altra avete contribuito a rendere speciali questi anni a Torino e questa mia esperienza. Betta tu sei l'amica che c'è, sempre. Ci sei per ridere e per piangere, sei colei che più mi è stata vicino in uno dei momenti più complicati per me, mi hai visto cambiare, fianco a fianco, mi hai visto sbagliare tante volte ma hai anche visto quanto questi sbagli mi abbiamo fatto crescere. Mi hai accompagnato in questa crescita riuscendo a starmi vicino e a capirmi anche senza parlare.

Grazie Giuli e Ale per le bevute, per le serate, per le passeggiate in Santa Rita, per i gelati alla Romana, per gli spritz al baracchino dello stadio, per le cene a base di friselle con pomodoro e vino rosso. Grazie per le serate da Botz e per il nostro essere sempre in allerta. Grazie per le chiacchierate infinite e profonde, per le battute e per le risate a squarciagola. Grazie per il bene e la stima che mostrate nei miei confronti e grazie per il vostro bisogno di consigli.

Grazie Uba, Cascio, Michi, Luchino, Pettino, Ciane e Mari. Persone diverse di uno stesso gruppo, mie guide, consiglieri, amici veri, entrati nella mia vita in momenti diversi, ma di cui non posso più fare a meno.

Grazie a "Quelli del quindi", mia certezza e costanza.

Grazie Anto per la tua positività, per la tua gioia, per le tue fissazioni, per i tuoi abbracci e consigli. Grazie perché ci sei, sempre. Grazie perché sei quell'amico di cui avevo bisogno ma temevo non esistesse.

Grazie Terri, per esserti fatta conoscere e per aver condiviso con me le paure e le incertezze che pensavo non ti appartenessero. Grazie per capirmi senza bisogno di parole.

E infine, grazie a me. Alla mia testardaggine, alla mia confusione, alle mie incertezze, alla mia forza. Grazie ai miei limiti di cui sto prendendo sempre più coscienza, che non mi stanno buttando giù ma, anzi, mi stanno dando ancora modo di riscoprimi e di cambiare, cercando di diventare quello che vorrei essere, cercando di non essere influenzata da ciò che qualcuno ha deciso per me.

Grazie a voi che avete reso questo percorso lungo ma corto allo stesso tempo, che avete fatto parte, artefici o no, di ogni momento divertente, emozionante, nervoso, ansioso, arrabbiato.

E grazie a me che ho vissuto tutto a mille, come faccio sempre.